Processing and characterization of Cu-Al_2O_3 and Al-Al_2O_3 composites: an evaluation for micro- and nano-particulate reinforcements

A Thesis submitted in partial fulfilment of the

requirements for the degree of

DOCTOR OF PHILOSOPHY

by

Khushbu Dash

(Roll No: 509mm101)

Department of Metallurgical and Materials Engineering

National Institute of Technology, Rourkela

Rourkela – 769008

INDIA

January 2014

Processing and characterization of Cu-Al_2O_3 and Al-Al_2O_3 composites: an evaluation for micro- and nano-particulate reinforcements

January, 2014 **Khushbu Dash**

Supervisors

Prof. Bankim Chandra Ray

Prof. Debasis Chaira

“Dedicated to my parents”

Department of Metallurgical and Materials Engineering,
National Institute of Technology
Rourkela-769008
India

CERTIFICATE

This is to certify that the thesis entitled "**Processing and characterization of Cu-Al_2O_3 and Al-Al_2O_3 composites: an evaluation for micro- and nano- particulate reinforcements"** submitted by **Khushbu Dash** to National Institute of Technology, Rourkela is a record of bonafide research work under our supervision and is worthy of consideration for the award of the degree of Doctor of Philosophy of the Institute. The candidate has fulfilled all prescribed requirements for the thesis, which is based on candidate's own work and has not been submitted elsewhere for a degree or diploma.

Prof. Bankim Chandra Ray — Supervisor

Prof. Debasis Chaira — Co-supervisor

Acknowledgement

The research work for my PhD programme has been carried out in Department of Metallurgical and Materials Engineering, National Institute of Technology, Rourkela.

My supervisors Prof. Bankim Chandra Ray and Prof. Debasis Chaira have supported me for my PhD work unconditionally. I am heartily indebted to my supervisors for training me in my journey to achieve a respectable degree in Metallurgical and Materials Engineering. Prof. Bankim Chandra Ray has been an inextinguishable fire of inspiration to me from the days I had not joined his group for doctoral work. My journey with him started as a student-teacher and progressed day by day converting him as my guiding light in all spheres of life. I take the liberty to dedicate this section of my thesis to him and thank him from the bottom of my heart for all that he has given me. I will cherish all the moments of enlightenment he has shared with me. Undoubtedly, a free thinker and believer, I will always remember him for his attitude of pushing all limits for his dear students.

I would take the pleasure of thanking all my doctoral scrutiny committee members for fulfilling their duties of assessing my PhD work without fail.

I am grateful to our director Prof. Sunil Kumar Sarangi to get encouraged and motivated by a magnanimous personality like him who is a core academician.

I thank all our collaborators Prof. Bikramjit Basu, Indian Institute of Technology, Kanpur, Prof. Sidhartha Das, Indian Institute of Technology, Kharagpur, Dr Sidhartha Pradhan Institute of Minerals and Materials Technology, Bhubaneshwar for unconditional help, prompt attention and effective support to bring this thesis into existence. I also take the privilege to thank Prof Anindya Basu, National Insitute of Technology, Rourkela for helping me to conduct wear measurements.

I am also thankful to laboratory members of Department of Metallurgical and Materials Engineering, NIT Rourkela, especially, R. Pattanaik, S. Pradhan, U. K. Sahu and S. Hembram for constant practical assistance and help whenever required.

I acknowledge the discussions and work done with my labmates Suvin Sukumaran and Sujata Panda.

My parents Laxmi Prasad Dash and Swadhini Dash have been a constant source of inspiration for my perseverance during my PhD tenure. I am thankful to my brother Apurv Dash to run small errands whenever I needed him.

I am thankful to my beloved husband Nachiketa Mishra to support me in my concluding months of PhD and being the most precious gift of my life.

All errors and limitations remaining in this thesis are mine alone.

Khushbu Dash
(January 2014)

Abstract

Composites are formed by the physical association of matrix and reinforcement and possess intermediate properties of the components' it is constituted of. Metal matrix composites (MMCs) reinforced with ceramic particles furnishes ductility along with strength and has been into practice since decades. The applications cater the aerospace and automobile industries such as turbine rotatory machinery components, rocket turbine housing, cryostat, cryo-pump impeller and cryo-pump inducer. Powder metallurgy has been a conventional still inevitable technique to serve the automotive and aerospace industries with components of utmost importance. The powder metallurgy process consists of several steps which are crucial to the end products' properties. This work aims at investigating some of the steps to assess the microstructure and properties of copper and aluminium based composites varying the reinforcement particle size and volume fraction. Structural integrity is a vital factor of a composite which accounts for the physical intimate bonding of matrix and reinforcement. This factor varies with the fabrication parameters and techniques which are also fundamental for effective stress transmissibility from matrix to reinforcement. Structural integrity of a composite material also fluctuates within the service life of the material, for eg. during harsh and hostile environment thermal exposures.

The preliminary part of the work consists of evaluation of the effect of processing parameters on the properties of Cu-Al_2O_3 and Al-Al_2O_3 composites. The effect of blending and planetary milling processes (powder mixing techniques) on the distribution, particle size and sintering response of Cu-Al_2O_3 and Al-Al_2O_3 composites were studied. Milling was performed for 2, 5 and 10 hours and blending was performed for 2, 4 and 8 hours followed by investigation of dispersion, microstructure and particle size analysis as well as mechanical properties of the composite powders and composites sintered at 900°C (Cu-Al_2O_3) and 600°C (Al-Al_2O_3) temperatures.

The effect of sintering atmosphere on the microstructure and mechanical properties of Cu-Al_2O_3 composites have been discussed too. Nitrogen, argon and hydrogen atmospheres were used for sintering and the comparison in matrix and reinforcement compatibility as well as study of microstructure and mechanical properties were made. Synthesis of microcomposites was carried out by reinforcing 5, 10 and 15 volume % of alumina powder particles (average size~5.71µm) in copper matrix via conventional sintering using N_2, H_2 and Ar atmospheres.

Maximum Vickers hardness of 60, 75 and 80 was obtained when the Cu-15 volume % Al_2O_3 was conventionally sintered in N_2, Ar and H_2 atmosphere respectively. It has been observed that Cu-Al_2O_3 metal matrix composite shows poor mechanical properties when it is conventionally sintered in N_2 or Ar atmosphere compared to that in H_2 atmosphere.

The synthesis, characterization and mechanical properties evaluation of Cu-Al_2O_3 and Al-Al_2O_3 micro- and nano-composites fabricated by conventional and spark plasma sintering was done to compare the attributes between the traditional and advanced methods of sintering. Status of the interfacial integrity of Cu-Al_2O_3 and Al-Al_2O_3 micro- and nano-composites with the variation in sintering temperature were investigated.

Nanocomposites of 1, 3, 5 and 7 vol. % Al_2O_3 (average size<50nm) and microcomposites having compositions 5, 10, 15, 20 vol. % of Al_2O_3 (average size~10μm) reinforced in copper and aluminium matrix were fabricated by powder metallurgy route. All the Cu-Al_2O_3 specimens were sintered conventionally at different sintering temperatures (850°C, 900°C, 1000°C) whereas all the Al-Al_2O_3 specimens were sintered conventionally at (500°C, 550°C, 600°C) temperatures to study the effect of temperature on the process and progress of sinterability of the reinforced micro- and nano-particles in the matrix. These micro- and nano-composites were characterized using X-ray diffraction and scanning electron microscopy followed by density, microhardness and wear measurements. The compression and flexural tests were also carried out in order to investigate the mechanical behaviour of the micro- and nano-composites for a fixed optimum sintering temperature. Fractography of the 3-point bend specimens was performed to investigate the fracture behaviour of the micro- and nano-composites. The flexural test results showed that the ultimate flexural strength decreases and flexural modulus increases with increase in reinforcement content.

Nanocomposites consisting 0.5, 1, 3, 5, 7 volume % alumina (average size<50nm) and microcomposites having 1, 5, 20 volume % of alumina (average size~10μm) reinforced in copper and aluminium matrix were fabricated by spark plasma sintering technique at a temperature of 700°C (copper) and 500°C (aluminium) respectively and pressure of 50 MPa for a holding time of 5 minutes. These micro- and nano-composites have been characterized using X-ray diffraction, scanning electron microscopy and transmission electron microscopy followed by density, microhardness, nanoindentation hardness and wear measurements. Spark plasma sintering rendered high densification, higher microhardness and wear resistance

to the composites improving the physical integrity of matrix and reinforcement to an appreciable extent in comparison to conventional method of sintering. We have obtained 95.82% densification as well as 93.17 $HV_{0.3}$ and 124 $HV_{0.3}$ microhardness for spark plasma sintered Cu-20 vol. % Al_2O_3 microcomposite and Cu-7 vol. % Al_2O_3 nanocomposite respectively. The wear rate is appreciably low i.e. 0.86 x 10^{-4} $mm^3N^{-1}m^{-1}$ for 20 vol. % alumina reinforced copper microcomposite. The alumina nanoparticles revealed appreciable physical intimacy with the aluminum matrix than that of alumina microparticles. The highest nanohardness recorded 0.85 GPa and 99% densification for 7 and 1 vol. % Al-Al_2O_3 nancomposites respectively. Spark plasma sintering imparts enhanced densification and matrix-reinforcement proximity which have been corroborated with the experimental results.

Copper and aluminium based composites find applications in aerospace and automobile sectors. These applications demand accelerated weathering study on these composites. Induced thermal stresses in these composites would affect the structural integrity and mechanical properties. The assessment of these variations would enable us to predict the behaviour of these composites in harsh and hostile conditions. Flexural test was used to explore the effect of thermal treatments i.e. high temperature and cryogenic environments on the mechanical property of Al_2O_3 particulate reinforced Cu and Al metal matrix micro- and nano-composites in ex-situ and in-situ conditions. Cu- Al_2O_3 and Al-Al_2O_3 reinforced with 5, 10, 15, 20 vol. % Al_2O_3 micro (10µm)- and 1, 3, 5, 7 vol. % Al_2O_3 nano (<50 nm)-composites were fabricated by powder metallurgy route. All the compositions of micro- and nano-composites were thermally shocked from positive to negative (down thermal shock) and negative to positive temperature (up thermal shock). Both the micro- and nano-composites were treated at +40°C temperature for 1 hour followed by -40°C temperature for 1 hour. This treatment was also done in the reverse order i.e. from -40°C to +40°C. The above stated thermal shock module was repeated with temperatures (+80°C to -80°C) and (-80°C to +80°C) with both micro- and nano-composites with 1 hour isothermal holding at each temperature. For thermal conditioning the micro- and nano-composites were exposed to +80°C for 1 hour and -80°C for 1 hour separately.

High temperature in-situ 3-point bend test was performed at 100°C and 250°C for the composites after temperature attainment. All the micro- and nano-composites subjected to thermal shock, thermal conditionings were tested in flexural mode at a span length of 26 mm and loading rate of 0.5 mm/min. The micro- and nano-composites were also tested at ambient temperature to note the difference after the thermal treatments. The fractured samples were

studied under field emission scanning electron microscopy. The improvement in flexural strength of thermally shocked and conditioned samples have been discussed in the light of fractography.

The composites' performance at high loading rate (crosshead velocity) differs considerably from that of low loading rates. Different loading rates are quite probable in several applications of metal matrix composites to evaluate their crashworthiness. High impact loading conditions are withstood at instances such as MMC armours, collision of cars and impact of foreign objects on aerospace structures. Cu-Al_2O_3 and Al-Al_2O_3 micro- and nano-composites were subjected to 3-point bend test under various loading rates to evaluate the flexural strength and its variation with volume fraction of alumina. The flexural strength with respect to crosshead speed of copper and aluminium based composites varies with size and content of alumina particles.

Keywords: Metal matrix composites; Spark plasma sintering; Scanning electron microscopy; Field emission scanning electron microscopy; Transmission electron microscopy; Structural integrity; Mechanical properties; Flexural strength; Thermal conditioning; Thermal shock; Cryogenic treatment; Loading rate.

Contents

Page No.

Certificate---------- i
Acknowledgement---------- ii
Abstract---------- iv
List of figures---------- xii
List of tables---------- xviii
Nomenclature---------- xix
Abbreviations---------- xxi

Chapter 1 Introduction **1-21**

1.1 Literature review---------- 3
1.1.1 Composite---------- 3
1.1.2 Metal matrix composite---------- 3
1.1.3 Fabrication routes---------- 4
1.1.3.1 Powder metallurgy---------- 5
1.1.3.2 Blending and milling---------- 5
1.1.3.3 Conventional sintering---------- 6
1.1.3.4 Spark plasma sintering---------- 9
1.1.4 Interface---------- 10
1.1.5 Characteristic features---------- 11
1.1.5a Fabrication of copper-alumina composites---------- 11
1.1.5b Fabrication of aluminium-alumina composites---------- 12
1.1.6 Thermal Loadings---------- ---------- 13
1.1.7 Loading rate---------- 15
1.2 Scope of the thesis---------- 15
References---------- 16

Chapter 2 Experimental details **22-29**

22
2.1 Fabrication---------- 22
2.1.1 Blending---------- 22
2.1.2 Milling---------- 23
2.1.3 Compaction---------- 23
2.1.4 Sintering---------- 23
2.1.4.1 Conventional sintering---------- 23
2.1.4.2 Spark plasma sintering---------- 24
2.2. Characterization---------- 24
2.2.1 Particle size analysis---------- 24
2.2.2 X-ray diffraction---------- 24
2.2.3 Scanning electron microscope---------- 25
2.2.4 Field emission scanning electron microscopy---------- 25
2.2.5 Transmission electron microscopy---------- 25
2.3 Mechanical property study---------- 25
2.3.1 Density measurement ---------- 25
2.3.2 Microhardness study---------- 25
2.3.3 Nanoindentation hardness---------- 26
2.3.4 Compression test---------- 26
2.3.5 Flexural test---------- 26
2.3.6 Wear---------- 26
2.4 Thermal treatment---------- 26
2.4.1 Furnace---------- 27
2.4.2 Ultra-low temperature chamber----------

Chapter 3 Results and Discussion **30-163**

3.1a Effect of milling and blending on the dispersion, microstructure and properties of Cu-Al_2O_3 and Al-Al_2O_3 composites. **30-44**

3.1a.1 Scope and objectives of the work---------- 30
3.1a.2 Fabrication of composites---------- 31
3.1a.3 Characterization of composites---------- 31
3.1a.3.1 X-ray diffraction---------- 31
3.1a.3.2 Particle size analysis---------- 33
3.1a.3.3 Scanning electron microscopy---------- 34
3.1a.3.3.1 Dispersion---------- 34
3.1a.3.3.2 Sintering response---------- 38
3.1a.4 Density and microhardness measurements---------- 40
3.1a.5 Summary and conclusions---------- 43
References---------- 44

3.1b Effect of sintering atmosphere on the microstructure and properties of Cu-Al_2O_3 composites **45-52**

3.1b.1 Scope and objectives of the work---------- 45
3.1b.2 Fabrication of microcomposites---------- 45
3.1b.3 Characterization of the microcomposites---------- 45
3.1b.3.1 X-ray diffraction---------- 46
3.1b.3.2 Scanning electron microscopy---------- 47
3.1b.4 Density and microhardness measurement---------- 49
3.1b.5 Summary and conclusions---------- 51
References---------- 52

3.2 Evaluation of processing and properties of Cu-Al_2O_3 and Al-Al_2O_3 composites by conventional and spark plasma sintering method **53-120**

3.2.1 Scope and objectives of the work---------- 53
3.2.2 Conventional sintering---------- 54
3.2.2.1 Fabrication of composites---------- 54
3.2.2.1a Copper-alumina composites---------- 54
3.2.2.1b Aluminium-alumina composite---------- 55
3.2.2.2 Characterization of the composites---------- 55
3.2.2.2a Copper-alumina composite---------- 55
3.2.2.2a.1 X-ray diffraction---------- 55
3.2.2.2a.2 Scanning electron microscopy ---------- 57
3.2.2.2b Aluminium-alumina composite---------- 60
3.2.2.2b.1 X-ray diffraction---------- 60
3.2.2.2b.2 Scanning electron microscopy ---------- 61
3.2.2.3 Mechanical testing---------- 63
3.2.2.3a Copper-alumina composite---------- 64
3.2.2.3a.1 Density---------- 64
3.2.2.3a.2 Microhardness---------- 65
3.2.2.3a.3 Compression test---------- 68
3.2.2.3a.4 3-point bend test---------- 70
3.2.2.3a.5 Fractography---------- 71
3.2.2.3a.6 Wear test---------- 73
3.2.2.3b Aluminium-alumina composite---------- 75
3.2.2.3b.1 Density---------- 75
77

3.2.2.3b.2 Microhardness---------- 78
3.2.2.3b.3 Compression test---------- 80
3.2.2.3b.4 3-point bend test---------- 81
3.2.2.3b.5 Fractography---------- 82
3.2.2.3b.6 Wear test---------- 84
3.2.3 Spark plasma sintering---------- 84
3.2.3.1 Fabrication of composites---------- 84
3.2.3.1a Copper-alumina composites---------- 84
3.2.3.1b Aluminium-alumina composites---------- 85
3.2.3.2 Characterization of composites---------- 85
3.2.3.2a Copper-alumina composite---------- 85
3.2.3.2a.1 X-ray diffraction---------- 87
3.2.3.2a.2 Scanning electron microscopy ---------- 89
3.2.3.2a.3 Transmission electron microscopy --------- 91
3.2.3.2b Aluminium-alumina composite---------- 91
3.2.3.2b.1 X-ray diffraction---------- 92
3.2.3.2b.2 Scanning electron microscopy ---------- 95
3.2.3.2b.3 Transmission electron microscopy --------- 97
3.2.3.3 Mechanical testing---------- 98
3.2.3.3a Copper-alumina composite---------- 98
3.2.3.3a.1 Density and microhardness study ---------- 101
3.2.3.3a.2 Wear study---------- 101
3.2.3.3a.2.1 Wear depth---------- 102
3.2.3.3a.2.2 Wear track---------- 104
3.2.3.2a.2.3 Wear rate and volume------- 105
3.2.3.2a.2.4 Wear mechanism---------- 107
3.2.3.2a.2.5 Wear debris---------- 107
3.2.3.3b Aluminium-alumina composite---------- 108
3.2.3.3b.1 Density measurement---------- 110
3.2.3.3b.2 Microhardness and Nanohardness------ measurement 111
3.2.3.3b.3 Wear study---------- 114
3.2.4 Summary and conclusions---------- 115
References---------- 121-156

3.3 Effect of thermal and cryogenic conditioning on flexural behaviour of thermally shocked Cu-Al_2O_3 and Al-Al_2O_3 micro- and nano-composites 121

3.3.1 Scope and objectives of the work---------- 122
3.3.2 Fabrication of composites---------- 122
3.3.2a Copper-alumina composite---------- 122
3.2.2b Aluminium-alumina composite---------- 122
3.3.3 Thermal shock---------- 123
3.3.3a Copper-alumina composite---------- 132
3.3.3a.1 Transmission electron microscopy---------- 133
3.3.3b Aluminium-alumina composite---------- 140
3.3.4 Thermal conditioning---------- 140
3.3.4a Copper-alumina composite---------- 143
3.3.4b Aluminium-alumina composite---------- 145
3.3.5 High temperature in-situ 3-point bend test---------- 145
3.3.5a Copper-alumina composite---------- 149
3.3.5b Aluminium-alumina composite----------
3.3.6 Comparison of mechanical behaviour of differently thermal treated composites---------- 152 154

3.3.7 Summary and conclusions---------- 155
References----------
157-163

3.4 An exploratory study on the effect of loading rate on flexural strength of Cu-Al_2O_3 and Al-Al_2O_3 micro- and nano-composites
157
3.4.1 Scope and objectives of the work---------- 157
3.4.2 Fabrication of composites---------- 157
3.4.2a Copper-alumina composite---------- 158
3.4.2b Aluminium-alumina composite---------- 158
3.4.3 Effect of loading rate on the flexural strength of composites---------- 158
3.4.3a Copper-alumina composite---------- 161
3.4.3b Aluminium-alumina composite---------- 162
3.4.4 Summary and conclusions---------- 162
References----------
164-167

Chapter 4 Summary and Conclusions
168

List of papers based on the thesis 170
Biography

List of Figures

Figure No.	Figure Description	Page No.
Chapter 1 Introduction		
Fig. 1.1	Schematic diagram of ball and powder collision	6
Fig. 1.2	Diffusion paths during sintering	7
Fig. 1.3	Schematic diagram of SPS process	9
Chapter 2 Experimental Details		
Fig. 2.1	XRD patterns of as received alumina micropowder and nanopowder	27
Fig. 2.2	SEM micrographs of as received alumina micropowder and nanopowder	27
Chapter 3.1a Effect of milling and blending on the dispersion, microstructure and properties of Cu-Al_2O_3 and Al-Al_2O_3 composites		
Fig. 3.1a.1	X-ray diffraction patterns of Cu-5 vol. % Al_2O_3 micro-composite powders after 2, 5, 10 hours of milling	32
Fig. 3.1a.2	X-ray diffraction patterns of Al-5 vol. % Al_2O_3 microcomposite powders after 2, 5, 10 hours of milling	32
Fig. 3.1a.3	Particle size distribution of Cu-5 vol. % Al_2O_3 microcomposite powders milled for different time periods	33
Fig. 3.1a.4	Particle size distribution of Al-5 vol. % Al_2O_3 microcomposite powders milled for different time periods	34
Fig. 3.1a.5	SEM micrographs of Cu-5 vol. % Al_2O_3 microcomposite powders after 2,5,10 hours of milling	35
Fig. 3.1a.6	SEM micrographs of Al-5 vol. % Al_2O_3 microcomposite powders after 2,5,10 hours of milling	36
Fig. 3.1a.7	SEM micrographs of Cu-5 vol. % Al_2O_3 microcomposite powders after 2 and 8 hours of blending	36
Fig. 3.1a.8	SEM micrographs of Cu-5 vol. % Al_2O_3 nanocomposite powders after 2 and 8 hours of blending	37
Fig. 3.1a.9	SEM micrographs of Al-5 vol. % Al_2O_3 nanocomposite powders after 2 and 8 hours of blending	37
Fig. 3.1a.10	SEM micrographs of Al-5 vol. % Al_2O_3 microcomposite powders after 2 and 8 hours of blending	38
Fig. 3.1a.11	SEM micrographs of Cu-5 vol. % Al_2O_3 microcomposite powders after 2,5,10 hours of milling and 8 hours of blending followed by sintering at 900°C temperature	39
Fig. 3.1a.12	SEM micrographs of Al-5 vol. % Al_2O_3 microcomposite powders after 2,5,10 hours of milling and 8 hours of blending followed by sintering at 600°C temperature	40
Fig. 3.1a.13	Density of Cu-5 vol. % Al_2O_3 composites sintered at 900°C composites after milling	41
Fig. 3.1a.14	Density of Al-5 vol. % Al_2O_3 composites sintered at 600°C composites after milling	41

Fig. 3.1a.15	Microhardness of Cu-5 vol. % Al_2O_3 composites sintered at 900°C after milling	42
Fig. 3.1a.16	Microhardness of Al-5 vol. % Al_2O_3 composites sintered at 600°C after milling	43
Chapter 3.1b Effect of sintering atmosphere on the microstructure and properties of Cu-Al_2O_3 composites		
Fig. 3.1b.1	XRD diffraction patterns of Cu-15 vol. % Al_2O_3 micro-composites sintered conventionally in nitrogen and hydrogen atmosphere	46
Fig. 3.1b.2	SEM micrographs and EDS analysis of Cu-15 vol. % Al_2O_3 sintered in nitrogen atmosphere	47
Fig. 3.1b.3	SEM micrographs and EDS analysis of Cu-15 vol. % Al_2O_3 sintered in hydrogen atmosphere	48
Fig. 3.1b.4	SEM micrographs and EDS analysis of Cu-15 vol. % Al_2O_3 sintered in argon atmosphere	49
Fig. 3.1b.5	Densification of Cu-Al_2O_3 microcomposites fabricated using nitrogen, hydrogen and argon sintering atmospheres by conventional sintering	50
Fig. 3.1b.6	Comparison of hardness of Cu-Al_2O_3 microcomposites fabricated using nitrogen, hydrogen and argon sintering atmospheres by conventional sintering	51
Chapter 3.2 Evaluation of processing and properties of Cu-Al_2O_3 and Al-Al_2O_3 composites by conventional and spark plasma sintering method		
Fig. 3.2.1	X-ray diffraction patterns of Cu–20 vol. % Al_2O_3 microcomposites sintered at 850°C, 900°C, 1000°C	56
Fig. 3.2.2	X-ray diffraction patterns of Cu–7 vol. % Al_2O_3 nano-composites sintered at 850°C, and 900° C	57
Fig. 3.2.3	SEM micrographs of Cu–10 vol. % Al_2O_3 microcomposites sintered at temperature (a) 850°C, (b) 900°C and (c) 1000°C (d) Cu-15 vol. % Al_2O_3 microcomposites sintered at 900°C temperature	58
Fig. 3.2.4	SEM micrographs of Cu–10 vol. % Al_2O_3 microcomposites sintered at temperature 1000°C	59
Fig. 3.2.5	FESEM micrographs of Cu–3 vol. % Al_2O_3 nanocomposites sintered at 1000°C temperature at (a) 100000X and (b) 200000X magnifications	59
Fig. 3.2.6	X-ray diffraction patterns of Al-Al_2O_3 microcomposites sintered at 600°C temperature	60
Fig. 3.2.7	X-ray diffraction patterns of Al-Al_2O_3 nanocomposites sintered at 600°C temperature	61
Fig. 3.2.8	FESEM micrographs of Al–5 vol. % Al_2O_3 microcomposite sintered at temperature 600°C captured at (a) 5000X and (b) 30000X magnification	62
Fig. 3.2.9	FESEM micrographs of Al–5 vol. % Al_2O_3 nanocomposites sintered at temperature 600°C captured at (a) 5000X and (b) 100000X magnification	62

Fig. 3.2.10	Compression strength of Cu-Al_2O_3 microcomposites sintered at 900°C	69
Fig. 3.2.11	Compression strength of Cu-Al_2O_3 nanocomposites sintered at 900°C	69
Fig. 3.2.12	Plot for ultimate flexural stress (MPa) vs. vol. % of reinforcement content for Cu-Al_2O_3 microcomposites	70
Fig. 3.2.13	Plot for ultimate flexural stress (MPa) vs. vol. % of reinforcement content for Cu-Al_2O_3 nanocomposites	71
Fig. 3.2.14	Fractographs of Cu-5 vol. % Al_2O_3 (a) microcomposites (b) nanocomposites sintered at 900°C	72
Fig. 3.2.15	Fractograph of Cu-10 vol. % Al_2O_3 microcomposites sintered at 900°C	72
Fig. 3.2.16	Plot for wear depth vs. time of Cu-Al_2O_3 microcomposites with different vol. % of Al_2O_3 sintered at 900°C temperature	73
Fig. 3.2.17	Plot for wear depth vs. time of nanocomposites with different vol. % of Al_2O_3 sintered at 900°C temperature	74
Fig. 3.2.18	SEM images of worn-out surfaces of (a) Cu-5 vol. % Al_2O_3 (microcomposite) (b) Cu-10 vol. % Al_2O_3 (microcomposite) (c) Cu-1 vol. % Al_2O_3 (nanocomposite)	75
Fig. 3.2.19	Densification plots of Al-Al_2O_3 microcomposites sintered at different temperatures	76
Fig. 3.2.20	Densification plots of Al-Al_2O_3 nanocomposites sintered at different temperatures	76
Fig. 3.2.21	Microhardness plots of Al-Al_2O_3 microcomposites sintered at different temperatures	77
Fig. 3.2.22	Microhardness plots of Al-Al_2O_3 nanocomposites sintered at different temperatures	78
Fig. 3.2.23	Compressive strength of Al-Al_2O_3 microcomposites sintered at 600°C	79
Fig. 3.2.24	Compressive strength of Al-Al_2O_3 nanocomposites sintered at 600°C	79
Fig. 3.2.25	Plot of flexural strength vs. vol. % of reinforcement of Al-Al_2O_3 microcomposites sintered at 600°C	80
Fig. 3.2.26	Plot of flexural strength vs. vol. % of reinforcement of Al-Al_2O_3 nanocomposites sintered at 600°C	81
Fig. 3.2.27	SEM fractographs of Al-5 vol. % Al_2O_3 (a) microcomposite (b) nanocomposite sintered at 600°C	82
Fig. 3.2.28	Wear depth vs time plot of Al-Al_2O_3 microcomposites sintered at 600°C	83
Fig. 3.2.29	Wear depth vs time plot of Al-Al_2O_3 nanocomposites sintered at 600°C	83
Fig. 3.2.30	XRD pattern of Cu-7 vol. % Al_2O_3 nanocomposite sintered by SPS	86
Fig. 3.2.31	XRD pattern of Cu-20 vol. % Al_2O_3 microcomposite sintered by SPS	87
Fig. 3.2.32	SEM micrograph of Cu-7 vol. % Al_2O_3 nanocomposite sintered by SPS	87

Fig. 3.2.33	SEM micrograph of Cu-5 vol. % Al_2O_3 microcomposite sintered by SPS	88
Fig. 3.2.34	TEM micrograph of Cu-5 vol. % Al_2O_3 nanocomposite sintered by SPS	89
Fig. 3.2.35	TEM micrograph of Cu-5 vol. % Al_2O_3 microcomposite sintered by SPS	90
Fig. 3.2.36	XRD patterns of Al-Al_2O_3 microcomposites sintered using SPS	91
Fig. 3.2.37	XRD patterns of Al-Al_2O_3 nanocomposites sintered using SPS	92
Fig. 3.2.38	SEM micrographs of (a) Al-5vol. % Al_2O_3 nanocomposite, (b) Al-7vol. % Al_2O_3 nanocomposite, (c) Al-5vol. % Al_2O_3 micro composite sintered using SPS	93
Fig. 3.2.39	TEM micrographs of (a) Al-1vol. % Al_2O_3, (b) Al-5vol. % Al_2O_3 nanocomposites sintered by SPS	95
Fig. 3.2.40	TEM micrograph of (a) Al-7vol. % Al_2O_3 nanocomposite, (b) Al-5vol. % Al_2O_3 microcomposite sintered by SPS	96
Fig. 3.2.41	TEM micrograph of (a) Al-7vol. % Al_2O_3 nanocomposite, (b) Al-5vol. % Al_2O_3 microcomposite sintered by SPS	97
Fig. 3.2.42	Plot for nanohardness of Cu-Al_2O_3 nanocomposites and microhardness of Cu-Al_2O_3 microcomposites	99
Fig. 3.2.43	Elastic modulus of Cu-Al_2O_3 nanocomposites fabricated by SPS	100
Fig. 3.2.44	Wear depth vs. time plot for Cu-Al_2O_3 nanocomposites sintered by SPS	101
Fig. 3.2.45	Wear depth vs. time plot for Cu-Al_2O_3 microcomposites sintered by SPS	102
Fig. 3.2.46	SEM micrographs of the worn surfaces showing wear track of (a) Cu-1 vol. % Al_2O_3 and (b) Cu-5 vol. % Al_2O_3 nanocomposite, (c) Cu-5 vol. % Al_2O_3 and (d) Cu-20 vol. % Al_2O_3 microcomposite	103
Fig. 3.2.47(a)	Wear rate vs. volume % of alumina of the Cu-Al_2O_3 composites	104
Fig. 3.2.47(b)	Wear volume vs. volume % of alumina of the Cu-Al_2O_3 composites	105
Fig. 3.2.48	SEM micrographs of worn surfaces of (a) Cu-5 vol. % Al_2O_3 nanocomposite, (b) Cu-5 vol. % Al_2O_3 microcomposite, (c) Cu 1 vol. % Al_2O_3 nanocomposite, (d) Cu-5 vol. % Al_2O_3 nanocomposite	106
Fig. 3.2.49	SEM micrographs of worn surfaces of Cu-7 vol. % Al_2O_3 nano-composite and Cu-20 vol. % Al_2O_3 microcomposite along with EDS analysis	106
Fig. 3.2.50	SEM micrograph of the worn surfaces showing wear debris of Cu-5 vol. % Al_2O_3 microcomposite and EDS of the whole micrograph	107
Fig. 3.2.51	SEM micrograph of worn surfaces of Cu-5 vol. % Al_2O_3 nanocomposite and EDS of the whole micrograph	108
Fig. 3.2.52	Wear depth vs time profile for Al-Al_2O_3 microcomposites fabricated by spark plasma sintering	111

Fig. 3.2.53	Wear depth vs time profile for Al-Al_2O_3 nanocomposites fabricated by spark plasma sintering	112
Fig. 3.2.54	SEM micrographs of worn out surface of (a) Al-20 vol. %Al_2O_3 microcomposite and (b) Al-5 vol.% Al_2O_3 nanocomposites fabricated by spark plasma sintering	113
Fig. 3.2.55	SEM micrographs of worn out surface of (a) Al-1 vol. % Al_2O_3 microcomposite and (b) Al-1 vol.% Al_2O_3 nanocomposites fabricated by spark plasma sintering	113
Chapter 3.3 Effect of thermal and cryogenic conditioning on flexural behaviour of thermally shocked Cu-Al_2O_3 and Al-Al_2O_3 micro- and nanocomposites		
Fig. 3.3.1	SEM micrographs of Cu-5 vol. % Al_2O_3 microcomposite before and after down thermal shock for a temperature gradient of 160°C	124
Fig. 3.3.2	SEM micrographs of Cu-5 vol. % Al_2O_3 nanocomposite before and after down thermal shock for a temperature gradient of 160°C	124
Fig. 3.3.3(a)	Variation of flexural strength of Cu-Al_2O_3 microcomposites after thermal shock of 80°C thermal gradient	125
Fig. 3.3.3(b)	Variation of flexural strength of Cu-Al_2O_3 microcomposites after thermal shock of 160°C thermal gradient	126
Fig. 3.3.4	SEM micrographs of Cu-10 vol. % Al_2O_3 microcomposite after down thermal shock of 80°C thermal gradient showing (a) particle pull-out and (b) interfacial de-cohesion	127
Fig. 3.3.5(a)	Variation of flexural strength of Cu-Al_2O_3 nanocomposites after thermal shock of 80°C thermal gradient	129
Fig. 3.3.5(b)	Variation of flexural strength of Cu-Al_2O_3 nanocomposites after thermal shock of 160°C thermal gradient	130
Fig. 3.3.6	SEM micrographs of Cu-5 vol. % Al_2O_3 nanocomposite after (a) up thermal and (b) down thermal shock for a temperature gradient of 80°C	131
Fig. 3.3.7	TEM micrographs of Cu-5 vol. % Al_2O_3 microcomposites at (a) ambient conditions, (b) after up thermal shock and (c) after down thermal shock for a thermal gradient of 160°C	132
Fig. 3.3.8	TEM micrographs of Cu-3 vol. % Al_2O_3 microcomposites at (a) ambient conditions, (b) after up thermal shock and (c) after down thermal shock for a thermal gradient of 160°C	133
Fig. 3.3.9	SEM micrographs of Al-5 vol. % Al_2O_3 microcomposite before and after down thermal shock of 160°C temperature gradient	134
Fig. 3.3.10	SEM micrographs of Al-5 vol. % Al_2O_3 nanocomposite before and after down thermal shock of 160°C temperature gradient	135
Fig. 3.3.11(a)	Variation of flexural strength of Al-Al_2O_3 microcomposites before and after thermal shock of 80°C thermal gradient	136
Fig. 3.3.11(b)	Variation of flexural strength of Al-Al_2O_3 microcomposites before and after thermal shock of 160°C thermal gradient	137
Fig. 3.3.12	SEM micrographs of Al-1 vol. % Al_2O_3 (a) microcomposite and (b) nanocomposite after down thermal shock of temperature gradient 160°C temperature gradient	137
Fig. 3.3.13(a)	Variation of flexural strength of Al-Al_2O_3 nanocomposites before and after thermal shock of 80°C thermal gradient	139

Fig. 3.3.13(b)	Variation of flexural strength of Al-Al_2O_3 nanocomposites before and after thermal shock of 160°C thermal gradient	139
Fig. 3.3.14	Flexural strength of Cu-Al_2O_3 microcomposites after thermal conditioning	141
Fig. 3.3.15	SEM micrographs of Cu-10 vol. % Al_2O_3 (a) & (b) microcomposite after thermal conditioning at +80°C	141
Fig. 3.3.16	Flexural strength of Cu-Al_2O_3 nanocomposites after thermal conditioning	142
Fig. 3.3.17	Flexural strength of Al-Al_2O_3 microcomposite after thermal conditionings	143
Fig. 3.3.18	Flexural strength of Al-Al_2O_3 nanocomposites after thermal conditionings	144
Fig. 3.3.19	SEM micrographs of Al-1 vol. % Al_2O_3 (a) & (b) nanocomposite thermal conditioned at -80°C	145
Fig. 3.3.20	High temperature flexural strength of Cu-Al_2O_3 micro-composites	146
Fig. 3.3.21	High temperature flexural strength of Cu-Al_2O_3 nano-composites	148
Fig. 3.3.22	SEM micrograph of Cu-5 vol. % Al_2O_3 nanocomposite after high temperature flexural test at 250°C	149
Fig. 3.3.23	High temperature flexural strength of Al-Al_2O_3 microcomposites	150
Fig. 3.3.24	High temperature flexural strength of Al-Al_2O_3 nanocomposites	151
Fig. 3.3.25	SEM micrographs of Al-5 vol. % Al_2O_3 nanocomposite after high temperature flexural test at (a) 100°C and (b) 250°C	151
Chapter 3.4 An exploration on the effect of loading rate on flexural strength of Cu-Al_2O_3 and Al-Al_2O_3 micro- and nanocomposites		
Fig. 3.4.1	Variation in flexural strength of Cu-Al_2O_3 microcomposites at different loading rates	159
Fig. 3.4.2	Variation in flexural strength of Cu-Al_2O_3 nanocomposites at different loading rates	160
Fig. 3.4.3	Variation in flexural strength of Al-Al_2O_3 microcomposites at different loading rates	161
Fig. 3.4.4	Variation in flexural strength of Al-Al_2O_3 nanocomposites at different loading rates	162

List of Tables

Table No.	Description	Page No.
Table 2.1	The compositions of micro- and nano-composite used for copper and aluminium matrix and their corresponding sintering temperatures	24
Table 2.2	Schematic diagram explaining the experimental process for thermal shock experiments	28
Table 2.3	Schematic diagram explaining the experimental process for thermal conditioning experiments	29
Table 3.2.1	Theoretical and sintered density values of Cu-Al_2O_3 micro- and nano-composites processed at different sintering temperatures	65
Table 3.2.2	Mean hardness and standard deviation of copper-alumina nano- and micro-composites	67
Table 3.2.3	Microhardness, sintered and theoretical density of Cu-Al_2O_3 micro- and nano-composites with varying alumina content	99
Table 3.2.4	% of theoretical density, microhardness and nanoindentation hardness values of Al-Al_2O_3 micro- and nano-composites	109

Nomenclature

$\Delta\sigma_{orowan}$	Dispersion/Orowan strengthening
$\dot{\varepsilon}$	Strain rate
G_m	Shear modulus of the matrix
K_{HP}	Strengthening coefficient
$\dot{e}$	Engineering/ Conventional strain rate
σ_0	Peierls stress
$\Delta\sigma_{HP}$	Grain boundary strengthening
$\Delta\sigma_{thermal}$	Strengthening resulting from the residual plastic strain due to thermal mismatch
ΔT	Difference between the processing and test temperatures
$\Delta\alpha$	Difference in coefficient of thermal expansion between matrix and particles
b	Burgers vector
d	Grain size
d_p	Particle diameter
ε	Thermal strain
f	Fractional volume of reinforcement
G	Final average grain size (chapter 1)
G	Shear modulus of material (chapter 3.2)
G_0	Initial average grain size
k	a constant (chapter 1)
K	a factor given by $K = K_0 * exp(-Q / RT)$ (chapter 1)
K_0	Material dependent factor
L	Length after time‘t’
L_0	Original length
m	A factor between 2 and 4
Me	Matrix

MO_n	Reinforcing oxide
Q	Molar activation energy
r	Particle radius
R	Ideal gas constant
T	Absolute temperature
t	Time
V_p	Particle volume fraction
W_a	Work of adhesion
ΔG^{O}_{r}	Gibbs free energy change
δT	Range of temperature experienced during processing
$\delta\alpha$	Difference between the thermal expansion coefficient of the reinforcement and the matrix
λ	Distance apart from the reinforcements (chapter 3.2)
λ	Interparticle distance (chapter 1)
λ	wavelength of CuK_α radiation (chapter 2)
v	crosshead velocity
ρ_G	Dislocation density in the reinforcement matrix interface (chapter 3.2)
τ_o	Stress required for a dislocation to pass reinforcement
ρ	Dislocation density (chapter 1)

Abbreviations

ASTM	American Society for Testing of Materials
at. %	Atomic percent
BSE	Back Scattered Electron
CTE	Coefficient of thermal expansion
Cu (ss)	Solid solution of copper
EDAX	Energy Dispersive X-ray Analysis
EDS	Energy Dispersive Spectrometry
FCC	Face Centered Cubic
FESEM	Field Emission Scanning Electron Microscopy
HIP	Hot Isostatic Pressing
HV	Vickers Pyramid Number
ITER	International Thermonuclear Experimental Reactor
MMC	Metal Matrix Composite
P/M	Powder Metallurgy
PCA	Process Control Agent
PSR	Particle Size Ratio
SE	Secondary Electron
SEM	Scanning Electron Microscopy
SPS	Spark Plasma Sintering
TEM	Transmission Electron Microscopy
vol. %	Volume percent
wt. %	Weight percent
XRD	X-Ray Diffraction

Chapter 1

Introduction

The central theme of the thesis revolves around the comparison of the microstructural and mechanical aspects in conventional microcomposites and advanced nanocomposites. Here, by micro- and nano-composites we refer to the variation in the reinforcement particle size, keeping the matrix particle size constant i.e. in micrometer scale. The applications of MMCs include catering the aerospace, automobile and military industries. The crucial parameters influencing the properties of a particle reinforced composites are size, shape, concentration and spatial distribution of the reinforcement, the concentration of impurities present in the constituent's phase of composites, thermal and chemical exposure environment and particular reinforcement size matrix alloy combination. The dominance of nanocomposites over microcomposites on micro as well as macro attributes has led to the comparative discussion of both. The nanoparticles in a metal matrix furnish intimate mixing with the matrix as well as higher degree of dispersion strengthening, except for clustering of nanoparticles at certain instances. The clustering of nanoparticles takes place in compositions with higher nanoparticle content.

The consolidation of metal matrix composites by conventional methods has been done since decades. The new era of materials include nanocomposites which cannot be consolidated effectively by conventional means. The advanced techniques of consolidation include hot

pressing, hot isostatic pressing and spark plasma sintering. These advanced techniques render microstructural evolution, elevated mechanical properties as well as varied structural integrity of matrix and reinforcement. The microstructural as well as mechanical attributes of a composite depend on several factors, out of which the reinforcement particle size is a vital one.

The variation in reinforcement particle size alters the overall chemistry and character of interface, microstructure and mechanical performance of the composite. The study of effect of fabrication parameters such as mixing of powders, sintering atmosphere and techniques has been done in detail. The synthesis and characterization of copper-alumina as well as aluminium-alumina micro- and nano-composites by conventional and spark plasma sintering techniques has been performed extensively. The comparison of microstructure, structural integrity, mechanical properties in conventionally fabricated and spark plasma sintered composites has been done. Copper and aluminium are metals with low hardness, so addition of alumina renders hardness to the metals as well inertness at high temperature. These systems of composites possess hardness and strength higher than monolithic metals. This dichotomy of strength and ductility offers applications in ample fields of engineering and technology.

The composites possess thermal residual stress by virtue of its processing parameters, and differential co-efficient of thermal expansion of matrix and reinforcement entities. The high, low as well as ultra low temperature applications of metal matrix composites have led to the study of their structural integrity and mechanical behaviour by inducing thermal stresses by different methods and modules. The advancement of science and technology has been rapidly demanding newer materials which can endure extreme weathering exposures and excursion. This may necessitate the design of experimental process and procedures to generate data and findings which would lead to the prediction of reliability of mechanical performance of material behaviour in unpredictably harsh and hostile environments. The response of mechanical behaviour and structural integrity to induced thermal stress of copper-alumina and aluminium-alumina micro- and nano-composites has been discussed in this thesis.

Metal matrix composites respond differently to high strain rate loading conditions as compared to monotonic or quasistatic loading. The high and low strain rate sensitivity of composites for a wide range of applications, necessitate the study of variation of loading rate

on the composites. The loading rate sensitivity of copper and aluminium based micro- and nano-composites have been elaborated comprehensively.

1.1 Literature Review

1.1.1 Composite

Composite is a multiphase material which consists of a matrix and one or many reinforcements. The matrix material could be polymer, metal or ceramic in nature. The nature of reinforcements varies over a wide range depending upon the desired quality and properties of the composite. The composites possess properties intermediate of that of matrix and reinforcement. Selection of nature of matrix and reinforcement as well as content of reinforcement is decisive of the tailoring of the composite for desired attributes. Out of the three kinds of matrices, in this thesis metal matrix composites embedded with ceramic particulates have been investigated.

1.1.2 Metal matrix composite

Metal matrix composites (MMCs) are excellent candidates for structural components in the aerospace and automotive industries due to their high specific modulus, strength, and thermal stability. Metal matrix composites (MMCs) combine both metallic properties (ductility and toughness) with ceramic properties (high strength and modulus) and possess greater strength in shear and compression and high service temperature capabilities. Nanocomposites are gaining tremendous popularity in the material industry for replacing the monoliths. On the other hand microcomposites have already been put into practice long back. The comparison of microstructural and mechanical attributes of nanocomposites and microcomposites is a burning area of research. The extensive use of MMCs in aerospace, automotive industries and in structural applications has increased over past 20 years due to the availability of inexpensive reinforcements and cost effective processing routes which give rise to reproducible properties [1]. The driving phenomena for generation of dislocations in MMCs are misfit strain, thermal misfit, allotropic misfit, lattice parameter misfit and elastic inhomogenity misfit [2]. In case of solid solution strengthening the dislocation motion gets impinged principally by elastic interaction between the dislocation and solute atoms as well as by alteration of the energy of stacking fault [3]. The physical and mechanical superiority of nano-structured materials has fascinated scientists in recent times [4]. The strengthening due

to grain refinement can be delegated to a number of theories such as the Hall-Petch relation, Orowan bowing mechanism, Taylor relationship and several other models [5].

Strengthening resulting from the grain size known as grain boundary strengthening $\Delta\sigma_{HP}$ can be represented as:

$$\Delta\sigma_{HP} = \sigma_0 + \frac{K_{HP}}{\sqrt{d}} \quad (1)$$

with σ_0 the Peierls stress, K_{HP} strengthening coefficient constant, and d the grain size expressed in m.

Strengthening resulting from oxide particle reinforcement, known as dispersion strengthening, can be shown as:

$$\Delta\sigma_{orowan} = \frac{0.13G_m b}{\lambda} ln\frac{r}{b} \quad (2)$$

with G_m the shear modulus of the matrix, b the Burgers vector , r the particle radius, and λ the interparticle distance given by

$$\lambda = d_p\left[\sqrt[3]{\frac{1}{2V_p}} - 1\right] \quad (3)$$

with d_p the particle diameter, and V_p the volume fraction particles.

Strengthening resulting from the residual plastic strain due to the thermal mismatch between particles and matrix during post-processing cooling, can be represented as:

$$\Delta\sigma_{thermal} = kG_m b\sqrt{\rho} \quad (4)$$

with k a constant, and ρ the dislocation density induced by plastic strain due to a thermal mismatch. This ρ is given by:

$$\rho = 12\frac{\Delta\alpha\Delta T V_p}{bd_p(1-V_p)} \quad (5)$$

with $\Delta\alpha$ the difference in the coefficient of thermal expansion between the matrix and the particles, b the burgers vector, and ΔT the difference between the processing and the test temperatures [6-10].

1.1.3 Fabrication routes

There exists a wide spectrum of routes of fabrication of metal matrix composites i.e. solid state routes, liquid state routes and gaseous state routes. Solid state routes include diffusion

bonding, in-situ fabrication, powder metallurgy, sintering, hot pressing and hot isostatic pressing. Liquid state routes consist of gas pressure infiltration, squeeze casting infiltration and pressure die infiltration.

1.1.3.1 Powder metallurgy

Powder metallurgy method fabricates complex components economically. Powder metallurgy promotes synthesis of prealloyed powders below melting temperature. The powder metallurgy route in case of oxide reinforcements has an added advantage as they follow the energy efficient method [11]. The greatest threat in this fabrication route is the absence of an integrated interface formation as the metal powders are less reactive in solid state [12]. Powder metallurgy route is one of the versatile routes for fabrication of MMCs because of less probability of particle segregation, undesirable brittle phase formation, free from cast defects, consistent distribution of reinforcement and superior mechanical properties [13-15]. Advantages of P/M route over casting comprises of eliminating segregation and defects associated with casting.

1.1.3.2 Blending and milling

Blending is the mixing of powders using a blender which works on the principle of tumbling, shaking or planetary action of movement. Blenders can be of several types such as double cone blender, turbula shaker mixer and V-mixer. Blending method involves only intermixing of powders.

Mechanical milling is a solid-state powder processing technique that involves repeated cold welding, fracturing, and re-welding of powder particles in a high-energy ball mill. In this process, the blended elemental powder mixture is loaded into the vials along with the grinding media, and the whole mass is agitated at a high speed for a definite period of time. Process control agent (PCA) (also referred to as lubricant or surfactant) is occasionally added, especially when ductile materials are being milled, to minimize the effect of cold welding and consequent formation of large lumps of powder.

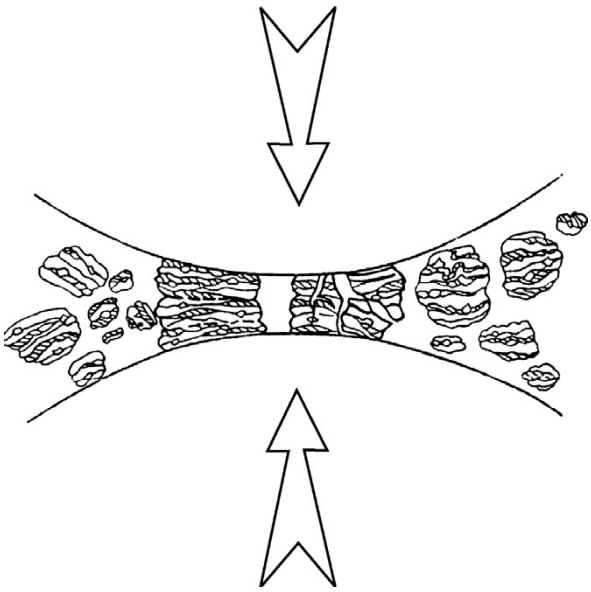

Fig. 1.1 Schematic diagram of ball and powder collision [11].

Milling uses balls for mixing as well as reducing the particle size of powders. Milling includes grinding of powders in specially designed vials in presence of balls with a process control agent. The powders are subjected to milling and milling parameters are decided keeping in concern the final size of powders required, nature of powders and content of powders. Fig. 1.1 illustrates the schematic diagram during ball and powder particles collision describing the mechanism of particle size reduction and fragmentation. Milling of powders is dependent on several factors: type of mill, mill speed, milling time, size distribution of the grinding medium, ball to powder weight ratio, milling atmosphere and process control agent.

1.1.3.3 Conventional sintering

The technique of consolidation without melting is a boon to the world of materials which is possible by thermal activation of mass transport processes [16]. The driving force for the former being reduction of surface and grain boundary energies, high sintering temperature is a desirable facet for formidable strength [17]. The consolidation of matrix and reinforcement powders is successful when the interfacial bonding along with the uniform distribution and other factors promote good mechanical properties. Sintering is a thermally activated diffusion of atoms to form desirable shapes. Thermodynamically sintering is driven by surface area reduction. Smaller particles sinter faster than large particles, and high temperature accelerates

the process of sintering [18]. Sintering is consolidation of compacted powders compacted into required shapes. Sintering comprises of three stages; initial stage being neck growth between contact particles, intermediate stage corresponding to pore rounding and onset of grain growth and finally the pores collapse into closed spheres impeding the grain growth.

Initial Stage: Transport from high energy convex particle surfaces to concave surfaces forming necks. Fusing increases surface area, pore volume and density remains almost constant (4-5% shrinkage, relative density 0.5-0.6).

Intermediate Stage: Interparticle neck growth takes place increasing the grain boundary area. Interparticle grain boundary flattens, pore diameter decreases (5-20% shrinkage, relative density upto 0.95).

Final Stage: Isolated pores may remain at triple points or inside grain matrix. These pores may be gradually eliminated. (relative density >0.95).

Fig. 1.2 reveals the play of different sintering mechanisms in the sintering process of green compacts.

Sintering mechanisms

1. Evaporation-condensation (higher vapour pressure over a convex surface compared to concave).
2. Diffusion (differences in vacancy concentration) (a) surface diffusion, (b) grain boundary diffusion, (c) volume diffusion.
3. Flow (pressure induced).
4. Dissolution-precipitation (liquid phase wetting the surface).

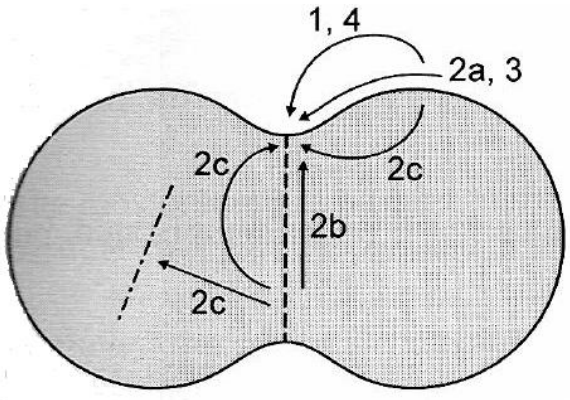

Fig.1.2 Diffusion paths during sintering. The numbers correspond to the numbers in the above paragraph [11].

Aftermath of sintering

An aggregate of fine grained crystal size increases in average grain size when heated at elevated temperatures. As the average grain size increases it is obvious that some grains must shrink and disappear. An equivalent way of looking at the grain growth is as the rate of disappearance of grains. Then the driving force for the process is the difference in energy between the fine grained material and the larger grain size product resulting from the decrease in grain boundary area and total boundary energy. This energy change corresponds to about 0.1-0.5 cal/g for the change from a 1 micron to 1 cm grain size.

Grain growth happens due to motion of atoms across a grain boundary. Convex surfaces have a higher chemical potential than concave surfaces, therefore grain boundaries will move towards their center of curvature. As smaller particles tend to have a higher radius of curvature this leads to smaller grains losing atoms to larger grains and shrinking. This is a process called Oswald ripening. Large grains grow at the expense of small grains. Grain growth in a simple model is found to follow:

$$G^m = G_0^m + Kt \tag{6}$$

Where G is final average grain size, G_0 is the initial average grain size, t is time, m is a factor between 2 and 4, and K is a factor given by:

$$K = K_0 * exp(-Q / RT) \tag{7}$$

Where Q is the molar activation energy, R is the ideal gas constant, T is absolute temperature, and K_0 is a material dependent factor.

The conventional method of sintering renders coarse microstructure, poor adhesion and density, low strength and hardness at high temperatures. There is a need of advanced sintering techniques to obtain finer microstructures.

1.1.3.4 Spark plasma sintering

The spark plasma sintering technique is becoming popular due to the intrinsic advantages of the method and the enhanced material properties, as well as lower processing temperature and shorter sintering time to consolidate powders compared to conventional methods. The differences between SPS and conventional methods include process efficiency and energy savings as well as microstructural and compositional implications. Sintering at lower temperatures and shorter times reduces the threat of vaporization, minimizes grain growth and renders cleaner grain boundary. Spark plasma sintering (SPS) uses high amperage, low voltage, pulse DC current and uniaxial pressure to consolidate powders [16]. The exciting results obtained in the sintering of composites by SPS can be ascribed to the differential activation of the matrix and reinforcement, as the existing theory for SPS proposes that the current pathway is unlike for conducting and non-conducting powders.

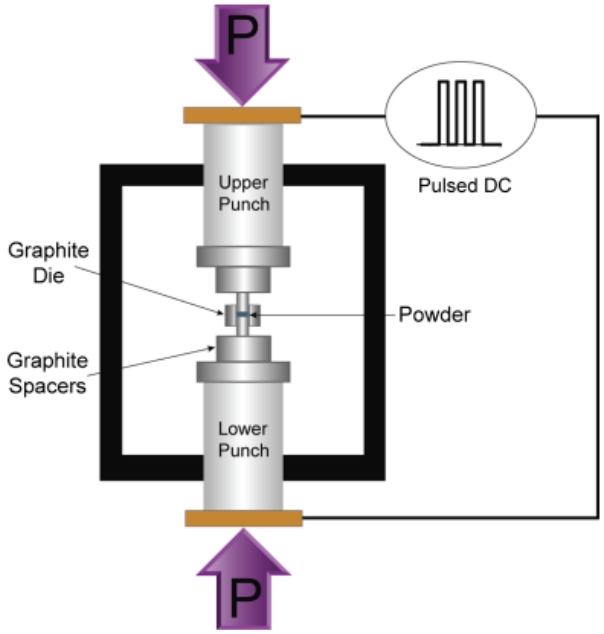

Fig.1.3 Schematic diagram of SPS process [18]

Fig. 1.3 shows the schematic process of SPS method illustrating the arrangement of die and sample. A combination of current flow through the sample and radiative heat loss on the die wall gives rise to a radial temperature distribution in conductive samples. The rapid increase in the use of SPS can be attributed largely to two broad considerations: (a) the intrinsic advantages of the method relative to conventional sintering methods and (b) the observations of enhanced properties of materials consolidated by this method. With respect to compositional

and microstructural changes, sintering at lower temperatures and for shorter times minimizes material loss due to vaporization, [19-22] undesirable phase transformation, [23] and suppression of grain growth [24-26]. The parameters that are associated with the SPS process include the current, the applied uniaxial pressure, and heating rate. Typically, the current and sintering temperature are dependent parameters as Joule heating is the source of thermal activation, either in the graphite die only (when the sample is nonelectrically conducting) or in the die and sample (when the sample is electrically conducting). The pressure has been recently shown to play a crucial role in the consolidation of materials, particularly in nanostructured powders. The maximum pressure that can be uniaxially applied in the SPS process is mostly decided by the mechanical property of the graphite die. The fabrication of nanocomposites via spark plasma sintering renders the grain boundaries clean, to avoid oxide interfacial layer. The highly reduced time of fabrication controls the grain growth of matrix particles as well as aids in better pinning effect and retention of nanostructure. Spark plasma sintering has the advantage of combining the effects of axial mechanical loading, temperature and electric current. The current plays two roles in SPS i.e. current is the source of heating by Joule effect and it also has the positive effect of enhanced diffusion rate during phase growth and intermetallic diffusion [26]. The advent of nanostructured material production techniques have led to an unprecedented growth in the area of metal matrix composites with extraordinary superior strengths.

1.1.4 Interface

The zone between the matrix and reinforcement phase (interface or interphase) is an essential part of MMC. Bonding between the two phases develops from interfacial frictional stress, physical and chemical interaction and thermal stresses due to mismatch between coefficient of thermal expansion of matrix and reinforcement. During the designing of a MMC the underlying interfacial phenomenon governing the transmission of thermal, electrical and mechanical properties is of utmost importance [12]. The physicochemistry of wetting and bonding of oxide reinforcements with the metal matrix (i.e. the non reactivity at the interface zone) in terms of Gibbs free energy change ΔG^{O}_{r} is as follows

$$n\,Me + m\,MO_n = n\,MeO_m + m\,M \qquad (8)$$

where Me is the matrix and MO_n is the reinforcing oxide. The Gibbs free energy is strongly positive in this case; therefore it has been proposed that the oxide reinforcements can have only Vander Waals kind of interaction with metal matrices arising from dispersion forces. Some groups [27-30] who were working on the thermodynamic aspects of wetting of metal/oxide couples have reported large variations between the experimental results and the theoretical considerations. The work of adhesion W_a plays a major role in determining the level of interaction of matrix and reinforcement. The more the work of adhesion W_a the better is the adhesion [15].

The interfacial failure needs to be evaluated accurately to estimate the performance of a metal matrix composite. The interfacial failure in case of particulate reinforced metal matrix composite has not been apprehended comprehensively till date. Several groups [31-34] have reported the basic mechanisms of interfacial failure in particle reinforced metal matrix composites as interface decohesion, damage accumulation, solute segregation, thermal misfit dislocation density, reinforcement geometry and clustering. To quantify the interfacial failure we need to understand the sintering response in context to the matrix-reinforcement alliance and the later depends directly on the reinforcement particle size and PSR (particle size ratio).

1.1.5 Characteristic Features

1.1.5a Fabrication of copper-alumina composites

Copper-alumina composites have a wide range of practical applications in electrical, automobile and aerospace industries [35]. The copper-alumina interaction is of utmost importance to certify specific applications. The surplus strength entitled to the material has to be compromised with the loss in ductility. The strength-ductility dichotomy can be alleviated by using small volume fraction of inclusions (reinforcements). Alumina is a strength boon to the matrix because it is chemically stable, inert and non reactive at high temperatures. Copper poses a threat in terms of mechanical pursuit, such as abrasion, sudden failure due to contact resistance (i.e. because of poor high temperature strength and wear performance) [36]. The electrical applications of copper demand high wear resistance to avoid abrasion failure in sliding contacts. Regarding reinforcements, oxide nanoparticles are most suitable because of their hardness, stability and insolubility in base metal and they also offer obstacles to dislocation motion at elevated temperatures without affecting the electrical and thermal conductivity [37]. Copper is an excellent material for electrical applications whose efficiency

can be enhanced by improving its mechanical properties [38]. When alumina particles are dispersed in copper matrix, they exhibit unique characteristics, such as high thermal and electrical conductivity, as well as high strength and excellent resistance to annealing [35]. The applications encompass resistance welding electrodes, lead frames and electrical connectors [39]. Its use has been suggested in International Thermonuclear Experimental Reactor (ITER). The first wall of the reactor has been proposed to be made out of austenitic stainless steel plate bonded to an alumina dispersed copper plate. Such critical applications of this material give way to their fabrication by powder metallurgy route. The studies on copper-alumina MMC along with their properties have been carried out by several groups [40-43]. Fathy et al. [40] have demonstrated improvement in compressive strength, hardness and wear resistance of Cu-Al_2O_3 system, Ritasalo et al. [41] have reported hardness value of 1.58 GPa for SPS sintered Cu-Al_2O_3 composite. The increase in arc erosion resistance of Cu-Al_2O_3 with the increase in alumina content has been reported by Wang et al. [42]. Nachum et al. [43] have studied the microstructural and mechanical properties of Cu-Al_2O_3 nanocomposites fabricated by HIPing, where the increase in strength and nanohardness has been highlighted. The fabrication of Cu-Al_2O_3 nanocomposites containing high volume fraction of alumina by SPS route has been performed by Michalski et al. [44], shows that it does not cater to the cost effectiveness factor of engineering industry. The influence of sintering atmosphere on the matrix-reinforcement bonding and subsequently other properties, such as densification and hardness, has not yet been understood in detail.

1.1.5b Fabrication of aluminium-alumina composites

Aluminium is a potent material for aerospace as well as military and electronics applications such as cryostats, cryo pump inducer and impeller, drive shafts and rotatory turbine machinery because it possesses high specific strength, high toughness and corrosion resistance [45]. Aluminium poses poor wear resistance which can be improved by the addition of ceramic reinforcements. Hesabi et al. [46] studied the compressibility of aluminium/nanometric alumina and have drawn a comparison between blended and milled powders. Rahimian et al. [47] have investigated that proper sintering parameters result in improved wear properties of Al-Al_2O_3 composites. Gudlur et al. [48] studied the variation in porosity with particle size and predicted the mechanical and thermal properties in Al-Al_2O_3 system. Tatar et al. [49] have reported the improvement of thermal conductivity of Al-Al_2O_3 composites with different alumina content. Zahibi et al. [50] have fabricated Al-Al_2O_3

composites by powder metallurgy and hot rolling processes, and showed that hot rolling process improved bonding of Al and Al_2O_3 as well distribution of Al_2O_3 in Al. Tahamtan et al. [51] synthesized Al-nano Al_2O_3 composites by ball milling followed by stir casting which resulted in better wettability of Al_2O_3 in Al, fair distribution of alumina particles in the matrix, low porosity and high tensile strength. Zebarjad and Sajjadi [52,53] milled Al–5 wt.% Al_2O_3 composite powders and noted that the alumina powders became finer and got dispersed more uniformly with increasing milling time and increase in microhardness of the composite. Prabhu et al. [54] milled Al–Al_2O_3 powder mixtures with different particle sizes (50 nm, 150 nm, and 5μm) and volume fractions (5, 10, 20, 30, and 50) of Al_2O_3. By milling the powder mixtures for different times in a SPEX mixer mill, the authors noted that a uniform dispersion of the reinforcement phase was obtained in all the cases after milling for about 20 h. Hesabi et al. [55] investigated the effect of Al_2O_3 powder particle size on the morphological and structural changes of Al–Al_2O_3 composites. They added 5 vol.% of nano- Al_2O_3 (with 35 nm particle size) and micro- Al_2O_3 (1μm particle size) to pure Al and milled these powders under identical conditions in a planetary ball mill. The milling stages include plastic deformation, microwelding, and particle fragmentation. These stages were found to occur earlier in the microcomposites than in the nanocomposites. On the other hand, longer milling time was found to be necessary to achieve the steady-state condition in the nanocomposites compared to the microcomposites. It was also noted that at the steady-state condition, the crystallite size and lattice strain of the Al matrix in the nanocomposite powder were smaller than in the microcomposites, suggesting a faster refinement process occurring in the nanocomposites. Zedah et al. [56] synthesized Al-Al_2O_3 adding mechanically activated nano-crystalline Al_2O_3 particles into aluminum matrix which showed finer microstructure, good dispersion and better mechanical attributes. Razavi-Tousi et al. [57] studied the effect of particle size and volume fraction of alumina on aluminium's compaction and densification and concluded that pressability decreases with decrease in particle size, with inhibition of grain growth.

1.1.6 Thermal Loadings

The ceramic phase which is generally used as reinforcement in MMC has a large difference in coefficient of thermal expansion with the metal phase. This thermal mismatch causes large residual thermal stresses near the interfaces of composite when they are cooled from the fabrication temperature [58-60]. Thermal stresses are important in design because they lead to plastic yielding or failure of the material. There are several mechanisms by which thermal

stresses can be relaxed which includes interface debonding, by microplasticity of the metal matrix and crack initiation and propagation [61]. These act as relaxation phenomenon to lower the internal strain in the composite.

The difference in thermal conductivity of the matrix and reinforcement generates a thermal gradient throughout the composite. The thermal mismatch of both constituents (matrix and reinforcement) plays a vital role in the thermo-mechanical reliability of devices. Some amount of thermal stress is relaxed by dislocation punching from the interface into the matrix via cooling from the processing temperature. This leads to high dislocation density and high yield strength. Thermal stress depends on: reinforcement volume fraction and morphology, matrix crystallographic texture, void or lack of adhesion at matrix reinforcement interface. Repetitive non reversible phenomena like thermal cycling leads to permanent deformation. The reinforcement particle geometry influences the degree of thermal stress as: reducing the size of the reinforcing particles would increase thermal fatigue resistance [62].
The thermal strain ε , developed at the interface of discontinuously reinforced MMCs due to thermal stress is expressed as

$$\varepsilon = \delta\alpha\, \delta T \tag{9}$$

Where δα is the difference between the thermal expansion coefficient of the reinforcement and the matrix and δT is the range of temperature experienced during processing. The generated thermal strain may exceed the local yield strain of matrix–reinforcement interface which will lead to the damage accumulation at the interface. The resultant phenomena of thermal stress are particulate fracture, de-bonding and cracking in the matrix–reinforcement interface, failure in the matrix via micro-void coalescence and shear fracture of the matrix which deteriorate the composite properties. The above failure mechanisms act as relaxation phenomena and lower the internal strain energy and entropy of the composite [63,64]. Characterization of damaged particles will be valuable in improving processing procedures and in understanding deformation and failure of MMCs.

The behaviour of metal matrix composites will be different from isothermal conditions when they are subjected to temperature cycling [65]. Plastic flow stress and strain hardening behaviour of the composites are affected by thermal cycling because of the triaxial state of stress generated at the particle–matrix interfaces. Residual stress can also have a considerable influence on the composites subjected to thermal cycling as they can initiate matrix phase

yielding which causes the formation of strain hysteresis loops between the heating and cooling segments of the cycle.

1.1.7 Loading rate

Loading rate corresponds to the crosshead velocity at which the mechanical test has been performed. Metal matrix composites respond differently to high strain rate loading conditions as compared to monotonic or quasistatic loading. As strain rate is increased from quasi-static to dynamic, the temperature conditions gradually change from isothermal to fully adiabatic. There is thermo-mechanical coupling in the adiabatic stress-strain curves i.e the effects of strain hardening, strain rate strengthening and thermal softening caused by the adiabatic temperature increase couple together. Structural applications require good performance during impact or high strain rate deformation [66]. Thermo-mechanical coupling effect has been observed in MMCs. Strain rate sensitivity of composites mostly adheres to the strain rate sensitivity behaviour of the corresponding matrices. Increasing particle content increases strain rate sensitivity. Strength of composites increases with increasing strain rate. The increase in strength with increasing strain rates was observed by some school of researchers, but some also concluded increase-decrease trend with increasing strain rates for stiffness and strength of materials. Flow stress also experiences an increasing trend with increasing strain rate [67]. Flow stress of matrix increases with increasing reinforcement content. At high strain rates local heat is generated which sometimes results in matrix melting. At high strain rates composites experience higher strain rate sensitivity than the monolithics.

1.2 Scope of the thesis

The organization of the rest of the thesis is as follows. A detailed experimental study and different experimental techniques are provided in chapter 2. All the equipments used for fabrication and characterization have been described. The thermal modules and processes followed for the thermal shock and conditioning experiments has also been tabulated.

In chapter 3.1a, a description of the effect of powder mixing techniques such as blending and milling experiments on the dispersion, microstructure and properties of Cu-Al_2O_3 and Al-Al_2O_3 micro- and nano-composites have been discussed in detail. A comparison of blending and milling procedures on several aspects such as dispersion of alumina particles in matrix particles, particle size variation and sintering response have been studied comprehensively.

Chapter 3.1b explains the effect of sintering atmosphere on microstructural evolution, structural integrity and properties of Cu-Al_2O_3 composites.

Chapter 3.2 is devoted to fabrication and characterization of Cu-Al_2O_3 and Al-Al_2O_3 micro- and nano-composites by conventional and spark plasma sintering. After fabrication and characterization of both systems mechanical properties were evaluated and a comparative study for micro- and nano-composites has been reported.

Chapter 3.3 describes the effects of induced thermal stress on the structural integrity and mechanical behaviour of Cu-Al_2O_3 and Al-Al_2O_3. A study on induced thermal stress by subjecting the copper and aluminium based micro- and nano-composites to thermal shock of different degrees, thermal conditioning, and high temperature flexural test with subsequent fractographies correlating microstructural integrity and mechanical behaviour has been conducted extensively for both the systems.

Chapter 3.4 is an exploratory study on the effect of loading rate sensitivity on the flexural strength of Cu-Al_2O_3 and Al-Al_2O_3 micro- and nano-composites. Different loading rates were maintained for flexural testing at ambient conditions and compared.
A summary of the main findings along with conclusions is presented in chapter 4.

References

[1] S.C. Tjong, Z.Y. Ma, Microstructural and mechanical characteristics of in situ metal matrix composites, *Mat. Sci. Eng. R* 29 (3) (**2000**) 49-113.

[2] A. Kelly, C. Zweben, Comprehensive Composite Materials Vol. 3, Elsevier Science Ltd., United Kingdom, first edition, **2000**, 1-50.

[3] G.E. Dieter, Mechanical Metallurgy, McGraw- Hill, London, United Kingdom, Third Edition **1988**.

[4] S.M. Choi, H. Awaji, Nanocomposites-a new material design concept, Sci. Technol. Adv. Mater. 6 (**2005**) 2-10.

[5] Y. Li, Y.H. Zhao, V. Ortalan, W. Liu, Z.H. Zhang, R.G. Vogt, N.D. Browning, E.J. Lavernia, J.M. Schoenung, Investigation of aluminium-based nanocomposites with ultra-high strength, Mat. Sci. Eng. A. 527 (**2009**) 305-316.

[6] W.Z. Eddine, P. Matteazzi , J-P. Celis, Mechanical and tribological behaviour of nanostructured copper-alumina cermets obtained by pulsed electric current sintering, *Wear* 297 (**2013**) 762-773.

[7] E.O. Hall, The deformation and ageing of mild steel: II Characteristics of the luders deformation, Proceedings of the physical society-section B, 64 (9) (**1951**) 742-747.

[8] N.J. Petch, The cleavage strength of polycrystals, *J. Iron. Steel. Res. Int.* 174 (**1953**) 25-28.

[9] Z. Zhang, D.L. Chen, Consideration of Orowan strengthening effect in particulate-reinforced metal matrix nanocomposites: a model for predicting their yield strength, *Scripta. Mater*. 54 (**2006**) 1321-1326.

[10] N. Ramakrishnan, An analytical study on strengthening of particulate reinforced metal matrix composites, *Acta. Mater*. 44 (1) (**1996**) 69-77.

[11] R.M. German, Powder Metallurgy, John Wiley and Sons, Inc., New York, Second Edition **1994**.

[12] S. Vaucher, O. Beffort, Bonding and interface formation in metal matrix composites, MMC-*Assess Thematic Network*, Volume 9. Thun: EMPA, **2001.**

[13] D.J. Lloyd, Particle reinforced aluminium and magnesium matrix composites, *Int. Mater. Rev.* 39 (**1994**) 1.

[14] L. Lu, M.O. Lai, G. Li, Influence of sintering process on the mechanical property and microstructure of ball milled composite compacts, *Mater. Res. Bull.* 31 (**1996**) 453-464.

[15] S. Suresh, A. Mortensen, A. Needleman, Fundamental of Metal Matrix Composites, Butterworth- Heinemann, **1993**.

[16] Z.A. Munir, D.V. Quach, M. Ohyanagi, Electric current activation of sintering: a review of the pulsed electric current sintering process, *J. Am. Ceram. Soc.* 94 (1) (**2011**) 1-19.

[17] M.T. Luke, Microstructural evolution of nickel during spark plasma sintering, *Master of Science Thesis*, Boise State University, Idaho, United States, **2010**.

[18] Z.Z. Fang, Sintering of advanced materials: fundamentals and processes, Woodhead publishing, **2010**.

[19] M. Eriksson, H. Yan, M. Nygren, M.J. Reece, Z. Shen, Low temperature consolidated lead-free ferroelectric niobate ceramics with improved electrical properties, *J. Mater. Res.* 25 (2) (**2010**) 240-247.

[20] S.L. Gallet, L. Campayo, E. Courtois, S. Hoffmann, Y. Grin, F. Bernard, F. Bart, Spark plasma sintering of iodine-bearing apatite, *J. Nuclear Mater*. 400 (3) (**2010**) 251-256.

[21] L. Campyao, S.L Gallet, Y. Grin, E. Courtois, F. Bernard, F. Bart, Spark plasma sintering of lead phosphovanadate $Pb_3(VO_4)_{1.6}(PO_4)_{0.4}$, *J. Eur. Ceram. Soc.* 29 (14) (**2009**) 77-84.

[22] Y. Kan, P. Wang, T. Xu, G. Zhang, D. Yan, Z. Shen, and Y-B. Cheng, Spark plasma sintering of bismuth titanate ceramics, *J. Am. Ceram. Soc*. 88 (6) (**2005**) 1631-1633.

[23] C. Drouet, C. Largeot, G. Raimbeaux, C. Estournes, G. Dechambre, C. Combes, C. Rey, Bioceramics: Spark Plasma Sintering (SPS) of calcium phosphates, *Adv. Sci. Technol*. 49, (**2006**) 45-50.

[24] A. Bassano, M.T. Buscaglia, V. Buscaglia, P. Nanni, Particle size and morphology control of perovskite oxide nanopowders for nanostructured materials, *Integr Ferroelectr*. 109 (1) (**2009**) 1-17.

[25] M. Okamoto, Y. Akimune, K. Furuya, M. Hatano, M. Yamanaka, M. Uchiyama, Phase transition and electrical conductivity of scandia-stabilized zirconia prepared by spark plasma sintering process, *Solid State Ionics* 176 (7) (**2005**) 675-680.

[26] N. Chennoufi, G. Majkic, Y.C. Chen, K. Salama, Temperature, current, and heat loss distributions in reduced electrothermal loss spark plasma sintering, *Metall. Mater. Trans. A*, 40 (10) (**2009**) 2401-2409.

[27] C.A. Handwerker, J.W. Cahn, J.R. Manning, Thermodynamics and kinetics of reactions at interfaces in composites, Mat. Sci. Eng. A 126 (1) (**1990**) 173-189.

[28] A. Koltsov, F. Hodaj, N. Eustathopoulos, Factors governing interfacial reactions in liquid metal/non-oxide ceramic systems: Ni-based alloy–Ti/sintered AlN system, *J. Eur. Ceram. Soc.* 29 (1) (**2009**) 145-154.

[29] P. Hicter, D. Chatain, A. Pasturel, N. Eustathopolous, An electronic model for thermodynamical adhesion in non reactive SP-metal-aluminate systems, J. de. Chim. Phys. 85 (**1988**) 941-945.

[30] D. Chatain, I. Rivollet, N. Eustathopolous, Thermodynamic adhesion in non reactive liquid metal alumina systems, J. de. Chim. Phys. 83 (**1986**) 561-567.

[31] G.G. Sozhamannan, S.B. Prabu, R. Paskaramoorthy, Failures analysis of particle reinforced metal matrix composites by microstructure based models**,** *Mater. Des.* 31 (**2010**) 3785-3790.

[32] X.J. Wang, K. Wu, W.X. Huang, H.F .Zhang, M.Y. Zheng, D.L. Peng, Study on fracture behaviour of particulate reinforced magnesium matrix composite using in situ SEM, *Compos. Sci. Technol.* 67 (11) (**2007**) 2253-2260.

[33] M. Gupta, M.K. Surappa, S. Qin, Effect of interfacial characteristics on the failure-mechanism mode of a SiC reinforced Al based metal-matrix composite, *J. Mater. Process. Technol.* 67 (1) (**1997**) 94-99.

[34] G. Liu, Z. Zitang, J.K. Shang, Interfacial microstructure and fracture of Al_2O_3 particulate reinforced Al-Cu composite, *Acta. metal. mater*. 42 (1) (**1994**) 271-282.

[35] M.S. Motta, P.K. Jena, E.Z. Brocchi, I.G. Solorzano, Characterization of Cu-Al_2O_3 nanoscale composites synthesized by in situ reduction. *Mat. Sci. Eng. C.* 15 (1) (**2001**) 175-177.

[36] H.W. Turner, C. Turner, Copper in electrical contacts, Technical note (edited version of an original script commissioned by Copper Development Association, ERA Technology Ltd., Leatherhead, Surrey) 23 (**1980**).

[37] M. Korac, Z. Kamberovic, M. Tasic, M. Gavrilovski, Nanocomposite powders for new contact materials based on copper and alumina, Chem. Ind. Chem. Eng. Q. 14 (4) (**2008**) 215-218.

[38] G.C. Efe, T. Yener, I. Altinsoy, M. Ipek, S. Zyetin, C. Bindal, The effect of sintering temperature on some properties of Cu-SiC composite, J. Alloy Compd. 509 (20) (**2011**) 6036-6042.

[39] H. Nishi, T. Araki, M. Eto, Diffusion bonding of alumina dispersion-strengthened copper to 316 stainless steel with interlayer metals, *Fusion Eng. Des.* 39-40 (1) (**1998**) 505-511.

[40] A. Fathy, F. Shehata, M. Abdelhameed, M. Elmahdy, *Mater. Des*. 36 (**2012**) 100-107.

[41] R. Ritasalo, X.W. Liu, O. Soderberg, A. Keski-Honkola, V. Pitkanen, S-P. Hannula, The microstructural effects on the mechanical and thermal properties of pulsed electric current sintered Cu-Al_2O_3 composites, *Proc. Eng.* 10 (**2011**) 124-129.

[42] X. Wang, S. Liang, P. Yang, and Z. Fan, Effect of Al_2O_3 content on electrical breakdown properties of Al_2O_3/Cu composite, *J. Mater. Eng. Perform*. 19 (9) (**2010**) 1330-1336.

[43] S. Nachum, N.A. Fleck, M.F. Ashby, A. Colella, P. Matteazzi, The microstructural basis for the mechanical properties and electrical resistivity of nanocrystalline Cu-Al_2O_3, *Mat. Sci. Eng. A* 527 (20) (**2010**) 5065-5071.

[44] A. Michalski, J. Jaroszewicz, M. Rosinski, D. Siemiaszko, K.J. Kurzydłowski, Nanocrystalline Cu-Al_2O_3 composites sintered by the pulse plasma technique, *Solid State Phenom*. 114 (**2006**) 227-232.

[45] S. Lim, T. Imai, Y. Nishida, T. Choh, High strain rate superplasticity of TiC particulate reinforced magnesium alloy composite by vortex method, *Scripta. Metall. Mater*. 32 (11) (**1995**) 1713-1717.

[46] Z.R. Hesabi, H.R. Hafizpour, A. Simchi, An investigation on the compressibility of aluminum/nano-alumina composite powder prepared by blending and mechanical milling**,** Mat. Sci. Eng. A 454-455 (**2007**) 89-98.

[47] M. Rahimian, N. Parvin, N. Ehsani, The effect of production parameters on microstructure and wear resistance of powder metallurgy Al–Al_2O_3 composite, *Mater. Des*. 32 (**2011**) 1031-1038.

[48] P. Gudlur, A. Forness, J. Lentz, M. Radovic, A. Muliana, Thermal and mechanical properties of Al/Al_2O_3 composites at elevated temperatures**,** Mat. Sci. Eng. A. 531 (1) (**2012**) 18-27.

[49] C. Tatar, N. Ozdemir, Investigation of thermal conductivity and microstructure of the α-Al_2O_3 particulate reinforced aluminium composites (Al/Al_2O_3-MMC) by powder metallurgy method**,** *Physica B* 405 (3) (**2010**) 896-899.

[50] M. Zabihi, M.R. Toroghinejad, A. Shafyei, Application of powder metallurgy and hot rolling processes for manufacturing aluminium/alumina composite strips Mat. Sci. Eng. A. 560 (10) (**2013**) 567-574.

[51] S. Tahamtan, A. Halvaee, M. Emamy, M.S. Zabihi, Fabrication of Al/A206-Al_2O_3 nano/micro composite by combining ball milling and stir casting technology, *Mater. Design.* 49 (**2013**) 347-359.

[52] S.M. Zebarjad, S.A. Sajjadi, Dependency of physical and mechanical properties of mechanical alloyed Al–Al_2O_3 composite on milling time. *Mater. Design.* 28 (7) (**2007**) 2113-2120.

[53] S.A. Sajjadi, H.R. Ezatpour, H. Beygi, Microstructure and mechanical properties of Al–Al_2O_3 micro and nano composites fabricated by stir casting. *Mat. Sci. Eng. A* 528 (29) (**2011**) 8765-8771.

[54] B. Prabhu, C. Suryanarayana, L. An, R. Vaidyanathan, Synthesis and characterization of high volume fraction Al–Al_2O_3 nanocomposite powders by high-energy milling, *Mat. Sci. Eng. A* 425 (**2006**) 192-200.

[55] Z.R. Hesabi, A. Simchi, S.M.S. Reihani, Structural evolution during mechanical milling of nanometric and micrometric Al_2O_3 reinforced Al matrix composites, *Mat. Sci. Eng. A.* 428 (**2006**) 159-168.

[56] M.H. Zadeh, M. Razavi, O. Mirzaee, R. Ghaderi, Characterization of properties of Al-Al_2O_3 nano-composite synthesized via milling and subsequent casting, Journal of King Saud University – Engineering Sciences 25 (1) (**2013**) 75-80.

[57] S.S. Razavi-Tousi, R. Yazdani-Rad, S.A. Manafi, Effect of volume fraction and particle size of alumina reinforcement on compaction and densification behaviour of Al-Al_2O_3 nanocomposites**,** *Mat. Sci. Eng. A.* 528 (3) (**2011**) 1105-1110.

[58] R.J. Arsenault, R.M. Fisher, Microstructure of fiber and particulate SiC in 6061 Al composites**,** *Scripta. metal*. 17 (1) (**1983**) 67-71.

[59] T. Christman, A. Needleman, S. Nutt, S. Suresh, On microstructural evolution and micromechanical modelling of deformation of a whisker-reinforced metal-matrix composite, *Mat. Sci. Eng. A*, 107 (**1989**) 49-61.

[60] A. Wang, H.J. Rack, Abrasive wear of silicon carbide particulate and whisker-reinforced 7091 aluminium matrix composites**,** *Wear* 146 (**1991**) 337-348.

[61] B.C. Ray, Temperature effect during humid ageing on interfaces of glass and carbon fibers reinforced epoxy composites**,** *J. Colloid. Interf. Sci*. 298 (1) (**2006**) 111-117.

[62] C.M.L. Wu, G.W. Han, Thermal fatigue behaviour of SiC_p/Al composite synthesized by metal infiltration**,** *Compos. Part A* 37 (11) (**2006**) 1858-1862.

[63] T.W. Clyne, P.J. Withers, An Introduction to Metal Matrix Composites, Cambridge University Press, Cambridge, **1993**.

[64] A.F. Whitehouse, T.W. Clyne, Effects of reinforcement content and shape on cavitation and failure in metal matrix composites, *Compos.* 3 (**1993**) 256-261.

[65] S.M. Pickard, B. Derby, The deformation of particle reinforced metal matrix composites during temperature cycling *Acta. Metall. Mater.* 38 (12) (**1990**) 2532-2552.

[66] Y. Zhou, Y. Xia, Experimental study of the rate sensitivity of SiC_p /Al composites and the establishment of a dynamic constitutive equation, *Compos. Sci. Tech.* 60 (**2000**) 403-410.

[67] Z.H. Tan, B.J. Pang, D.T. Qin, J.Y. Shi, B.Z. Gai, The compressive properties of 2024 Al matrix composites reinforced with high content SiC particles at various strain rates, *Mat. Sci.Eng. A* 489 (**2008**) 302-309.

Chapter 2

Experimental Details

2.1 Fabrication

2.1.1 Blending

Copper (Loba Chemie, purity > 99.7%, average size~11µm) aluminium (Loba Chemie, purity > 99.7%, average size~22µm and alumina (Sigma Aldrich, average size~10µm (micro) and <50 nm (nano)) powders were blended separately in turbula shaker mixer (T2F, LCR Hi Tester, Switzerland) for 8 hours at 45 rpm. Copper-5 vol. % micron size alumina, copper-5 vol. % nano size alumina, aluminium-5 vol. % micron size alumina and aluminium-5 vol. % nano size alumina compositions were blended. The compositions blended for conventional sintering are Cu-1, 3, 5, 7 vol. % Al_2O_3 nanocomposites and Cu-5, 10, 15, 20 vol. % Al_2O_3 microcomposites. The compositions used for spark plasma sintering of nanocomposites were 0.5, 1, 3, 5, and 7 vol. % of alumina nanoparticles in copper and aluminium matrix. Another set of specimens having compositions of 1, 5, 20 vol. % micron size alumina were used to synthesize microcomposites by spark plasma sintering. The blended powders were collected at 2, 4, 8 hours and characterized by scanning electron microscopy.

2.1.2 Milling

Mixture of copper-alumina and aluminium-alumina powders were milled separately at a speed of 300 rpm in a dual drive planetary mill (the design and make of the mill is available

in an Indian patent "*Synthesis of stable nanocrystalline iron carbides by reaction milling in a dual-drive planetary mill" patent application no. 1021/DEL/2007, Dated: 10.05.07*"). Copper-5 vol. % micron size alumina and aluminium-5 vol. % micron size alumina compositions were milled for 10 hours. The powders were collected at intervals of 2, 5, 10 hours and characterized for particle size analysis, scanning electron microscopy and x-ray diffraction.

2.1.3 Compaction

The copper-alumina and aluminium-alumina milled powders were compacted at 700 MPa and 400 MPa respectively in a uniaxial press (SoilLab). Specimens for 3-point flexural test were compacted using a rectangular die of dimension (31.5x12.5x6.35 mm^3). Compression test samples were prepared using cylindrical die of diameter 10 mm.

2.1.4 Sintering

2.1.4.1 Conventional sintering

Sintering of the cylindrical pellets was carried out in a super kanthal heated tubular furnace (Naskar, India). Commercially pure nitrogen, hydrogen and argon gas were used as sintering atmosphere to prevent oxidation during heating. The samples were held at their different sintering temperatures for 60 minutes followed by furnace cooling at a heating rate of 5°C/minute, the details of sintering temperature and compositions of composites used for fabrication is tabulated in Table 2.1.

2.1.4.2 Spark plasma sintering

The micro- and nano-composites were fabricated via spark plasma sintering (SPS) (DR SINTER LAB SPS Syntex INC, model: SPS-515S, Kanagawa, Japan) method at a temperature of 700ºC (copper) and 500°C (aluminium) maintaining a soaking time of 5 minutes at a ram pressure of 50 MPa. The heating rate for the whole process was maintained at 80ºC/minute for both cases.

Composition	Conventional sintering temperature (°C)	Composition	Spark plasma sintering temperature (°C)
Copper-1,3,5,7 vol. % nanoalumina	**850, 900, 1000**	**Copper-0.5,1,3,5,7 vol. % nanoalumina**	**700**
Copper-5,10,15,20 vol. % microalumina	**850, 900, 1000**	**Copper-1,5,20 vol. % microalumina**	**700**
Aluminium-1,3,5,7 vol. % nanoalumina	**500, 550, 600**	**Aluminium-0.5,1,3,5,7 vol. % nanoalumina**	**500**
Aluminium- 5,10,15,20 vol. % microalumina	**500, 550, 600**	**Aluminium-1,5,20 vol. % microalumina**	**500**

Table 2.1 The compositions of micro- and nano-composite used for copper and aluminium matrix and their corresponding sintering temperatures.

2.2 Characterization

2.2.1 Particle size analysis

The particle size was measured in a laser particle size analyzer (Malvern, Mastersizer 2000, UK). The dispersion for paricle size analysis was prepared by dispersing the powder particles in sodium hexa metaphosphate solution made by dissolving 2gms in 100 ml of water.

2.2.2 X-ray diffraction

X-ray diffraction of the as milled powders, and sintered composite samples were performed using the diffractometer (PANalytical model: DY-1656). The radiations used were CuK_{α} (λ=1.542A°). X-ray diffraction was carried out with a scan speed of 2°/minute. The XRD patterns of as-received alumina micropowder and nanopowder has been plotted in Fig. 2.1.

2.2.3 Scanning electron microscopy

The SEM micrographs of as received powder, blended powder, milled powder, sintered samples and fracture surfaces were obtained using the scanning electron microscope (JEOL JSM 6480 LV). The images were taken in both secondary electron (SE) and back scattered electron (BSE) mode according to requirement. The elemental detection analysis (EDS) was also done in order to study the elements present in the samples which is equipped with INCA

software. SEM micrographs of as-received alumina micropowder and nanopowder have been illustrated in Fig. 2.2.

2.2.4 Field emission scanning electron microscopy

The sintered composites and fracture surfaces of flexural bend test samples were captured under field emission electron microscope (NOVA NANOSEM 450). The FESEM micrographs were obtained at high magnifications such as 100000X and 200000X magnifications also.

2.2.5 Transmission electron microscopy

Transmission electron microscopy (TECNAI G2 20S-TWIN) equipped with an energy dispersive X-ray analyser was used to obtain transmission electron micrographs of composite samples and thermally treated samples. The samples were prepared by punching 3 mm discs from the sample whose thickness had been reduced to 100μm. The discs were then dimpled to around below 10μm and then ion milled for 1 hour for perforation.

2.3 Mechanical property study

2.3.1 Density measurement

Density of sintered specimens was measured by Archimedes water immersion method. The density measurement kit (Contech model no: CB-300) was used for measuring the suspended weight and soaked weight of the specimens.

2.3.2 Microhardness study

Microhardness of the specimens was measured by Vickers hardness tester (Leco Microhardness Tester LM248AT) at a load of 0.3kgf for a dwell time of 5 seconds. A minimum of 4 readings was taken for each specimen.

2.3.3 Nanoindentation hardness

The nanoindentation hardness and elastic modulus of the nanocomposites were determined using nanoindentation (Fisher-Cripps UMIS) technique by applying a load of 20mN for a dwell time of 10 seconds. The readings were recorded at ten equivalent locations for each specimen and the closest values were considered.

2.3.4 Compression test

According to ASTM standard E9-89 compression test was conducted with the aid of universal testing machine (INSTRON SATEC series servo-hydraulic machine) with specimen dimensions of 10 mm diameter and 8 mm height at a strain rate of $1min^{-1}$. Graphite powder was used to minimize friction between the sample and fixture of compression machine. A reduction of 50% in height was maintained for all the specimens. The end surfaces were kept normal to the axis of the specimen.

2.3.5 Flexural test

A set of specimens having dimensions of 31.5 x12.7 x 6.3 mm^3, in accordance with ASTM standard B925-08 were fabricated following the above mentioned route for both copper and aluminium matrix micro- and nano-composites except for maintaining the sintering holding time for 90 minutes. A span length of 26mm and crosshead velocity of 0.5mm/minute was maintained during the flexural tests which were carried out in universal testing machine (INSTRON-5967).

2.3.6 Wear test

Sliding wear tests were performed using a ball on plate type wear machine (DUCOM TR-208-M1) using hardened steel ball (SAE 52100) indenter of 2 mm diameter, with an applied load of 2 Kgf and sliding time of 15 minutes at a speed of 30 rpm. The hardened steel ball slides unidirectionally on fixed samples. The tests were carried out in laboratory atmosphere at a relative humidity of around 50-60% and temperature of about 25°C. The wear depth vs sliding time data was obtained from the inbuilt WINCOM software in the wear machine. The worn surfaces were characterized by SEM.

2.4 Thermal treatment

2.4.1 Furnace

The composites were subjected to high temperatures in furnace (OE motors India Ltd.) for thermal shock and thermal conditioning treatments.

2.4.2 Ultra-low temperature chamber

The composites were subjected to ultra low temperature in a chamber (S.D. Scientific) for thermal shock and thermal conditioning treatments.

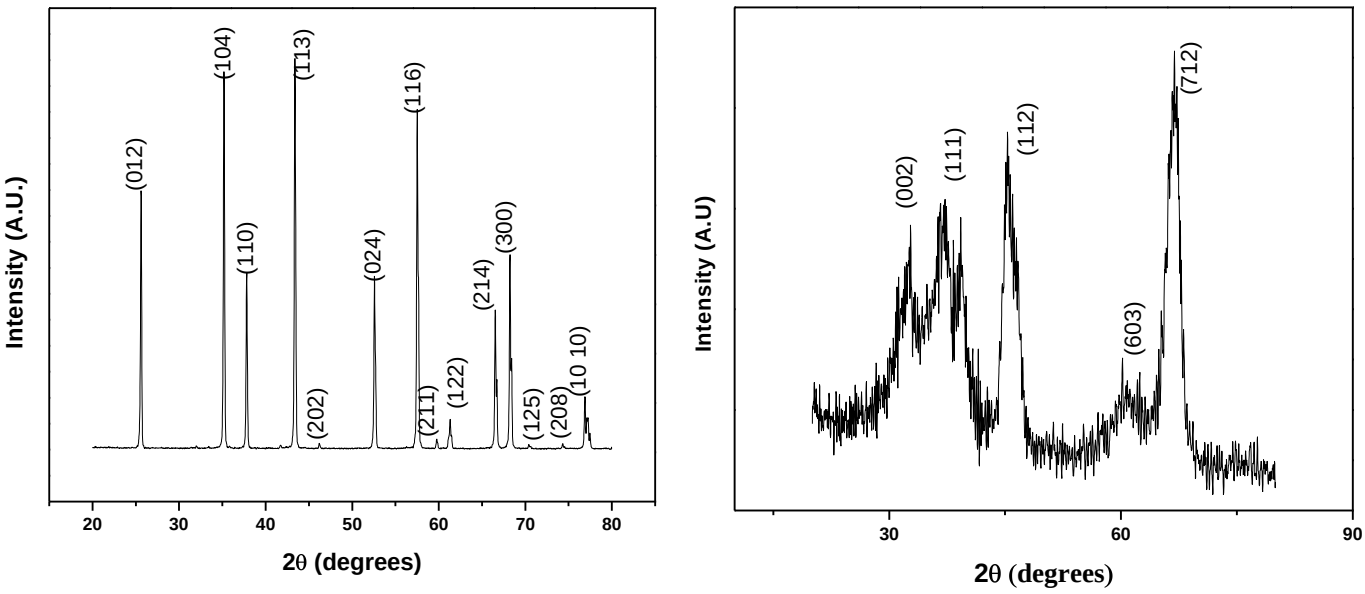

Fig. 2.1 XRD patterns of as-received alumina micropowder (left) and nanopowder (right)

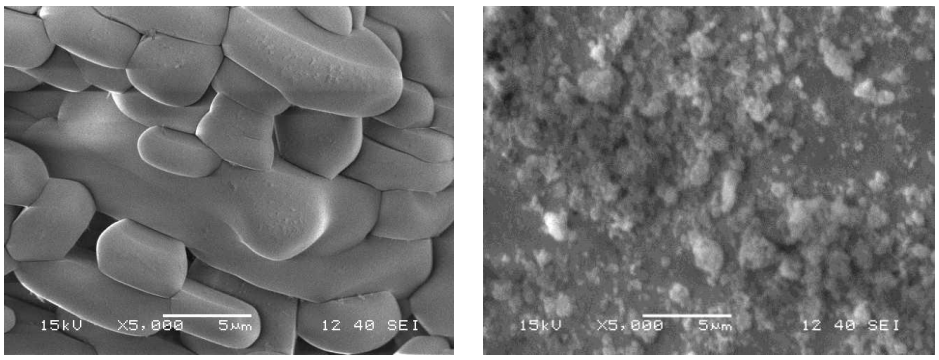

Fig. 2.2 SEM micrographs of as-received alumina micropowder (left) and nanopowder (right)

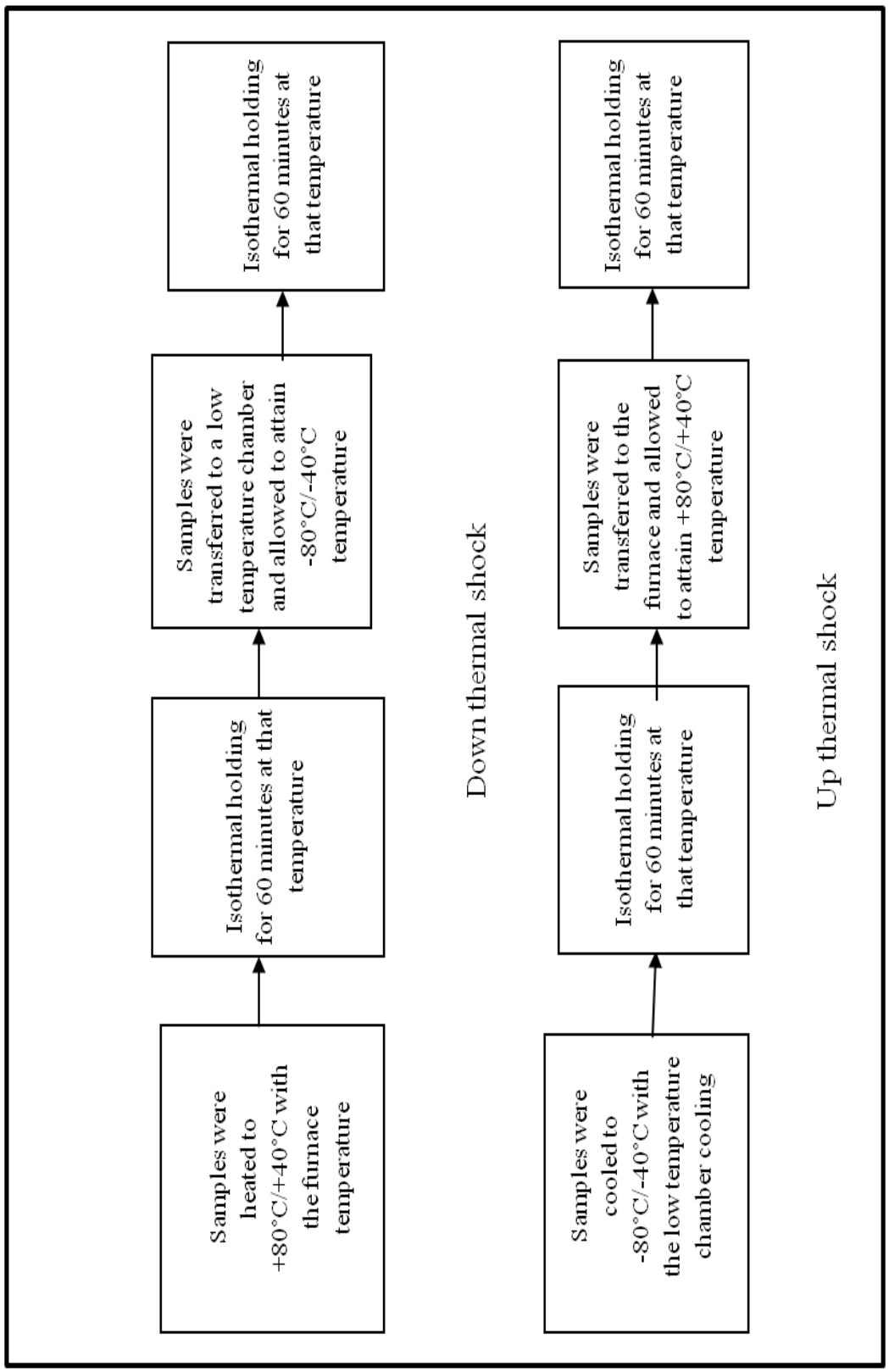

Table 2.2 Schematic diagram explaining the experimental process for thermal shock experiments.

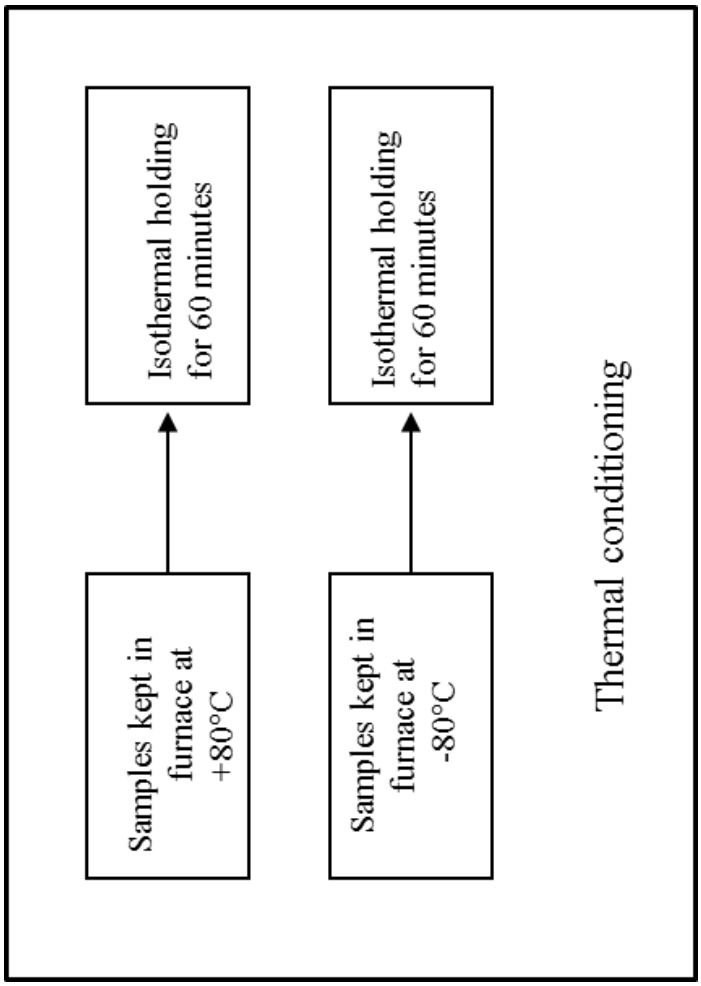

Table 2.3 Schematic diagram explaining the experimental process for thermal conditioning experiments.

Chapter 3

Results and Discussion

3.1a Effect of milling and blending on the dispersion, microstructure and properties of Cu-Al_2O_3 and Al-Al_2O_3 composites

3.1a.1 Scope and objectives of the work

During fabrication of MMC, homogeneous dispersion of reinforcement into metal matrix is always a great challenge. Blending and milling are widely used for this purpose. Here, turbula shaker mixer has been used for uniform dispersion of reinforcement into matrix. The 3-D movement of the jar results in homogeneous mixing. High energy planetary milling has also been used to reduce powder particle size as well for mixing powder particles. The comparison between milling and blending of powders in terms of dispersion and sintering response of milled and blended powders after consolidation has been investigated in this chapter.

3.1a.2 Fabrication of composites

Blending

The Cu-5 vol. % micro- as well as nano-alumina powders were blended separately in a turbula shaker mixer for 2, 4 and 8 hours and consolidation was done using conventional sintering method.

Milling

The Cu-5 vol. % micro-alumina powder was milled in a dual drive planetary mill for 2, 5 and 10 hours and consolidation was done using conventional sintering method. A ball to powder weight ratio of 10:1 was used during milling. Milling was conducted under toluene to prevent oxidation.

Consolidation

The milled and blended powders were compacted uniaxially and sintered conventionally in a tubular furnace at 900°C for copper-alumina and at 600°C for aluminium-alumina composites for 1 hour in both cases.

3.1a.3 Characterization of composites

3.1a.3.1 X-Ray diffraction

Fig. 3.1a.1 shows XRD pattern of Cu-5 vol. % Al_2O_3 microcomposite powders milled for different time periods. The XRD patterns show broadening and reduced intensity of copper and alumina peaks with increasing milling time. Heavy deformation of powders due to collision between ball-powder, powder-powder results in decrease in crystallite size and increase in lattice strain. Fig. 3.1a.2 shows XRD pattern of Al-5 vol. % Al_2O_3 micro-composite powders milled for different periods. It shows the intensity of aluminium and alumina peaks gradually decreases with milling demonstrating decrease in crystallite size, severe lattice distortion and grain refinement [1].

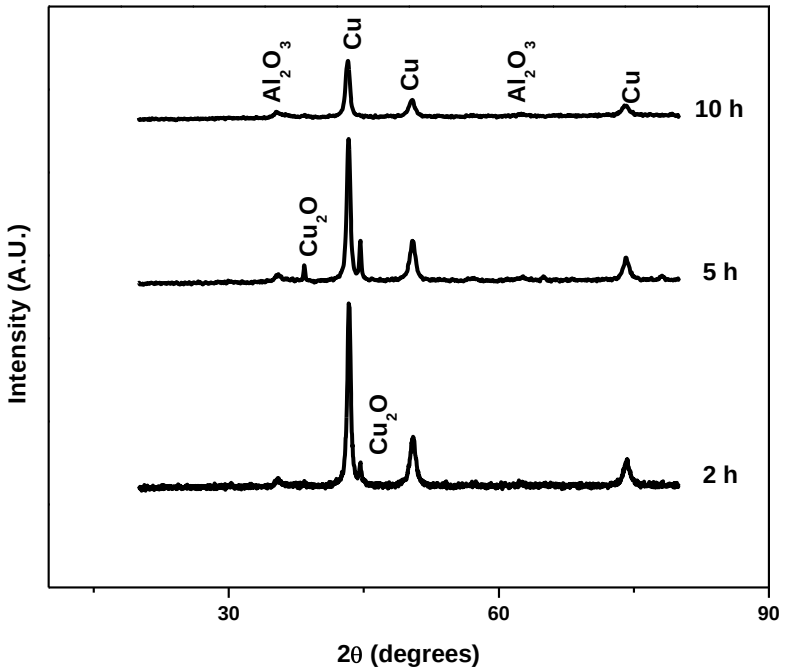

Fig. 3.1a.1 X-ray diffraction patterns of Cu-5 vol. % Al_2O_3 microcomposite powders after 2, 5, 10 hours of milling

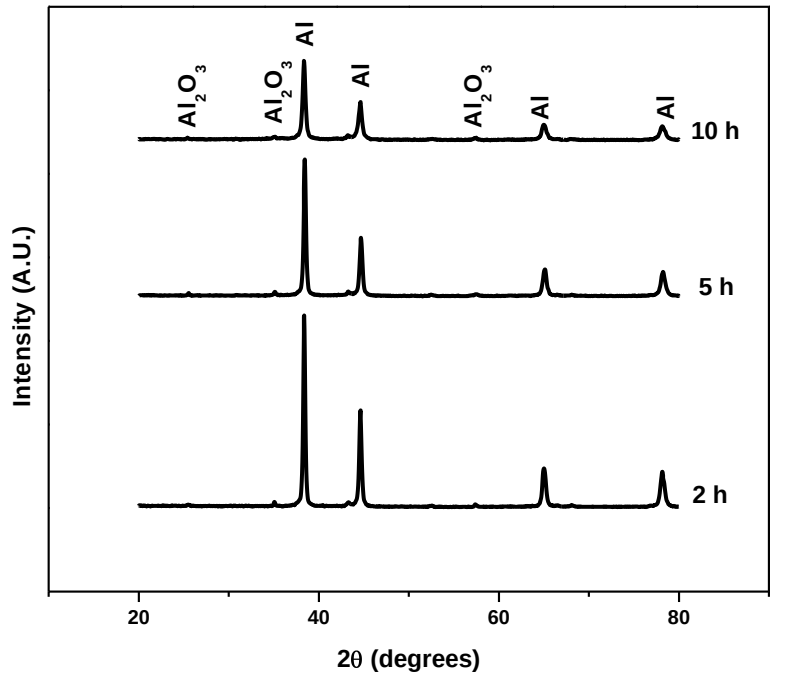

Fig. 3.1a.2 X-ray diffraction patterns of Al-5 vol. % Al_2O_3 microcomposite powders after 2, 5, 10 hours of milling

3.1a.3.2 Particle size analysis

The particle size analysis (Fig. 3.1a.3 & 3.1a.4) reveals that the particle size initially increases and then decreases with further milling for both Cu-5 vol. % Al_2O_3 and Al-5 vol. % Al_2O_3 micro-composite powders. As copper and aluminium are ductile and soft in nature during initial stage of milling the particles weld and become flat in shape [2].

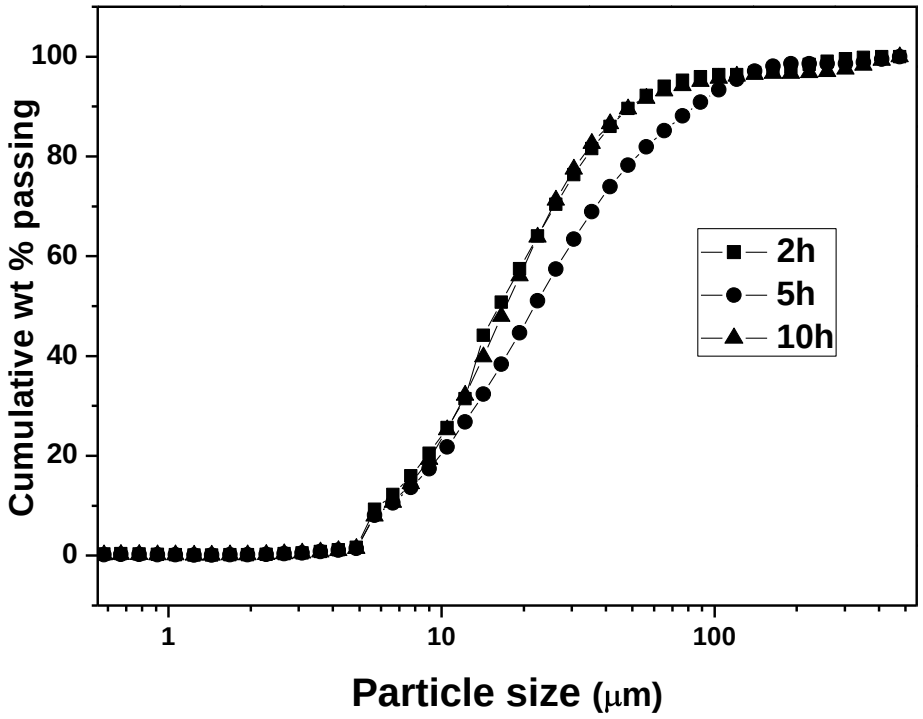

Fig. 3.1a.3 Particle size distribution of Cu-5 vol. % Al_2O_3 microcomposite powders milled for different time periods

The flattening of particles is followed by welding of flat particles with each other. Further milling leads to work hardening and result in particle fragmentation [3].

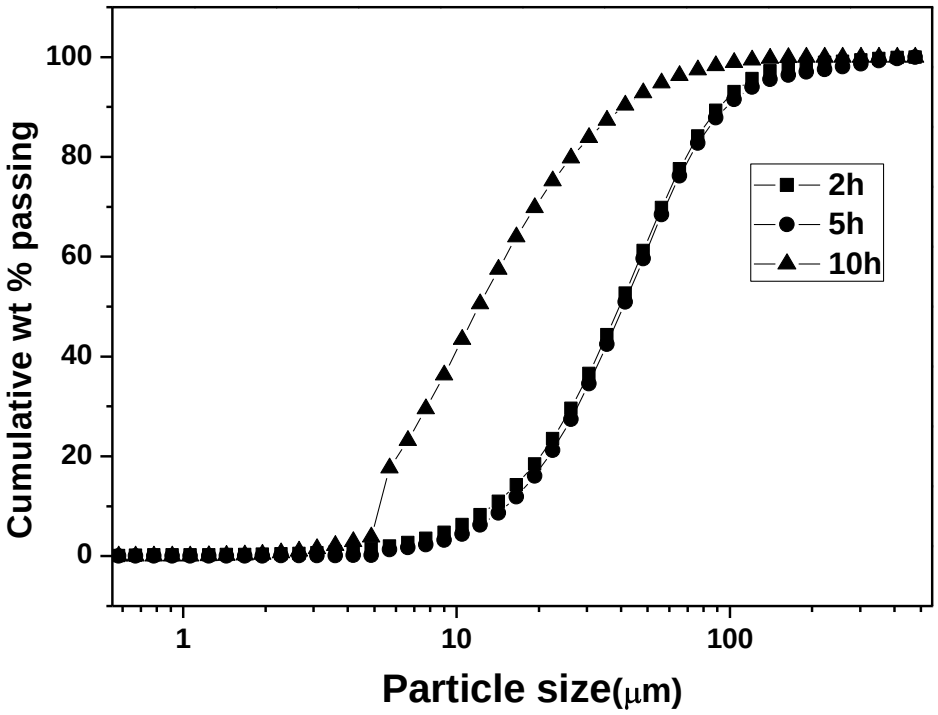

Fig. 3.1a.4 Particle size distribution of Al-5 vol. % Al_2O_3 microcomposite powders milled for different time periods

3.1a.3.3 Scanning electron microscopy

3.1a.3.3.1 Dispersion

The SEM micrographs in Fig. 3.1a.5 show the Cu-5 vol. % Al_2O_3 microcomposite powders after 2, 5 and 10 hours of milling. The micrographs show increase in particle size and become flaky after 2 hours of milling and then decreases after 10 hours of milling. After 10 hours of milling particles become almost spherical in nature.

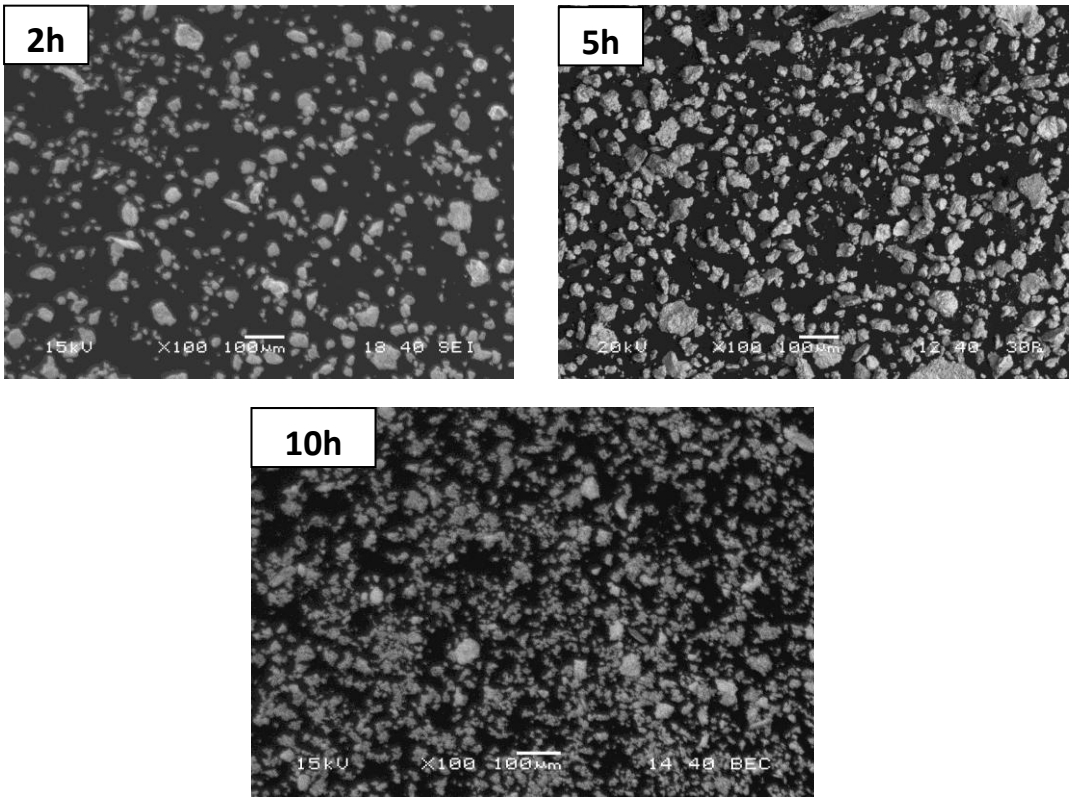

Fig. 3.1a.5 SEM micrographs of Cu-5 vol. % Al_2O_3 microcomposite powders after 2,5,10 hours of milling

Fig. 3.1a.6 shows the SEM micrographs Al-5 vol. % Al_2O_3 microcomposite powders milled for different times. The particle size gradually reduces as milling progresses. Agglomeration of particles is visible at places due to surface activation during milling. The initial stage of milling results in particle size increase due to flattening of particle as aluminium is ductile. The flattened particles then weld with each other forming stacked flat particles. These stacks then get strain hardened with milling and then particle fragmentation takes place, reducing the particle size appreciably.

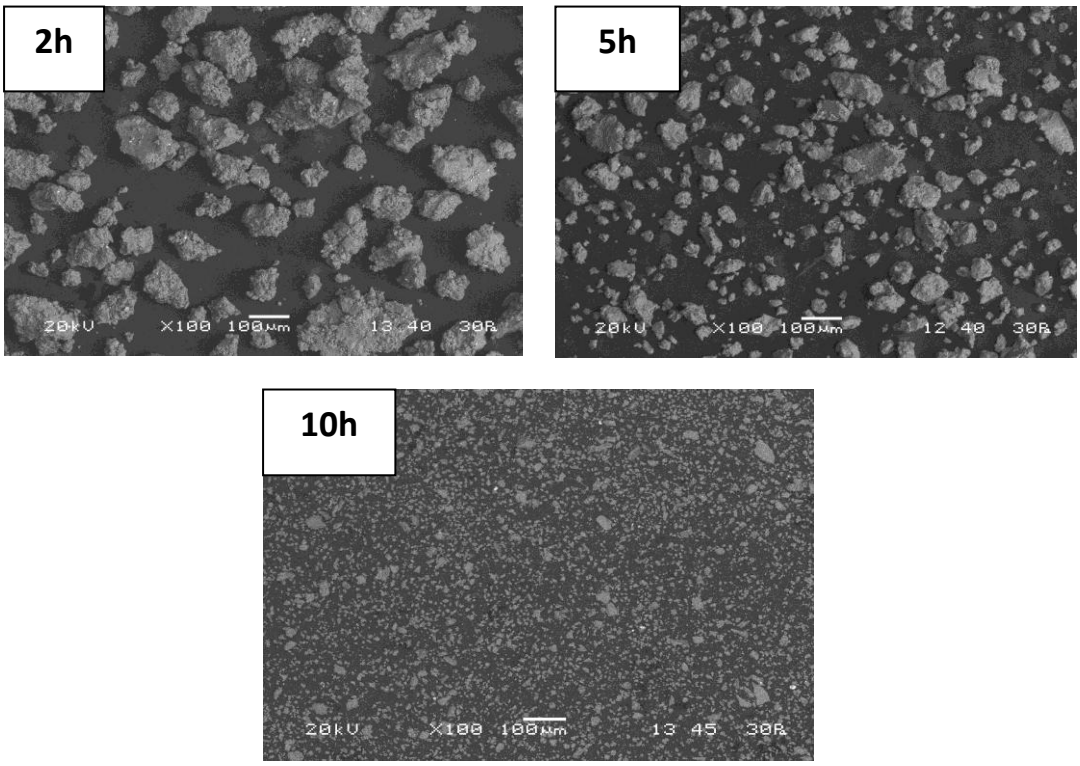

Fig. 3.1a.6 SEM micrographs of Al-5 vol. % Al_2O_3 microcomposite powders after 2,5,10 hours of milling

Fig. 3.1a.7 & 3.1a.8 reveal fair distribution of micron size alumina particles in copper matrix. As the blending time increase the distribution gets better.

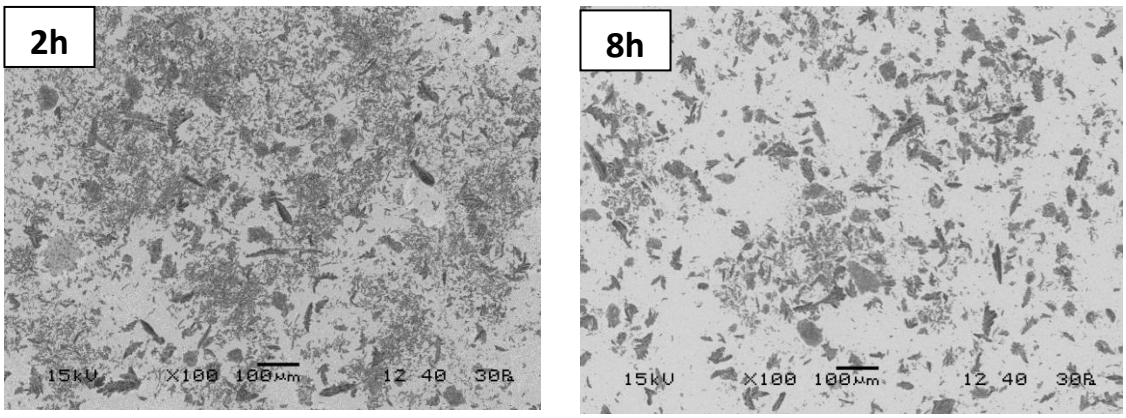

Fig. 3.1a.7 SEM micrographs of Cu-5 vol. % Al_2O_3 microcomposite powders after 2 and 8 hours of blending

The nanoalumina particles show appreciable distribution in copper particles, which improves with increase in blending time. Th copper particles show dendritic shape and alumina particles are spherical in shape.

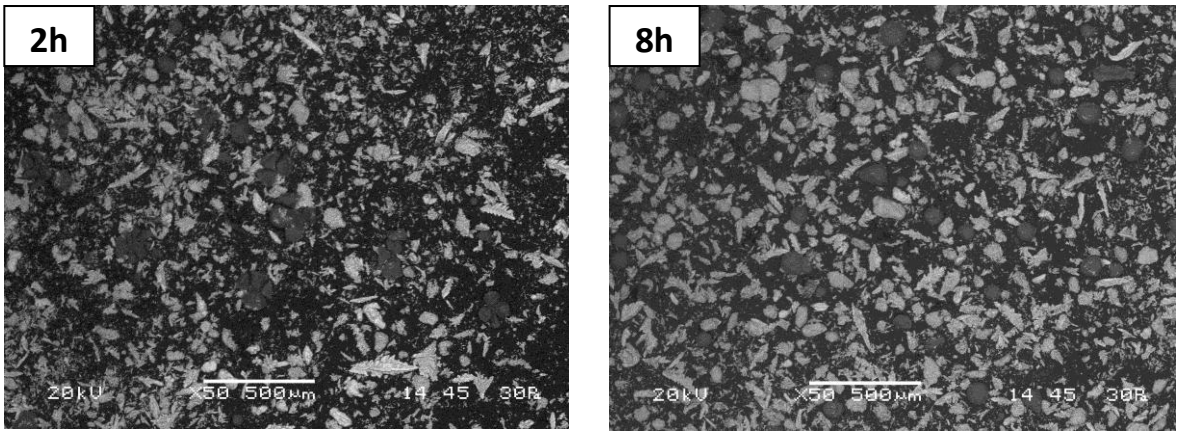

Fig. 3.1a.8 SEM micrographs of Cu-5 vol. % Al_2O_3 nanocomposite powders after 2 and 8 hours of blending

The Al-5 vol. % Al_2O_3 micro and nano-composite powders show good distribution of alumina particles in the aluminium matrix powders.

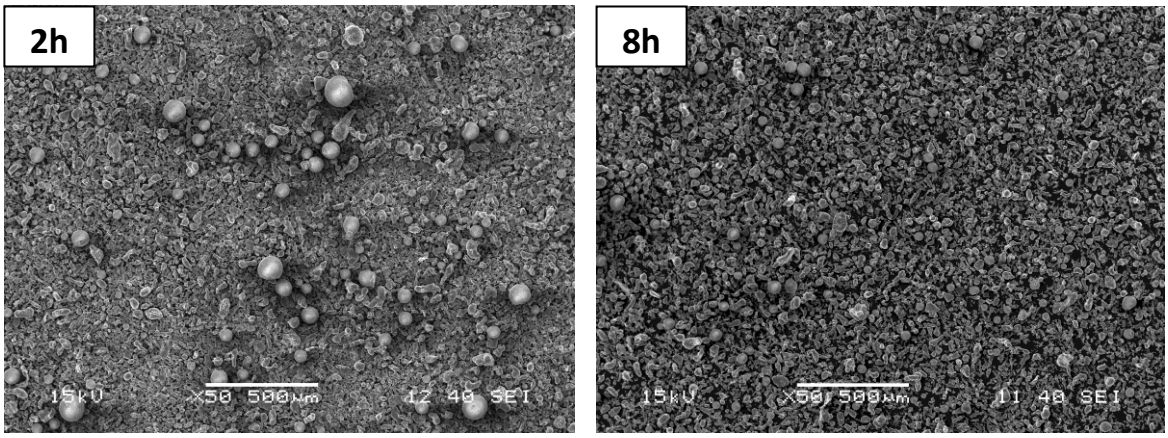

Fig. 3.1a.9 SEM micrographs of Al-5 vol. % Al_2O_3 nanocomposite powders after 2 and 8 hours of blending

Fig. 3.1a.9 & 3.1a.10 show alumina particles in aluminium matrix powders well distributed throughout the aluminium matrix powders. The powders at 8 hours of blending show finer distribution than in 2 hours of blending. The reason may be the tumbling action of turbula mixer which helps in breakage of agglomerated particles by shaking action.

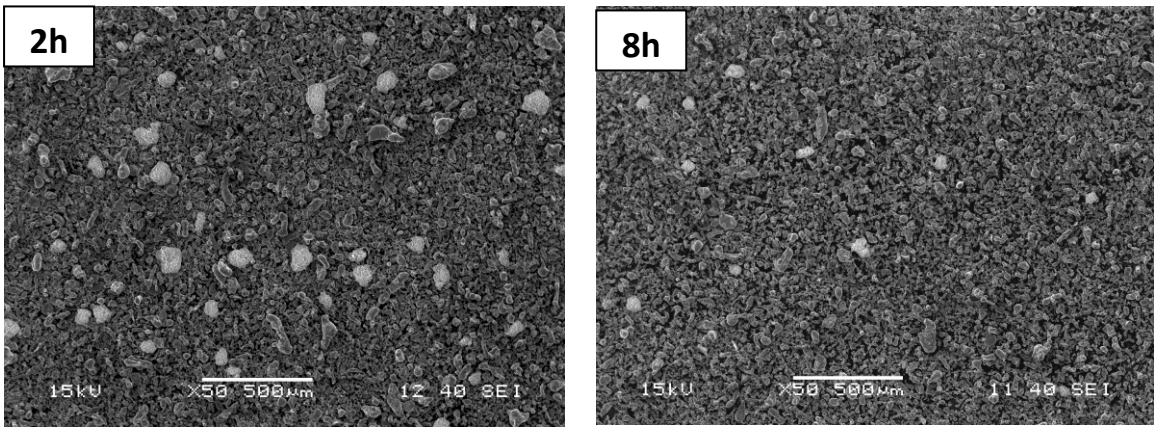

Fig. 3.1a.10 SEM micrographs of Al-5 vol. % Al_2O_3 microcomposite powders after 2 and 8 hours of blending

3.1a.3.3.2 Sintering response

Fig. 3.1a.9 & 3.1a.10 illustrates the SEM micrographs of sintered specimens of Cu-5 vol. % Al_2O_3 and Al-5 vol. % Al_2O_3 microcomposites after 2, 5 and 10 hours of milling. The sintering response of milled powders improves with increase in milling time. Milling activates the powder particles and introduces lattice defects like vacancy and dislocations. The increase in milling time also results in grain refinement of the matrix.

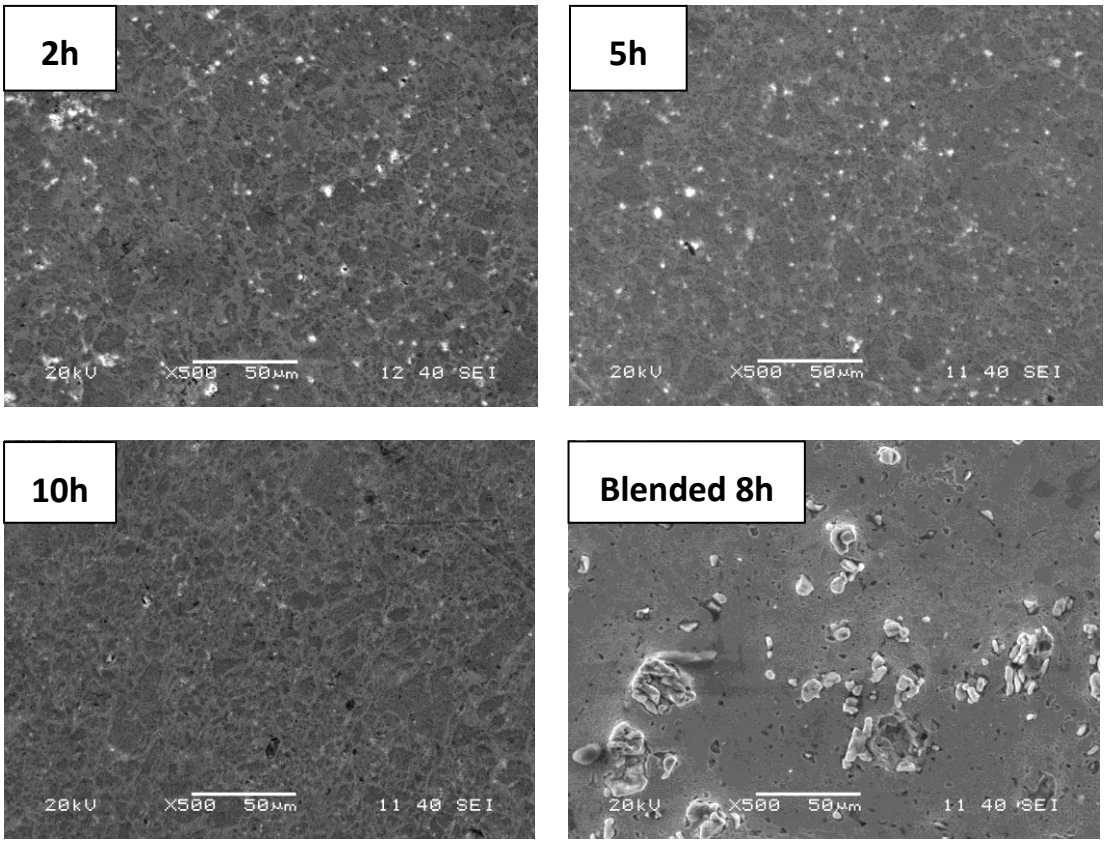

Fig. 3.1a.11 SEM micrographs of Cu-5 vol. % Al_2O_3 microcomposite powders after 2,5,10 hours of milling and 8 hours of blending followed by sintering at 900°C temperature

The SEM micrographs of blended and sintered samples do not show any grain refinement, as blending could not reduce particle size. Milling also reduces the reinforcement particle size which results in effective grain boundary pinning.

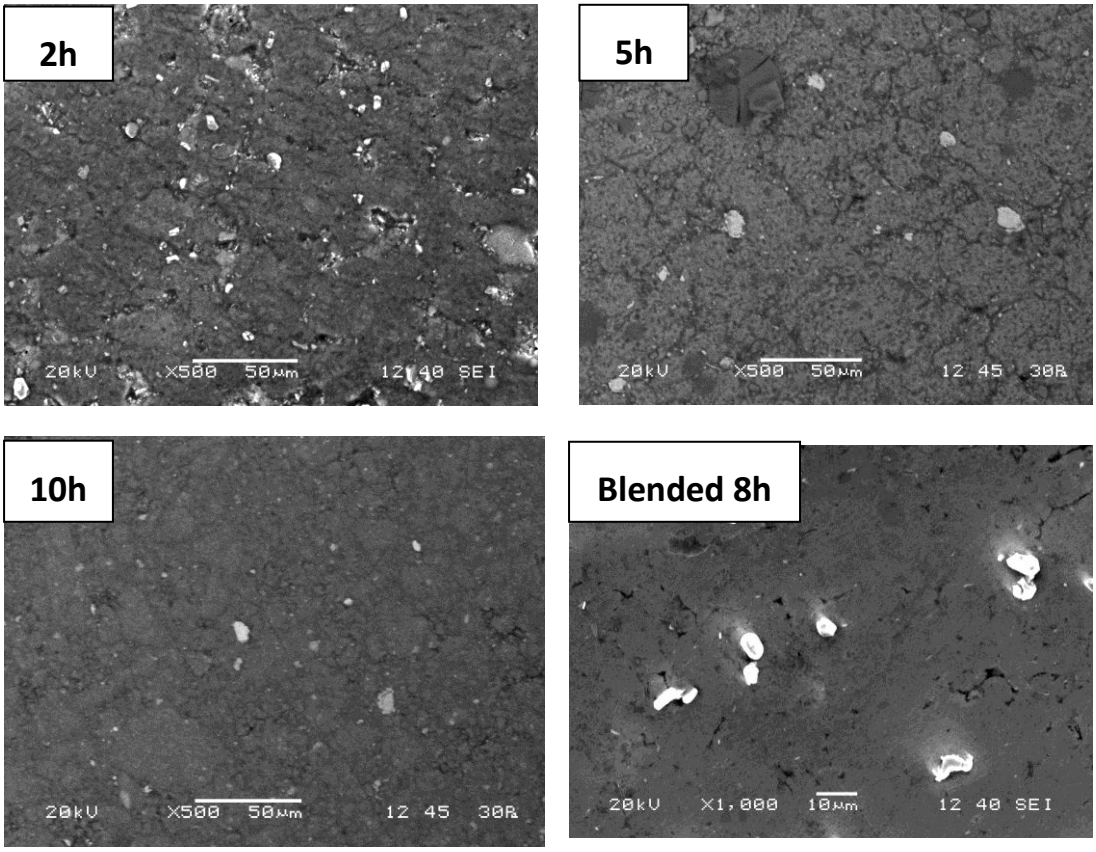

Fig. 3.1a.12 SEM micrographs of Al-5 vol. % Al_2O_3 microcomposite powders after 2,5,10 hours of milling and 8 hours of blending followed by sintering at 600°C temperature

3.1a.4 Density and microhardness measurements

The density of the composites prepared using blending and milling was measured using Archimedes method. The Vickers microhardness measurements were done at a load of 0.3kgf for a dwell time of 5 seconds. The density of milled samples decreases with milling time (Fig. 3.1a.13 & 3.1a.14). The density of milled samples decreases due to brittleness of particles in the course of milling. As milling progresses particles become brittle due to strain hardening and their compressibility reduces [4]. The density values of milled samples maintain a negative trend with increase in milling time, as milling time increases more ball and powder collisions lead to brittleness of particles and surface activation leads to agglomeration of particles which impedes the compressibility of powders.

The Cu-5 vol. % Al_2O_3 composite synthesized by blending shows 86.2 and 91.2% of theoretical density for nano-composite and micro-composite respectively. The Al-5 vol. %

Al_2O_3 blended micro-composite and nano-composite show 92.39 and 91.3% of theoretical density.

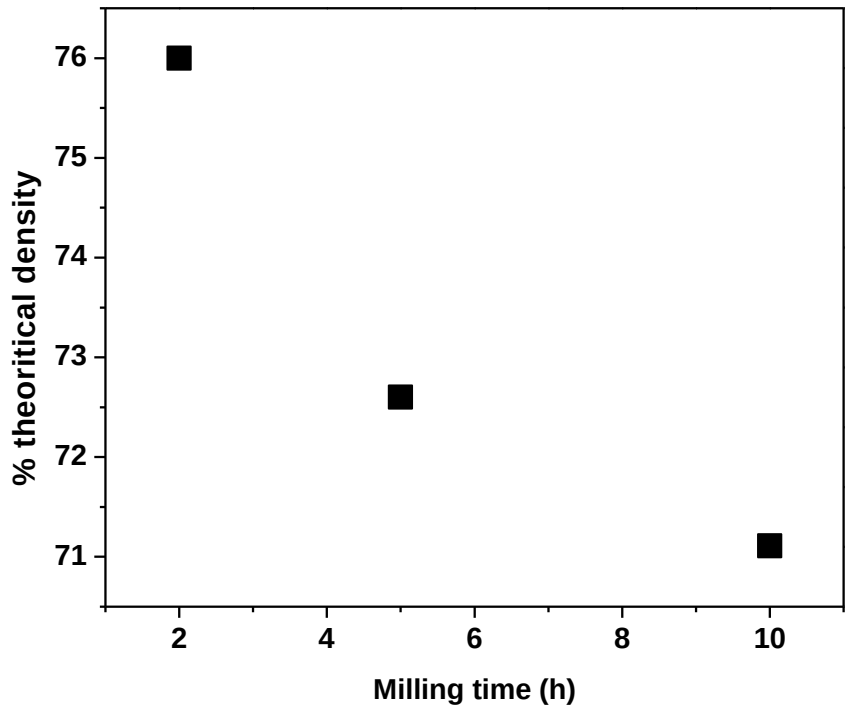

Fig. 3.1a.13 Density of Cu-5 vol. % Al_2O_3 sintered at 900°C after milling

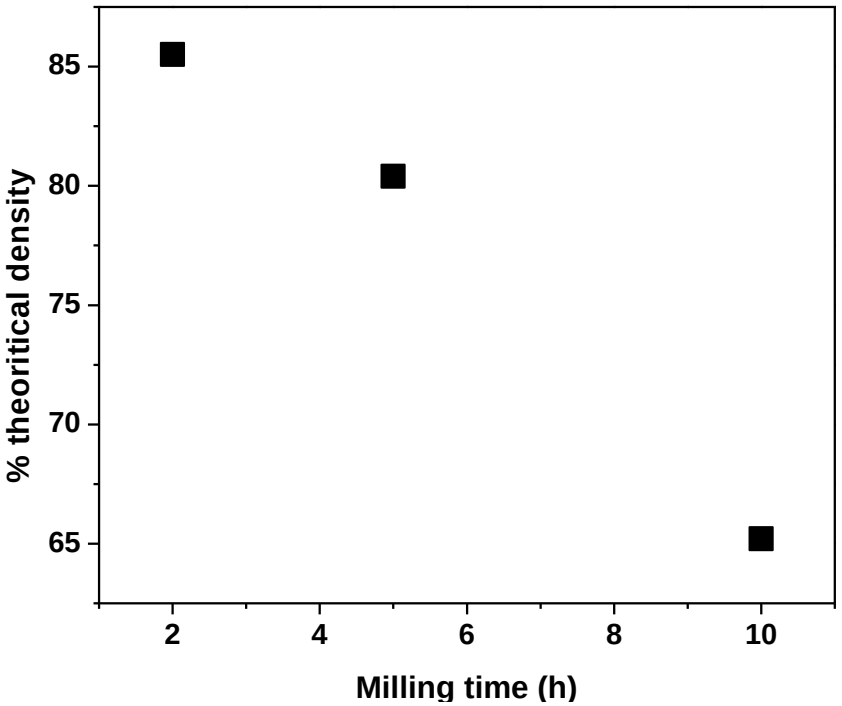

Fig. 3.1a.14 Density of Al-5 vol. % Al_2O_3 sintered at 600°C after milling

Fig. 3.1a.15 & 3.1a.16 show variation of microhardness of sintered samples of Cu-5 vol. % Al_2O_3 and Al-5 vol. % Al_2O_3 composites with milling time**.**

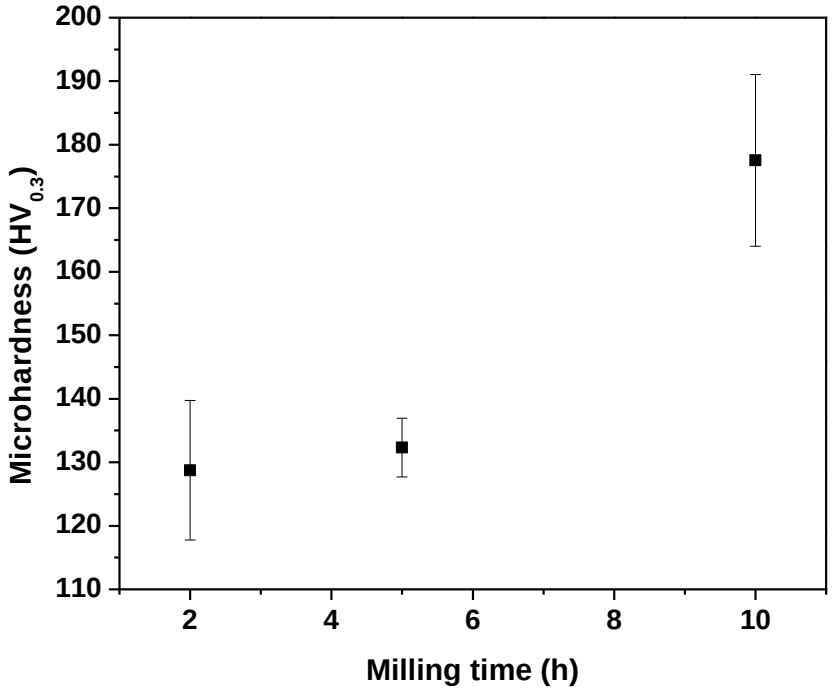

Fig. 3.1a.15 Microhardness of Cu-5 vol. % Al_2O_3 sintered at 900°C after milling

The microhardness value for sintered Cu-5 vol. % Al_2O_3 microcomposite recorded was 25.9 HV and for nanocomposite was 47.25 HV after blending. The microhardness values for milled samples are higher than that of blended samples. The reason is that milling mechanically activates the powder particles and also refines powders. As a result milled powder shows higher sintering response than blending. The microhardness values for aluminium-alumina blended samples were 35.77 HV for microcomposite and 31.65 HV for nanocomposite. The milled samples possess brittleness, as well as grain refinement. After 5 hours the microhardness values decrease as particles get welded and flattened and then after 10 hours of milling, the microhardness values increase as particle fragmentation takes place.

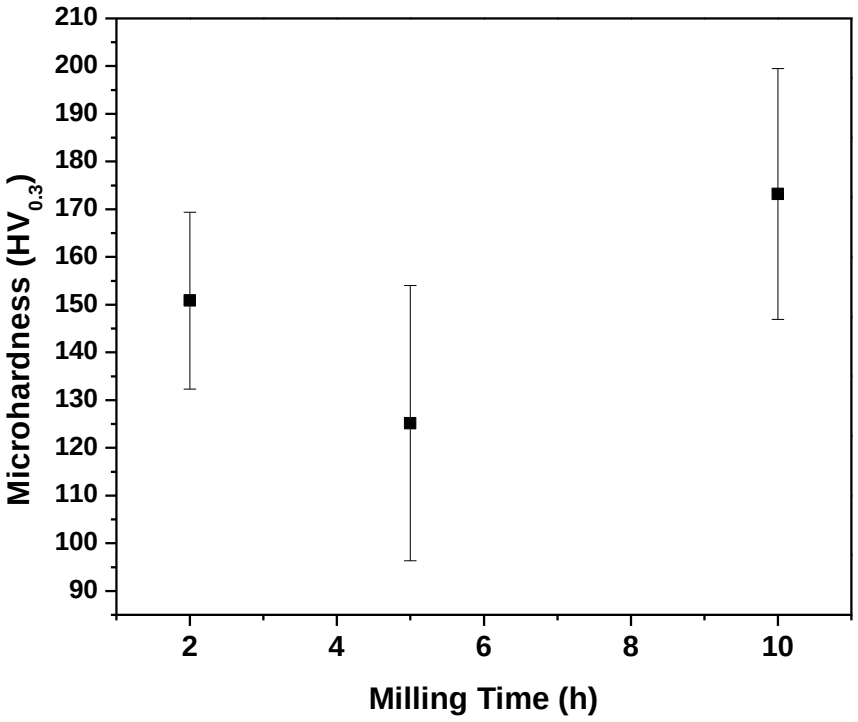

Fig. 3.1a.16 Microhardness of Al-5 vol. % Al_2O_3 sintered at 600°C after milling

3.1a.5 Summary and Conclusions

Cu-5 vol. % Al_2O_3 and Al-5 vol. % Al_2O_3 micro-and nano-composites were fabricated by milling and blending of copper and alumina, aluminium and alumina powders followed by conventional sintering. Milling reduces the particle size of composite powders with increasing milling time. X-ray diffraction, particle size analysis and microstructure reveal particle size reduction and good distribution of alumina particles in copper and aluminium matrix powders. Microhardness of milled samples is higher than blended samples. Blending of powders followed by sintering impart higher density than milled and sintered samples. Grain refinement of copper and aluminium is observed with increasing milling time. Milling process demonstrates plastic deformation, micro-welding and particle fragmentation in SEM micrographs.

References

[1] C. Suryanarayana, N. Al-Aqeeli, Mechanically alloyed nanocomposites, *Prog. Mater. Sci*. 58 (4) (**2013**) 383-502.

[2] C. Suryanarayana, Mechanical alloying and milling, *Prog. Mater. Sci.* 46 (**2001**) 1-184.

[3] C.P. Samal, J.S. Parihar, D. Chaira, The effect of milling and sintering techniques on mechanical properties of Cu-graphite metal matrix composite prepared by powder metallurgy route, *J. Alloy Compd.* 569 (**2013**) 95-101.

[4] C. Suryanarayana, Synthesis of nanocomposites by mechanical alloying, *J. Alloy Compd.* 509 (1) (**2011**) 229-234.

3.1b Effect of sintering atmosphere on the microstructure and properties of Cu-Al_2O_3 composites

3.1b.1 Scope and objectives of the work

Sintering atmosphere plays a crucial role in the sintering response of the material. Synthesis of microcomposites via conventional sintering using N_2, H_2 and Ar atmospheres has been investigated here. It has been observed that Cu-Al_2O_3 metal matrix composite (MMC) shows poor mechanical properties and physical bonding of matrix and reinforcement when it is conventionally sintered in N_2 or Ar atmosphere compared to those in H_2 atmosphere. The structural integrity of the microcomposites with the variation in sintering atmosphere differs, hence providing a scope for tailoring the properties of copper-alumina composites by changing sintering environments.

3. 1b.2 Fabrication of microcomposites

The as-received copper (Loba Chemie, purity > 99.7%, average size-11µm) and alumina (Sigma Aldrich, average size-5.71µm) powders were mixed and blended separately using turbula shaker mixer for 8 hours at a speed of 45 rpm to ensure homogeneous mixing. The reinforcement (alumina) content added to copper was 5, 10, 15 volume %. The powders were compacted into cylindrical pellets (diameter: 15 mm) using uniaxial hydraulic press at an applied pressure of 700 MPa for 2 minutes. The green samples were then sintered by conventional sintering in a tubular furnace at 900°C for a holding time of 60 minutes in nitrogen (Asiatic gases Ltd., 99.8% purity) atmosphere at a heating rate of 5°C/minutes. In another set of experiments, specimens of same constituents were fabricated by sintering them in hydrogen (99% purity) atmosphere, while keeping the other parameters fixed. The third set of specimens with similar composition as above were synthesized by sintering them in argon atmosphere (British oxygen company, 99.994% purity), maintaining rest of the parameters fixed.

3.1b.3 Characterization of the microcomposites

Sintered specimens were characterized by X-Ray diffraction (PANalytical model: DY-1656) CuKα, and scanning electron microscope (JEOL 6480 LV). The micrographs of the specimen

were obtained by chemically etching the samples by a mixture of 5 g $FeCl_3$ and 50 ml HCl in 100 ml distilled water.

3.1b.3.1 X-Ray diffraction

The X-Ray diffraction of sintered samples was carried out to study the phases present after sintering. The alumina peaks confirm to be monoclinic in nature. The X-Ray diffraction patterns of the specimen sintered conventionally in nitrogen, hydrogen and argon atmosphere, illustrated in Figs.3.1b.1 show the presence of cuprous oxide (Cu_2O) along with Cu and Al_2O_3 in both cases. In the composites sintered in argon atmosphere, the peak for cuprous oxide is not that intense, but the presence of oxygen has been further verified by EDAX.

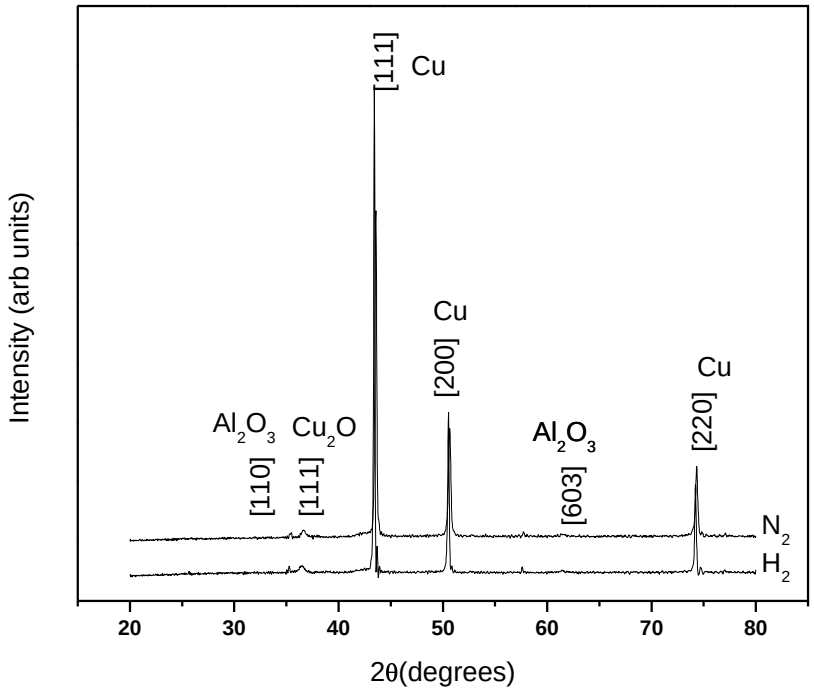

Fig. 3.1b.1 XRD diffraction patterns of Cu- 15 vol. % Al_2O_3 microcomposites sintered conventionally in nitrogen and hydrogen atmosphere

3.1b.3.2 Scanning electron microscopy

The microstructure obtained by scanning electron microscope (SEM) gives ample information about the pore density, distribution, alignment and nature of porosity along with the matrix-reinforcement bonding. Figs. 3.1b.2, 3.1b.3 & 3.1b.4 depict the microstructure of Cu-Al_2O_3 MMC, the white patches showing alumina and the grey area referring to the copper matrix. The scanning micrographs reveal the clear difference between the bonding of copper and alumina in N_2, Ar and H_2 atmospheres. The specimen sintered in hydrogen atmosphere, (Fig.3.1b.3), shows good copper-alumina interfacial bonding, as compared to the composites sintered in nitrogen and argon atmosphere, (Figs. 3.1b.2 & 3.1b.4). There exists a discontinuity in bonding of the alumina particles with the copper matrix in the composites sintered in argon atmosphere (Fig. 3.1b.4).

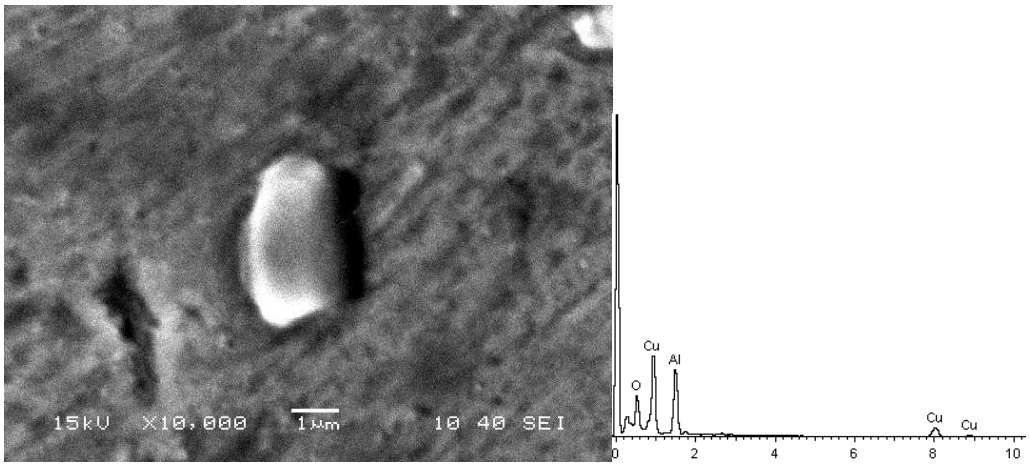

Fig. 3.1b.2 SEM micrographs and EDS analysis of Cu-15 vol. % Al_2O_3 sintered in nitrogen atmosphere

The proximity and degree of physical attachment of the alumina and copper particles in the sintered composites can be ranked in order of nitrogen, argon and hydrogen (in increasing order). It is desirable to remove cuprous oxides from the interface of Cu-Al_2O_3 composite to enhance mechanical properties. This fact can be attributed to the high bond strength of Cu/Al_2O_3 than those of Cu_2O/Al_2O_3 and Cu/Cu_2O [1-3]. This could possibly be attributed to the formation of cuprous oxide at low temperatures (tentatively 700°C) and possibility of beginning the decomposition at higher temperatures close to 1000°C.

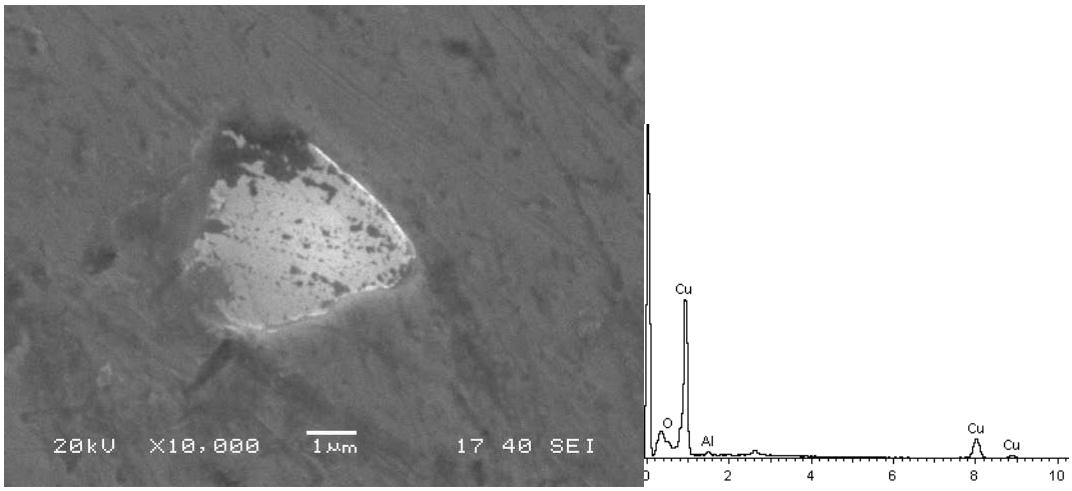

Fig. 3.1b.3 SEM micrographs and EDS analysis of Cu-15 vol. % Al_2O_3 sintered in hydrogen atmosphere

The decomposition yields copper and oxygen; in this process the oxygen escapes from the surface creating voids and expanding them eventually. The creation of voids impedes the densification causing swelling in addition as the oxygen released from the copper oxide formed at the copper-alumina interface disturbs the continuity in bonding of copper and alumina. Ghasemi et al. have reported that in reducing atmosphere the Cu_2O particles will be reduced to Cu and the removal of Cu_2O particles from the interface results in the substitution of Cu_2O/Al_2O_3 and Cu/Cu_2O interfaces by a Cu/Al_2O_3 interface [4]. Chiang et al. [2] and Sun, Discoll investigations [5] have shown that the strength of Cu/Al_2O_3 interface is higher than that of Cu_2O/Cu interface. Therefore, an improved alumina-copper contact surface and a decreasing stress concentration, owing to the absence of Cu_2O particles, resulted in an increase of bond strength. These micrographs also depict the fact that as the alumina content increases the tendency of embedment of alumina particles in the copper matrix deteriorates. Elements with less stable oxides than alumina will be reactive only to the extent that they obtain oxygen from other sources (e.g.: atmosphere) [6].

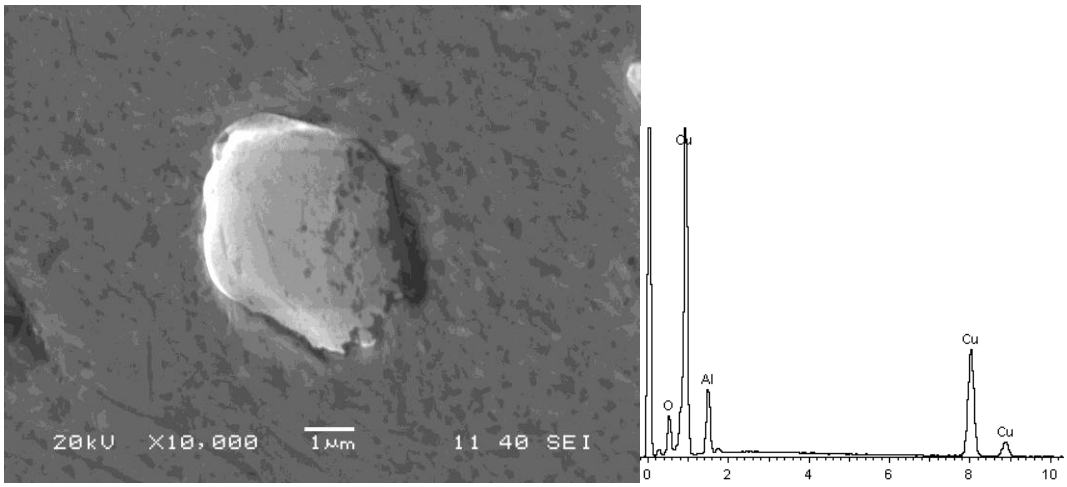

Fig. 3.1b.4 SEM micrographs and EDS analysis of Cu-15 vol. % Al_2O_3 sintered in argon atmosphere

The EDS analysis of the specimen (the whole micrograph in Figs. 3.1b.2, 3.1b.3, 3.1b.4) was selected for EDS analysis) sintered in nitrogen, hydrogen and argon atmosphere is shown in Figs. which shows a noticeable difference in the oxygen content of the samples. The elemental composition of oxygen estimated in Cu-15 vol. % Al_2O_3 MMC sintered in N_2, H_2 and Ar atmosphere is 21.02, 4 and 12.99% respectively. It is evident from the EDAX values that a smaller amount of O_2 is present in the composite sintered in H_2 atmosphere compared to that in N_2 atmosphere. The oxygen content present in the specimens sintered in argon atmosphere is somewhere in between of that of nitrogen and hydrogen.

3.1b.4 Density and microhardness measurement

The densification of all the specimens has been estimated using Archimedes method. The micro-hardness values of all the specimens were determined by Vickers hardness tester (Leco LV 700) applying a load of 0.3 kgf and a dwell time of 1 sec. The readings were recorded here at four equivalent locations for each specimen.

The densities of all the specimens recorded using Archimedes method shown in; Fig. 3.1b.5 indicates that the composites sintered by conventional method in nitrogen atmosphere show a slight increase in densification as the alumina content increases. With the number of finer particles increasing (alumina particles are finer than copper particles), the particle packing

and particle–particle contact increases, hence the density of the compacts increases. The densification process in argon atmosphere is peculiar i.e. it increases up to 10 vol. % of alumina and then a slight decrease takes place. This could be supported by the fact that as the amount of alumina increases to 15 % there is some chemical interfacial phenomenon taking place at this particular composition [7] which can be further confirmed by high resolution electron microscope. The trend in densification for the compacts sintered in hydrogen atmosphere is opposite to that obtained in the nitrogen atmosphere, which needs further study to clarify. The amount of cuprous oxide (Cu_2O) formed in H_2 atmosphere is less as compared to that in N_2 atmosphere. The composites sintered in nitrogen atmosphere have considerably low density due to the fact that during decomposition of cuprous oxide, oxygen gets released expanding the sintered compact by creating voids.

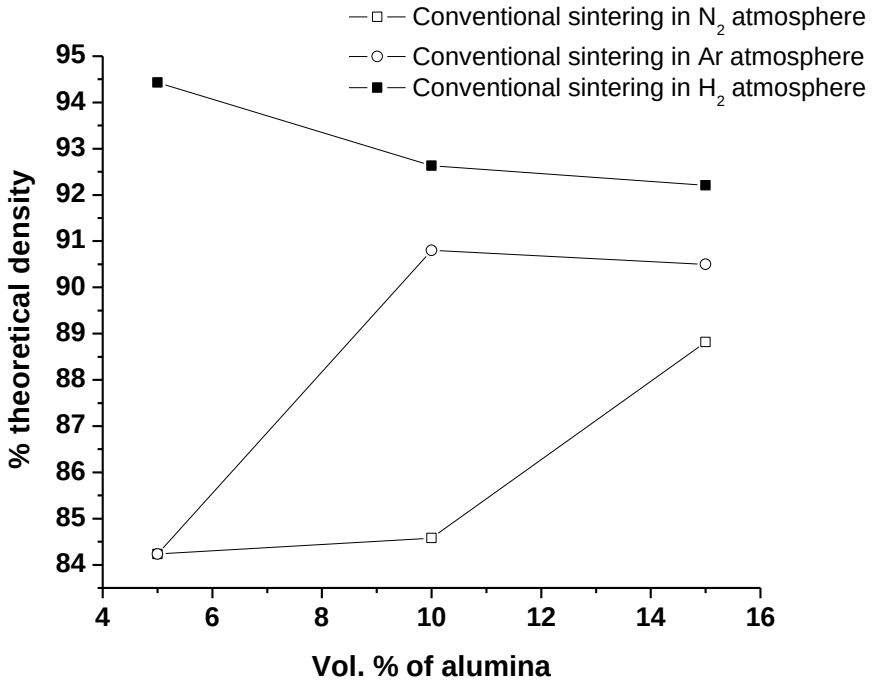

Fig. 3.1b.5 Densification of Cu-Al_2O_3 microcomposites fabricated using nitrogen, hydrogen and argon sintering atmospheres by conventional sintering

The hardness studies of microcomposites sintered in nitrogen as well as hydrogen atmosphere, shown in Fig. 3.1b.6, indicate that the microcomposites sintered in hydrogen atmosphere show higher hardness values than those sintered in nitrogen atmosphere. The microcomposites sintered in argon atmosphere possess hardness values close to that of nitrogen atmosphere.

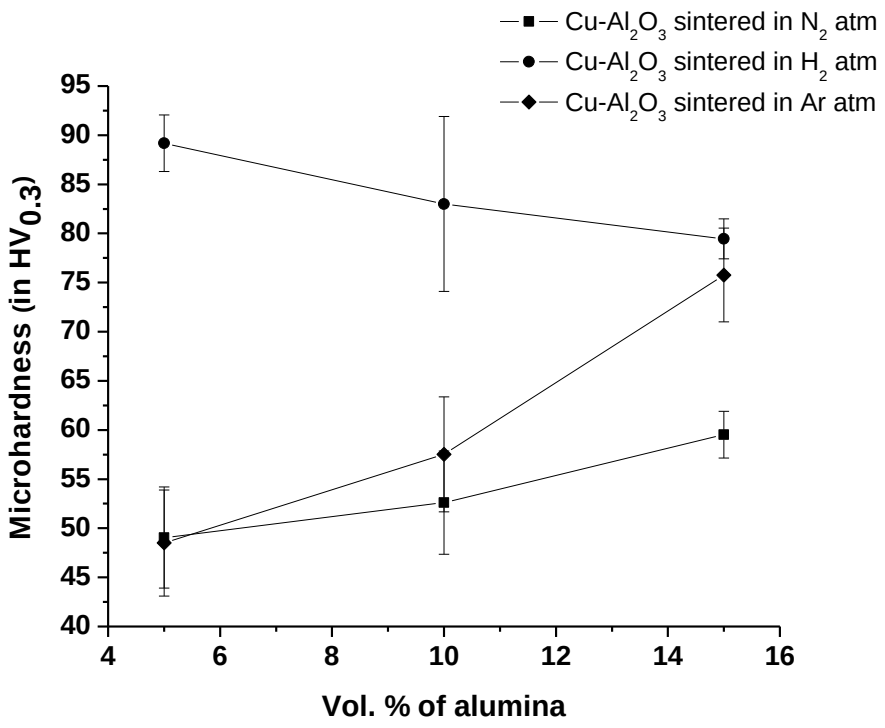

Fig. 3.1b.6 Comparison of hardness of Cu-Al_2O_3 microcomposites fabricated using nitrogen, hydrogen and argon sintering atmospheres by conventional sintering

The underlying fact can be correlated with the densification study: the density is higher for the microcomposites sintered in hydrogen atmosphere, complementing the hardness data. The proposed reason possibly could be the basis of argument in the comparison of hardness profiles of microcomposites.

3.1b.5 Summary and Conclusions

The Cu-Al_2O_3 microcomposites were fabricated using conventional sintering route in nitrogen, argon as well as hydrogen atmospheres. The densification process is more efficient in the case of hydrogen atmosphere than in nitrogen or argon atmosphere. The microstructure of the composites sintered in hydrogen atmosphere reveals better matrix-reinforcement bonding. The problem of poor interfacial bonding caused in the nitrogen and argon atmosphere has been addressed up to a certain extent using hydrogen atmosphere. The EDS analysis also proves the same. The formation of Cu_2O in the case of sintering in nitrogen as well as argon atmosphere reduced the extent of bonding of copper with alumina. The density

and hardness values are also in accordance to the above fact. The poor bonding between copper and alumina leads to inefficient load transfer during mechanical loading of the composite.

References

[1] Y. Yoshino, Role of oxygen in bonding copper to alumina, *J. Am. Ceramic Soc.* 72 (8) (**1989**) 1322-1327.

[2] W.L. Chiang, V.A. Greenhut, D.J. Shanefield, L.A. Johnson, R.L. Moore, Gas-metal eutectic bonded Cu to Al_2O_3 substrate mechanism and substrates additives effect study, *Ceramic Eng. Sci. Proc.* 14 (9) (**2008**) 802-812.

[3] K.P. Trumble, Thermodynamic analysis of aluminate formation at Fe/Al_2O_3 and Cu/Al_2O_3, *Acta. Metall. Mater.* 40 (**1992**) 105-110.

[4] H. Ghasemi, A.H. Kokabi, M.A.F. Sani, and Z. Riazi, Alumina-copper eutectic bond strength: contribution of preoxidation, cuprous oxides particles and pores, *Mater. Forum.* 32 (**2008**) 90-97.

[5] Y.S. Sun, J.C. Discroll, A new hybrid power technique utilizing a direct copper to ceramic bond, *IEEE. T. Electron. Dev.* 23 (8) (**1976**) 961-967.

[6] A.G. Metcalfe, Academic Press, New York, Interfaces in metal matrix composites Vol. 1, **1974**.

[7] A. Upadhyaya, G.S. Upadhyaya, Sintering of copper-alumina composites through blending and mechanical alloying powder metallurgy routes, *Mater. Des.* 16 (1) (**1995**) 41-45.

3.2 Evaluation of processing and properties of Cu-Al_2O_3 and Al-Al_2O_3 composites by conventional and spark plasma sintering method

3.2.1 Scope and Objectives of the work

Nanocomposites containing 1, 3, 5 and 7 vol. % Al_2O_3 (average size<50nm) and microcomposites having compositions 5, 10, 15, 20 vol. % of Al_2O_3 (average size~10μm) reinforced in copper and aluminium matrix individually were fabricated by powder metallurgy route. All the copper-alumina specimens were sintered conventionally at different sintering temperatures (850°C, 900°C, 1000°C) to study the effect of temperature on the process and progress of sinterability of the reinforced micro- and nano-particles in the matrix. All the aluminium-alumina specimens were sintered conventionally at different sintering temperatures (500°C, 550°C, 600°C). These micro- and nano-composites were characterized using X-ray diffraction and scanning electron microscopy followed by density, microhardness and wear measurements. The compression and flexural tests were also carried out in order to investigate the mechanical behaviour of the micro- and nano-composites for a fixed optimum sintering temperature. Fractography of the 3-point bend specimens was performed to investigate the fracture behaviour of the micro- and nano-composites.

In the second part of this chapter, copper-alumina and aluminium-alumina nanocomposites of 0.5, 1, 3, 5, 7 vol. % alumina (average size<50nm) were fabricated using spark plasma sintering (SPS) technique. Another set of microcomposites containing 1, 5, 20 vol. % of alumina (average size~10μm) had been fabricated for both copper and aluminium matrices to compare the physical as well as mechanical attributes of composites with variation of reinforcement particle size. These micro- and nano-composites have been characterized by X-ray diffraction (XRD), scanning electron microscopy (SEM), transmission electron microscopy (TEM) followed by microhardness, nanoindentation hardness and wear measurements.

3.2.2 Conventional Sintering

In this section, the physical integrity and sinterability of reinforcement particle in the matrix at different sintering temperatures was investigated by SEM. Sintering response and microstructure of Cu-Al_2O_3(p) and Al-Al_2O_3(p) composites with the variation of Al_2O_3 content as well as size and sintering temperature were investigated extensively. Subsequently, phase analysis, percentage of theoretical density, microstructure, hardness, compression strength, flexural strength and failure mode of the composites were elaborately investigated to arrive at a conclusive particle size – process parameter – microstructure – properties correlation. The microscopic deformation behaviour of Cu-Al_2O_3(p) and Al-Al_2O_3(p) composites were investigated by 3-point bend test followed by fractography and wear test.

3.2.2.1 Fabrication of composites

3.2.2.1a Copper-alumina composite

Cu powder (Loba Chemie average particle size~11.09μm, purity >99.7%), Al_2O_3 micropowder (Sigma Aldrich, average particle size~10 μm) and Al_2O_3 nanopowder (Sigma Aldrich, average particle size<50nm) were used to fabricate the Cu- Al_2O_3 micro- and nano-composites. Cu and Al_2O_3 (5, 10, 15 and 20 vol. %) micro-powders were blended using turbula shaker mixer followed by compaction to 15 mm diameter cylindrical pellets in an electrically operated uni-axial cold compaction machine (Soil Lab) at an applied pressure of 700 MPa for 2 minutes. Three sets of specimen were prepared and sintered in a tubular furnace (Naskar) at three different sintering temperatures (850°C, 900°C, 1000°C) for 1 hour in argon atmosphere. The above procedure was also followed for Cu and Al_2O_3 (1, 3, 5, 7 vol. %) nanopowder to fabricate nanocomposites with the same variation in sintering temperature and conditions.

3.2.2.1b Aluminium-alumina composite

Al powder (Loba Chemie average particle size~22.09μm, purity >99.7%), Al_2O_3 micropowder (Sigma Aldrich, average particle size~10 μm) and Al_2O_3 nanopowder (Sigma Aldrich, average particle size<50nm) were used to fabricate the Al-Al_2O_3 micro- and nano-composites. Al and

Al_2O_3 (5, 10, 15 and 20 vol. %) micro-powders were blended using turbula mixer followed by compaction to 15 mm diameter cylindrical pellets in an electrically operated uni-axial cold compaction machine (Soil Lab) at an applied pressure of 400 MPa. Three sets of specimen were prepared and sintered in a tubular furnace (Naskar) at three different sintering temperatures (500°C, 550°C, 600°C) for 1 hour in argon atmosphere. The above procedure was also followed for Al and Al_2O_3 (1, 3, 5, 7 vol. %) nanopowder to fabricate nanocomposites with the same variation of sintering temperature and conditions.

3.2.2.2 Characterization of the composites

The specimens were characterized using X-Ray diffraction (PANalytical model: DY-1656) CuK_α and scanning electron microscopy (JEOL 6480 LV). The SEM micrographs of the specimen were obtained by treating the samples with ferric chloride solution (5 g $FeCl_3$ and 50 ml HCl in 100 ml distilled water) for Cu-Al_2O_3 and Keller's reagent for Al-Al_2O_3 as an etchant.

3.2.2.2a Copper-alumina composite

3.2.2.2a.1 X-Ray Diffraction

The X–ray diffraction patterns of Cu-Al_2O_3(p) microcomposites sintered at 850°C, 900°C and 1000°C sintering temperature are illustrated in Fig. 3.2.1. The X-ray peaks confirm the presence of Cu, Al_2O_3 and Cu_2O phases. As the vol. % of Al_2O_3 increases the intensity of the Al_2O_3 peaks increases. The formation of Cu_2O at 900°C and 1000°C can be attributed to high sintering temperatures as well as high susceptibility of oxide formation of Cu at high temperatures. With the increase in Al_2O_3 content the intensity of Cu_2O peak increases.

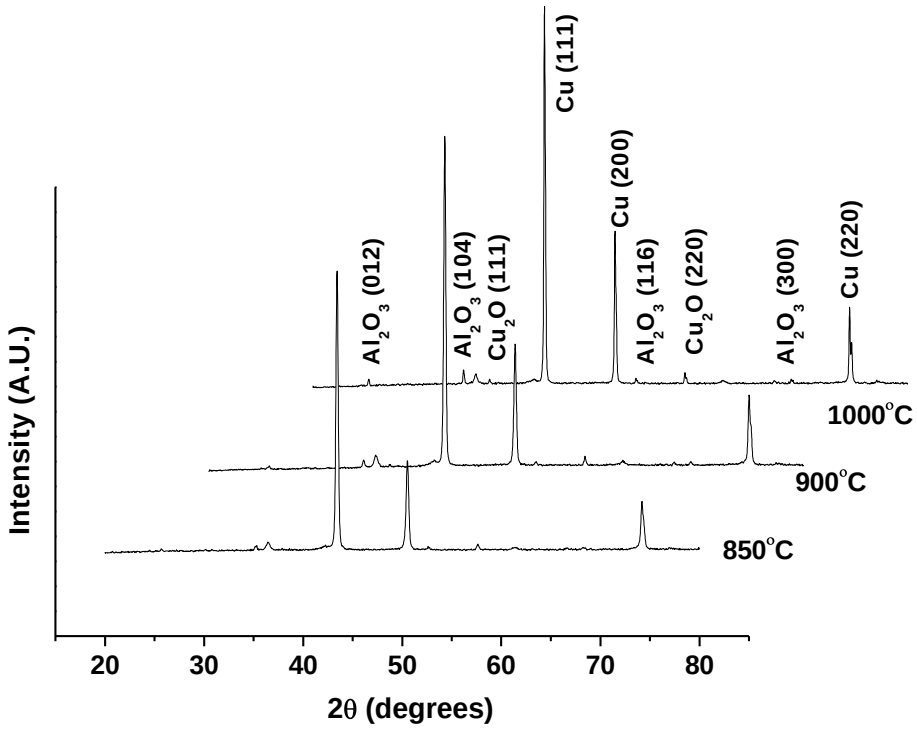

Fig. 3.2.1 X-ray diffraction patterns of Cu–20 vol. % Al_2O_3 microcomposites sintered at 850°C, 900°C and 1000°C

This can be attributed to the enhanced formation of interface with increasing Al_2O_3 content resulting in generation of new surface which gets exposed to oxide formation [1]. Fig. 3.2.2 refers to the X-ray diffraction patterns of the Cu-Al_2O_3(p) nanocomposites sintered at 850°C and 900°C temperatures. The cuprous oxide peaks are prominent in the diffraction patterns of nanocomposites than in microcomposites. This may be due to the presence of Al_2O_3 nanoparticles in Cu matrix leading to higher interface area resulting in higher amount of Cu matrix exposed for oxidation.

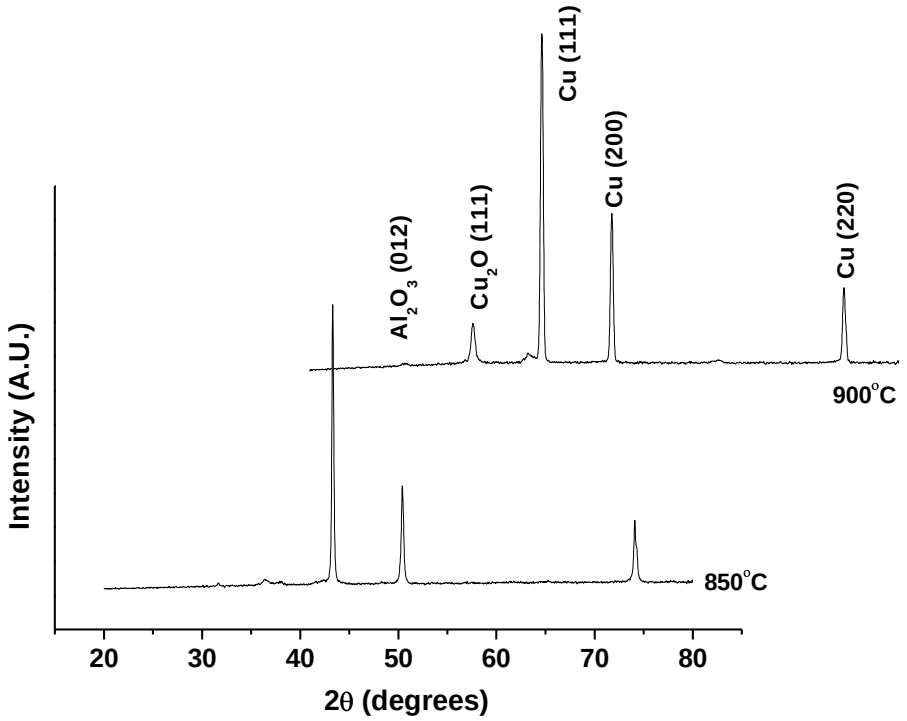

Fig. 3.2.2 X-ray diffraction patterns of Cu–7 vol. % Al_2O_3 nanocomposites sintered at 850°C, and 900°C

3.2.2.2a.2 Scanning electron microscopy

The SEM micrographs give abundant information about the reinforcement distribution, status of physical intimacy between Cu and Al_2O_3, clustering and mechanical phenomena like twinning. The black regions in the SEM micrographs indicate the Al_2O_3 particles while the white portion corresponds to the Cu matrix captured in back scattered electron mode. (Fig. 3.2.3 (a, b (SE mode) & c)) illustrate the distribution of Al_2O_3 in Cu matrix in the micro-composites sintered at various sintering temperatures.

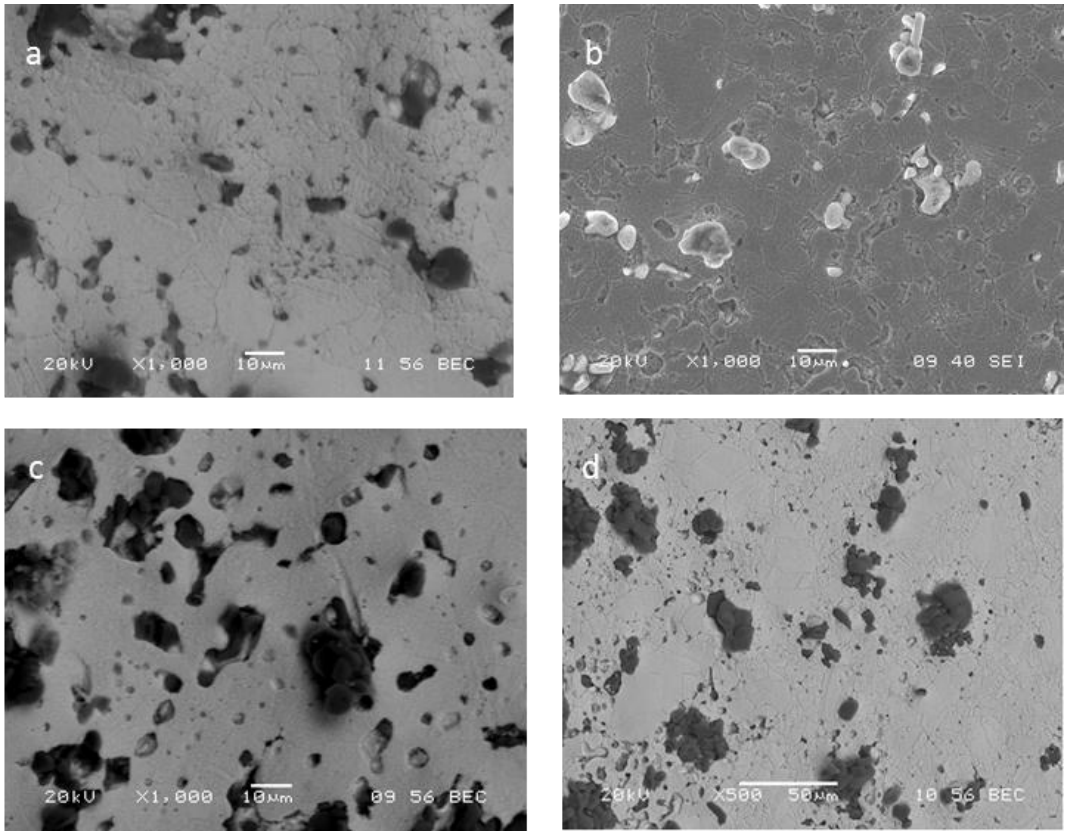

Fig. 3.2.3 SEM micrographs of Cu–10 vol. % Al_2O_3 microcomposites sintered at temperature (a) 850°C, (b) 900°C and (c) 1000°C (d) Cu–15 vol. % Al_2O_3 microcomposites sintered at 900°C temperature

With the increase in volume fraction of Al_2O_3 the efficiency of distribution becomes remarkably better (Fig. 3.2.3(d)). The density difference between the matrix and reinforcement also leads to the formation of clusters sometimes at high vol. % of the reinforcement [2]. Annealed twin bands have been observed in Fig. 3.2.3 (b) of Cu-10 vol. % Al_2O_3 composite sintered at 900°C. Twinning is a predominant phenomenon in Cu composites which gives a good indication in terms of mechanical value [3].

The presence of twins (Fig. 3.2.3 (b)) in the composites signifies the reduction in dislocations' mobility or dislocation structure stabilization which is the important condition for improving the mechanical properties of the composites [4]. On the contrary no twin bands are to be seen in Fig. 3.2.3 (c) of Cu-10 vol. % Al_2O_3 composite sintered at 1000°C. The matrix grain growth is quite pronounced at 1000°C than at 900°C and 850°C. The physical contact between matrix and reinforcement seemingly improves with increasing sintering temperature (Fig. 3.2.4).

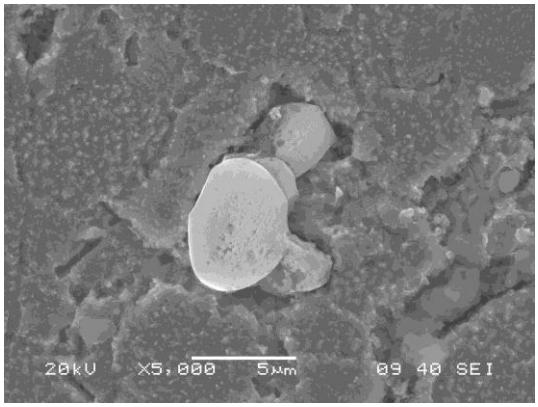

Fig. 3.2.4 SEM micrographs of Cu–10 vol. % Al_2O_3 microcomposites sintered at temperature 1000°C

The SEM micrographs of Cu-Al_2O_3 nanocomposites illustrate improved distribution of Al_2O_3 in the matrix compared to that in microcomposites (Fig. 3.2.5 (a & b)) [5]. The agglomeration of Al_2O_3 nanoparticles is quite vigilant in the SEM micrograph. The embedment of Al_2O_3 nanoparticles in Cu matrix is appreciably intimate than in the microcomposites (Fig. 3.2.5 (b)).

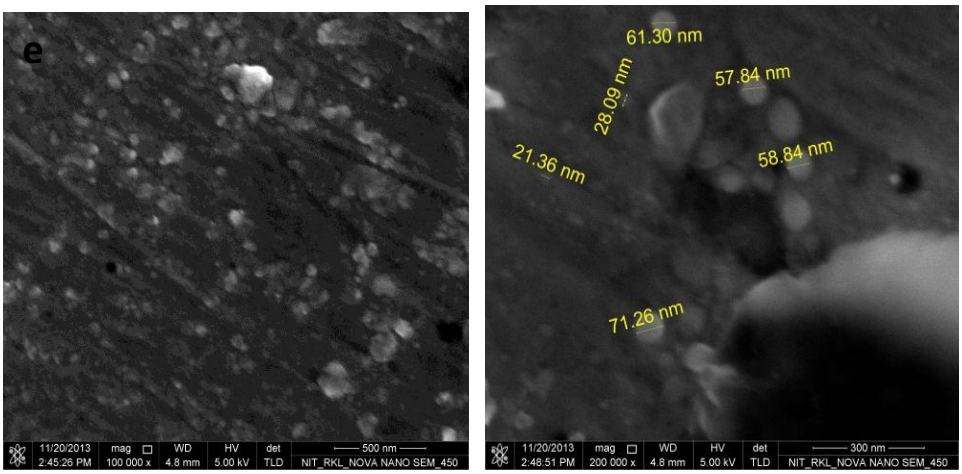

Fig. 3.2.5 FESEM micrographs of Cu–3 vol. % Al_2O_3 nanocomposites sintered at 1000°C temperature at (a) 100000X and (b) 200000X maginifcations

The enhanced physical contact of Al_2O_3 nanoparticles with the matrix can be attributed to the high atomic diffusivity of the nanoparticles [6]. The stabilization of the surface energy of nanoparticles is a thermodynamically driven phenomenon; hence it is quite obvious that the physical adherence of Cu with Al_2O_3 is better in nanocomposites.

3.2.2.2b Aluminium-alumina composite

3.2.2.2b.1 X-Ray Diffraction

The X-ray diffraction patterns of Al-Al_2O_3 microcomposites sintered at 600°C is illustrated in Fig. 3.2.6. The patterns show the presence of Al and Al_2O_3 peaks. It has been found that no other intermediate phase is formed during sintering. As reported literature suggests, the formation of any other phase is not feasible. Hence composites sintered at rest of the sintering temperatures (i.e. 500°C and 550°C) also shows similar x-ray diffraction patterns.

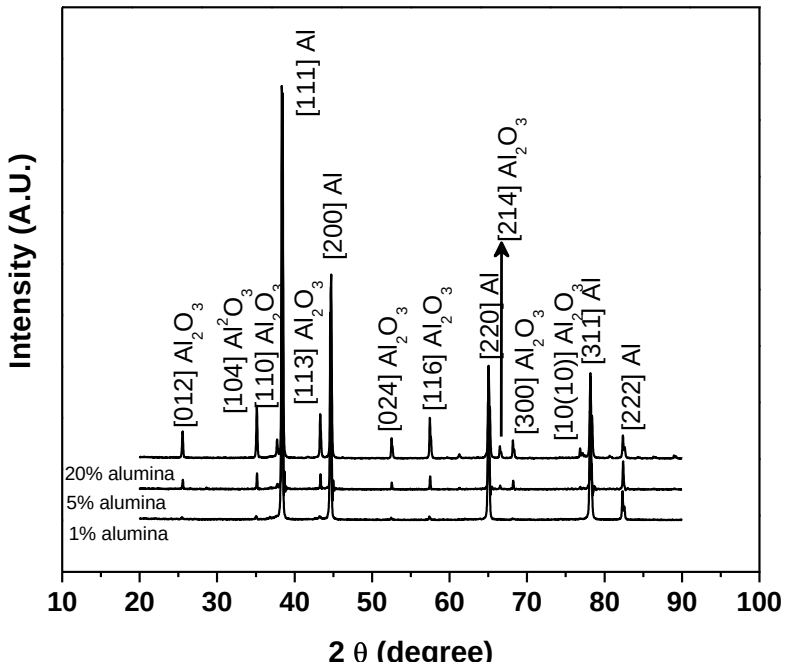

Fig. 3.2.6 X-ray diffraction patterns of Al-Al_2O_3 microcomposites sintered at 600°C temperature

The x-ray diffraction patterns of Al-Al_2O_3 nanocomposites sintered at 600°C is shown in Fig. 3.2.7. The peaks for Al_2O_3 are not distinct because of nanosize effect, i.e. peak broadening and reduced intensity. The X-ray diffraction patterns show similar peaks for all the microcomposites and nancomposites at all temperatures.

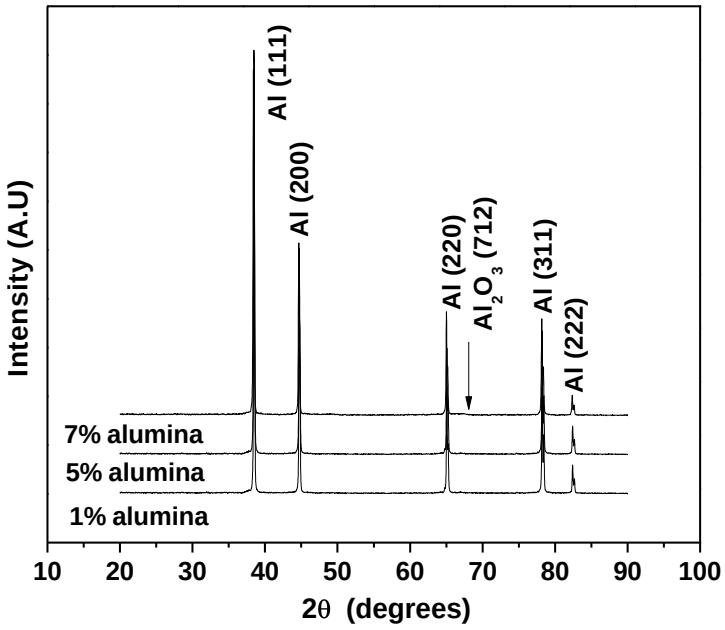

Fig. 3.2.7 X-ray diffraction patterns of Al-Al_2O_3 nanocomposites sintered at 600°C temperature

3.2.2.2b.2 Scanning electron microscopy

The FESEM micrographs of Al-Al_2O_3 microcomposites sintered at 600°C temperature is illustrated in Fig. 3.2.8 (a & b). The distribution of alumina particles is fair in the aluminium matrix. Fig. 3.2.8 (b) shows good compatibility of alumina microparticles in the matrix. Fig. 3.2.9(a & b) shows distribution of alumina nanoparticles in aluminium matrix. The alumina nanoparticles are evenly distributed in the matrix and also aid in grain boundary pinning of aluminium grains. Fig. 3.2.9(b) illustrates good embedment of alumina nanoparticles in the matrix.

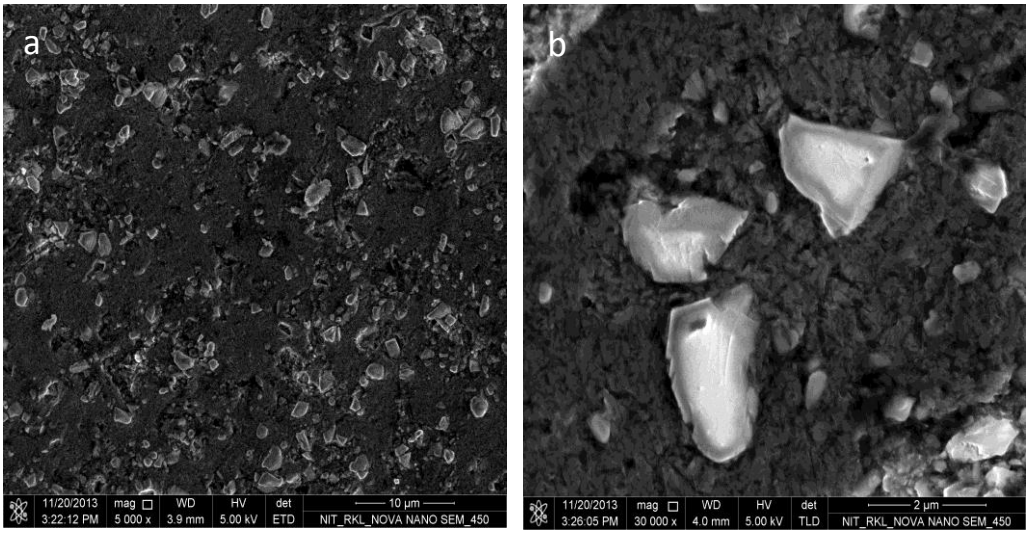

Fig. 3.2.8 FESEM micrographs of Al–5 vol. % Al_2O_3 microcomposite sintered at temperature 600°C captured at (a) 5000X and (b) 30000X magnification

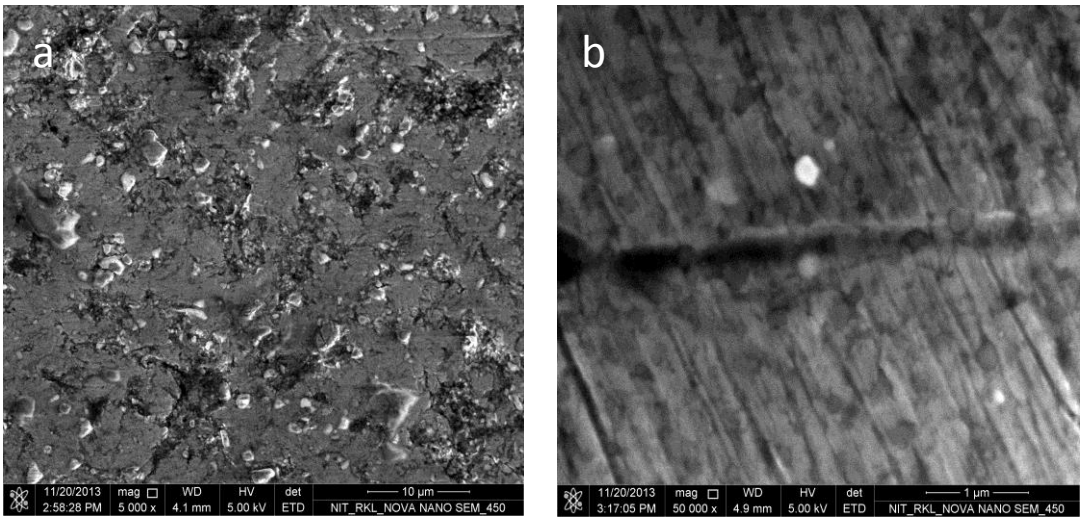

Fig. 3.2.9 FESEM micrographs of Cu–5 vol. % Al_2O_3 nanocomposites sintered at temperature 600°C captured at (a) 5000X and (b) 100000X magnification

3.2.2.3 Mechanical testing

Sintered density of the copper-alumina and aluminium-alumina pellets was determined by Archimedes method. Microhardness of the specimen was measured by Vickers hardness tester (Leco Microhardness Tester LM248AT) at a load of 0.3kgf for a dwell time of 5 seconds. The readings were recorded here at four equivalent locations for each specimen. For compression test, flexural test and wear test, sintered samples of copper-alumina sintered at 900°C and aluminium-alumina sintered at 600°C temperature were tested. According to ASTM standard E9-89 compression test was conducted with the aid of universal testing machine (INSTRON SATEC series servo-hydraulic machine) with specimen dimensions of 10 mm diameter and 8 mm height at a strain rate of $1min^{-1}$. Graphite powder was used to minimize friction between the sample and fixture of compression machine. A reduction of 50% in height was maintained for all the specimens. The end surfaces were kept normal to the axis of the specimen. A set of specimens having dimensions of 31.5 x12.7 x 6.3 mm^3, in accordance with ASTM standard B925-08 were fabricated following the above mentioned route for both micro- and nano-composites. A span length of 26mm and cross-head velocity of 0.5mm/minute was maintained during the flexural tests which were carried out in universal testing machine (INSTRON-5967). Fractography of the 3-point bend test specimens was carried out by scanning electron microscopy (JEOL 6480 LV). The copper based micro- and nano-composites which were sintered at $900^{\circ}C$ were subjected to wear test at a load of 20N at a speed of 30 rpm for a time period of 10 minutes. Aluminium-alumina composites sintered at 600°C temperature were tested at a load of 10N at a speed 30 rpm for a time period of 10 minutes. The wear tested specimens were examined by scanning electron microscopy.

3.2.2.3a Copper-alumina composite

3.2.2.3a.1 Density

Density measurements were carried out using the Archimedes water immersion method. The theoretical and sintered density values of all the specimens have been tabulated (Table.3.2.1). Table 3.2.1 demonstrates that the percentage of theoretical density (calculated by rule of mixtures) decreases with increasing content of Al_2O_3 micro- and nano-particles. This may be due to low density value of Al_2O_3 particles than that of Cu [7]. With the increase in sintering temperature from 900^{o}C to 1000^{o}C the % theoretical density also increases for microcomposites.

Percentage of theoretical density of the microcomposites increases at a temperature of 1000^{o}C as compared to the 900^{o}C sintering temperature. This may be due to the enhanced viscosity of the Cu matrix at higher sintering temperature which results in efficient pore filling. In case of nanocomposites as the interfacial area is more, the detrimental effect of interfacial phenomenon (de-cohesion, void formation) are more likely to prevail at high sintering temperature as compared to lower sintering temperature. The maximum density value was observed for the sintering temperature at 850°C. The rise in sintering temperature triggers enhanced formation of Cu_2O (Fig. 3.2.1) representing that the matrix is more susceptible to oxide formation at higher sintering temperature.

The pullout of cuprous oxide by evolution of O_2 gas (decomposition of cuprous oxide into Cu and oxygen) creates voids in the matrix and interface expanding the matrix eventually. The creation of voids in the matrix hinders the densification and impedes the continuity in intimacy contact of Cu and Al_2O_3 [1,5]. Hence, the interfacial area being more in nanocomposites the degree of oxidation is higher thus limiting densification at higher sintering temperatures. Shehata et al. [8] have investigated the densification% of Cu-5 vol. % Al_2O_3 at 950°C sintering temperature (with finer Al_2O_3) to be 93.9% and our results show 94.47% densification for the same composition at 1000°C sintering temperature.

Sintering Temperature				
		850˚C	**900˚C**	**1000˚C**
Composition	**Theoritical density (g/cc)**	**Sintered density (g/cc)**	**Sintered density (g/cc)**	**Sintered density (g/cc)**
Pure copper	**8.9**	**8.05**	**8.4**	**8.49**
Cu- 1% nanoalumina	**8.85**	**8.31**	**7.92**	**7.54**
Cu- 3% nanoalumina	**8.75**	**8**	**7.55**	**7.51**
Cu- 5% nanoalumina	**8.65**	**7.61**	**7.37**	**7.2**
Cu- 7% nanoalumina	**8.55**	**7.26**	**7.27**	**6.97**
Cu- 5% microalumina	**8.69**	**7.62**	**7.9**	**8.22**
Cu- 10% microalumina	**8.49**	**7.36**	**7.64**	**7.75**
Cu- 15% microalumina	**8.14**	**7.04**	**7.3**	**7.35**
Cu- 20% microalumina	**7.9**	**6.7**	**7.03**	**6.88**

Table 3.2.1 Theoretical and sintered density values of Cu-Al_2O_3 micro- and nano-composites processed at different sintering temperatures

3.2.2.3a.2 Microhardness

The hardness of the micro- and nano- composites increases with the increase in Al_2O_3 content in the matrix. As Al_2O_3 is inherently harder than Cu, its presence leads to a higher hardness in the composite. It was observed from (Table 3.2.2) that by increasing the amount of Al_2O_3 from 0% to 20 % in microcomposites, the hardness value increases from 53.7 to 103 HV at a sintering

temperature of 900°C. The hardness enhancement is an indication to good physical bonding at Cu-Al_2O_3 interface [9].

As the sintering temperature increases from 900˚C to 1000˚C the hardness value decreases which may be due to matrix grain coarsening [10]. At high volume fraction of reinforcement, surface area of Al_2O_3 particles reduces due to clustering which minimizes the effect of grain boundary pinning resulting in lower hardness value. In case of nanocomposites, nano-Al_2O_3 which have high hardness impedes the movement of dislocation during plastic deformation. Nano-Al_2O_3 restricts the grain growth of the Cu matrix by effective pinning [11]. The hardness of the composite gets improved with increase in the reinforcement content. The hardness values are maximum for the composites sintered at 850°C temperature. This can be further complemented by the density values. The Al_2O_3 nanoparticles tend to agglomerate which decreases the Orowan strengthening effect. The hardness values trend represents better hardness of Cu-Al_2O_3 nanocomposites at low sintering temperature such as 850°C.

The highest hardness values recorded are 109.27 HV for 7 vol. % reinforced Cu-Al_2O_3 nanocomposites. The density hierarchy complements the hardness trends followed at different sintering temperatures. The lowest sintering temperature imparts highest density to the nanocomposites. This can be ascribed to the fact that the interface dimension in the nanocomposites is high, leading to increased susceptibility for interfacial de-cohesion. Hence at higher sintering temperature exposed area for oxidation is higher, so the hardness values are lower due to subsequent decomposition of cuprous oxide and matrix expansion. Tjong et al. [12] have reported 101 HV Vickers microhardness for Cu-20 vol. %SiC HIPed composite whereas in our results we have obtained 103 HV Vickers microhardness for Cu-20 vol. % Al_2O_3 microcomposites with conventional sintering.

Sintering Temperature						
	850°C		900°C		1000°C	
Composition	Mean Hardness ($HV_{0.3}$)	Standard deviation	Mean Hardness ($HV_{0.3}$)	Standard deviation	Mean Hardness ($HV_{0.3}$)	Standard deviation
Cu- 1% nanoalumina	68.52	0.93	53.1	2.12	40.22	0.42
Cu- 3% nanoalumina	76.87	3.66	88.55	5.04	48.82	3.37
Cu- 5% nanoalumina	100.35	5.09	52.8	1.83	49.55	0.73
Cu- 7% nanoalumina	109.27	3.98	85.17	3.12	68.70	2.57
Cu- 5% microalumina	66.05	4.44	84.97	9.31	67.83	4.20
Cu- 10% microalumina	72.63	2.20	95.73	11.74	88.19	15.24
Cu- 15% microalumina	78.38	4.80	102.80	6.36	63.33	8.46
Cu- 20% microalumina	73.03	2.99	103.43	10.37	60.08	2.43

Table 3.2.2 Mean hardness and standard deviation of copper-alumina nano- and micro-composites

3.2.2.3a.3 Compression Test

The compression test results of Cu-Al_2O_3 micro- and nano-composites have been illustrated in (Fig.3.2.10 & 3.2.11). The results indicate that the compression strength decreases with the increase in Al_2O_3 content (with exceptions for Cu-15 vol. % Al_2O_3 microcomposite and Cu-3 vol. % Al_2O_3 nanocomposite). The compression strength of Cu-Al_2O_3 microcomposites decreases with increasing amount of Al_2O_3 at a strain rate of $1min^{-1}$. Localized softening of the composite (difference in thermal conductivity of the Cu and Al_2O_3 constituents) at high volume fraction of reinforcement during compressive testing may possibly decrease the compressive strength [13]. The compressive strength for Cu-Al_2O_3 nanocomposites increases as the Al_2O_3 content increases till 3 vol. % of Al_2O_3 followed by downfall of compressive strength values. The decrease after 3 vol. % may be attributed to the agglomeration of Al_2O_3 nanoparticles at higher vol. % of Al_2O_3. The agglomeration leads to increases in damage density and hence early fracture. For composites, the presence of particles induces an inhomogeneous elastic strain due to the elastic modulus mismatch of matrix Cu (117 GPa) and reinforced Al_2O_3 particle (300 GPa). The elastic strain leads to the generation of high geometrically necessary dislocation density ρ_G at the composite interface. For nano particles the increased geometrically necessary dislocation density ρ_G leads to a higher work hardening in the matrix, thus leads to a higher composite flow stress [14]. With increase in reinforcement content nanocomposite tends to fail through void nucleation, growth, and coalescence in the matrix regions near particles.

The above failure mechanisms lead to the decrease in strain hardening exponent. The compressive strength of 3 vol. % alumina reinforced copper nanocomposite was recorded to be around 800 MPa whereas Fathy et al. [15] reported around 600 MPa for 12.5 wt. % Cu-Al_2O_3 nanocomposite at 10^{-2} sec^{-1} strain rate. The composite reinforced with microparticles tends to fail through particle fracture which leads to decrease in strain hardening exponent.

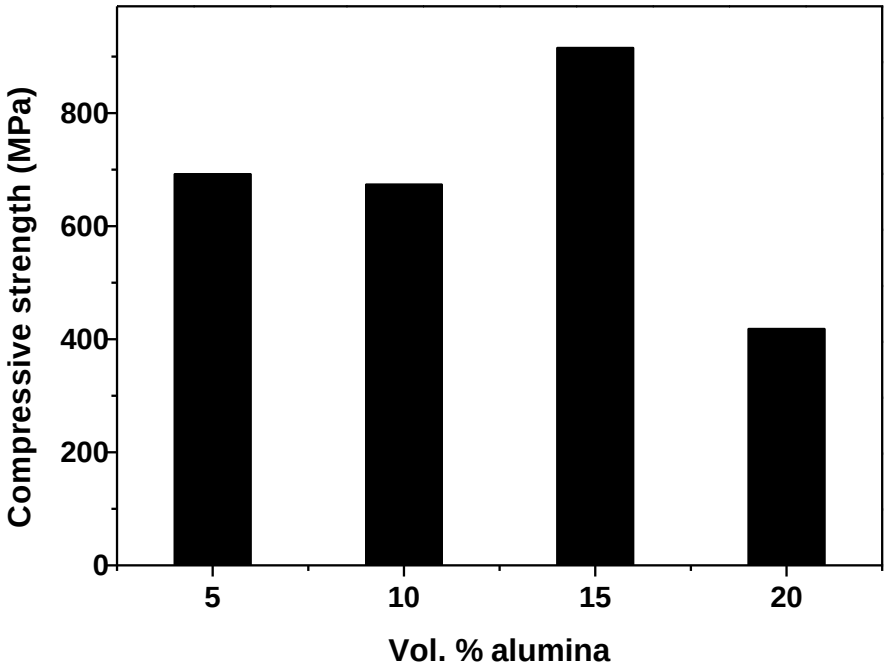

Fig. 3.2.10 Compression strength of Cu-Al_2O_3 microcomposites sintered at 900°C

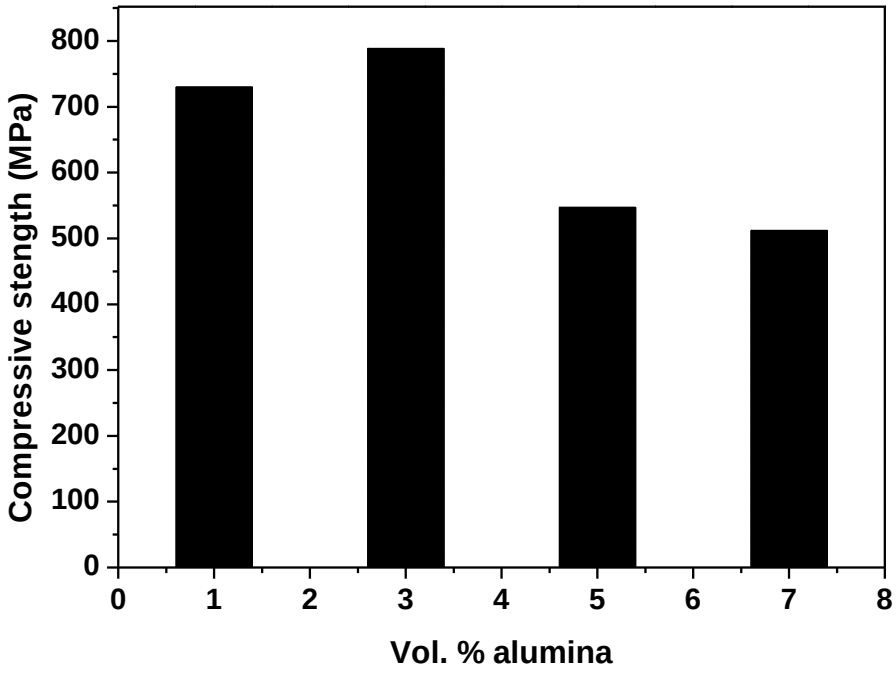

Fig. 3.2.11 Compression strength of Cu-Al_2O_3 nanocomposites sintered at 900°C

3.2.2.3a.4 3-point bend test

From the 3-point bend test results it was found that the ultimate flexural strength value decreases with increase in volume fraction of the reinforcement as illustrated in (Fig. 3.2.12 & 3.2.13). The underlying reason could be the addition of ceramic particles which decreases its ductility component, hence lowering the ultimate flexural strength. This may be due to the enhancement in damage sites with increase in reinforcement content.

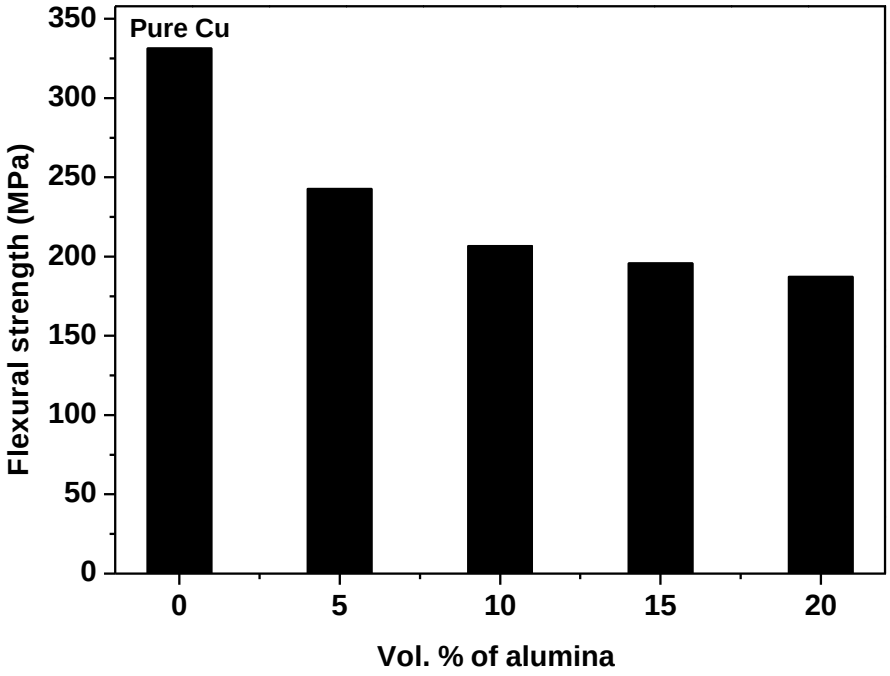

Fig. 3.2.12 Plot for ultimate flexural stress (MPa) vs. vol. % of reinforcement content for Cu-Al_2O_3 microcomposites

Early fracture possibly occurs by linking the damage in clustered regions, as a result ultimate flexural strength value decreases. According to Griffith criterion, cracked particle in the clustered region hinders dislocation strengthening which decreases the ultimate flexural strength value. Defects such as porosity, macro-, micro-cracks and interface de-union promote premature failure and ultimate fracture occurs early.

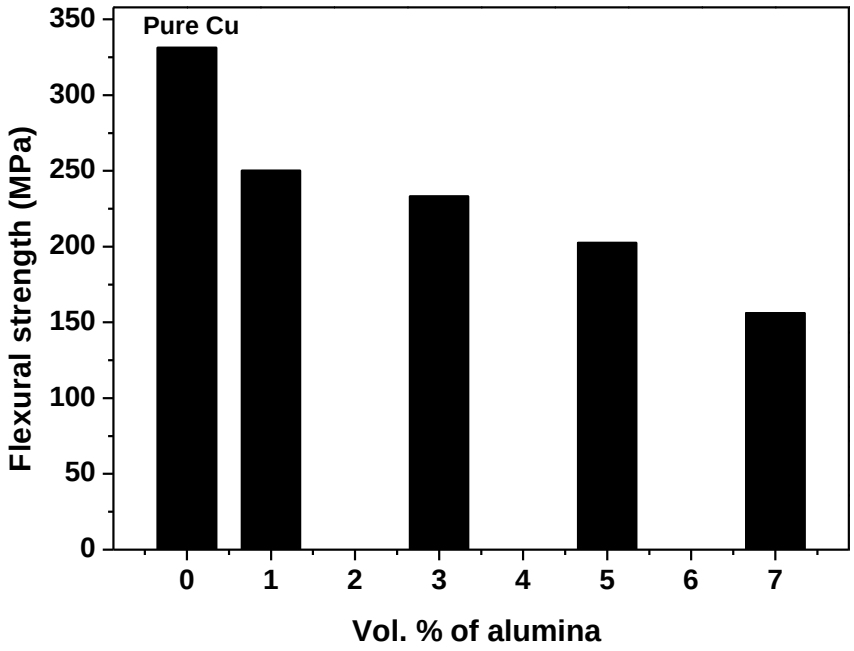

Fig. 3.2.13 Plot for ultimate flexural stress (MPa) vs vol. % of reinforcement content for Cu-Al_2O_3 nanocomposites

3.2.2.3a.5 Fractography

Fracture surface of the three-point flexural test microcomposite and nanocomposite specimens have been shown in (Fig. 3.2.14 (a & b)). The fracture mode for the micro- and nano-composites is seemingly mixed mode. The dimple fracture surface suggests ductile fracture as the principal mode of fracture in the microcomposite. Fracture surface of the microcomposite exhibit micro-void coalescence in the matrix and particle cracking or matrix-particle interface de-cohesion (Fig. 3.2.14 (a) & 3.2.15). No secondary cracks are observed in the brittle Al_2O_3 particle which indicates the premature failure of the composite [16].

Damage is possibly nucleated by interfacial de-cohesion, particle cracking, void growth and finally coalescence of voids in the matrix around the reinforcement particles. The dimple size decreases with increase in Al_2O_3 content. Dimple growth is hindered by the presence of Al_2O_3 particles. The sharp micro-cracks that develop due to particle fracture can enhance localized plastic flow within the ductile matrix which aids in failure phenomena such as ductile separation of the matrix by void growth and shear bands [17].

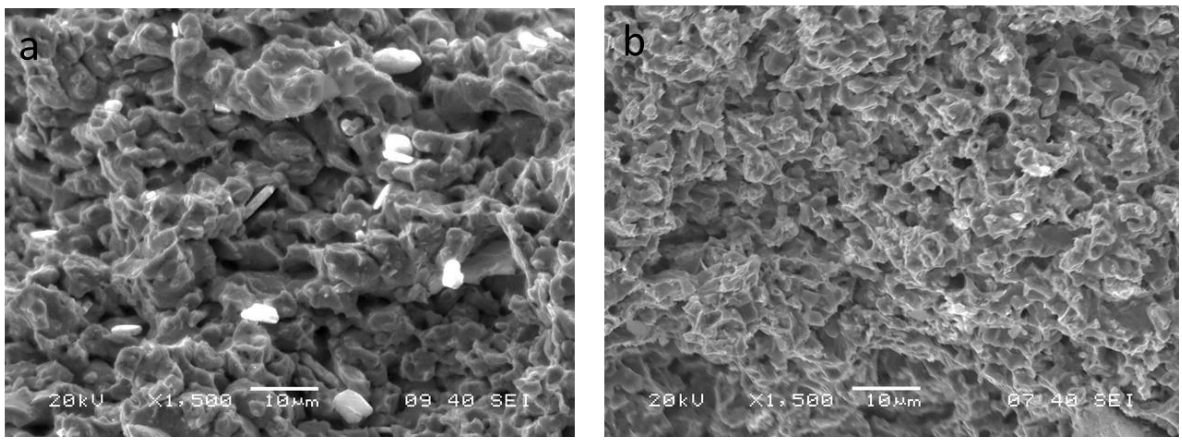

Fig. 3.2.14 Fractographs of Cu-5 vol. % Al_2O_3 (a) microcomposites (b) nanocomposites sintered at 900°C

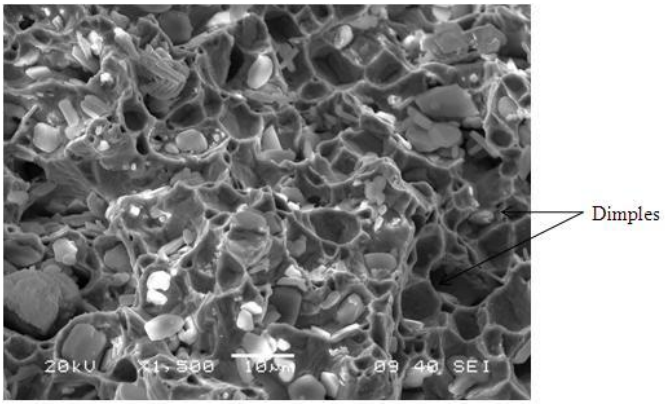

Fig. 3.2.15 Fractograph of Cu-10 vol. % Al_2O_3 microcomposites sintered at 900°C

The fracture mode for nanocomposites also depict mixed mode, showing quasi-cleavage type of fracture. The fracture surface of nanocomposites exhibits more of void formation and matrix-reinforcement debonding. For high volume fraction of reinforcement content, early fracture of material occurs with minimal plastic deformation. The macroscopic features of the fracture surface of Cu-Al_2O_3 nanocomposites indicate nearly flat surface, minimal plastic deformation preceding the fracture and rapid crack growth accompanied by loud noise [18]. The microscopic characteristics include faceted fracture surface at certain instances and transgranular fracture of Cu grains in the nanocomposites.

3.2.2.3a. 6 Wear test

The abrasive wear rate is greatly reduced as Al_2O_3 content in the composite increases (Fig. 3.2.16 & 3.2.17).

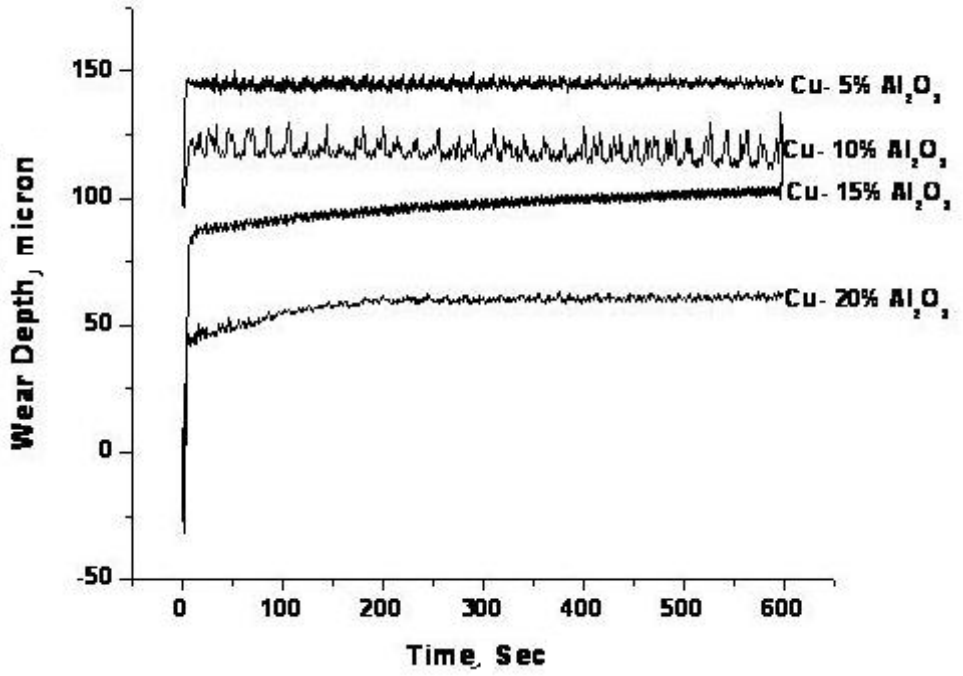

Fig. 3.2.16 Plot for wear depth vs. time of Cu-Al_2O_3 microcomposites with different vol. % of Al_2O_3 sintered at 900°C temperature

Al_2O_3 being inherently harder than Cu, hence the wear resistance of the composites are higher than native Cu. However, as the number of Al_2O_3 microparticles increase, the resistance to the penetration of abrasive particles increases (Hardness increases with increases in the reinforcement content) and hence the wear depth decreases [8]. The drastic reduction in wear rate may be attributed by (1) enhancement in hardness of the composite reinforced by Al_2O_3 particles and (2) greater reduction of direct load contact between the Cu/Al_2O_3 composite surface and disk in comparison with pure Cu due to load bearing component action of hard Al_2O_3 particles [19].

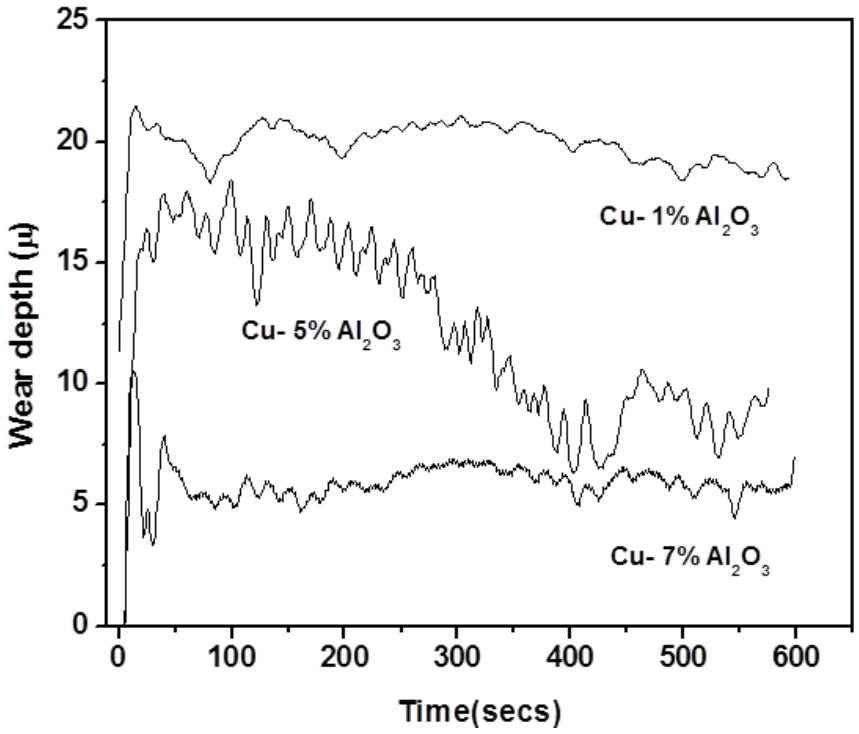

Fig. 3.2.17 Plot for wear depth vs. time of Cu-Al_2O_3 nanocomposites with different vol. % of Al_2O_3 sintered at 900°C temperature

The worn out specimens' SEM micrographs (Fig. 3.2.18(a) & (b)) represents that with increase in reinforcement content the surface roughness decreases. As nano particles act as obstacle for the smooth removal of material, the abrasion resistance also increases. The wear mechanisms operating can be enlisted as grooving and micro-plastic ploughing. The microploughing has eventually created long grooves, and the removed material has been pushed to the ridges of the grooves (Fig. 3.2.18(b)). The intensity of microploughing decreases as the Al_2O_3 content in the composites increases [15]. Fig. 3.2.18(c) shows microcrack formation in the nanocomposite during wear.

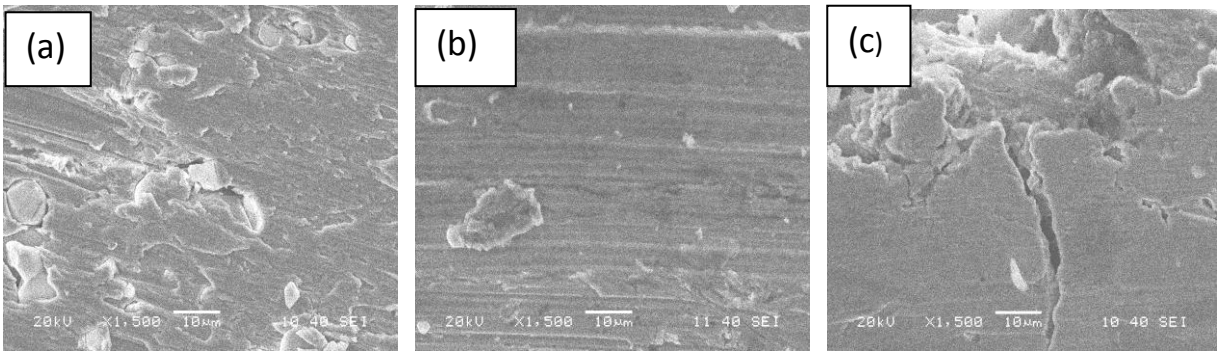

Fig. 3.2.18 SEM images of worn-out surfaces of (a) Cu-5 vol. % Al_2O_3 (microcomposite) (b) Cu-10 vol. % Al_2O_3 (microcomposite) (c) Cu-1 vol. % Al_2O_3 (nanocomposite)

3.2.2.3b Aluminium-alumina composite

3.2.2.3b.1 Density

Densification of aluminium-alumina micro- and nano-composites at different sintering temperatures were recorded and plotted in Fig. 3.2.19 & 3.2.20. It has been found that the % of theoretical density decreases with increasing alumina content in both cases. As alumina is hard and brittle; addition of alumina decreases compressibility in both composites. For the same composition nanocomposites show lower density than microcomposites. The reason is higher degree of agglomeration of nanoparticles than micron-size particles leads to lesser densification. The density of samples sintered at higher temperature exhibits higher sinterability and increased pore filling. These events lead to higher density at higher sintering temperature. From the densification plots for both micro- and nano-composites it is observed that densification behaviour does not follow any trend with sintering temperature. The nanocomposites with higher content of alumina at sintering temperature of 600°C show lower value of density, as agglomeration of alumina nanoparticles takes place to a higher degree impeding effective densification. The nanocomposites with 5 and 7 vol% of alumina show high density for sintering temperature of 550°C, because lower temperature leads to lower degree of clustering compared to higher temperatures.

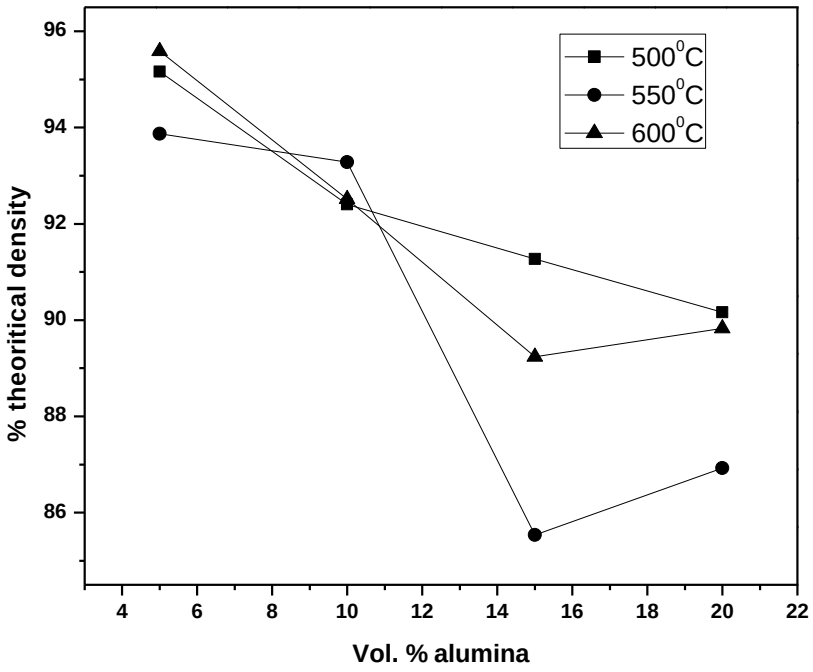

Fig. 3.2.19 Densification plots of Al-Al_2O_3 microcomposites sintered at different temperatures

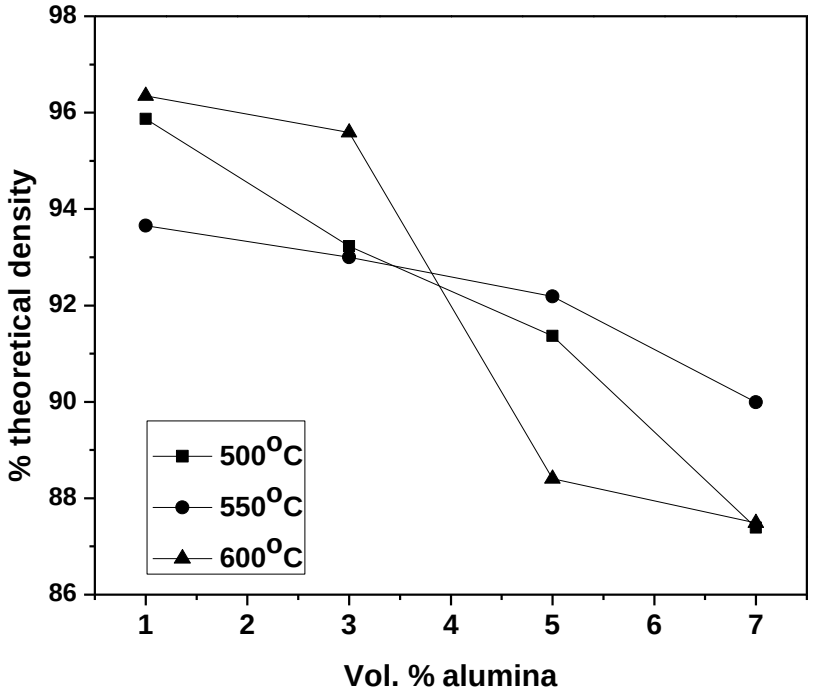

Fig. 3.2.20 Densification plots of Al-Al_2O_3 nanocomposites sintered at different temperatures

3.2.2.3b.2 Microhardness

Fig. 3.2.21 reveals higher microhardness for Al-Al_2O_3 microcomposite samples sintered at lowest sintering temperatures. Microcomposites with higher alumina content show higher hardness due to higher pinning effect of alumina particle, hence higher resistance to indentation. The samples sintered at higher sintering temperature i.e. 600°C show lower microhardness due to grain coarsening at higher temperatures. Fig. 3.2.22 shows Al-Al_2O_3 nanocomposites sintered at low sintering temperature possessing high hardness for lower content of alumina. It has been observed that the samples sintered at 600°C show higher hardness than other temperatures due to higher sinterability and increased pore filling.

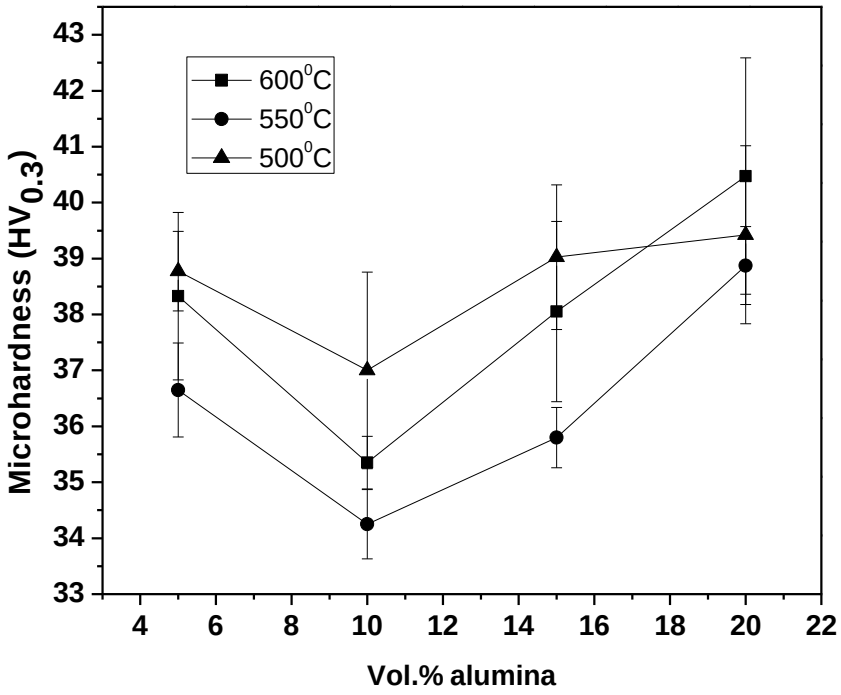

Fig. 3.2.21 Microhardness plots of Al-Al_2O_3 microcomposites sintered at different temperatures

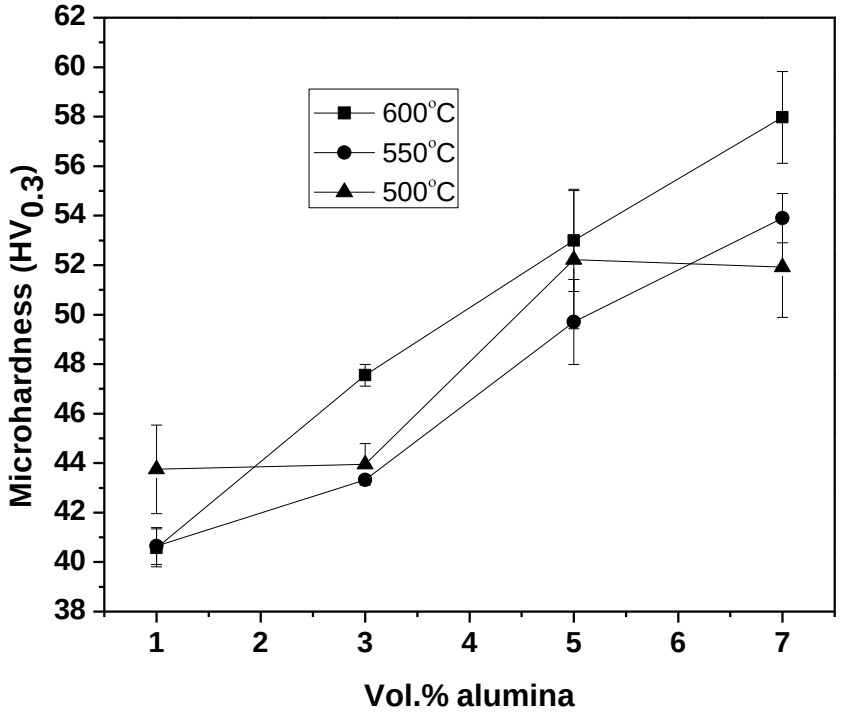

Fig. 3.2.22 Microhardness plots of Al-Al_2O_3 nanocomposites sintered at different temperatures

3.2.2.3b.3 Compression Test

Compressive strength of Al-Al_2O_3 microcomposites have been shown in Fig. 3.2.23. The compressive strength of 5, 10, 15, 20 vol. % of alumina revolve around the same values, the highest value being for 5 vol. % alumina. The higher alumina content reduces the ductility of the composite leading to premature cracking of samples during compressive loading. The compressive strength of 5 vol. % alumina microcomposites is 240MPa. Compressive strength of nanocomposites is illustrated in Fig. 3.2.24 which demonstrates that both 1 vol. % and 5 vol. % alumina reinforced nanocomposite possess high strength than other compositions. The higher content of nanoparticles induce brittleness and lead to cracking of samples before bearing the compressive load, hence the strength decreases. The premature cracking of higher content of alumina causes the incomplete load bearing of nanocomposites. The compressive strength of nanocomposite is higher than microcomposites as lower compositions of nanocomposites possess same strength as higher compositions of microcomposites. The lowering of strength for 3 and 7 vol. % alumina reinforced nanocomposites is due to high surface area of nanoparticles and agglomeration which gives rise to early breakage of samples.

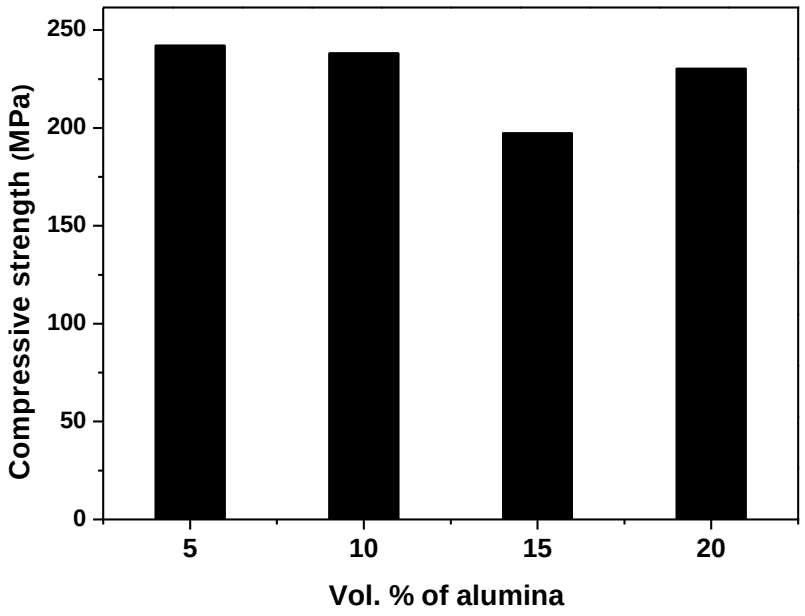

Fig. 3.2.23 Compressive strength of Al-Al_2O_3 microcomposites sintered at 600°C

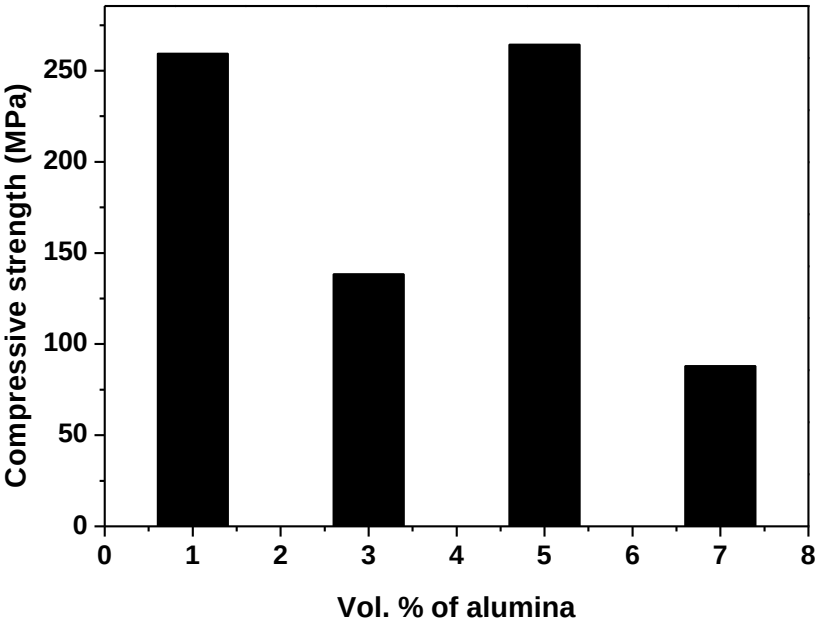

Fig. 3.2.24 Compressive strength of Al-Al_2O_3 nanocomposites sintered at 600°C

3.2.2.3b.4 3-point bend test

The flexural tests of microcomposites reveal that the former shows low flexural strength than pure aluminium strength. The flexural test is a combination of tensile and compressive tests, hence gives us a combined idea of the mechanical strength of the composites. The microcomposites possess low strength than pure aluminium because the alumina particles act as defects during flexural loading. During flexural loading the microvoids formed in the vicinity of alumina particles leading to the coalescence of the same. Flexural strength of 10 vol. % alumina reinforced microcomposite is high among all the compositions, showing that it is the optimum composition (Fig. 3.2.25). Flexural strength of nanocomposites is also lower than pure aluminium following the same principle as described above. Fig. 3.2.26 shows that 3 vol. % alumina reinforced nanocomposite possess high flexural strength compared to other compositions proving it to be an optimum composition among nanocomposites. The flexural strength of nanocomposites containing low percent of alumina is same as microcomposites having high high content of alumina. The 5 vol. % alumina reinforced nanocomposite possess flexural strength lower than 3 vol. % alumina composition because higher alumina nanoparticles content leads to clustering of nanoparticles and lowering of strength due to increased density of defects.

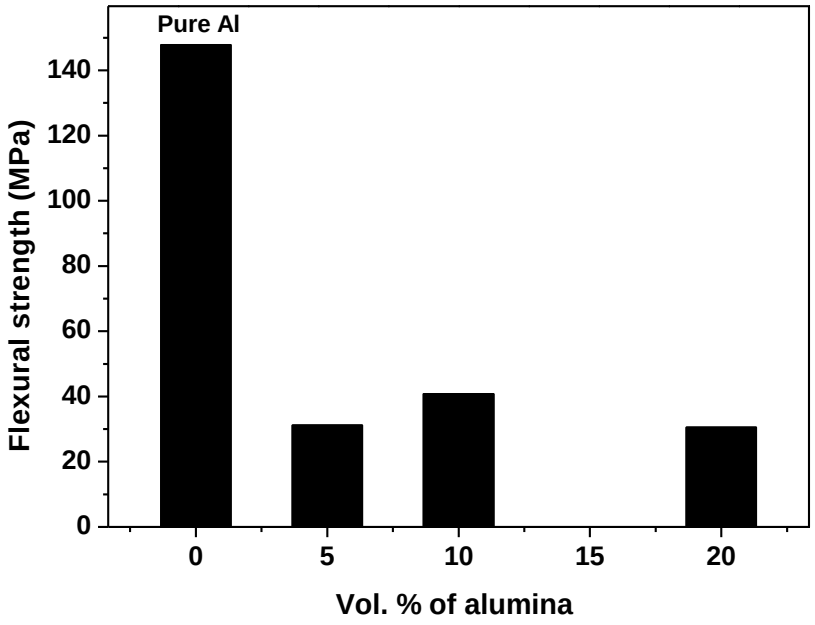

Fig. 3.2.25 Plot of flexural strength vs. vol. % of reinforcement of Al-Al_2O_3 microcomposites sintered at 600°C.

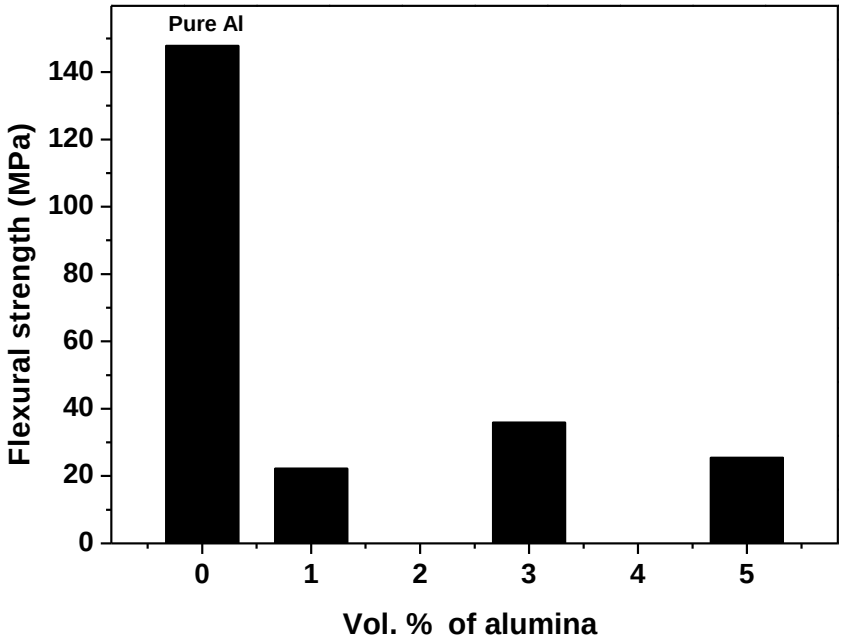

Fig. 3.2.26 Plot of flexural strength vs. vol. % of reinforcement of Al-Al_2O_3 nanocomposites sintered at 600°C

3.2.2.3b.5 Fractography

Fig. 3.2.27(a & b) illustrates SEM fractographs of Al-5 vol. % alumina microcomposite and nanocomposite respectively sintered at 600°C. The fracture surface shows intergranular fracture, as aluminium is a soft and ductile metal, the grain boundaries are harder compared to the interior of grains. The nanocomposites show pores on the fracture surface. These pores symbolize the release of trapped gas formed during sintering. Alumina particles have been covered by aluminum particles, hence the contrast is not visible in the fractographs. The nanocomposite's fractograph reveal that there is higher oxide formation of matrix particles in nanocomposites than microcomposites as suggested by increased number of pores. It has been observed that the microcomposites show dimpled structure representing higher ductility than nanocomposites.

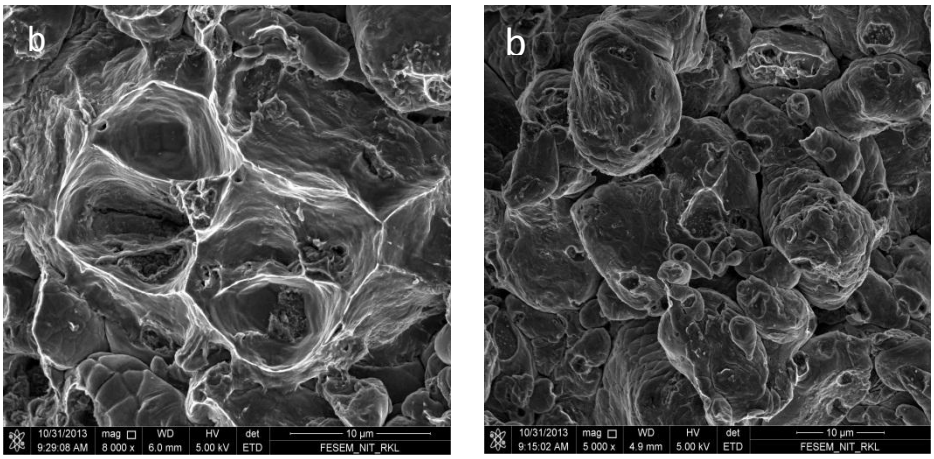

Fig. 3.2.27 SEM fractographs of Al-5 vol. % Al_2O_3 (a) microcomposite (b) nanocomposite sintered at 600°C

3.2.2.3b.6 Wear test

Fig.3.2.28 & 3.2.29 show wear depth vs. sliding time for Al-Al_2O_3 micro and nanocomposites sintered at 600°C. The general trend here is that the wear depth decreases with alumina content in both cases. Al_2O_3 being hard and brittle, impart high wear resistance i.e. the wear depth decreases. As the number of Al_2O_3 particles increases the wear indenter encounters Al_2O_3 particles more than the soft matrix. For the same composition it is found that the nanocomposite (~6µm) reflects lower wear depth than microcomposite (~10µm) due to higher hardness. The nanocomposites having low alumina percentage show almost equal wear depth as the microcomposites containing higher amount of alumina

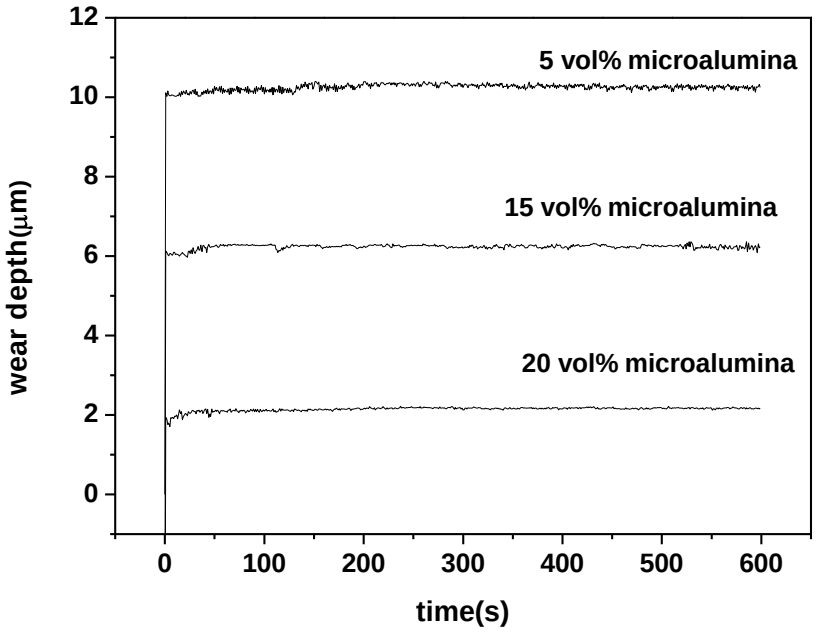

Fig. 3.2.28 Wear depth vs. time plot of Al-Al_2O_3 microcomposites sintered at 600°C

.

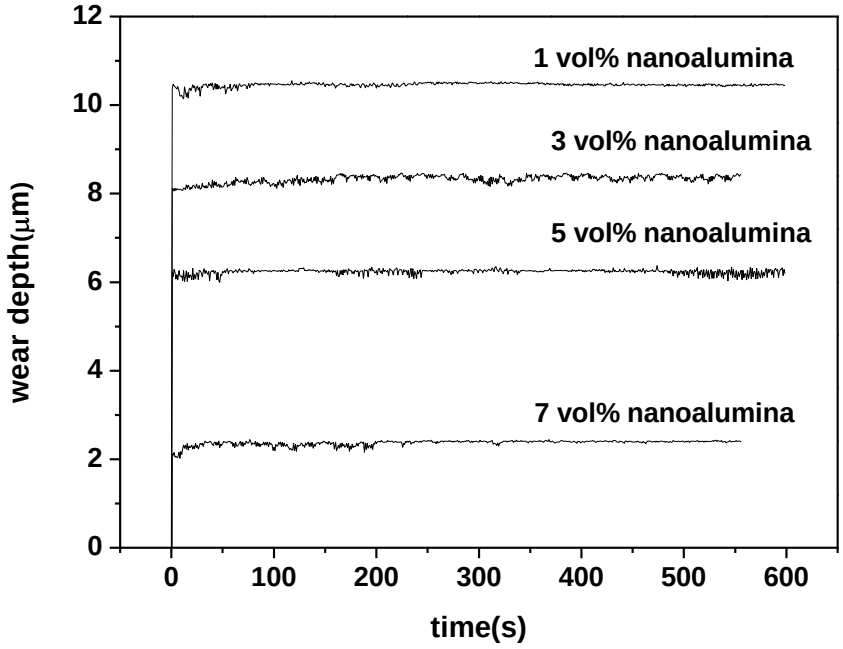

Fig. 3.2.29 Wear depth vs. time plot of Al-Al_2O_3 nanocomposites sintered at 600°C

3.2.3 Spark Plasma Sintering

This investigation focuses on the fabrication of copper-alumina microcomposites and nanocomposites by spark plasma sintering technique. The subsequent microstructural studies and mechanical properties assessment and correlation helps in understanding the science and technology of microcomposites and nanocomposites reflecting each ones dominance on another on every aspect. The characterization of micro- and nano-composites using X-ray diffraction, scanning electron microscopy and transmission electron microscopy followed by microhardness, nanohardness and wear measurements have been studied.

3.2.3.1. Fabrication of Composites

3.2.3.1a Copper-alumina composite

Copper (Loba Chemie, purity > 99.7%, average size~11.09µm) and alumina (Sigma Aldrich, average size~10µm (micro) and <50 nm (nano) both having purity > 99.7%) powders were blended separately in turbula shaker mixer. The compositions used for fabricating nanocomposites were 0.5, 1, 3, 5, and 7 volume % of alumina nanoparticles in copper matrix. Another set of specimens having compositions of 1, 5, 20 volume % micron size alumina were used to synthesize microcomposites. The micro- and nano-composites were fabricated via spark plasma sintering (SPS) (DR SINTER LAB SPS Syntex INC, model: SPS-515S, Kanagawa, Japan) method at a temperature of 700ºC maintaining a soaking time of 5 minutes at a pressure of 50 MPa. The heating rate for the whole process was maintained at 80ºC/minute.

3.2.3.1b Aluminium-alumina composite

The as-received aluminium (Loba Chemie, purity > 99.7%, average size~22.09µm) and alumina (Sigma Aldrich, average size~10µm and <50 nm) (surface area: 40 m^2/g for alumina nanopowder) powders were mixed and blended separately using agate mortar for 60 minutes to ensure homogeneous mixing. Nanocomposites containing 0.5, 1, 3, 5 and 7 vol. % of Al_2O_3 (average size<50nm) were fabricated by blending the matrix and reinforcement powders,

followed by spark plasma sintering (SPS) (DR SINTER LAB SPS Syntex). Another set of specimens having compositions of 1, 5, 20 volume% were chosen to fabricate microcomposites. SPS was carried out at a temperature of 500ºC and an applied pressure of 50MPa for 5 minutes under vacuum with a heating rate of 80ºC/minute for nanocomposites as well as the microcomposites.

3.2.3.2 Characterization of Composites

The specimens were characterized by X-Ray diffraction (PANalytical model: DY-1656) with CuK_{α} radiation, scanning electron microscopy (JEOL JSM 6480 LV) and transmission electron microscopy (TECNAI G2 20S-TWIN) equipped with an energy dispersive X-Ray analyzer. The sample preparation for conducting TEM study was done by punching 3 mm discs from the sample whose thickness had been reduced to 100µm. The discs were then dimpled to around below 10µm and then ion milled for 1 hour for perforation.

3.2.3.2a Copper-alumina composite

3.2.3.2a.1 X-Ray Diffraction

To study phase evolution during composite fabrication by SPS process, X-ray diffraction was conducted. The XRD patterns (Fig. 3.2.30 & 3.2.31) confirm the presence of Cu, Al_2O_3 and $CuAlO_2$ phases for both micro and nanocomposites. The copper, alumina and $CuAlO_2$ peaks have also been indexed in the X-ray diffraction patterns. The formation of $CuAlO_2$ in Cu-Al_2O_3 system has been reported by many groups such as Trumble et al. [20], Seager et al. [21], Kim et al. [22] and Fathy et al. [15]. The thermodynamics of the interaction between copper and alumina point towards the fact that the formation of $CuAlO_2$ is feasible in the present processing conditions [23].

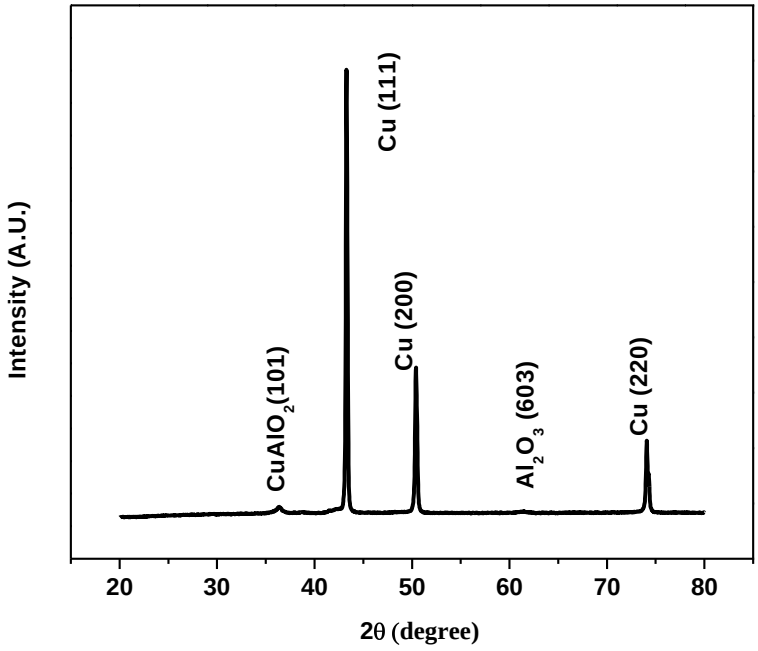

Fig. 3.2.30 XRD pattern of Cu-7 vol. % Al_2O_3 nanocomposite sintered by SPS

The formation of $CuAlO_2$ as a function of temperature at the Cu(ss)/Al_2O_3 interface can be represented as [20]

$$[\text{at. \% } \underline{O}_{Cu(ss)}] = \exp(-18100/T + 9.1) \qquad (700\text{-}1050°C) \qquad (1)$$

The formation of $CuAlO_2$ starts at the isothermal sintering time, i.e. after the formation of Cu_2O the same reacts with alumina to form the aluminate.

$$Cu_2O + Al_2O_3\,(\text{Heated}) \rightarrow 2CuAlO_2\,[24] \qquad (2)$$

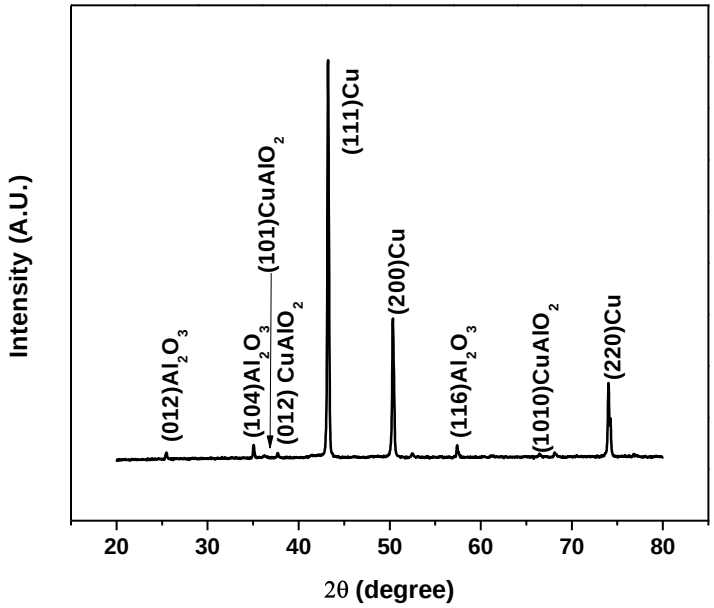

Fig. 3.2.31 XRD pattern of Cu-20 vol. % Al_2O_3 microcomposite sintered by SPS

3.2.3.2a.2 Scanning electron microscopy

Fig. 3.2.32 & 3.2.33 show the SEM micrographs of nanocomposites and microcomposites respectively. The distribution of nanoparticles is better compared to microparticles in the copper matrix [5].

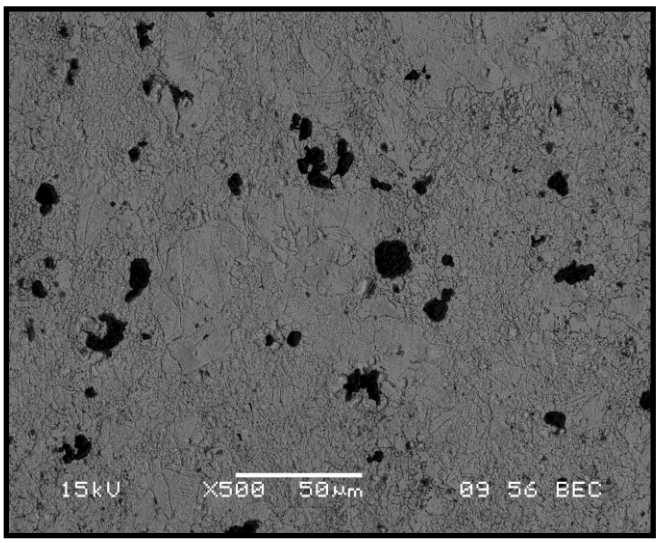

Fig. 3.2.32 SEM micrograph of Cu-7 vol. % Al_2O_3 nanocomposite sintered by SPS

There are several pores visible on the grain boundary of the copper grains in the microcomposites which indicate the poor intermixing of matrix and reinforcement powder particles in the microcomposites compared to the nanocomposites. The intermixing of alumina nanoparticles and the copper matrix particles is quite intimate and the alumina particles have penetrated into the voids of copper-copper particle contact unlike the micron sized alumina particles. The difference in the intermixing and embedment of the micron size particle and the nano sized particle is visible in the SEM micrographs.

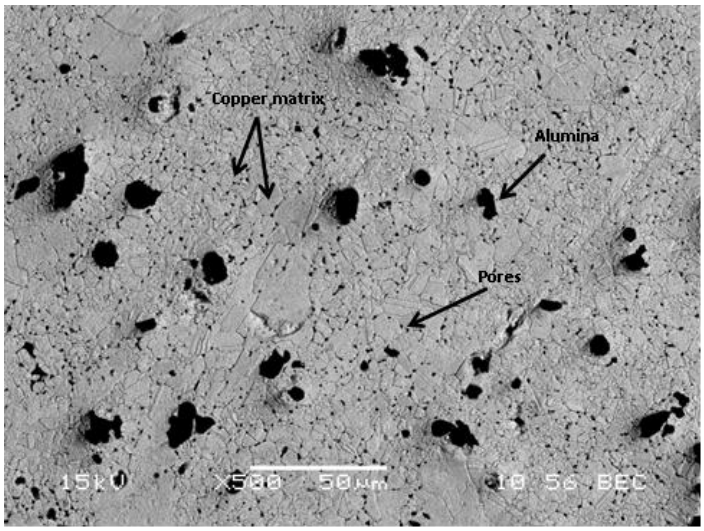

Fig. 3.2.33 SEM micrograph of Cu-5 vol. % Al_2O_3 microcomposite sintered by SPS

The copper and alumina interaction has also aided in the formation of a new phase i.e. $CuAlO_2$ which has been identified from XRD and TEM analysis. Diminished grain growth of copper can be observed (Fig. 3.2.32) in the areas where the distribution is proficient due to the pinning effect of the nanosized alumina particles [25]. In nanocomposites, as the interparticle distance decreases, interaction between the dislocations and particles increases, and this results in faster dislocation multiplication. The matrix-reinforcement bonding seems to have improved in the nanocomposites sintered by SPS. The reason could be anticipated as the high surface energy of the particles compelling them to compensate their thermodynamic instability by efficient bonding.

3.2.3.2a.3 Transmission electron microscopy

To have more insight on microstructure of the fabricated composites, TEM was conducted. Sintered compacts exhibit annealing twins and sub-grain boundaries for both micro- and nano-composites (Fig. 3.2.34 & 3.2.35). Twinning might have occurred during the high temperature sintering stage. Conditions for twin formation are achieved when large number of obstacles is formed in the crystal, blocking the dislocation movement.

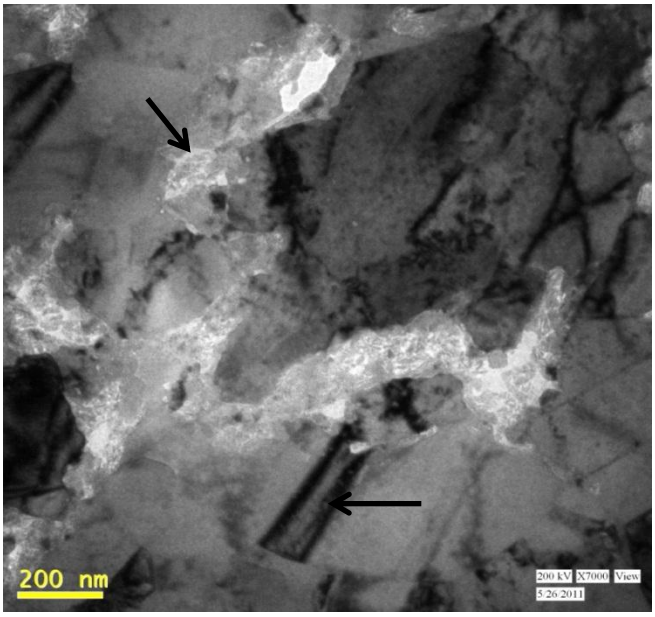

Fig. 3.2.34 TEM micrograph of Cu-5 vol. % Al_2O_3 nanocomposite sintered by SPS

Dislocations accumulate on obstacles causing increase of internal strain in local areas, which together with external strain induce twin formation. Presence of twins indicated lower mobility of dislocations, in other words the stabilization of dislocation structure, which is primary condition for improvement of mechanical properties of dispersion strengthened materials. Increase of dislocation density is caused by the difference between the thermal expansion coefficient of the particles and matrix. In agreement with this, suggests the predominant effect of dislocation density in the strengthening of the composite caused by thermal expansion mismatch during processing [24,26]. The thermal expansion coefficient of Cu and Al_2O_3 are 16.6 $x10^{-6}$ k^{-1} and 5.4 x 10^{-6} k^{-1} respectively. The alumina ceramic particles present in the composite are the source of thermal stresses which can be released by plastic deformation of the matrix. The

thermal stresses during the production process could generate dislocations in the matrix and inside the particles that is clearly visible in the alumina particles [27].

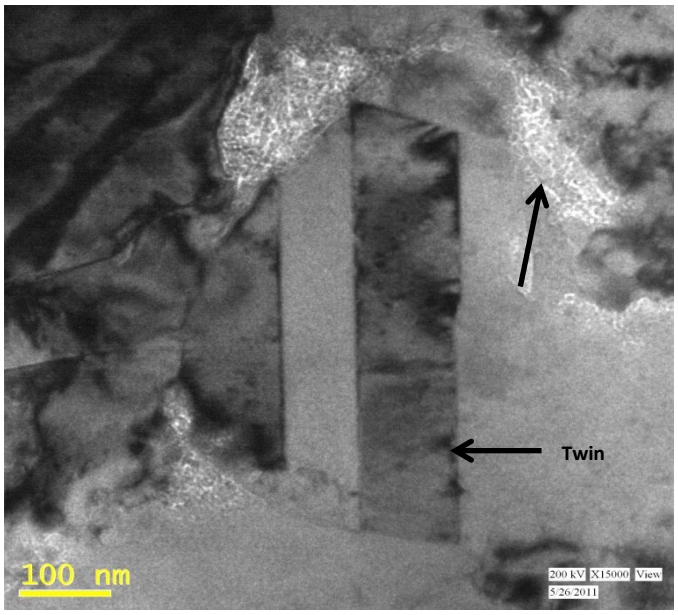

Fig. 3.2.35 TEM micrograph of Cu-5 vol. % Al_2O_3 microcomposite sintered by SPS

The TEM micrographs represent nano twinning in case of 5 vol. % reinforced nanocomposite. A milky white appearance of the new phase formed is quite prominent in Fig. 3.2.34. The interaction of alumina nanoparticles is far more proficient than the alumina microparticles which can be realized from the amount of $CuAlO_2$ formed in the TEM micrographs. The difference in contrast in the TEM micrographs suggests the presence of Cu (grey), Al_2O_3 (black) and $CuAlO_2$ (white region). Formation of $CuAlO_2$ can also be anticipated due to its presence in the proximity with the alumina particles. The formation of intermediate phase is highly concentrated around the alumina particles. The XRD study also supports the presence of $CuAlO_2$.

3.2.3.2b Aluminium-alumina composite

3.2.3.2b.1 X-ray diffraction

The X-Ray diffraction patterns obtained from the SPS sintered compacts of the Al-Al_2O_3 nanocomposites reveal aluminium as well as alumina phases. The X-Ray diffraction patterns of the Al-Al_2O_3 microcomposites and nanocomposites are shown in Fig. 3.2.36 & 3.2.37 respectively. The patterns depict small peaks of alumina present in the X-Ray patterns of nanocomposites (the combined effect of peak broadening and low intensity peaks of alumina nanoparticles) whereas in case of microcomposites, the alumina peaks are quite distinct and clear.

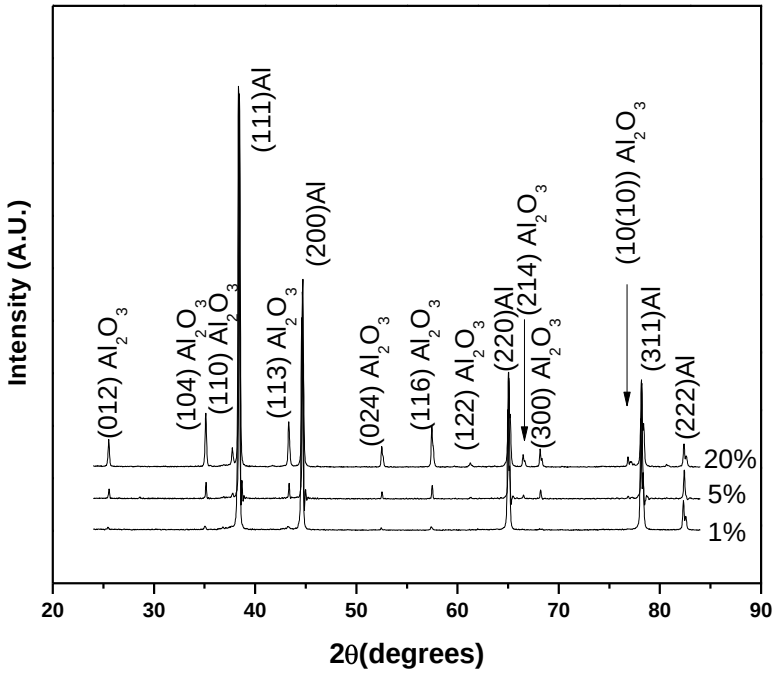

Fig. 3.2.36 XRD patterns of Al-Al_2O_3 microcomposites sintered using SPS

The XRD patterns confirm that no new phase was formed in the nano- and microcomposites. The alumina peaks are distinct in the 20 vol. % reinforced Al-Al_2O_3 microcomposite due to higher amount of alumina.

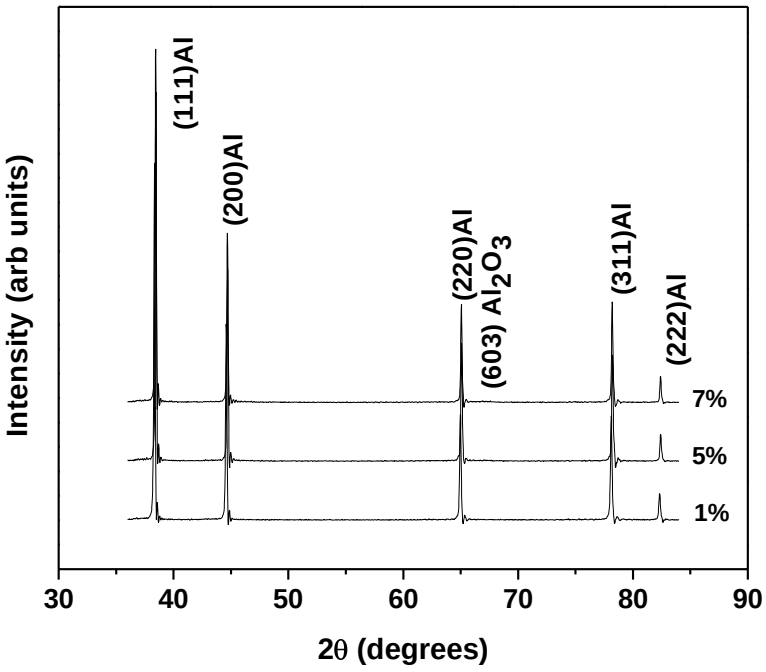

Fig. 3.2.37 XRD patterns of Al-Al_2O_3 nanocomposites sintered using SPS

3.2.3.2b.2 Scanning electron microscopy

The back scattered scanning electron micrographs of Al-Al_2O_3 nanocomposites and microcomposites are illustrated in Fig. 3.2.38(a), (b) & (c) indicating grey and black regions which correspond to the aluminum and alumina respectively confirmed by EDS analysis. Fig. 3.2.38 (a) shows the EDS analysis of the black region in the figure depicted by arrow mark. The alumina nanoparticles are present in the interspaces of aluminium particles. The distribution of reinforcement particles in Al-Al_2O_3 nanocomposites is proficient than in the case of microcomposites. The well-established mathematical relation (Eq. (2)) which explains the requirement of uniform dispersion of reinforcement in the matrix

$$\lambda = \frac{4(1-f)r}{3f} \qquad (3)$$

Where λ is distance apart from the reinforcements, f is the fractional volume of reinforcement; r is the radius of the particles (assuming them to be spherical). The SEM micrographs of the nancomposites suggest presence of network of the alumina particles within the intergranular spaces of the aluminium matrix. The micrographs connote the intimate level of mixing of matrix

and reinforcement powders in the nanocomposites which is seemingly due to the aluminium-alumina bonding in the composite. The proximate level of intermixing of alumina nanoparticles in the aluminium matrix has supposedly given rise to such a microstructure. A striking difference regarding the mode of interaction of alumina nanoparticle and alumina microparticle with the aluminium matrix individually can be realized from the micrographs. The differential interaction of nanoparticles and microparticles could be implicated to the reason of clustering in composites, the closer the ratio of reinforcement particle size to the matrix particle size (PSR) is to 1, the lower is the possibility of clustering [28]. The clustering which is apparently visible in the case of microcomposite is due to the deviation of the ratio from the value 1.

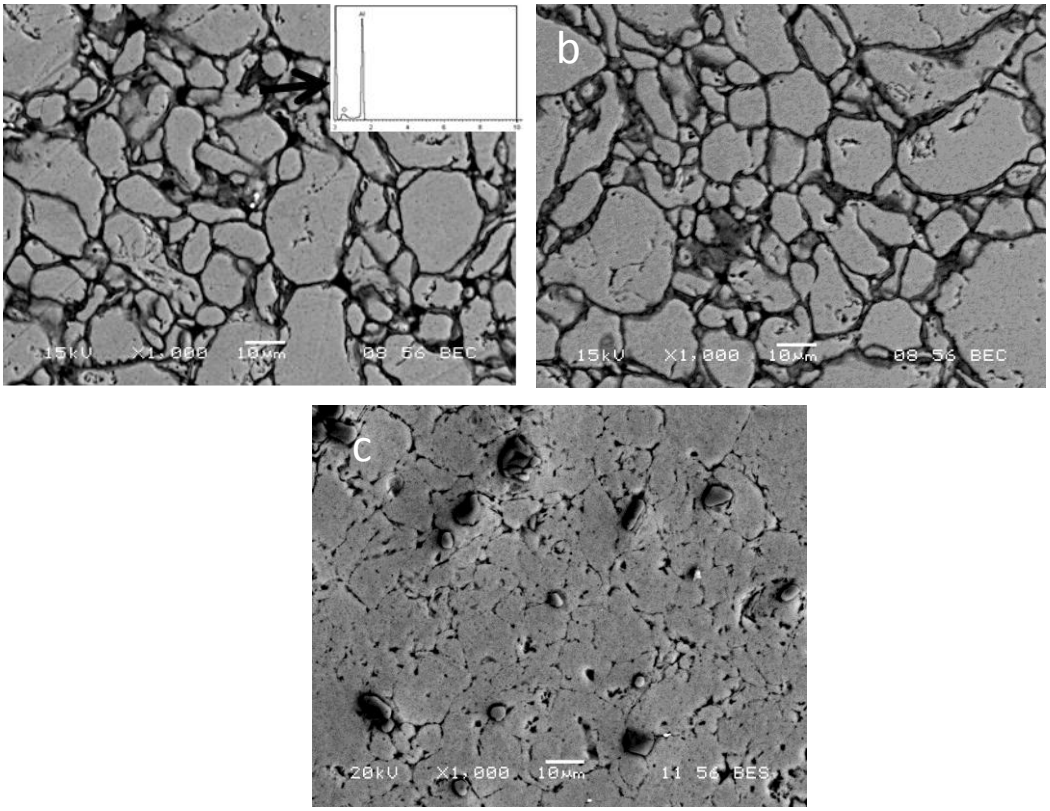

Fig. 3.2.38 SEM micrographs of (a) Al-5vol. % Al_2O_3 nanocomposite, (b) Al-7vol. % Al_2O_3 nanocomposite, (c) Al-5vol. % Al_2O_3 microcomposite sintered using SPS

In nanocomposites, the reinforcement particle size is much smaller than the matrix particle size, and hence the inter-particle voids created by the consolidation of aluminium particles have been occupied by the alumina nanoparticles. The conspicuous bonding of nanoparticles with the matrix particles can also be due to the fact that the atomic diffusivity of the nanoparticles is quite

high than the micron-sized particles [6]. The accommodation of alumina nanoparticles is better in the aluminium matrix i.e. the alumina nanoparticles have occupied the interparticle spaces in the aluminium matrix which is not the case with microcomposites. The grain growth in the microcomposites is likely to occur to a greater extent than in nanocomposites. This observation could be attributed to the inability of the alumina microparticles to pin down the grain growth at a larger scale. The thermal stability against grain growth observed in the nanocomposites can be ascribed to the presence of alumina nanoparticles which are expected to hinder the grain boundary movement via Zener pinning [29].

Incipient fusion phenomenon probably has occured which can be observed in the nanocomposites in between the intergranular spaces of aluminium, which can be ascribed to plasma formation at interparticle contacts at the time of sintering. The pores present in the nanocomposites are sparse in number which can be observed in SEM micrograph i.e. Fig. 3.2.38 (a) & (b) as compared to the microcomposites shown in Fig. 3.2.38 (c). The poor bonding of aluminium and alumina nanoparticles has been reported in literature by conventional sintering [30]. The distribution of alumina in nanocomposites is better than in the microcomposites. The improved bonding between the matrix and reinforcement by spark plasma sintering method can be attributed to the pressure assisted sintering as well as the grain boundaries rendered clean in the process of SPS.

Olevsky et al. [31] have investigated the impact of thermal diffusion in spark plasma sintering which reflects that the non-uniform distribution of temperature causes local melting at the interparticle contacts. Munir et al. [32] have demonstrated higher diffusion co-efficient for spark plasma sintering. Xie et al. [33] have studied the spark plasma sintering of aluminium powders and have reported the presence of a clean interface from high resolution TEM experiments. In the present investigation, clean interface (absence of interphase or reaction products) and a reasonable amount of physical contact of the alumina particles to the aluminum particles has also been observed. The dispersion of reinforcements in the matrix is the blue print of the degree of strengthening rendered by the reinforcement particles.

3.2.3.2b.3 Transmission electron microscopy

The transmission electron microscope (TEM) micrographs illustrate the dispersion of alumina particles in aluminium matrix. The grey region symbolizes aluminium matrix and the black area depict alumina particles which have been confirmed by EDAX analysis. The TEM micrographs of the sintered specimen show clean and sound interface in case of both nano- and microcomposites as suggested by Durai et al. [34]. The alumina particle size can be estimated to be around 50 nm from the TEM micrograph in Fig. 3.2.39 (a) & (b), frank fault loops can be observed inside the alumina particles marked by arrows in Fig. 3.2.39 (a) [35].

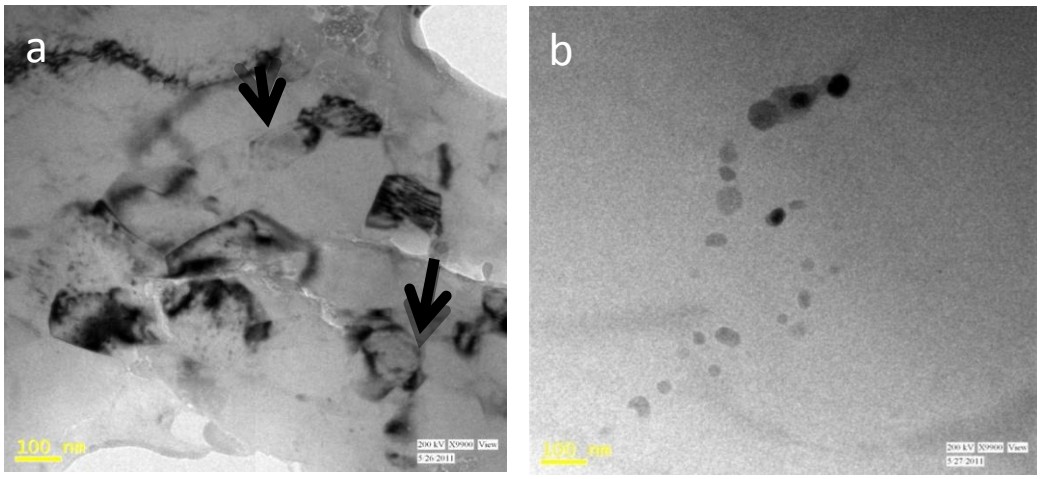

Fig. 3.2.39 TEM micrographs of (a) Al-1vol. % Al_2O_3, (b) Al-5vol. % Al_2O_3 nanocomposites sintered by SPS

These loops impart a conviction of the strengthening mechanisms operating in the composite [36]. Fig. 3.2.40 (a) shows that large numbers of dislocations have accumulated at the triple junction of Al-7% reinforced Al_2O_3 nanocomposite. It can also be observed that the dislocations are pinned and piled up at the Al/Al_2O_3 interface. Fig. 3.2.40 (b) illustrates the presence of screw dislocations in Al-Al_2O_3 microcomposites. The dislocation lines are straight, long and tangled indicating high dislocation density, which probably arises during spark plasma sintering process. During SPS the powder mass has undergone heavy deformation due to simultaneous application of pressure and high temperature. Pure tilt boundaries are visible in Fig. 3.2.41 (a) [37]. The deformed FCC crystals when annealed lead to interactions between 1/2<*110*> dislocations

resulting in the formation of low-energy networks and sub-boundaries. This refers to: when dislocations' motion is impeded from moving in their slip plane by interacting with other dislocations, sub-boundaries, and others, the strain energy can be minimized by the dislocations climbing out of slip planes where they align in low energy configurations, e:g: cell walls. The high dislocation density at the sub-boundaries can be attributed to the large difference in thermal conductivity of aluminium (24 x 10^{-6}/°C) and alumina (7.92 x 10^{-6}/°C). Cooling of the composite furnishes limited deformation of aluminium inhibited by alumina particles, hence high dislocation density is visible at the boundaries [38].

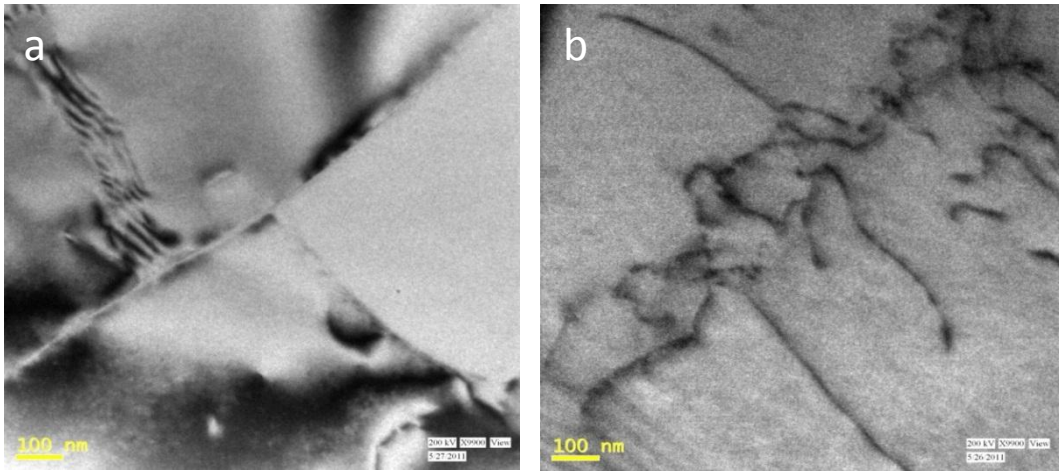

Fig. 3.2.40 TEM micrograph of (a) Al-7vol. % Al_2O_3 nanocomposite, (b) Al-5vol. % Al_2O_3 microcomposite sintered by SPS

Fig. 3.2.41 (b) shows a stacking fault [35] present in the microcomposite, which could be explained as follows: the intermixing of alumina microparticles in the matrix is inappreciable; therefore there may be formation of some sessile dislocations during packing of matrix and microparticle powders. As dislocation is a temperature driven phenomenon, the sessile dislocations formed must have resulted in stacking fault at the time of sintering [36].

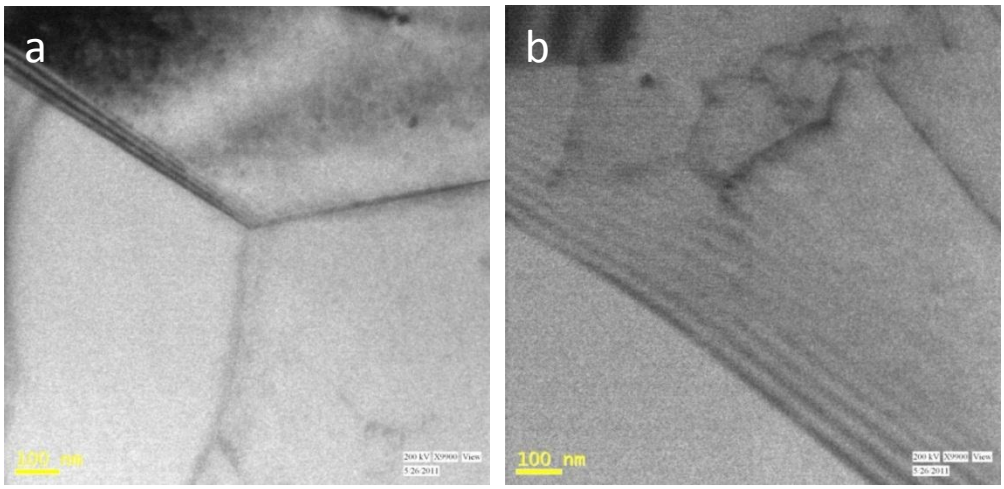

Fig. 3.2.41 TEM micrograph of (a) Al-7vol. % Al_2O_3 nanocomposite, (b) Al-5vol. % Al_2O_3 microcomposite sintered by SPS

During sintering, the energy supplied by the combined elasto-plastic (compression) and electro-magnetic (discharge) processes imparts sufficient mobility for movement of edge dislocations [39]. A sessile dislocation can move only by the diffusion of atoms or vacancies to or from the fault. The width of the stacking fault ribbon is directly proportional to the stacking fault energy which is quite prevalent in case of aluminium.

3.2.3.3 Mechanical Testing

The density of the composites was measured using Archimedes method. The elastic modulus of nanocomposites was determined using nanoindentation (Fisher-Cripps UMIS) technique applying a load of 20mN for a dwell time of 10 seconds. The readings were recorded here at ten equivalent locations for each specimen and the closest values were considered. The micro-hardness values of the microcomposites were determined by Vickers hardness tester (Leco LV 700) applying a load of 0.3 kgf and a dwell time of 5 seconds. The readings were recorded here at four equivalent locations for each specimen. Sliding wear tests were performed using a ball on plate type wear machine (DUCOM TR-208-M1) using hardened steel ball (SAE 52100) indenter

of 2 mm diameter, with an applied load of 2 Kgf and time period of 15 minutes at a speed of 30 rpm. The hardened steel ball slides unidirectionally on fixed samples. The tests were carried out in laboratory atmosphere at a relative humidity of around 50-60% and temperature of about 25°C. The wear depth vs time data was obtained from the inbuilt WINCOM software in the wear machine. The worn surfaces were characterized by SEM.

3.2.3.3a Copper-alumina composite

3.2.3.3a.1 Density and microhardness study

The density and hardness values for both micro and nanocomposites are tabulated in Table 3.2.3. The density values for 1 and 5 vol. % alumina reinforced microcomposites are 95.25 and 95.39% of theoretical density, whereas for same composition of nanocomposites density values are 93.22% and 92.17% of theoretical density. It is observed from the table that density value is lower in case of nanocomposites than microcomposites for the same composition. The reason could be attributed to the higher surface energy of alumina nanoparticles which lead to agglomeration and higher copper-copper contacts hindering densification. Higher number of agglomerates of hard alumina particles shields the copper deformability which does not take place in microcomposites [40].

Fig. 3.2.42 shows the variation of microhardness and nano indentation hardness values with alumina content. The nanohardness values of the nanocomposites are higher than that the corresponding microhardness values of nanocomposites. This can be attributed to the indentation size effect [41].

Composition	Microhardness ($HV_{0.3}$)	Sintered density (g/cm^3)	% theoretical density
Cu- 0.5%Al_2O_3(nano)	76.02	7.51	84.66
Cu- 1% Al_2O_3 (nano)	77.42	8.25	93.22
Cu- 3 % Al_2O_3 (nano)	98.55	8.23	94.05
Cu- 5 % Al_2O_3 (nano)	124.5	8.01	92.17
Cu- 7 % Al_2O_3 (nano)	76.17	7.60	88.93
Cu- 1% Al_2O_3 (micron)	58.97	8.43	95.25
Cu- 5% Al_2O_3 (micron)	82.47	8.29	95.39
Cu- 20% Al_2O_3 (micron)	93.17	7.57	95.82

Table 3.2.3 Microhardness, sintered and theoretical density of Cu-Al_2O_3 micro- and nano-composites with varying alumina content

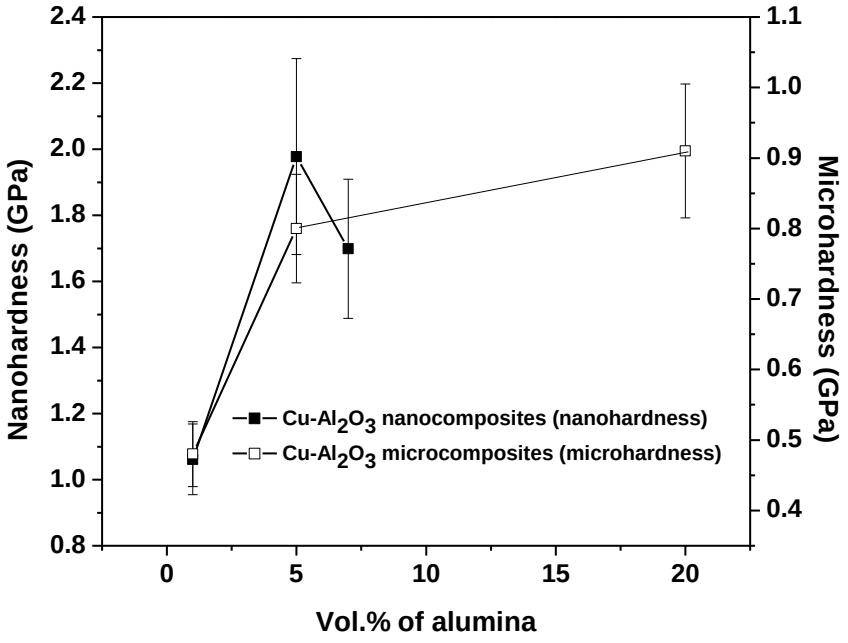

Fig. 3.2.42 Plot for nanohardness of Cu-Al_2O_3 nanocomposites and microhardness of Cu-Al_2O_3 microcomposites

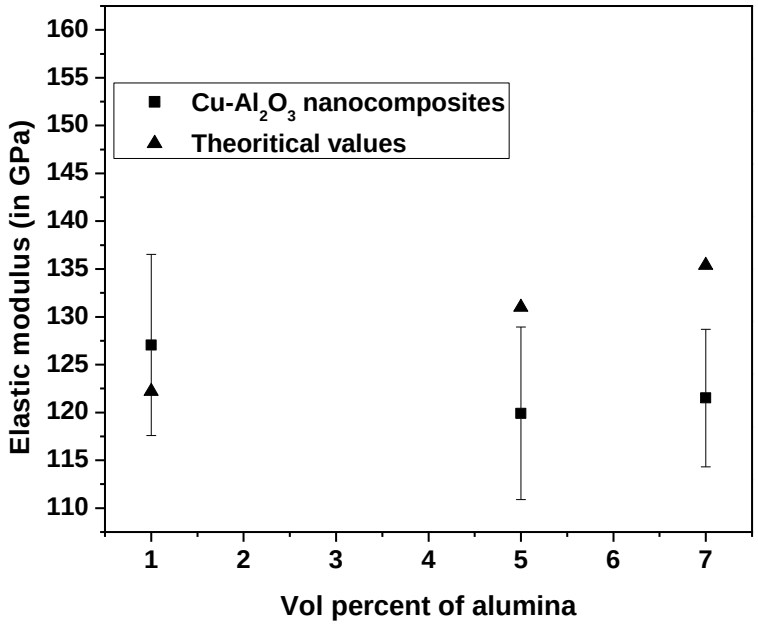

Fig. 3.2.43 Elastic modulus of Cu-Al_2O_3 nanocomposites fabricated by SPS

The elastic modulus values obtained from nanoindentation hardness measurements have been reported against the volume percentage of alumina which is shown in Fig. 3.2.43. Elastic modulus values of the nanocomposites revolve around the theoretical values obtained from rule of mixture. The elastic modulus value of reinforced Cu-1 vol. % Al_2O_3 nanocomposite is higher than the corresponding theoretical value calculated using rule of mixtures. The rest of the compositions i.e. reinforced Cu-5 and 7 vol. % Al_2O_3 nanocomposites display lower elastic modulus values than the theoretical data. The decrease in hardness after 5 vol. % can be attributed to the agglomeration of nanoparticles eventually increasing the interparticle distance. The formation of a new phase $CuAlO_2$ (from XRD and TEM) suggested is a soft phase. The $CuAlO_2$ phase when present discontinuously result in toughening of the interface by crack pinning and enhances the strength of the composite [42].

3.2.3.3a.2 Wear study

3.2.3.3a.2.1 Wear depth

The wear depth vs. time plot for nanocomposites and microcomposites has been illustrated in Fig. 3.2.44 & 3.2.45.

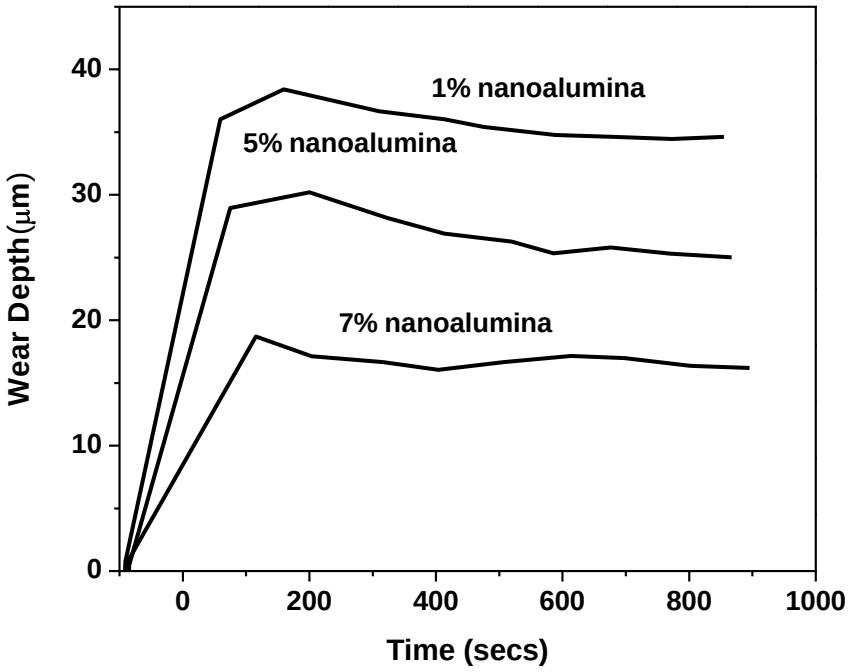

Fig. 3.2.44 Wear depth vs. time plot for Cu-Al_2O_3 nanocomposites sintered by SPS

The wear resistance of microcomposites is higher than nanocomposites for the same compositions [43]. The reason could be ascribed to the fact that the wear indenter in case of microcomposites has a higher retention of contact with the microparticle in microcomposites in comparison to the nanoparticles in nanocomposites. The microparticles render higher time of contact with the wear indenter than the nanoparticles. The reason could be the higher area of contact with the wear indenter in case of microparticles, which is less likely for the nanoparticles reinforced composites. Moreover, the microparticles also prevent origination of sub-surface cracks.

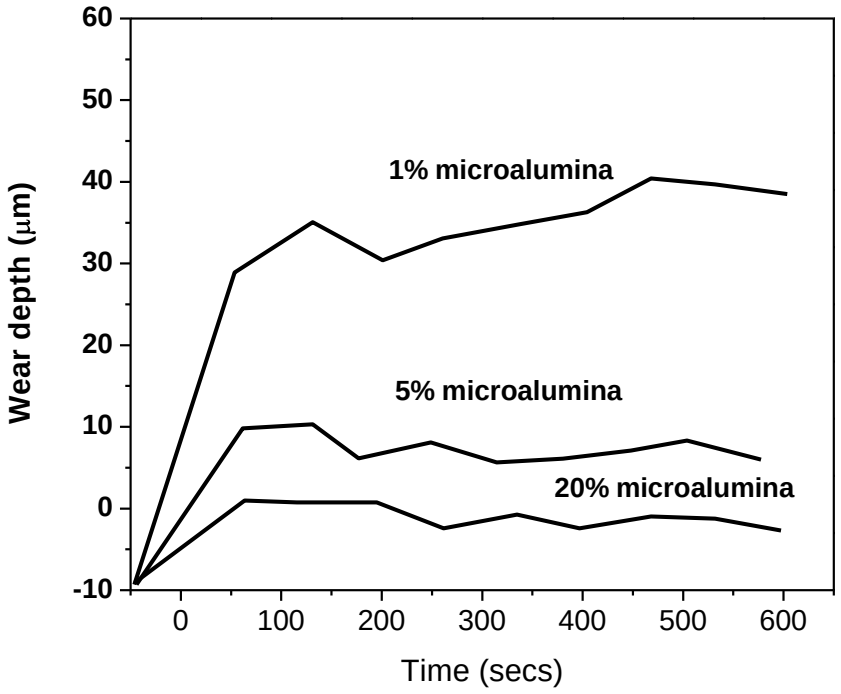

Fig. 3.2.45 Wear depth vs. time plot for Cu-Al_2O_3 microcomposites sintered by SPS

It has also been found that wear resistance increases as the alumina content increases in both the cases due to hard and brittle nature of alumina reinforcement. Alumina particles support contact stresses and prevent plastic deformation. The wear resistance of the specimens is in accordance with the hardness trends. In some cases negative slopes can be seen from wear depth vs. time plot. This may be due to the welding of the soft copper phase with the steel ball (indenter) which results in decrease in wear depth [44].

3.2.3.3a.2.2 Wear track

The wear tracks of Cu-Al_2O_3 nano- and micro-composites have been illustrated in Fig. 3.2.46 (a)-(d). The wear track of Cu-1vol. % Al_2O_3 nanocomposite is wider as compared to Cu-5 vol. % Al_2O_3 nanocomposite.

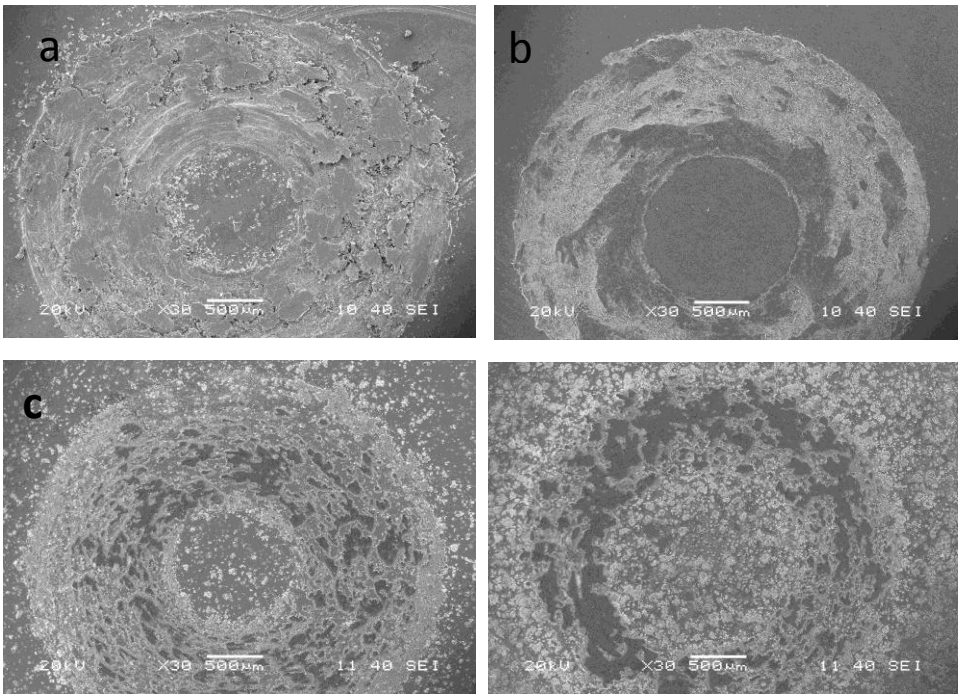

Fig. 3.2.46 SEM micrographs of the worn surfaces showing wear track of (a) Cu-1 vol. % Al_2O_3 and (b) Cu-5 vol. % Al_2O_3 nanocomposite, (c) Cu-5 vol. % Al_2O_3 and (d) Cu-20 vol. % Al_2O_3 microcomposite

The wear track of nanocomposite with low content of alumina has been observed to get more eroded in comparison to higher content of alumina.

The wear track of microcomposites is narrower than that of nanocomposites. The reason could be attributed to the fact that the alumina microparticles being larger in size, do not allow the wear indenter to erode the surface continuously. The alumina nanoparticles are hard but the surface exposed to the wear indenter is quite small to prevent erosion.

3.2.3.3a.2.3 Wear rate and volume

The wear rate and volume have been plotted against volume content of alumina in Fig. 3.2.47 (a) & (b). The wear rate and volume have been calculated using the following equations [45]

Wear volume (mm^3) = 2π x track radius x track width x wear depth (III)

Wear rate ($mm^3N^{-1}m^{-1}$) = wear volume / (normal load x sliding distance) (IV)

The wear rate and volume of micro- and nano-composites follow the same trend. The wear rate decreases as the amount of alumina increases in the composites. The steel ball indenter-copper matrix contact causes erosion from the surface which gets minimized as the alumina content increases. Hence the metal-ceramic contact results in higher wear resistance and lower wear rate and volume.

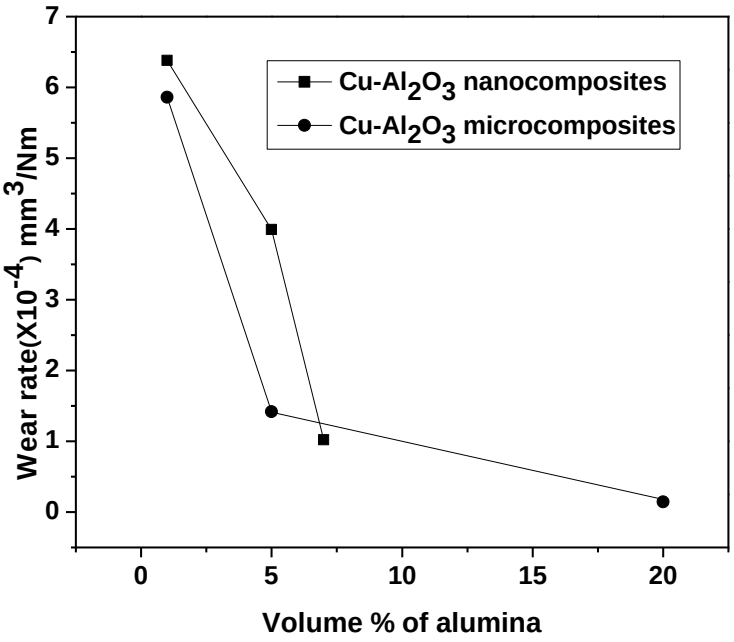

Fig. 3.2.47(a) Wear rate vs. volume % of alumina of the Cu-Al_2O_3 composites

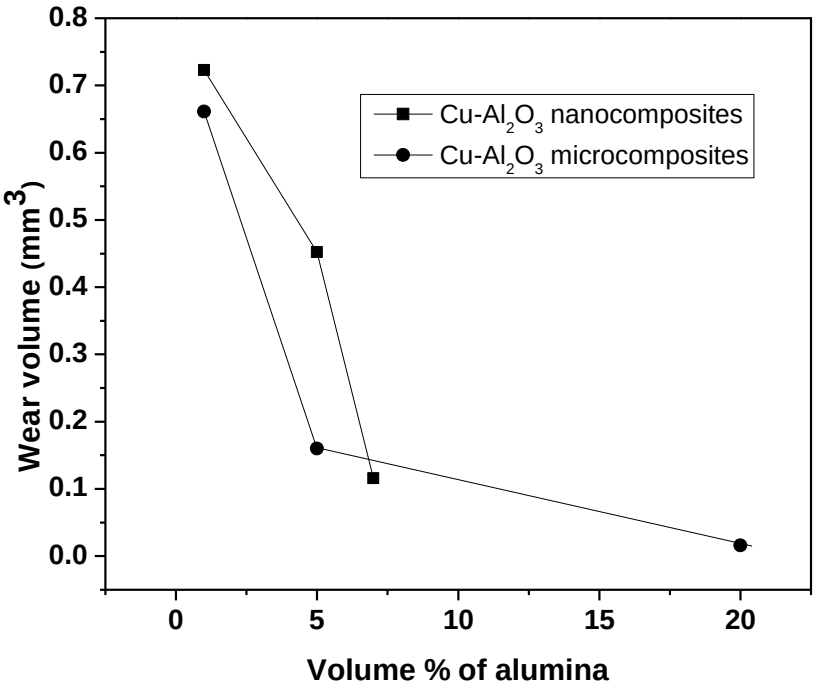

Fig. 3.2.47(b) Wear rate vs. volume % of alumina of the Cu-Al_2O_3 composites

3.2.3.3a.2.4 Wear mechanism

To have an idea about wear mechanism, worn surface was studied under SEM. The SEM micrographs of worn surfaces of microcomposites show formation of grooves (Fig. 3.2.48 (a)) by shearing action of friction. Fig. 3.2.48 (b) shows pores on the worn surface after particle pull-out which results in minimized effective contact area between sample and indenter increasing stress [44].

The wear mechanisms at low loads mostly are grooving and microploughing [46]. The wear mechanisms operating in nanocomposites show delamination and microploughing (Fig. 3.2.48 (c) & (d)) [47]. Large flakes of delaminated material can be observed in Fig. 3.2.48 (c). The wear debris in process of microploughing can be seen in Fig. 3.2.48 (d) which is in the form of spherical nanoparticle-agglomerates [44]. Plastic deformation leads to plastic instability resulting in crack formulation [48]. Microcracks can be observed in Fig. 3.2.49 (left).

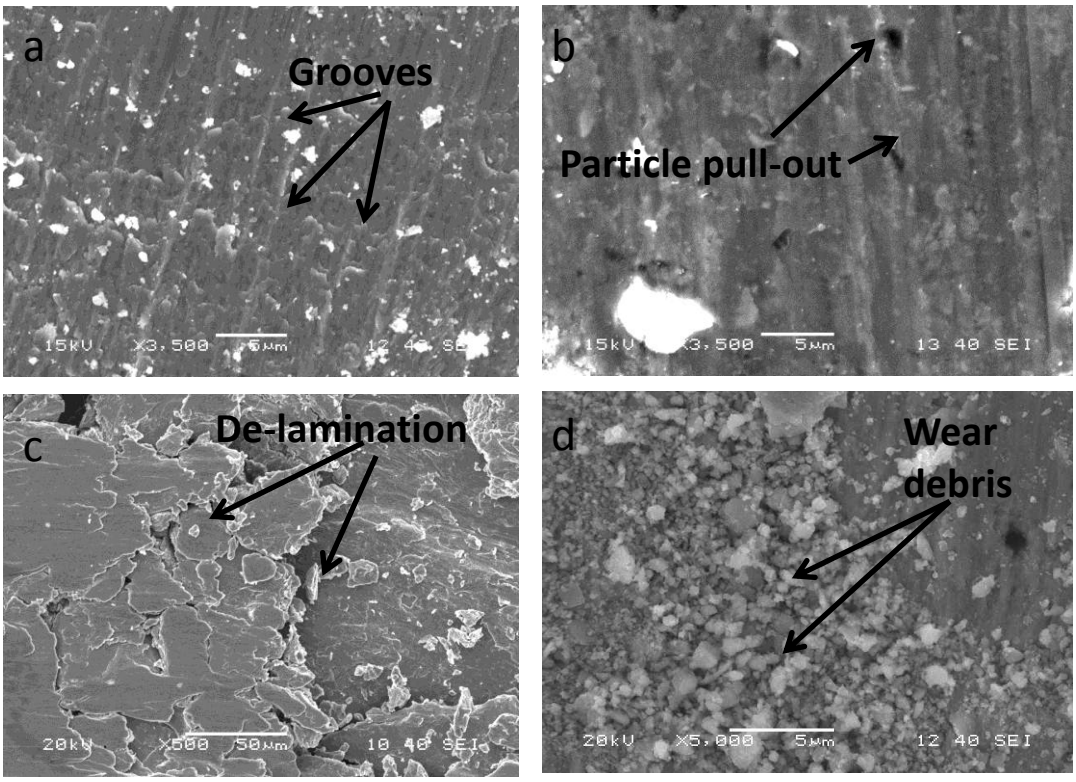

Fig. 3.2.48 SEM micrographs of worn surfaces of (a) Cu-5 vol. % Al_2O_3 nanocomposite, (b) Cu-5 vol. % Al_2O_3 microcomposite, (c) Cu-1 vol. % Al_2O_3 nanocomposite, (d) Cu-5 vol. % Al_2O_3 nanocomposite

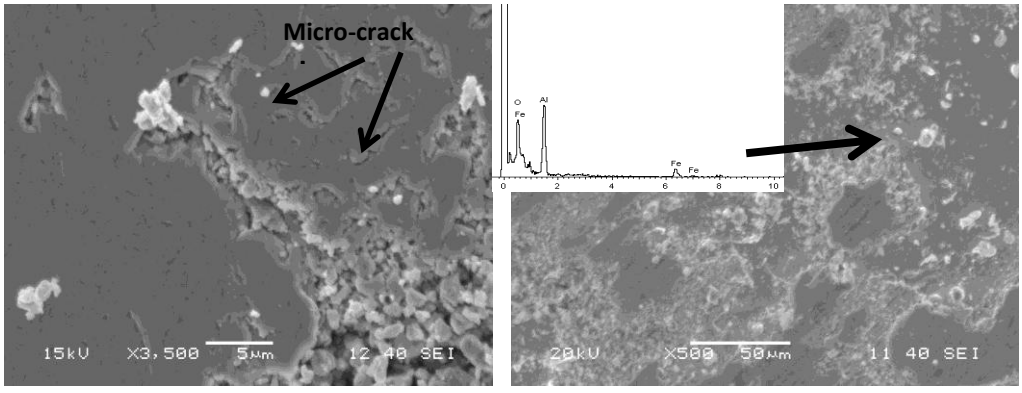

Fig. 3.2.49 SEM micrographs of worn surfaces of Cu-7 vol. % Al_2O_3 nanocomposite (left) Cu-20 vol. % Al_2O_3 microcomposite along with EDS analysis (right)

Fig. 3.2.48 (right) shows SEM micrograph of worn surface and corresponding EDS spectra. The EDS spectrum shows the presence of Fe on the worn surfaces of microcomposite which attribute wear of steel ball by hard and brittle alumina particles. The formation of tribolayer has also been observed with microcomposites as well as low concentration of alumina in nanocomposites [49]. The adhesive wear action could be seen by the presence of wear debris sliding from one site to another on the composite. The abrasive wear mechanism was evident by the presence of iron particles in the wear debris of the composites. The wear rate of copper-7.5% alumina reinforced Cu investigated by Fathy et al.[15] has been reported as higher than $2x10^{-4}$ g/m whereas in our experiments we have obtained $1x10^{-4}$ mm^3/Nm for copper-7 vol. % alumina.

3.2.3.3a.2.5 Wear debris

The wear debris of microcomposites shows flakes whereas the wear debris of nanocomposites is spherical in shape (Fig. 3.2.50 & 3.2.51). The nature of wear debris is different in micro- and nano-composites due to the higher deformability of microcomposites because of presence of less hard alumina microparticles in comparison to nanoparticles.

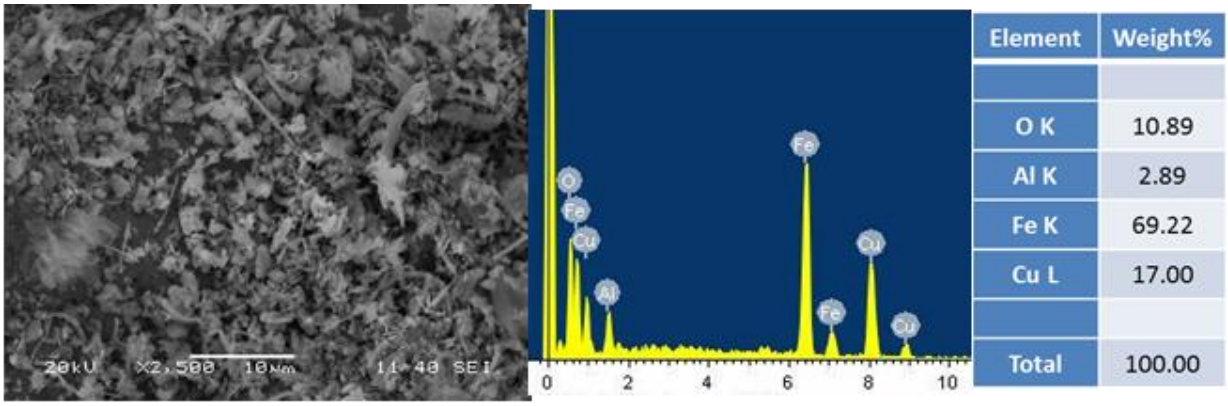

Fig. 3.2.50 SEM micrograph of the worn surfaces showing wear debris of Cu-5 vol. % Al_2O_3 microcomposite (left), EDS of the whole micrograph (right)

The wear debris formation may be attributed to the fact that copper being soft in nature gets eroded by the steel ball indenter, thereby exposing the alumina particles to the surface. The wear debris of microcomposites was analyzed for element detection by the help of EDS. The EDS

analysis showed that the wear debris of microcomposite contains higher content of iron than that of nanocomposites (Fig. 3.2.50).

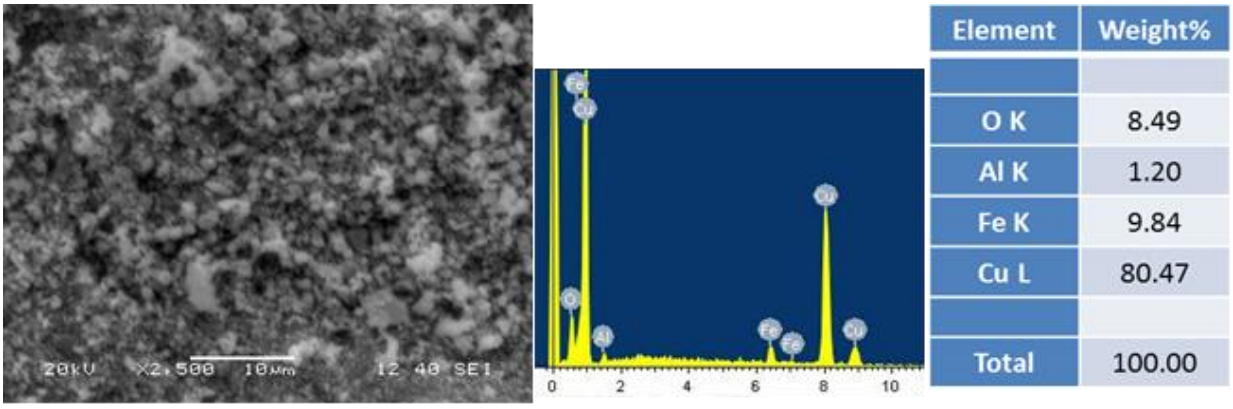

Element	Weight%
O K	8.49
Al K	1.20
Fe K	9.84
Cu L	80.47
Total	100.00

Fig. 3.2.51 SEM micrograph of worn surfaces of Cu-5 vol. % Al_2O_3 nanocomposite (left), EDS of the whole micrograph (right)

This observation points towards the fact that the abrasion of wear indenter with microcomposites is higher than nanocomposites. The abrasive wear actions of the composites lead to the abrasion of the steel ball wear indenter.

3.2.3.3b Aluminium-alumina composite

3.2.3.3b.1 Density measurement

The density measurements exhibit close values to % of theoretical density for microcomposites and nanocomposites (Table 3.2.4). The microcomposites exhibit poor bonding and compatibility of alumina in the aluminium matrix. The % of theoretical density of microcomposites and nanocomposites falls as the volume of alumina increases. The density values of 5 vol. % alumina reinforced microcomposite are higher than the corresponding nanocomposite density values. The underlying reason could be that the compressibility of hard nanoparticles in a ductile matrix is tedious. The compressibility of hard and non-deformable particles in a ductile matrix decreases with increasing content of the hard particles (reinforcements) [50]. Moreover the formation of networks also retards compaction. This is the same reason for which the density plot shows a steep fall from 1 to 5 vol. % of alumina.

Composition (alumina content in wt. %)	% theoretical density	Microhardness (GPa)	Nanoindentation hardness (GPa)
Nanocomposites			
0.5	95.5	0.36±0.02	
1	99.5	0.32±0.01	0.60±0.07
3	90.1	0.35±0.01	
5	93.6	0.51±0.06	0.49±0.07
7	93.6	0.38±0.03	0.85±0.14
Microcomposites			
1	98.8	0.37±0.01	
5	97.1	0.46±0.04	
20	92.5	0.55±0.02	

Table 3.2.4 % of theoretical density, microhardness and nanoindentation hardness values of Al-Al_2O_3 micro- and nano-composites

The density data for nanocomposites are scattered but the trend of density values with increasing amount of reinforcement is negative. This can be attributed to the plastic deformation of aluminium particles through particle contact during compaction. The higher alumina content increases alumina-alumina contact which impedes the deformability of aluminium particles [51]. Hence, the densification trend shows a downfall with the increase in alumina content. The major concern of nanoparticles is agglomeration as well as the tendency to form interconnected networks. The problem of agglomeration in nanoparticles leads to lesser densification in nanocomposites whereas this does not impair the densification of microcomposites to a larger extent. This is due to the fact that the specific surface of coarser particles is lower and the powder compressibility is higher [52]. Rahimian et al. [29] have obtained 96.8% of relative density for Al-10 wt. % Al_2O_3 conventionally sintered at 500°C where as we have reported

98.8% for Al-1 vol. %Al_2O_3 microcomposite and 99.5% relative density for Al-1 vol. %Al_2O_3 nanocomposite.

3.2.3.3b.2 Microhardness and nanohardness measurements

The microhardness measurements show high hardness values for nanocomposites than for microcomposites which are visible in Table 3.2.4. In case of nanocomposites hardness increases upto 5 vol. % of alumina due to the positive effect of dispersion strengthening but after that it decreases due to agglomeration of nanoparticles. The micron sized particles have lower tendency to agglomerate compared to nanoparticles hence, it is attributed to the effect of positive dispersion strengthening. The micron-sized particles were inefficient to pin down the grain growth of the aluminium grains compared to the alumina nanoparticles. Agglomeration of nanoparticles results in the increase of interparticle distance subsequently reducing the particle-dislocation interaction. Moreover less strength is required to move a dislocation where the interparticle distance is large. The nanoparticles possess high yield stress and are sensitive to work hardening so render lesser compressibility. Hence, nanocomposites possess higher microhardness (for 5 vol. %) referring to greater hardening response [51]. The grain growth stagnation in nanocomposites occurs due to Zener effect [53]. Solute segregation is another method for grain growth stagnation. Since the alumina particles are hard and in nanoscale range, high energy is required for the movement of dislocations when they encounter a hard nanoparticle (Dieter, 1976).

$$\tau_0 = \frac{Gb}{\lambda} \qquad (4)$$

where τ_0 is the stress required for a dislocation to pass reinforcement, G is the shear modulus of the material and b is the burger vector of the dislocation. It is very difficult to make exact comparison of microstructure and mechanical properties of composites fabricated by conventional sintering and present SPS method as the processing parameters and raw materials sizes are different. However, we have achieved higher hardness at lower processing temperature and time as compared to conventional sintering [29].

The nanohardness values of the nanocomposites are higher than the corresponding microhardness values (Table 3.2.4). This could be attributed to the indentation size effect explained by Mukhopadhyay and Paufler [41]. In microhardness measurements the hardness values of microcomposites (for 5 vol. % of alumina) is lower than that of nanocomposites. The enhanced strength of the nanocomposites can be attributed to the stronger diffusional bonds and structural integrity achieved due to greater diffusional activity [54] by sintering the alumina nanoparticles and aluminium matrix particles by spark plasma sintering. The highest value of microhardness is revealed by the 20 vol. % alumina reinforced microcomposite. The highest amount of alumina could be the reason for the highest value of microhardness.

3.2.3.3b.3 Wear study

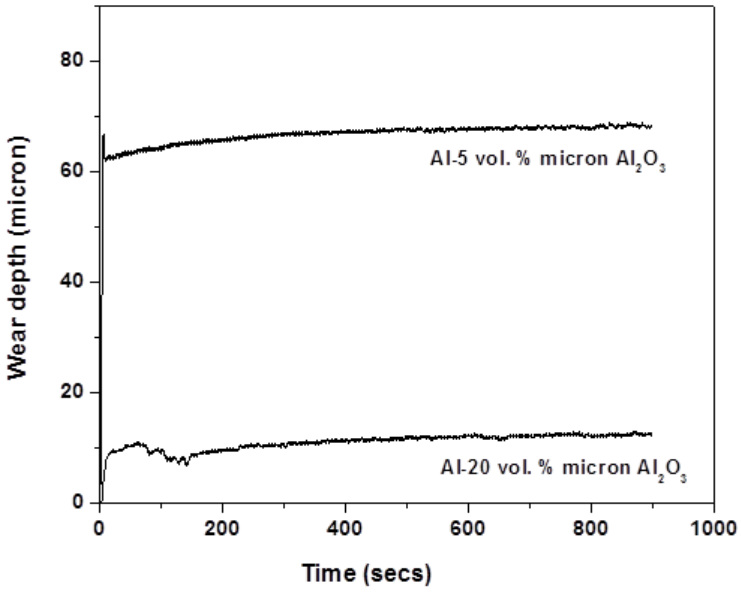

Fig. 3.2.52 Wear depth vs time profile for Al-Al_2O_3 microcomposites fabricated by spark plasma sintering

Fig. 3.2.52 & 3.2.53 demonstrate the wear depth vs time graphs for Al-Al_2O_3 micro- and nano-composites fabricated by spark plasma sintering. The wear depth is higher for nanocomposites than microcomposites. The microcomposites show better wear resistance than nanocomposites which could be attributed to the fact that the microcomposites contain alumina microparticles and as wear is a surface phenomenon the microparticles have higher surface exposed to the wear

indenter compared to nanoparticles. Hence, the microparticles prevented the wear indenter to erode the matrix to a higher degree compared to the nanoparticles.

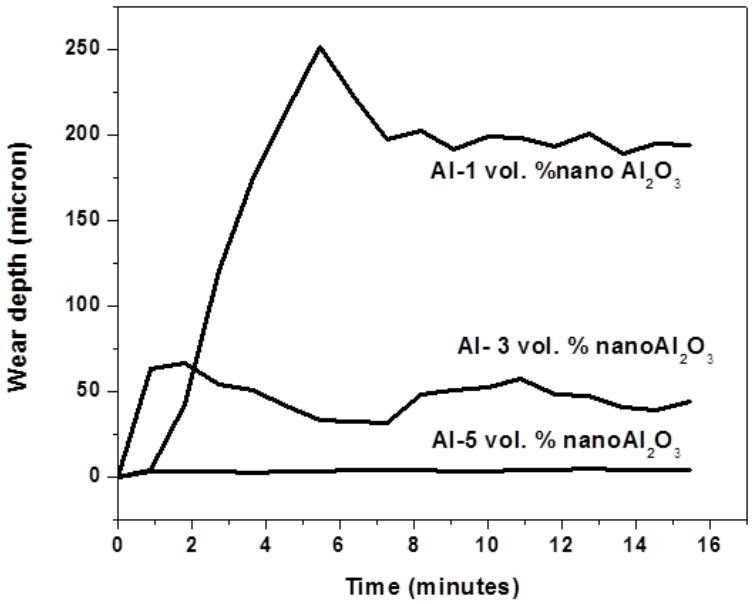

Fig. 3.2.53 Wear depth vs time profile for Al-Al_2O_3 nanocomposites fabricated by spark plasma sintering

Fig. 3.2.54 (a & b) illustrates the wear tracks of Al-Al_2O_3 microcomposites and nanocomposites respectively. The wear tracks reveal low wear resistance for nanocomposites.

The Al-20 vol. % Al_2O_3 microcomposite showed a narrow wear track than for Al-5 vol. % Al_2O_3 nanocomposite. Fig. 3.2.55 showed wear mechanisms operating in micro- and nano-composites. The nanocomposites seem to have got eroded proficiently creating microcracks and distinct delamination was visible for microcomposites.

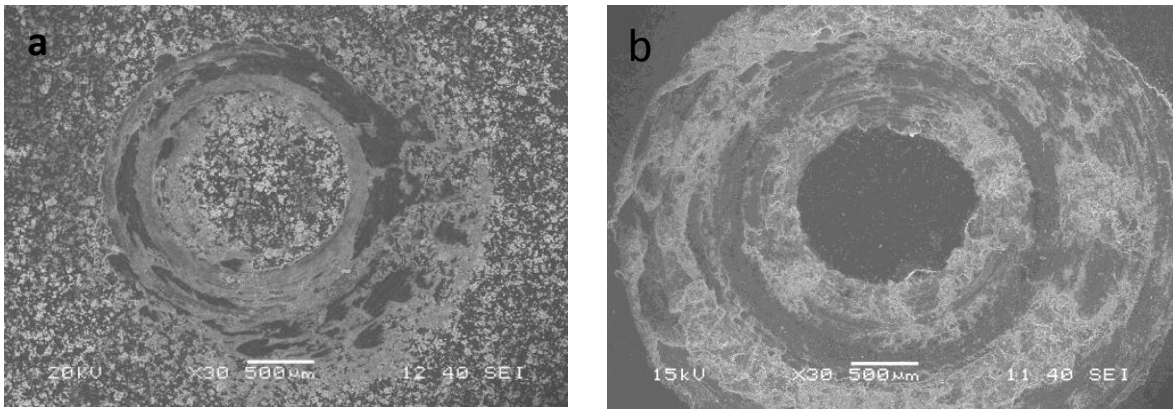

Fig. 3.2.54 SEM micrographs of worn out surface of (a) Al-20 vol. % Al_2O_3 microcomposite and (b) Al-5 vol. % Al_2O_3 nanocomposites fabricated by spark plasma sintering

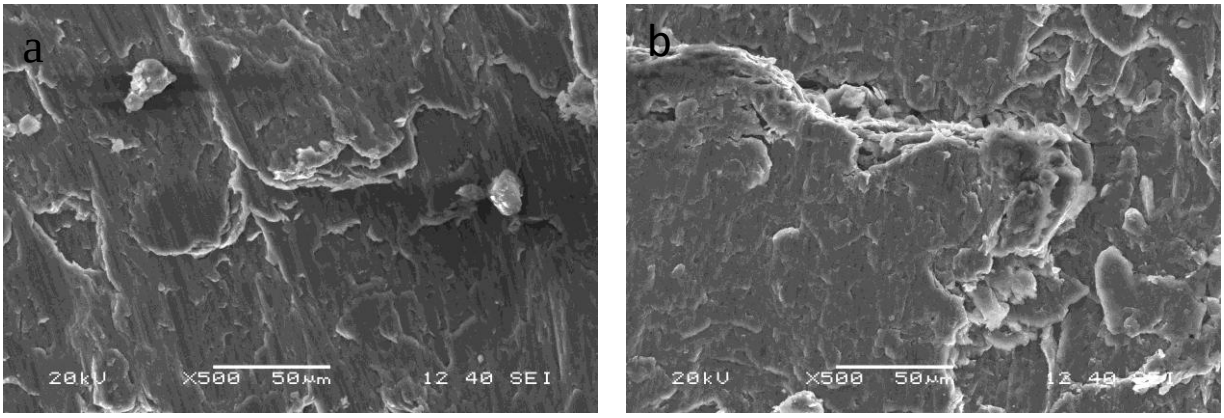

Fig. 3.2.55 SEM micrographs of worn out surface of (a) Al-1 vol. % Al_2O_3 microcomposite and (b) Al-1 vol. % Al_2O_3 nanocomposites fabricated by spark plasma sintering

3.2.4 Summary and Conclusions

The Cu-Al_2O_3 and Al-Al_2O_3 micro- and nano-composites were fabricated by blend-compact-sinter powder metallurgy route at different sintering temperatures. The microcomposites possess better properties (density and hardness) at higher sintering temperatures. In nanocomposites density and hardness are better at lower sintering temperatures. The incorporation of Al_2O_3 nanoparticles strengthens the matrix to a greater extent resulting in increase of microhardness compared to Al_2O_3 microparticles. The microstructures of micro- as well as nano-composites demonstrate better distribution in the later. Compressive strength is highest for the Cu-15 vol. % Al_2O_3 microcomposites. The flexural modulus of nanocomposites is higher as compared to the microcomposites. Fractography of the microcomposites and nanocomposites revealed mixed mode of fracture in both the cases. The wear resistance of nanocomposites is higher than the microcomposites under the same experimental conditions. The rise in reinforcement content imparts higher microhardness, low density and high wear resistance values for both the systems.

Cu-Al_2O_3 and Al-Al_2O_3 micro-(1, 5, 20 vol. %) and nano-(0.5, 1, 3, 5, 7 vol. %) composites were fabricated by spark plasma sintering technique. XRD analysis shows the presence of Cu, Al_2O_3 and $CuAlO_2$ in both the micro- as well as nano-composites. The SEM micrographs show the presence of annealing twins during fabrication by SPS in both nano and micro-composites. TEM micrographs suggest the formation of a third phase i.e. $CuAlO_2$ (copper aluminate) around the alumina particles. The hardness measurements show that the nanocomposites are harder than microcomposites. The wear resistance of microcomposites is higher than the nanocomposites. The possible wear mechanisms for both composites are microploughing, delamination as well as microcrack formation. The wear mechanisms operating in the micro- and nano-composites is dominated by the reinforcement particle size effect and their implications. We have obtained 95.82% densification and 93.17 HV hardness for spark plasma sintered Cu-20 vol. % Al_2O_3 microcomposite. The elastic modulus of Cu-1% alumina nanocomposite is obtained as 128 GPa. The wear rate is appreciably low i.e. 0.86 x 10^{-4} $mm^3N^{-1}m^{-1}$ for 20 vol. % alumina reinforced copper microcomposite.

The distribution of alumina particles in the aluminium matrix is homogeneous and uniform both in nanocomposites and microcomposites (slightly better distribution in nanocomposites than microcomposite). The interface of aluminium and alumina in nanocomposites is seemingly sound than in the case of microcomposite i.e. the compatibility of alumina in aluminium matrix in nanocomposites is better than in the microcomposites. The TEM and SEM micrographs reveal a lack of intimate proximity between matrix and reinforcement entities in microcomposites. Almost full densification in case of 1 vol. % alumina reinforced nano- and microcomposites have been achieved. The density of microcomposites as well as nanocomposites decreases with increasing alumina content. The nanohardness of nanocomposites is higher than the corresponding microhardness values. The highest nanohardness recorded was 0.85 GPa for 7 vol. % Al-Al_2O_3 nancomposites.

References

[1] H. Ghasemi, A.H. Kohabi, M.A.F. Sani, Z. Riazi, Alumina-copper eutectic bond strength: contribution of preoxidation, cuprous oxides particles and pores, *Mater. Forum* 32 (**2008**) 90-97.

[2] A. Slipenyuk, V. Kuprin, Y. Milman, V. Goncharuk, J. Eckert, Properties of P/M processed particle reinforced metal matrix composites specified by reinforcement concentration and matrix-to-reinforcement particle size ratio, *Acta. Mater*. 54 (1) (**2006**) 157-166.

[3] R.W. Hertzberg, Deformation and Fracture Mechanics of Engineering Materials, John Wiley and Sons Inc., Canada, fourth edition, **1996**.

[4] M. Korac, Z. Kamberovic, M. Tasic, M. Gavrilovski, Nanocomposite powders for new contact materials based on copper and alumina, *Chem. Ind. Chem. Eng. Q* 14 (4) (**2008**) 215-218.

[5] K. Dash, B.C. Ray, D. Chaira, Synthesis and characterization of copper-alumina metal matrix composite by conventional and spark plasma sintering, *J. Alloy. Compd.* 516 (**2012**) 78-84.

[6] G.S Upadhaya, Future directions in sintering research, *Sci. Sinter.* 43 (**2011**) 3-8.

[7] G.C. Efe, T. Yener, I. Altinsoy, M. Ipek, S. Zeytin, C. Bindal, The effect of sintering temperature on some properties of Cu-SiC composite, *J. Alloy. Compd*. 509 (20) (**2011**) 6036-6042.

[8] F. Shehata, A. Fathy, M. Abdelhameed, S.F. Moustafa, Fabrication of copper-alumina nanocomposites by mechano-chemical routes, *J. Alloy. Compd.* 476 (1) **(2009**) 300-305.

[9] W.M. Daoushb, B.K. Lim, C.B. Mo, D.H. Nam, S.H. Hong, Electrical and mechanical properties of carbon nanotube reinforced copper nanocomposites fabricated by electroless deposition process, *Mater. Sci. Eng. A* 513-514 (**2009**) 247-253.

[10] V. Rajkovic, D. Bozic, M.T. Jovanovic, Properties of copper matrix reinforced with various size and amount of Al_2O_3 particles, *J. Mater. Process. Technol*. 200 (1) (**2008**) 106-114.

[11] B. Tian, P. Liu, K. Song, Y. Li, Y. Liu, F. Rena, J. Sua, Microstructure and properties at elevated temperature of a nano-Al_2O_3 particles dispersion-strengthened copper base composite, *Mater. Sci. Eng. A* 435-436 (**2006**) 705-710.

[12] S.C. Tjong, K.C. Lau, Tribological behaviour of SiC particle-reinforced copper matrix composites**,** *Mater. Lett.* 43 (5) (**2000**) 274-280.

[13] Z.H. Tan, B.J. Pang, D.T. Qin, J.Y. Shi, B.Z. Gai, The compressive properties of 2024Al matrix composites reinforced with high content SiC particles at various strain rates**,** *Mater. Sci. Eng. A* 489 (1) **(2008**) 302-309.

[14] R. Fernandez, G. Bruno, G. Gonzalez-Doncel, Residual stress evolution with compressive plastic deformation in 6061Al-15 vol.% SiC_w composites as studied by neutron diffraction**,** *Mater. Sci. Eng. A* 403 (1) (**2005**) 260-268.

[15] A. Fathy, F. Shehata, M. Abdelhameed, M. Elmahdy, Compressive and wear resistance of nanometric alumina reinforced copper matrix composites. *Mater. Des*. 36 (**2012**) 100-107.

[16] F. Akhtar, S.J. Askari, K.A. Shah, X. Du, S. Guo, Microstructure, mechanical properties, electrical conductivity and wear behaviour of high volume TiC reinforced Cu-matrix composites, *Mater. Charact*. 60 (4) (**2009**) 327-336.

[17] A. Rabiei, L. Vendra, T. Kishi, Fracture behavior of particle reinforced metal matrix composites, *Composites: Part A* 39 (2) (**2008**) 294-300.

[18] ASM Handbook Committee, ASM Handbook Vol. 12, Fractography, ASM International-The materials information company, **1987**.

[19] C.S. Ramesh, R.N. Ahmed, M.A. Mujeebu, M.Z. Abdullah, Development and performance analysis of novel cast copper–SiC–Gr hybrid composites**,** 2009 *Mater. Des.* 30 (6) (**2009**) 1957-1965.

[20] K.P. Trumble, Prediction of a critical temperature for aluminate formation in alumina/copper–oxygen eutectic bonding, *J. Am. Ceram. Soc.* 82 (10) (**1999**) 2919-2920.

[21] C.W. Seager, K. Kokini, K. Trumble, M.J.M Krane, The influence of $CuAlO_2$ on the strength of eutectically bonded Cu/Al_2O_3 interfaces, *Scripta. Mater* 46 (5) (**2002**) 395-400.

[22] S.T Kim, C.H. Kim, Interfacial reaction product and its effect on the strength of copper to alumina eutectic bonding. *J. Mater. Sci***.** 27 (**1992**) 2061-2066.

[23] A.M. Hassan, A. Alrashdan, M.T. Hayajneh, A.T. Mayyas. Wear behavior of Al-Mg-Cu-based composites containing SiC particles. *Tribol. Int*. 42 (8) (**2009**) 1230-1238.

[24] A. Afshar, A. Simchi, Flow stress dependence on the grain size in alumina dispersion-strengthened copper with a bimodal grain size distribution. *Mat. Sci. Eng. A*. 518 (1) (**2009**) 41-46.

[25] Z.R. Hesabi, A. Simchi, S.M.S. Reihani, Structural evolution during mechanical milling of nanometric and micrometric Al_2O_3 reinforced Al matrix composites, *Mat. Sci. Eng. A* 428 (1) (**2006**) 159-168.

[26] J. Tian, K. Shobu, Hot-pressed AlN-Cu metal matrix composites and their thermal properties, *J. Mater. Sci.* 39 (**2004**) 1309-1313.

[27] A. Kostka, J. Lelatko, M. Gigla, H. Morawiec, A. Janas, TEM study of the interface in ceramic-reinforced aluminium-based composites. *Mat. Chem. Phy.* 81 (2) (**2003**) 323-325.

[28] A. Kelly, C. Zweben, Comprehensive Composite Materials, Elsevier Science Ltd., United Kingdom, Vol. 3, first edition, **2000**, pp. 139-149.

[29] M. Rahimian, N. Ehsani, N. Parvin, H.R. Baharvandi, The effect of particle size, sintering temperature and sintering time on the properties of $Al\text{-}Al_2O_3$ composites, made by powder metallurgy, *J. Mater. Process. Technol*. 209 (14) (**2009**) 5387-5393.

[30] M. Rahimian, N. Parvin, N. Ehsani, The effect of production parameters on microstructure and wear resistance of powder metallurgy Al-Al_2O_3 composite, *Mater. Design* 32 (2) (**2011**) 1031-1038.

[31] E.A. Olevsky, L. Froyen, Impact of thermal diffusion on densification during SPS, *J. Am. Ceram. Soc*. 92 (1) (**2009**) 122-132.

[32] Z.A. Munir, D.V. Quach, M. Ohyanagi, Electric Current Activation of Sintering: A Review of the Pulsed Electric Current Sintering Process, *J. Am. Ceram. Soc.* 94 (1) (**2011**) 1-19.

[33] G. Xie, O. Ohashi, M. Song, K. Furuya, T. Noda, Behavior of Oxide Film at the Interface between Particles in Sintered Al Powders by Pulse Electric-Current Sintering, *Mett. Trans. A* 34 (**2003**) 699-703.

[34] T.G. Durai, K. Das, S. Das, Synthesis and characterization of Al matrix composites reinforced by in situ alumina particulates, *Mat. Sci. Eng. A* 445–446 (**2007**) 100–105.

[35] J.W. Edington, Interpretation of transmission electron micrographs, Macmillan, London, **1975**.

[36] G.E. Dieter, Mechanical Metallurgy, McGraw-Hill, London, United Kingdom, Third Edition **1988**.

[37] T. Zhang, Q. Meng, Y. Wang, Y. Zhou, G. Song, Dislocation behavior in ZrC particles during elevated temperature compressive deformation of a 30 vol.% ZrCp/w composite, *J. Mater. Sci. Technol*. 27 (**2011**) 553-558.

[38] H. Wang, G. Li, Y. Zhao, G. Chen, In situ fabrication and microstructure of Al_2O_3 particles reinforced aluminium matrix composites**,** *Mat. Sci. Eng. A* 527 (**2010**) 2881-2885.

[39] A. Fais, M. Leoni, P. Scardi, Fast Sintering of Nanocrystalline Copper, *Metall. Mater. Trans. A.* 43 (**2012**) 1517-1521.

[40] C.A. Leon, G. Rodriguez-Ortiz, E.A. Aguilar-Reyes, Cold compaction of metal-ceramic powders in the preparation of copper base hybrid materials, *Mat. Sci. Eng. A* 526 (1) (**2009**) 106-112.

[41] N.K. Mukhopadhyay, P. Paufler, Micro and nanoindentation techniques for mechanical characterization of materials, *Int. Mater. Rev.* 51 (**2006**) 209-245.

[42] I.E. Reimanis, K.P. Trumble, K.A. Rogers, B.J. Dalgleish, Influence of Cu_2O and $CuAlO_2$ interphases on crack propagation at Cu/α-Al_2O_3 interfaces, *J. Am. Ceramic. Soc.* 80 (**1997**) 424-432.

[43] S. Chung, B.H. Hwang, A microstructural study of the wear behaviour of SiC_p/Al composites**,** *Tribol. Int*. 27 (5) (**1994**) 307-314.

[44] G. Parida, D. Chaira, M. Chopkar, A. Basu, Synthesis and characterization of Ni-TiO_2 composite coatings by electro-co-deposition**,** *Surf. Coat. Technol*. 205 (21) (**2011**) 4871-4879.

[45] A. Jain, B. Basu, B.V.M. Kumar, H. Vardhan, J. Sarkar, Grain size-wear rate relationship for titanium in liquid nitrogen environment**,** *Acta. Mater.* 58 (7) (**2010**) 2313-2323.

[46] M. Hashempour, H. Razavizadeh, H. Rezaie, Investigation on wear mechanism of thermochemically fabricated W-Cu Composites, *Wear* 269 (**2010**) 405-415.

[47] J. Hemanth, Abrasive and slurry wear behaviour of chilled aluminium alloy (A356) reinforced with fused silica (SiO_{2p}) metal matrix composites, *Composites Part B* 42 (**2011**) 1826-1833.

[48] J. Jiang, F.H. Stott, M.M. Stack, A mathematical model for sliding wear of metals at elevated temperatures**,** *Wear* 181-183 (**1995**) 20-31.

[49] S.G. Sapate, A. Uttarwar, R.C. Rathod, R.K. Paretkar, Analyzing dry sliding wear behaviour of copper matrix composites reinforced with pre-coated SiC_p particles, *Mater. Design* 30 (**2009**) 376-386.

[50] C.A. Leon, G. Rodriguez-Ortiz, E.A. Aguilar-Reyes, Cold compaction of metal-ceramic powders in the preparation of copper base hybrid materials, *Mat. Sci. Eng. A* 526 (**2009**) 106-112.

[51] S.S. Razavi-Tousi, R. Yazdani-Rad, S.A. Manafi, Effect of volume fraction and particle size of alumina reinforcement on compaction and densification behaviour of Al-Al_2O_3 nanocomposites**,** *Mat. Sci. Eng. A.* 528 (3) (**2011**) 1105-1110.

[52] D. Roy, A. Sinha, P.P. Chattopadhyay, I. Manna, Nanoindentation behaviour of bulk metastable $Al_{65}Cu_{20}Ti_{15}$ alloy prepared by consolidation of the ball milled powder**,** *Mat. Sci. Eng. A* 528 (28) (**2011**) 8047-8050.

[53] Z.R. Hesabi, A. Simchi, S.M.S. Reihani, Structural evolution during mechanical milling of nanometric and micrometric Al_2O_3 reinforced Al matrix composites**,** *Mat. Sci. Eng. A* 428 (1) (**2006**) 159-168.

[54] S.K. Karak, J.D. Majumdar, W. Lojkowski, A. Michalski, L. Ciupinski, K.J. Kurzydłowski, I. Manna, Microstructure and mechanical properties of nano-Y_2O_3 dispersed ferritic steel synthesized by mechanical alloying and consolidated by pulse plasma sintering, *Philos. Mag.* 92 (**2012**) 516-534.

3.3 Effect of thermal and cryogenic conditioning on flexural behaviour of thermally shocked Cu-Al_2O_3 and Al-Al_2O_3 micro- and nano-composites

3.3.1 Scope and Objectives of the work

This investigation has used flexural test to explore the effect of thermal treatments i.e. high temperature and cryogenic environments on the mechanical property of Al_2O_3 particulate reinforced Cu and Al metal matrix micro- and nano-composites in ex-situ and in-situ conditions. Cu- Al_2O_3 and Al-Al_2O_3 reinforced with 5, 10, 15, 20 vol. % Al_2O_3 micro- (~10μm) and 1, 3, 5, 7 vol. % Al_2O_3 nano- (<50 nm)composites were fabricated by powder metallurgy route. Both the micro- and nano-composites were treated at +40°C temperature for 1 hour followed by -40°C temperature for 1 hour. This treatment was also done in the reverse order i.e. from -40°C to +40°C. The above stated thermal shock module was repeated with temperatures (+80°C to -80°C) and (-80°C to +80°C) with both micro- and nano-composites with 1 hour isothermal holding at each temperature. For thermal conditioning the micro- and nano-composites were exposed to +80°C for 1 hour and -80°C for 1 hour separately. High temperature 3- point bend test was performed at 100°C and 250°C for the composites after temperature attainment. All the micro- and nano-composites subjected to thermal shock, thermal conditionings were tested in flexural mode at a span length of 26 mm and loading rate of 0.5 mm/min. The micro- and nano-composites were also tested at ambient temperature to note the difference after the thermal treatments. The fractured samples were studied under field emission scanning electron microscopy. All the fractured samples obtained after various thermal treatments were studied under scanning electron microscope (SEM). The development of thermal stresses quite often results in concentration of residual stresses at the particle/matrix interface eventually weakening it. Enhancement of flexural strength was recorded for down- as well as for up-thermal shock in microcomposites. The high temperature flexural strength of micro- and nano-composites is lower than that at ambient temperature. The amelioration and declination in mechanical properties as a consequence of thermal shock, thermal conditioning and high temperature flexural testing have been discussed in the light of fractography. The objective of this investigation is to assess the

variation in mechanical property with the thermal treatments, but not so much emphasis on evaluating the absolute values of mechanical properties. The absolute value of different properties might differ with the route of fabrication techniques.

3.3.2 Fabrication of composites

3.3.2a Copper-alumina composite

Copper powder (Loba Chemie) (average particle size~11μm, purity >99.7%) was used as the matrix material. Alumina powders (Sigma Aldrich, purity >99.7%)) (average particle size~10μm and < 50 nm) were selected as the reinforcement material. The Cu with 5, 10, 15, 20 vol. % Al_2O_3 (10 μm) microcomposites and Cu with 1, 3, 5, 7 vol. % Al_2O_3 (< 50 nm) nanocomposites powders were blended separately. The specimens having dimensions (31.5 x 12.7 x 6.3 mm^3) were prepared by compacting the powders at a pressure of 500 MPa as per ASTM B 925-08 for 3-point flexural test. The compacted specimens were sintered conventionally at 900°C for 90 minutes in argon atmosphere.

3.3.2b Aluminium-alumina composite

Aluminium powder (Loba Chemie) (average particle size~22μm, purity- >99.7%) was used as the matrix material. Alumina powders (Sigma Aldrich, purity >99.7%)) (average particle size~10μm and < 50 nm) were selected as the reinforcement material. The Al- 5, 10, 20 vol. %Al_2O_3 (10 μm) microcomposites and Al- 1, 3, 5 vol. % Al_2O_3 (< 50 nm) nanocomposites powders were blended separately. The specimens having dimensions (31.5 x12.7 x 6.3 mm^3) were prepared by compacting the powders at a pressure of 400 MPa as per ASTM B 925-08 for 3-point flexural test. The compacted specimens were sintered conventionally at 600°C for 90 minutes in argon atmosphere.

3.3.3 Thermal shock

The 3-point flexural test standard specimens were subjected to thermal shock environment with a 160°C and 80°C temperature gradients by two separate routes. For one batch of specimens (micro- and nano-composites) the treatment started from +80°C temperature to -80°C temperature (down thermal shock) and for the other batch it was in the reverse order (up thermal shock). For second batch of specimens (micro- and nano-composites) the treatment started from

+40°C temperature to -40°C temperature (down thermal shock) and for the other batch it was in the reverse order (up thermal shock). Choice of temperatures between +80°C and -80°C was made to promote accelerated weathering which readily induces significant scale of damage and development in shorter span of time, this accelerated weathering data may be used to predict long term durability for application at higher temperatures than -80°C. The same is true for +80°C**.**

After each thermal shock treatment, 3-point flexural test of each sample was performed immediately in an universal testing machine (Instron-5967) at a cross-head speed of 0.5 mm/min and span length of 26 mm. The fractured specimens of all the thermal shock treatments i.e. (+80°C to -80°C temperature), (-80°C to +80°C temperature), (+40°C to -40°C temperature) and (-40°C to +40°C temperature) were characterized by both field emission scanning and conventional scanning electron microscopy for fracture surface analysis.

3.3.3a Copper-alumina composite

The microstructures of Cu-5 vol. % Al_2O_3 microcomposites before and after down thermal shock treatment have been illustrated in Fig. 3.3.1. The fabricated microcomposites show good dispersion of alumina particles in copper matrix, whereas the down-thermal shock treated microcomposites show particle cracking and particle pull out too. The thermal shock induces compressive stresses on the alumina particle as copper expands at +80°C, successively releasing the stress at -80°C. The alumina particles crack under stresses and lead to interfacial de-cohesion which also gives rise to particle pull-out.

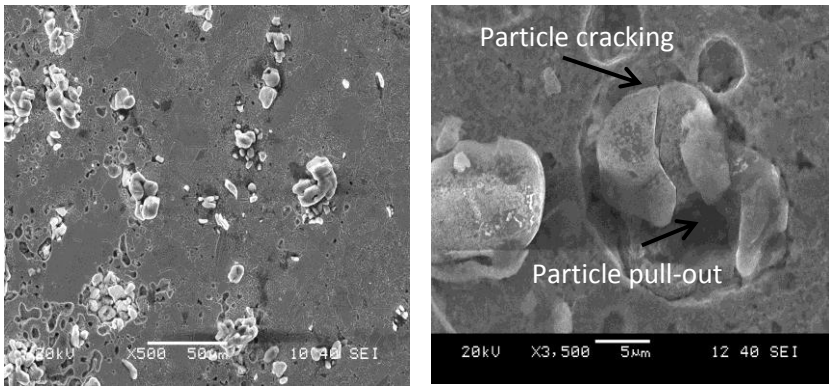

Fig. 3.3.1 SEM micrographs of Cu-5 vol. % Al_2O_3 microcomposite before (left) and after (right) down thermal shock for a temperature gradient of 160°C

Fig. 3.3.2 shows micrographs of Cu-5 vol. % Al_2O_3 nanocomposites before and after down-thermal shock treatment. The nanocomposite before treatment has been marked with alumina

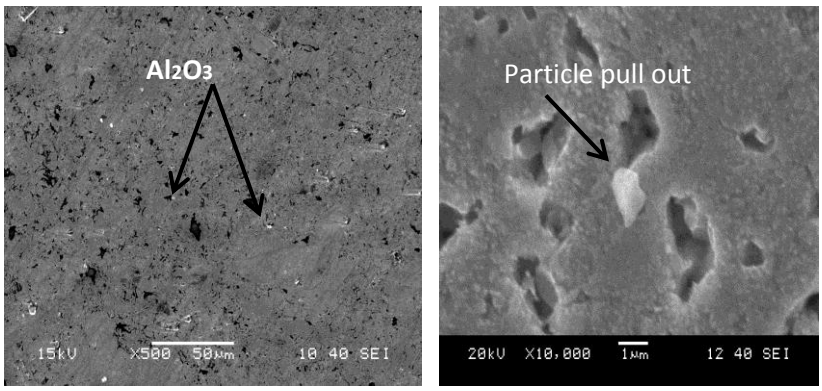

Fig. 3.3.2 SEM micrographs of Cu-5 vol. % Al_2O_3 nanocomposite before (left) and after (right) down thermal shock for a temperature gradient of 160°

nanoparticles which show almost uniform distribution. The microstructure of nanocomposite after down-thermal shock shows pulled out agglomerated particle lying on the matrix.

Microcomposite

The variation in flexural strength has been plotted against the alumina content in the microcomposites after down- (+40°C to -40°C temperature) and up- (-40°C to +40°C temperature) thermal shock treatment (Fig. 3.3.3(a)). The down thermal shock treatment leads to

increase in flexural strength when compared to the ambient flexural strength. The subjection of the composites to +40°C temperature results in expansion of matrix enhancing the microstructural integrity or mechanical keying of the alumina particle with the matrix. At low temperature i.e. at -40°C the matrix contracts leading to generation of gap at the interface due to outgripping of alumina particle by the copper matrix.

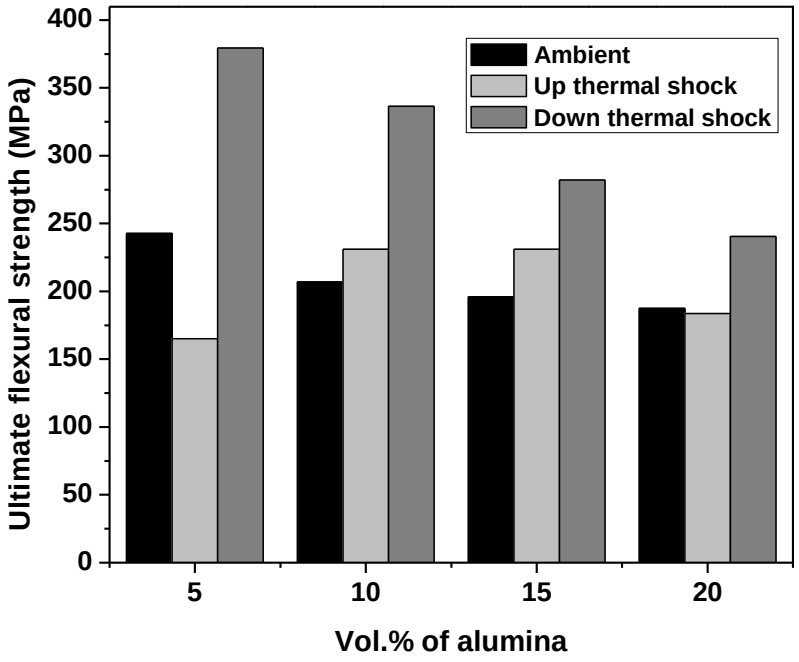

Fig. 3.3.3(a) Variation of flexural strength of Cu-Al_2O_3 microcomposites after thermal shock of 80°C temperature gradient

The up-thermal shock from -40°C to +40°C temperature treated microcomposites show an increase in flexural strength with increasing vol. % of alumina and then decreases at 20 vol. % composition. The extent of matrix shrinkage decreases as the alumina content increases because the increasing number of alumina particles poses a barrier for excessive shrinkage of matrix. The Cu-20 vol. % alumina composition probably results in clustering of alumina particles, hence the keying and un-keying of alumina particle with the matrix is ineffective.

The variation in flexural strength has been plotted against the alumina content in the microcomposites after down- (+80°C to -80°C temperature) and up- (-80°C to +80°C temperature) thermal shock treatment (Fig. 3.3.3(b)). At +80°C temperature treatment the

mechanical keying and un-keying effect diminishes with the increase in vol. % of alumina. The underlying reason could be attributed to the fact of agglomeration at higher vol. % of alumina. The agglomeration of microparticles would lead to the formation of a cluster which would possess an uneven complex shaped contour. Hence, this uneven contour prevents effective gripping or outgripping of alumina particle with the matrix at high and low temperatures respectively.

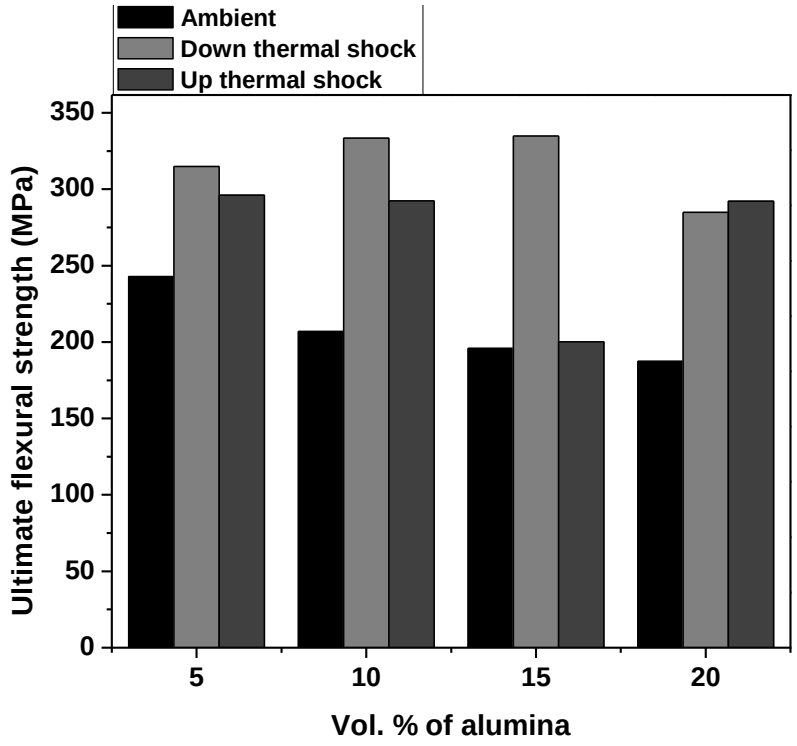

Fig. 3.3.3(b) Variation of flexural strength of Cu-Al_2O_3 microcomposites after thermal shock of 160°C temperature gradient

The increase in flexural strength is higher after a thermal shock of 80°C temperature gradient (ie. From +40° to -40°C and from -40°C to +40°C temperature) than the shock of 160°C temperature gradient (ie. From -80°C to +80°C and from +80°C to -80°C temperature) in the second module. The degree of enhancement of flexural strength decreases as the range of shock temperature increases i.e. the increase in flexural strength is higher at 80°C temperature shock rather than after 160°C temperature shock.

The fractography studies reveal particle pull-out and physical detachment of alumina particle from copper matrix (Fig. 3.3.4 (a) & (b)). The down-thermal shock (i.e. +80°C to-80°C) promoted the intimate physical bonding of reinforcement-matrix.

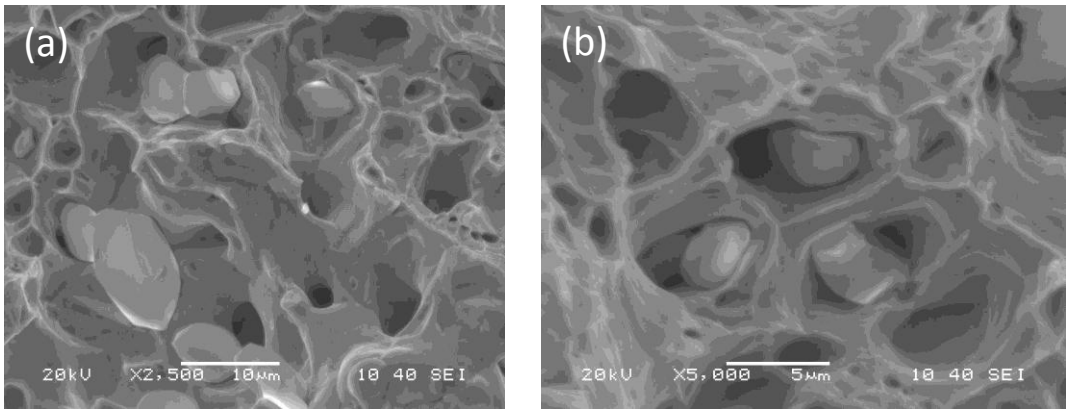

Fig. 3.3.4 SEM micrographs of Cu-10 vol. % Al_2O_3 microcomposite after down thermal shock of 80°C temperature gradient showing (a) particle pull-out and (b) interfacial de-cohesion

The reason could be attributed to the following: at +80°C temperature the matrix around the alumina particles expands and it imparts a compressive force on the alumina particle which could lead to particle fragmentation sometimes [1]. This also leads to better mechanical keying of the particle with the matrix [2]. Whereas on the contrary when cooling occurs from the processing temperature during fabrication of composite, the matrix shrinks around the reinforcement particle rendering residual tensile stresses/strains in the matrix and compressive stresses/strains in the reinforcement [3]. The increase of flexural strength in down-thermally shocked microcomposite is slightly higher than in up-thermal shock because the prior conditioning effect predominates over the later shock (which means that the thermal shock from (+80°C to -80°C) is manifested as prior conditioning at +80°C temperature followed by immediate exposure to -80°C temperature i.e. the specimen was conditioned at +80°C temperature for 1 hour and then immediately exposed to -80°C temperature. Thus the prior thermally conditioned specimen has experienced a thermal shock of 160°C temperature). For the microcomposites subjected to up-thermal shock (i.e. from -80°C to +80°C) the contraction of matrix (copper) takes place to a larger extent than the reinforcement particle (alumina). The reason for this could be the higher co-efficient of thermal expansion of copper (16.6 $x10^{-6}$ k^{-1}) than alumina (5.4 x 10^{-6} k^{-1}), which also aids the

presence of dislocation density at the interface [4]. This may lead to physical de-cohesion (Fig. 3.3.4(b)) at the particle/matrix conjunction which has been observed earlier by Ray et al. [5] in inorganic fiber/polymer composite. The dislocations present in the reinforcement proximity also get pinned down when the composite is subjected to -80°C. The pinning of dislocations strengthens the composite by resisting the plastic flow of the matrix [6]. The interfacial de-cohesion which had possibly occurred at ultra low temperature could not be restored at +80°C on the same scale. The conditioning at -80°C for 60 minutes might have created a large interfacial mismatch at the interface which is manifested by the presence of differential co-efficient of thermal expansion between copper matrix and alumina reinforcement particle [2].

Nanocomposite

The ultimate flexural strength value increases for up-thermal shock (-40°C to +40°C temperature) whereas the strength values decreases for down-thermal shock (+40°C to -40°C temperature) which is confirmed from Fig 3.3.5(a). The trend in the variation in flexural strength in nanocomposites at (+80°C to -80°C temperature) and (-80°C to +80°C temperature) is same as that of the microcomposites for the same thermal shock treatment (Fig. 3.3.5(b)). The (-40°C to +40°C temperature) up thermal shock initiates the contraction of matrix resulting in physical detachment of reinforcement particle from the matrix followed by expansion of matrix which probably bridges the gap at the interface to some extent. This series of events delays the crack initiation and propagation due to initial arrest of dislocations and plastic deformation. The SEM micrographs Fig. 3.3.6(a) & (b) show quasi-cleavage in thermally shocked nanocomposites.

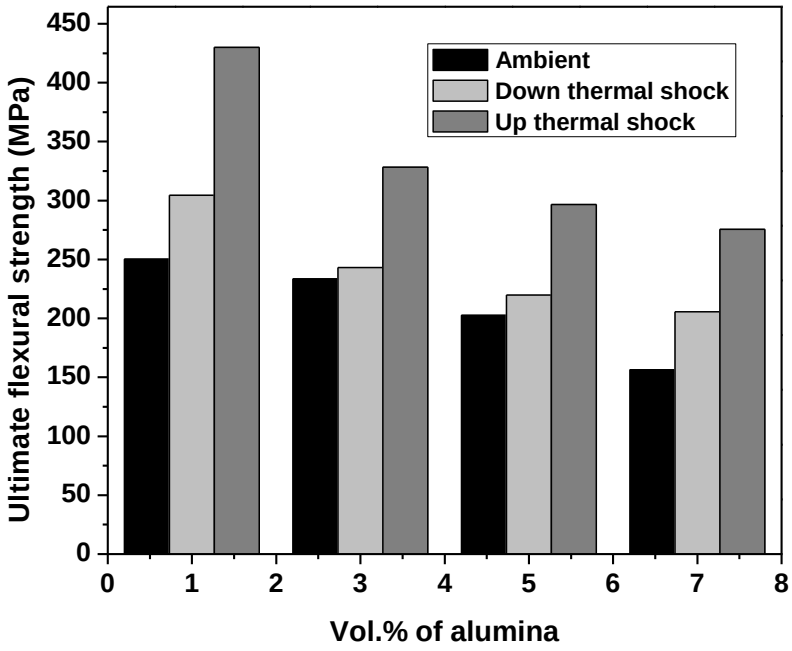

Fig. 3.3.5(a) Variation of flexural strength of Cu-Al_2O_3 nanocomposites after thermal shock of 80°C temperature gradient

Fig. 3.3.6(a) denotes crack entrapment in the up thermally shocked nanocomposite which reveals indirect strengthening, hence the elevation in flexural strength [7]. The declination of surface diffusivity of alumina nanoparticles which took place at -80°C was unlikely to be restored by the treatment at +80°C temperature. The effect of primary treatment is predominant over the following treatment. The trend of variation in flexural strength of copper-alumina nanocomposites after up-thermal shock at (-40°C to +40°C temperature) and at (-80°C to +80°C temperature) treatment is opposite. The reason could be attributed to the fact that at -80°C the surface diffusivity/activity of alumina nanoparticles is lowered drastically, but -40°C is not enough to lower its surface diffusivity to a greater extent, hence after the -40°C to +40°C temperature treatment the flexural strength is elevated. The ultimate flexural strength value decreases for up-thermal shock whereas the strength values increases for down-thermal shock which is confirmed from Fig 3.3.5(a).

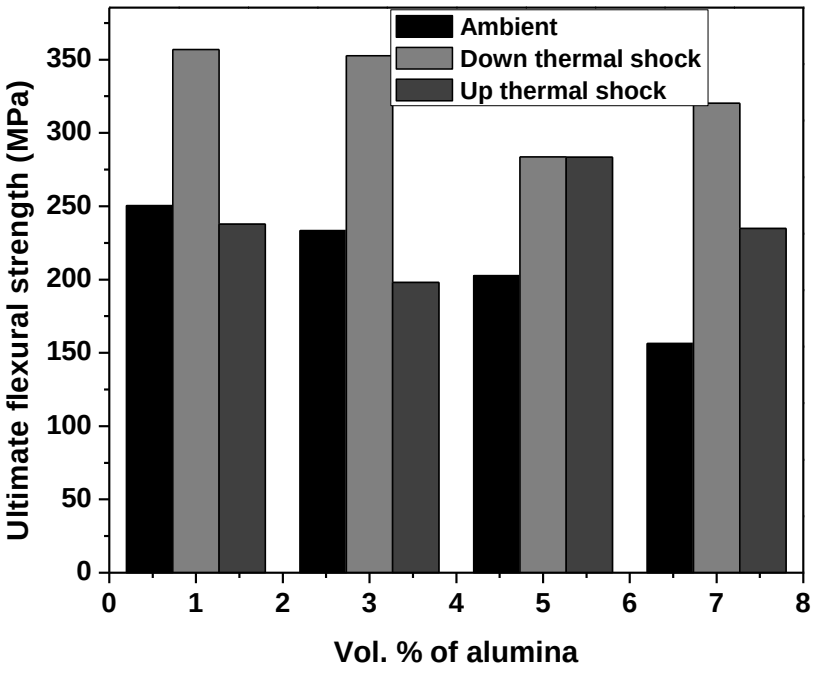

Fig. 3.3.5(b) Variation of flexural strength of Cu-Al_2O_3 nanocomposites after thermal shock of 160°C temperature gradient

In case of up-thermal shock the matrix in the vicinity of the particle contracts at -80°C temperature possibly leading to interfacial de-cohesion. The surface area of the nano particles being higher, the degree of de-union anticipated is also high rendering the interfacial bond weak. The above being a physical phenomenon cannot be reversed/restored at +80°C temperature, hence the ultimate flexural strength decreases. The surface deactivation of alumina nanoparticles which took place at -80°C was unlikely to be restored at +80°C. The adverse effect of prior thermal conditioning treatment on the composites is not being reversibly reinstated by the subsequent treatment; this could be a possible reason for a reduced value of flexural strength. In the case of down-thermal shock, the degree of physical contact of matrix and the reinforced nanoparticle increases at +80°C temperature (The expansivity of copper matrix is much higher compared to that of alumina particle. So, the expansion of matrix onto the particle at +80˚C leads to enhanced gripping of alumina by the matrix. This enhanced proximity leads to mechanical strengthening of the interface which is reflected by the increased flexural strength values). The improved integrity can also be attributed to the enhanced surface diffusivity of nanoparticles at high temperature. The physical integrity of copper and alumina has been shown by flexural

strength. Nanoparticles have high surface energy leading to high surface diffusivity. At high temperature it is reasonably expected that the surface diffusivity of nanoparticles gets improved, and at sub-zero temperature surface diffusivity gets reduced, as diffusion is a temperature dependent phenomenon.

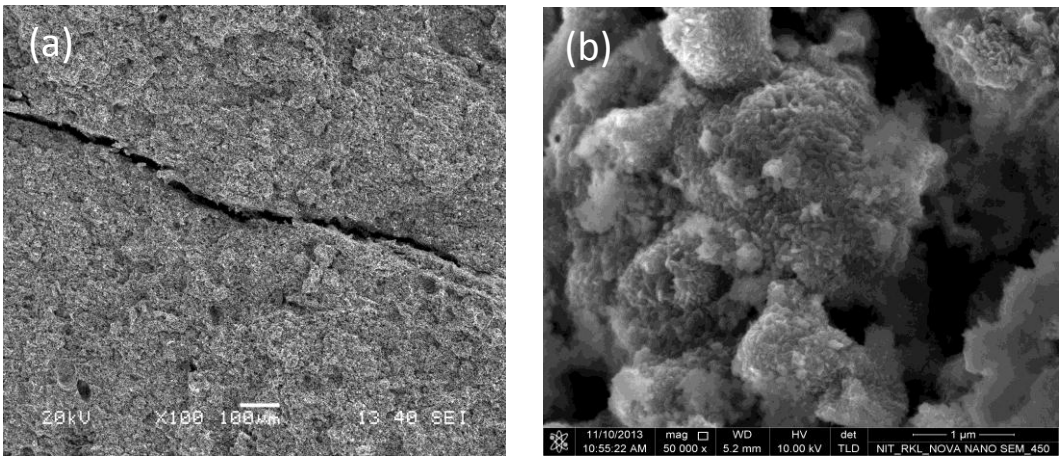

Fig. 3.3.6 SEM micrographs of Cu-5 vol. % Al_2O_3 nanocomposite after (a) up thermal and (b) down thermal shock for a temperature gradient of 80°C

The ultimate flexural strength increases due to the high surface area of nanoparticles and hence leading to enhanced interaction of nanoparticles with the matrix at high temperature. Later the exposure at -80°C temperature could not induce damage on the same scale as the prior treatment at +80°C. Fig. 3.3.6(b) shows flaky appearance of fracture surface, the flakes of white alumina nanoparticles are covering the copper matrix surface. The Al/AlN composites were synthesized by squeeze casting, and were solution treated at 530°C and quenched in water for 2 hours followed by aging for 10 hours at 160°C. Thermal cycling led to increase in tensile strength, elastic limit and yield strength, and overall properties' stability of the composites, which is in accordance with our case, where flexural strength increases with thermal shock treatment [8]. Bhattacharya et al. [9] have reported increase in microhardness and decrease in density (due to formation of voids) after thermal cycling in Al-SiC composites. Cracks at the interface have been observed due to thermal strain in the composite in the clustered region of reinforcement. Our investigation also reports particle cracking after thermal shock treatment.

3.3.3a.1 Transmission electron microscopy

Fig. 3.3.7 illustrates the TEM micrographs for the fractured samples of Cu-5 vol. % Al_2O_3 microcomposites at (a) ambient conditions, (b) after up thermal shock and (c) after down thermal shock. The TEM micrographs reveal a typical dislocation sub-structure for all the specimens. The down thermally treated samples exhibit smaller size of dislocation cells than the specimen tested at ambient conditions. As the temperature increases the cell size decreases. Curly dislocations are visible for up thermally shocked samples. A dense dislocation forest indicates dislocation entanglement which leads to strengthening of the microcomposite as the dislocation mobility gets arrested [10].

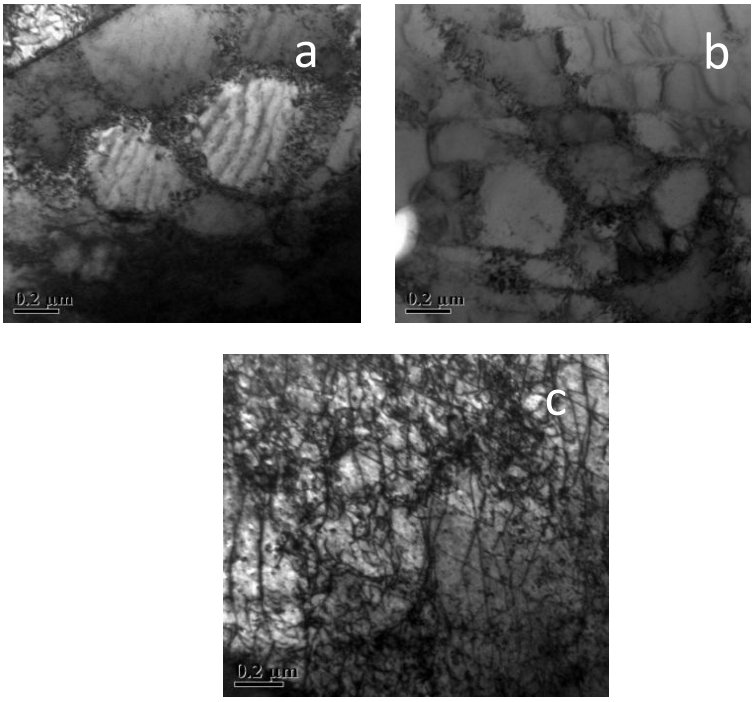

Fig. 3.3.7 TEM micrographs of Cu-5 vol. % Al_2O_3 microcomposites at (a) ambient conditions, (b) after up thermal shock and (c) after down thermal shock for a temperature gradient of 160°C

The cell structure differs for different deformation temperatures. The cell size usually increases with increase in the temperature. The rise in temperature is accompanied by sharpening of cell walls. This phenomenon is an avenue for stress relaxation.

Fig. 3.3.7(a) shows a ragged cell wall structure with dislocations inside the cells. After up thermal shock treatment the cell walls become smaller in size and almost clear of dislocations.

The down thermally treated samples show a dense dislocation forest with presence of slip planes. The low temperature treatment has arrested the dislocation mobility by entanglement and coiling of dislocations. Dislocations move short distances at lower temperatures. Fig. 3.3.8 demonstrates the dislocation sub-structure for Cu-5 vol. % Al_2O_3 nanocomposites (a) at ambient conditions, (b) after up thermal shock and (c) after down thermal shock. Strengthening mechanisms in FCC metals operate through dislocation forest formation [11]. The nanocomposites also show a typical dislocation sub-structure showing supercoiling of dislocations, the overall number of dislocations can be estimated to be low as compared to microcomposites.

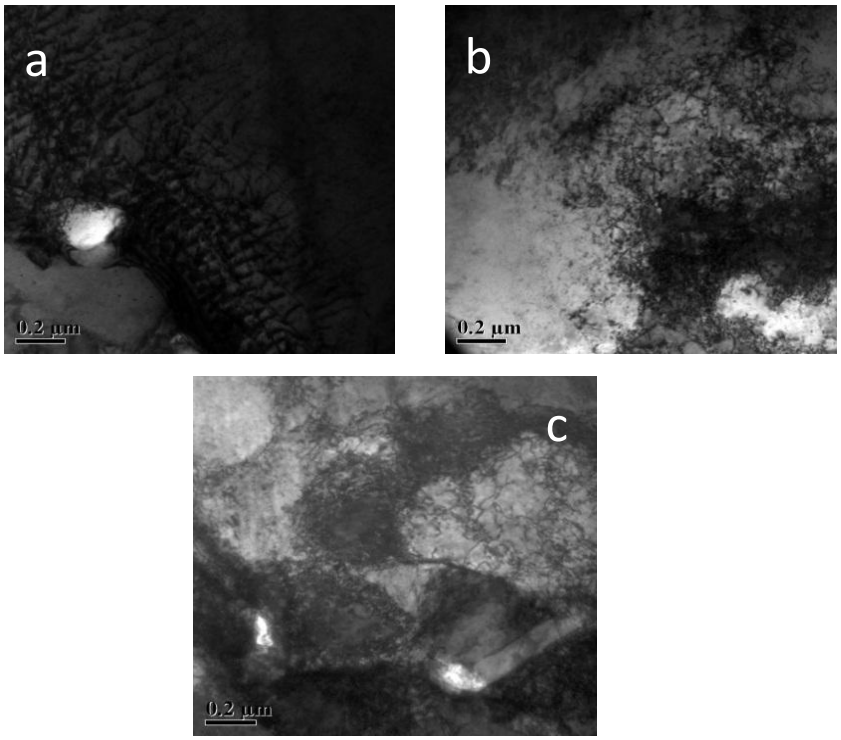

Fig. 3.3.8 TEM micrographs of Cu-3vol. % Al_2O_3 nanocomposites at (a) ambient conditions, (b) after up thermal shock and (c) after down thermal shock for a temperature gradient of 160°C

3.3.3b Aluminium-alumina composite

The microstructures obtained after sintering of Al-Al_2O_3 for micro- and nano-composites show good distribution of alumina in the aluminium matrix (Fig. 3.3.9 & 3.3.10).

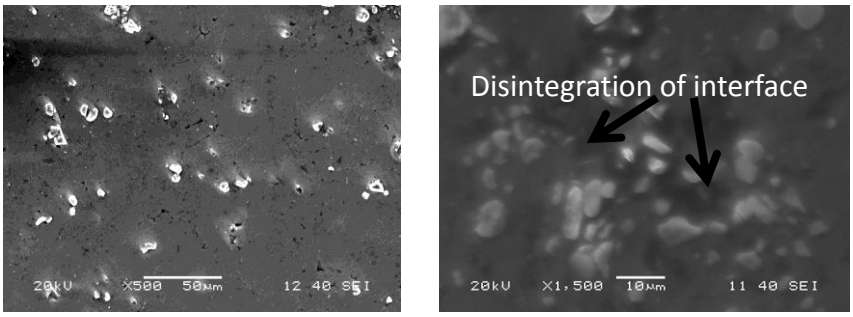

Fig. 3.3.9 SEM micrographs of Al-5 vol. % Al_2O_3 microcomposite before (left) and after (right) down thermal shock of 160°C temperature gradient

The alumina nanoparticles have intimately mixed with the matrix and are distributed almost uniformly in aluminium. The grain boundary pinning is also effective as seen from the micrographs. The physical integrity of aluminium-alumina seems to be appreciable as no third phase forms in this system. The thermal shock treatment has induced differential expansion and contraction of matrix and reinforcement. Down thermal shock consists of treatment at +80°C temperature followed by immediate treatment at -80°C temperature. At +80°C temperature the aluminium matrix expands and exerts a compressive force on alumina so that physical integrity of aluminium and alumina gets improved. The thermal shock experienced when exposed to -80°C temperature induces contraction of aluminium and alumina leading to interfacial de-cohesion of alumina from matrix due to higher contraction of aluminium than alumina. The reverse phenomenon takes place during up-thermal shock. Alumina nanoparticles possess high surface area and as a result the interfacial decohesion and physical integrity induced by thermal shocks have a higher magnitude in case of nanocomposites. The microcomposites also exhibit decohesion and disintegration in the microstructure (Fig. 3.3.9). The thermally shocked nanocomposites show decohesion of nanoparticle from the matrix and defect generation in the matrix (Fig. 3.3.10).

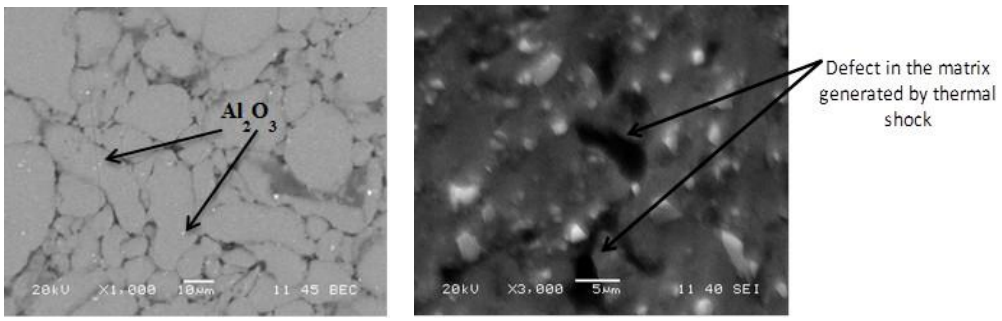

Fig. 3.3.10 SEM micrographs of Al-5 vol. % Al_2O_3 nanocomposite before (left) and after (right) down thermal shock of 160°C temperature gradient

Microcomposite

The variation of flexural strength of Al-Al_2O_3 microcomposites after thermal shock of 80°C and 160°C temperature gradients is illustrated in Fig. 3.3.11 (a) & (b). The thermal shock with conditioning treatment can be divided into three steps. For down thermal shock the first step starts with primary conditioning at +80°C temperature for one hour. The second step is the shock experienced by the composites when the samples are exposed to -80°C temperature immediately after the first step. The third step is the secondary conditioning which consists of holding the samples for one hour at -80°C temperature. In up-thermal shock the same steps are followed with reversion in temperature i.e. from positive to negative temperature and vice versa.

The flexural strength of microcomposites increases after down- and up-thermal shocks irrespective of volume percentage of alumina used (with the highest values at 10 vol. %, which is anticipated to be the optimum composition). The co-efficient of thermal expansion (CTE) of aluminium ($24x10^{-6}$/°C) is almost five times higher than alumina ($5.4x10^{-6}$/°C). Due to this large difference in CTE values the thermal shock gradient imposes higher expansion of matrix than the alumina particle in the first step in case of down thermal shock. This expansion leads to improved mechanical keying of alumina with aluminium matrix, elevating the particle strengthening effect which is visible in this case. The second step i.e. shock at -80°C results in contraction of matrix followed by interfacial de-cohesion.

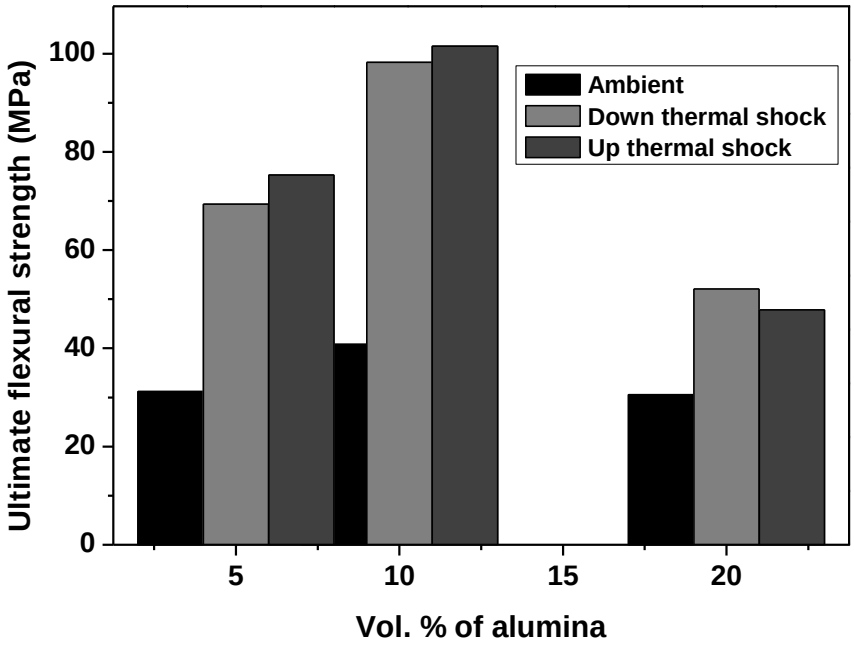

Fig. 3.3.11(a) Variation of flexural strength of Al-Al_2O_3 microcomposites before and after thermal shock of 80°C temperature gradient

The secondary conditioning for one hour at -80°C further promotes de-cohesion at the matrix/particle junction. The attribution of mechanical keying effect during primary conditioning is being counteracted by two consecutive de-registry effects during shock as well as secondary conditioning. In up thermal shock the primary conditioning results in interfacial de-cohesion due to matrix shrinkage. The second step exposes the samples to shock at +80°C allowing aluminium matrix to grip alumina by differential expansion of matrix. The secondary conditioning also follows the same route of particle gripping by aluminium matrix. During up thermal shock the gripping effect counteracts the interfacial de-cohesion effect. As the changes taking place in the composite after the primary steps are physical phenomenon, they cannot be reinstated to the same scale and degree after secondary shock treatments.

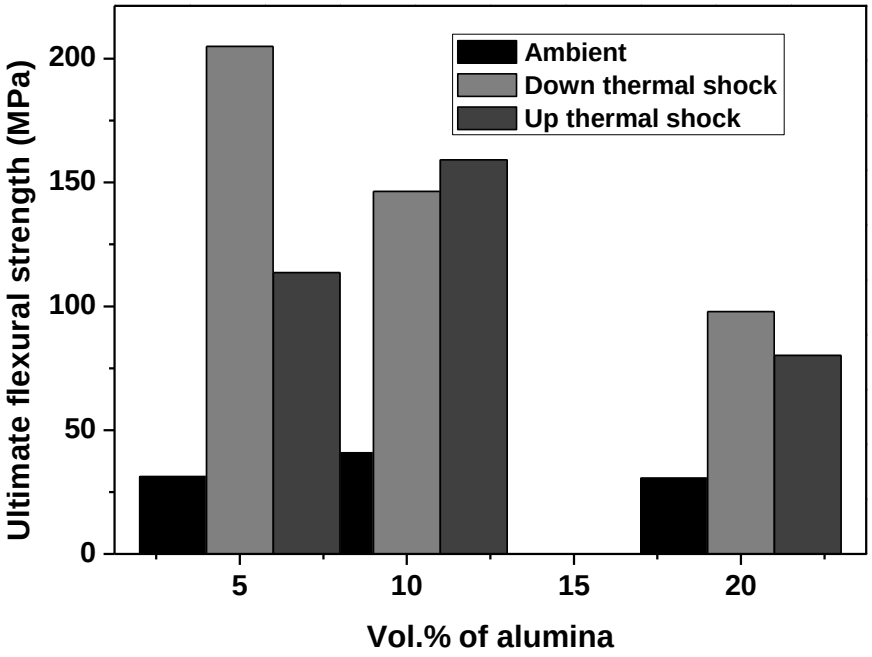

Fig. 3.3.11(b) Variation of flexural strength of Al-Al_2O_3 microcomposites before and after thermal shock of 160°C temperature gradient

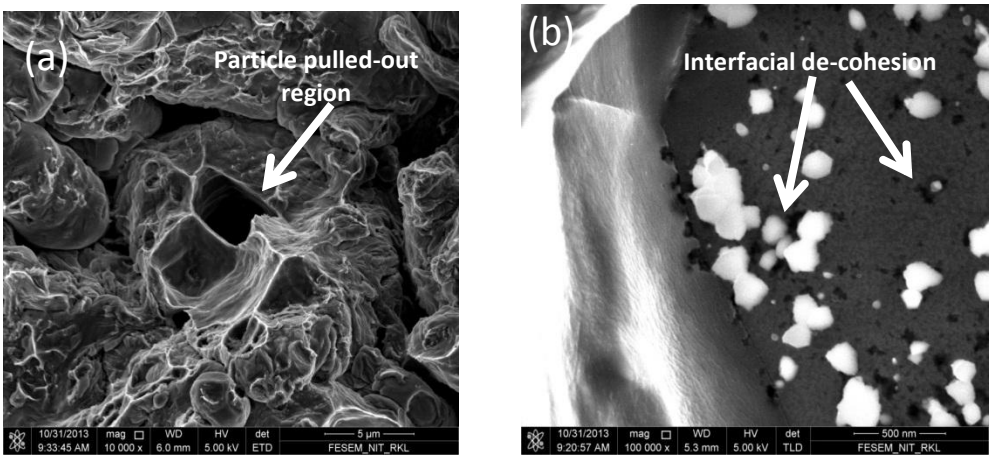

Fig. 3.3.12 SEM micrographs of Al-1 vol. % Al_2O_3 (a) microcomposite and (b) nanocomposite after down thermal shock of 160°C temperature gradient

Nanocomposite

The flexural strength of Al-Al_2O_3 nanocomposites after subjection to thermal shock of 80°C and 160°C thermal gradient is shown in Fig. 3.3.13 (a) & (b). In nanocomposites the same series of events take place during down- and up-thermal shocks. The flexural strength also increases after thermal shock treatment with highest value for 3 volume percent of alumina reinforced aluminium nanocomposite. The exceptions in variation of flexural strength in nanocomposites for some instances of shock treatments could be attributed to agglomeration of nanoparticles. Agglomeration is a common occurrence in nanoparticles and that is why mechanical keying and un-keying effect may not be effective as anticipated. This may be case sensitive from sample to sample which leads to wide fluctuation in strength values. The distribution of alumina particle in the matrix, tendency of agglomeration, agglomerated size of particle may not be ascertained throughout the matrix and from sample to sample. The degree of increase in flexural strength in micro- and nano-composites after thermal shocks is higher for a shock of 160°C than for 80°C. The reason could be the higher expansion/contraction of matrix for a shock of 160°C, compared to shock of 80°C. In this case the thermal conditioning effect predominates on the shock effect and hence the increase of strength for the former is higher than the later.

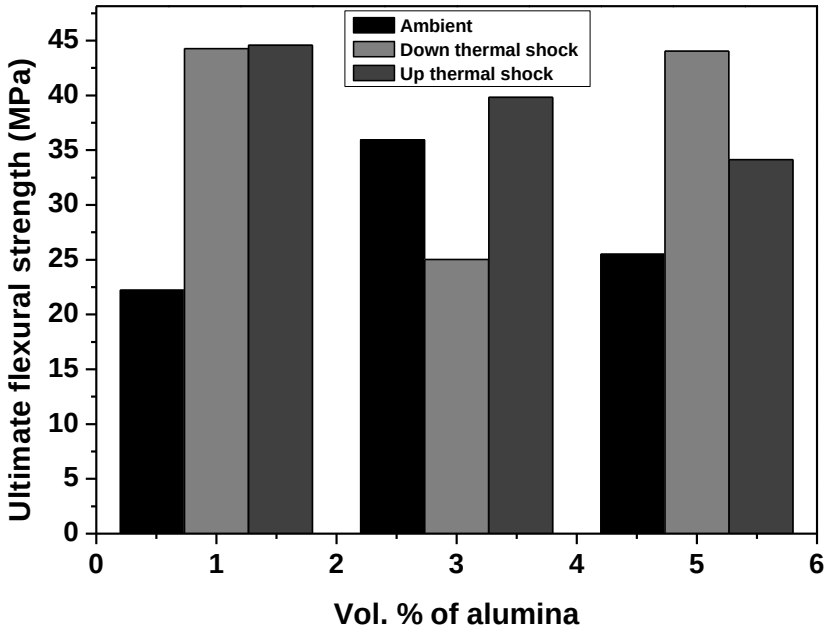

Fig. 3.3.13(a) Variation of flexural strength of Al-Al_2O_3 nanocomposites before and after thermal shock of 80°C temperature gradient

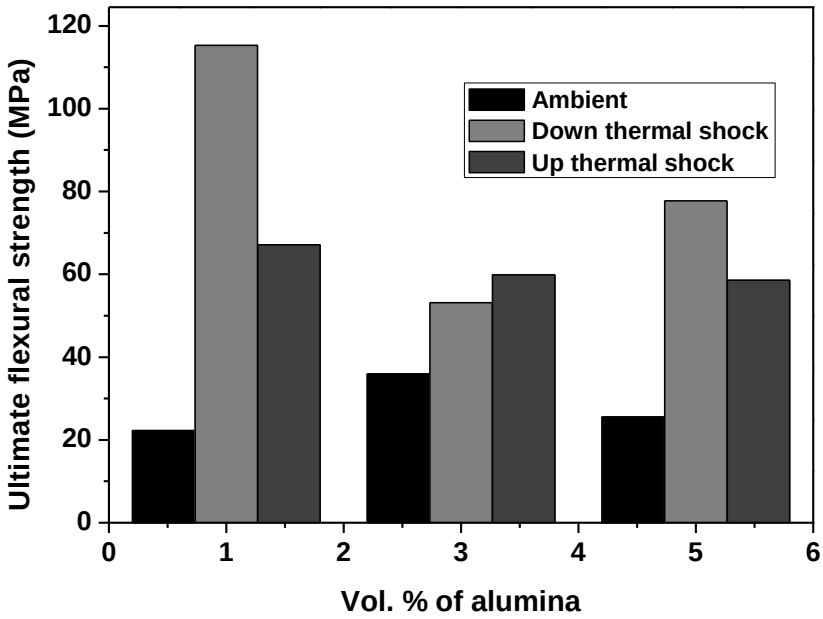

Fig. 3.3.13(b) Variation of flexural strength of Al-Al_2O_3 nanocomposites before and after thermal shock of 160°C temperature gradient

3.3.4 Thermal conditioning

In order to treat the samples for thermal conditioning the samples were categorized into 3 groups. The first group was treated at +80°C in muffle furnace for 60 minutes isothermally. The blower of the furnace was on function for heat circulation and uniform heating of the samples. The second set of samples were treated at -80°C in an ultra low temperature chamber for 60 minutes by isothermal holding. The third batch of samples was maintained at ambient temperature. 3-point flexural test was conducted immediately at room temperature after each thermal conditioning treatment. The loading rate and span length was maintained at 0.5 mm/min and 26mm respectively for all the 3-point bend tests.

3.3.4a Copper-alumina composite

Microcomposite

The 3-point flexural strength values at various conditioning temperatures are illustrated in Fig. 3.3.14. As the expanding elastic matrix imparts a compressive force on the reinforcement particle, this results in particle fragmentation (abundantly visible in SEM micrograph Fig. 3.3.15(a) & (b)) which leads to composite softening. This differential expansion also leads to localized stresses and strain fields in the microcomposite [12]. The ultra low temperature conditioning at -80°C may impart shrinkage of matrix which causes interfacial de-cohesion, decreasing the flexural strength of microcomposite. At low temperature the degree of contraction of matrix is higher than the reinforcement particle shrinkage. As the probability of particle cracking decreases, this results in decrease of the detrimental softening effect.

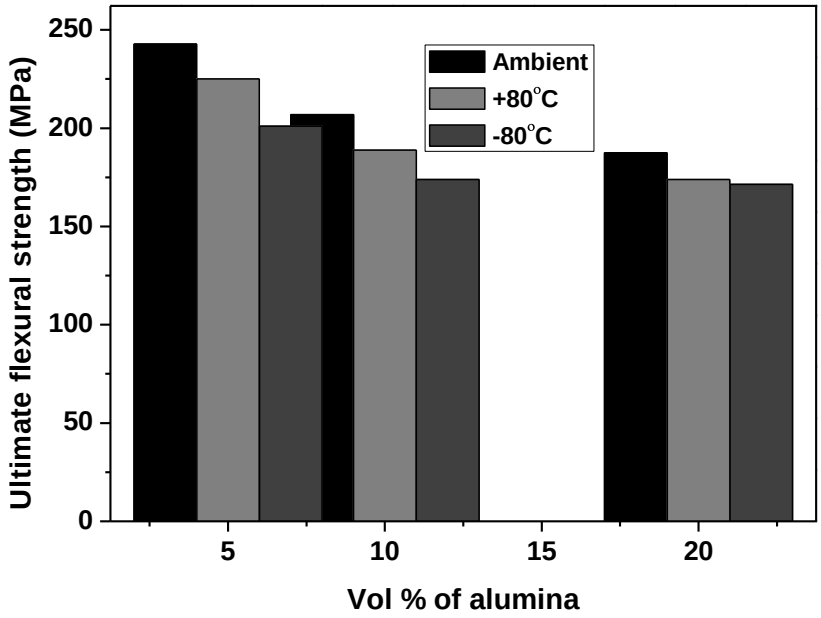

Fig. 3.3.14 Flexural strength of Cu-Al_2O_3 microcomposites after thermal conditioning

So, the decrease in ultimate flexural strength is less pronounced as compared to the +80°C conditioning.

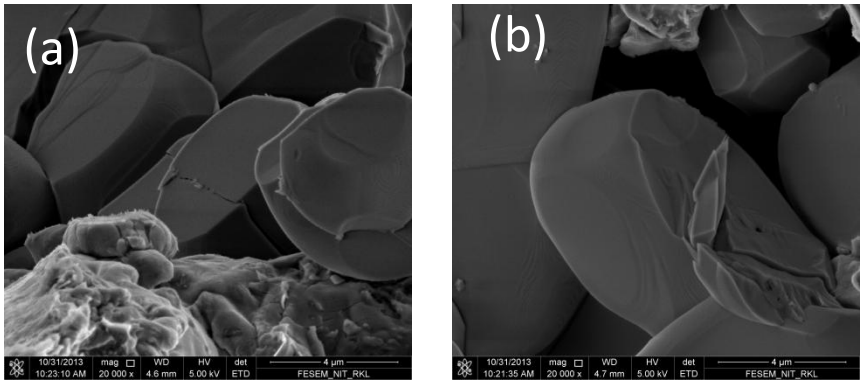

Fig. 3.3.15 FESEM micrographs of Cu-10 vol. % Al_2O_3 (a) & (b) microcomposite after thermal conditioning at +80°C

Nanocomposite

At +80°C temperature, the ultimate flexural strength increases in comparison to the untreated sample (Fig. 3.3.16). The nano alumina particles impede the dislocation motion leading to the dislocation pileups at the reinforcement particle-matrix boundary, which leads to strain hardening of the composite. The enhanced surface diffusivity of nanoparticles at high temperature could be another reason for proficient interfacial interaction and subsequent composite strengthening. On the contrary the ultralow temperature conditioning of the nanocomposite at -80°C decreases the composite strength. As the movement of dislocations is a temperature driven phenomena, at low temperature the movement of dislocations get arrested which restricts the dislocation pile up consequently decreasing the density of dislocation forest [13]. At low temperature the surface diffusivity of alumina nanoparticles is quite likely to get lowered in comparison to enhanced diffusivity at high temperature, hence the thermal conditioning effect in nanocomposites is pronounced.

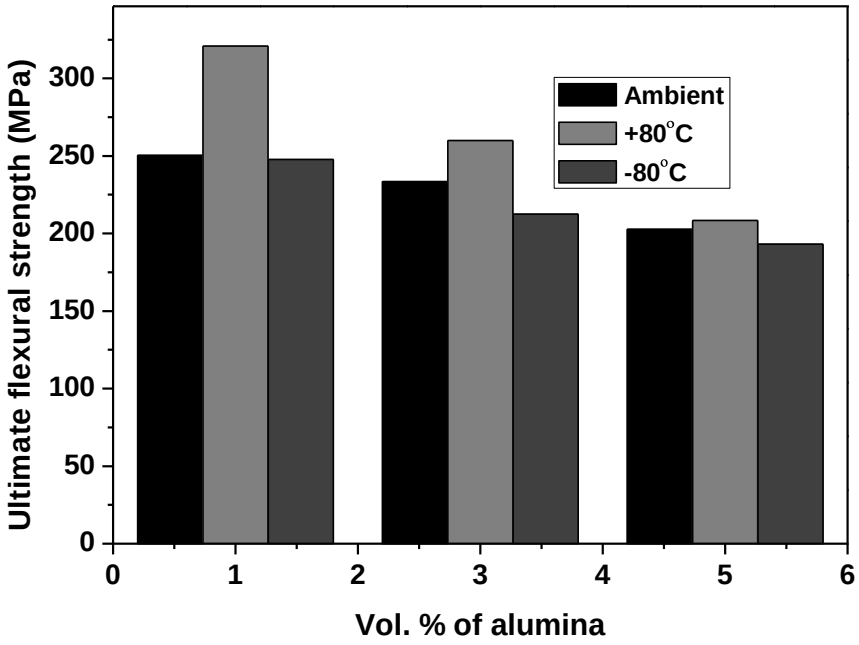

Fig. 3.3.16 Flexural strength of Cu-Al_2O_3 nanocomposites after thermal conditioning

3.3.4b Aluminium-alumina composite

Microcomposite

Flexural strength of thermally conditioned samples of Al-Al_2O_3 microcomposites has been demonstrated in Fig. 3.3.17 respectively. The residual stresses generated by virtue of fabrication i.e. compaction and sintering might have developed defects such as macro- and micro-cracks. The conditioning of samples at -80°C temperature leads to contraction of aluminium matrix resulting in closure of many potential cracks. The differential contraction between matrix and particulate reinforcement may lead to de-registry at the interface which may lead to release/relaxation of built in residual stresses after fabrication. These could be the reason attributed to strengthening of composite after -80°C temperature thermal conditioning.

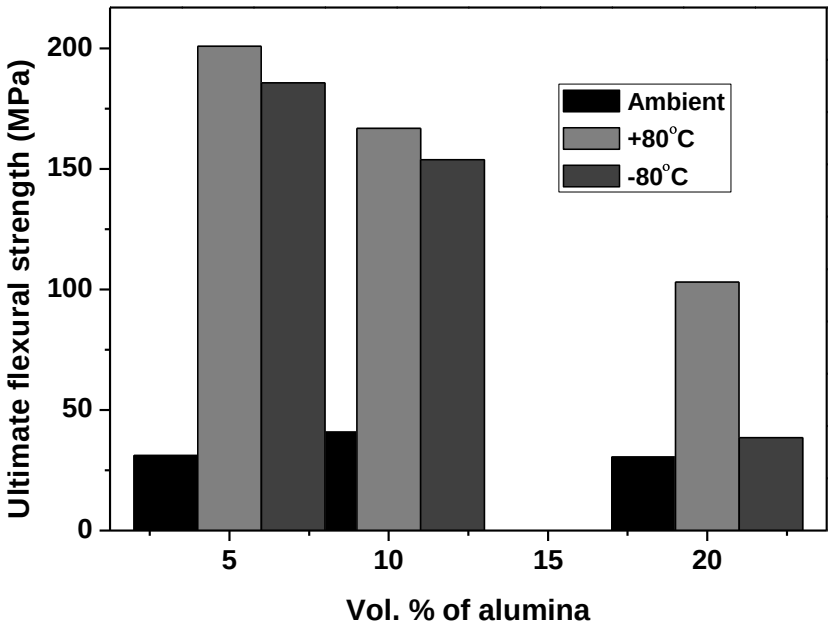

Fig. 3.3.17 Flexural strength of Al-Al_2O_3 microcomposite after thermal conditionings

Nanocomposite

The flexural strength of Al-Al_2O_3 nanocomposites improves post thermal conditioning both for +80°C and -80°C temperatures. The elevation in strength can be realised through FESEM fractographs which indicate strengthening mechanisms such as crack bifurcation (Fig. 3.3.19(a)).

Fig. 3.3.19(b) shows serrations as a damage characteristic and ample alumina nanoparticles are present on the matrix. The increase in strength indicates that the thermal conditioning treatment has acted in a positive manner for the nanocomposites. At +80°C temperature the matrix expands and tightly bonds with the alumina particle resulting in high flexural strength. At -80°C temperature the matrix shrink and in this course leads to rise in the crack nucleation threshold value via many crack blunting mechanisms.

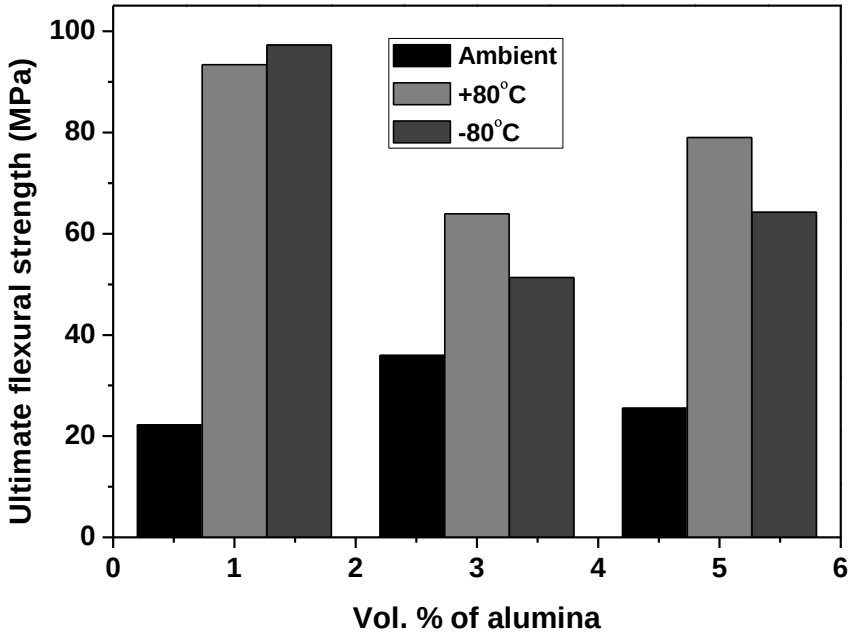

Fig. 3.3.18 Flexural strength of Al-Al_2O_3 nanocomposites after thermal conditionings.

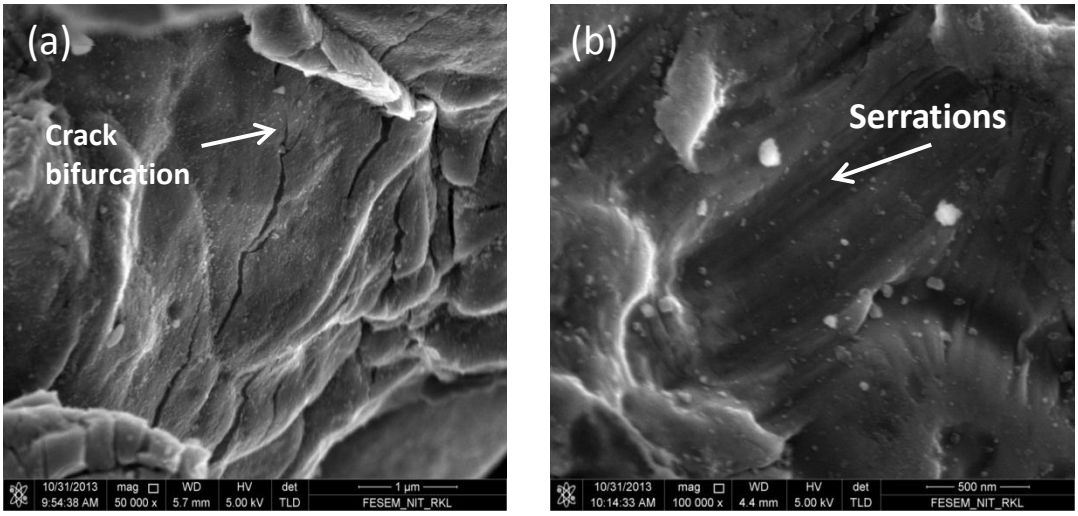

Fig. 3.3.19 FESEM micrographs of Al-1 vol. % Al_2O_3 (a) & (b) nanocomposite thermally conditioned at -80°C.

3.3.5 High temperature in-situ 3-point bend test

High temperature 3-point flexural test was carried out at a temperature of 100°C, 250°C on the micro- and nano-composites. The samples were kept inside the furnace chamber and the furnace was allowed to reach the required temperature. The 3-point flexural test was conducted just after the temperature attainment under in-situ conditions.

3.3.5a Copper-alumina composite

Microcomposite

At 100°C temperature the copper matrix expands resulting in tensile and compressive stress in the matrix and reinforcement respectively enhancing the mechanical locking between matrix and reinforcement [14]. This leads to the direct strengthening of the composite and as a result the ultimate flexural strength of the composite increases from the ambient test value (illustrated in Fig. 3.3.20).

At 250°C temperature the ultimate flexural strength values decreases from the room temperature test value. At higher operating temperatures plasticity of the composite increases due to (1)

dislocation annihilation (2) activation of dislocation motion by different mechanism other than glide (3) relaxation of internal stress at the matrix-particle front, (4) enhancement of dislocation recovery at the interface [15]. All the above stated phenomena decrease the strain hardening exponent of the composite leading to decrease in ultimate flexural strength of the composite.

The microcomposites' flexural strength decreases when excursed to high temperature testing at 100°C and 250°C temperature (Fig. 3.3.20). The matrix softening along with de-cohesion of alumina particle from the softened matrix leads to the lowering of flexural strength at elevated temperatures [16]. As reported by Wu et al. [17] thermal fatigue resistance increases as the reinforcement particle size decreases.

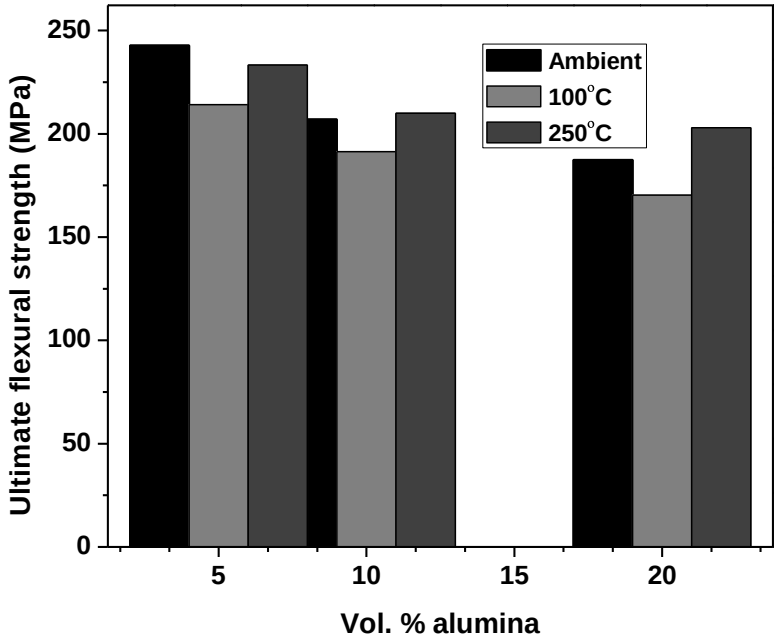

Fig. 3.3.20 High temperature flexural strength of Cu-Al_2O_3 microcomposites

Nanocomposite

Fig. 3.3.21 illustrates increase of flexural strength in nanocomposites when tested at 100°C, indicating the enhancement of microstructural integrity and the mechanical keying of the

alumina particle with the copper matrix. The deviation in the variation of flexural strength of Cu-5 vol. % Al_2O_3 nanocomposite from rest of the two compositions could be attributed to the agglomerating effect of alumina nanoparticles which impedes excessive softening of matrix. This hinders the lowering of flexural strength. The temperature of 100°C acts as a thermal conditioning to enhance the flexural strength of nanocomposites. The decrease of strength at 250°C reveals the softening of matrix and the outgripping of alumina particle from the copper matrix. With increase in operating temperature the strengthening mechanisms that operate at low temperature get relaxed which decrease the strength of the composite [14]. The fractography studies (Fig. 3.3.22) reveal that the failure characteristic features of the composite at 250°C temperature can be characterized by dimple markings (matrix softening at elevated temperature). The nanocomposites do not show pronounced dimples in ambient conditions of testing, whereas at high temperature of testing presence of dimples suggest matrix softening to a certain extent.

The microcomposites' strength is better at 250°C than nanocomposites due to softening of matrix at 250°C and as the interfacial area is high in nanocomposites, the de-cohesion of alumina nanoparticle from the matrix leads to drastic lowering of strength. Whereas at 100°C the nanocomposites show high strength than the microcomposites, the reason could be attributed to the conditioning effect of 100°C on the nanocomposites to improve its structural integrity as well as enhances the interlocking of alumina nanoparticles with the matrix [18]. The high temperature properties of copper-alumina nanocomposites are appreciably high at 100°C, with adversity to 250°C.

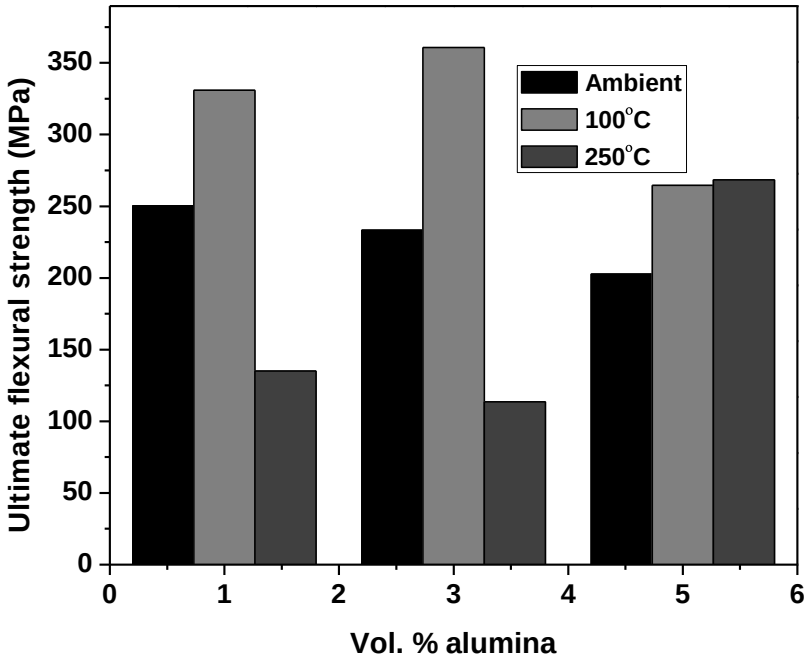

Fig. 3.3.21 High temperature flexural strength of Cu-Al_2O_3 nanocomposites

Uematsu et al. subjected Al-SiC composites to high temperature testing, showing decrease in tensile strength with increase in testing temperature such as 150˚C and 250˚C [19]. The fracture surface indicated particle fracture and particle/matrix crack intiation due to softening of matrix at high temperature which is in agreement with our results.

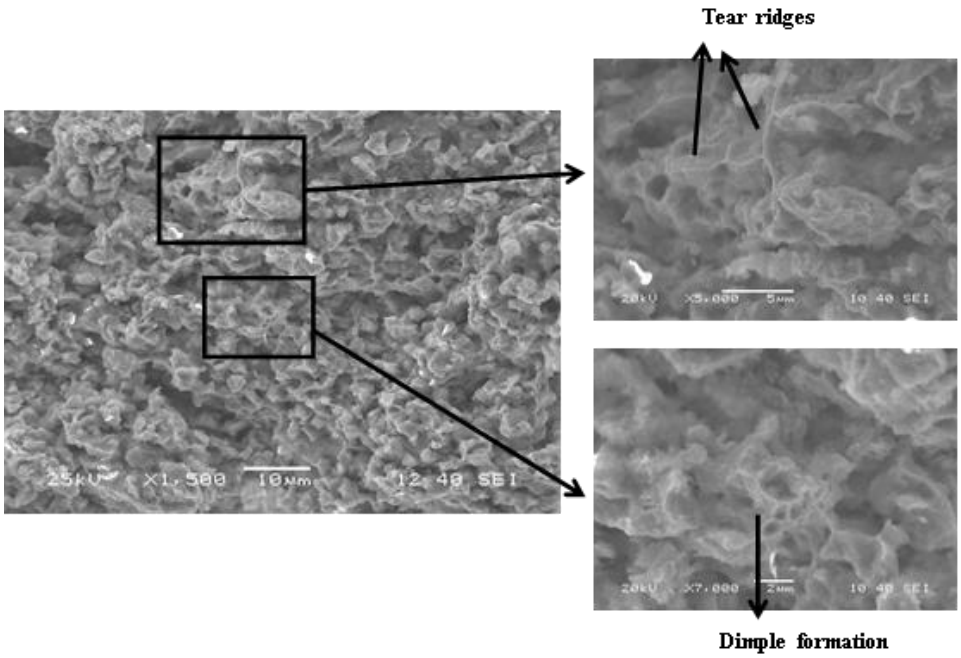

Fig. 3.3.22 SEM micrograph of Cu-5 vol. % Al_2O_3 nanocomposite after high temperature flexural test at 250°C

3.3.5b Aluminium-alumina composite

Microcomposite

The in-situ high temperature testing at 100°C and 250°C demonstrated increase in flexural strength from the ambient test values (Fig. 3.3.23). At 100°C the aluminium matrix expands and exerts a compressive stress on the particle resulting in gripping of particle in the matrix. This gripping leads to closer proximity of alumina particle with the matrix aiding in effective stress transfer from the matrix to the particle. The higher content of alumina composition show decreased effect of high temperature testing, the higher alumina content promotes clustering. Hence, the surface area of the alumina microparticle interacting with the matrix will get reduced effectively because of clustering. This may be the supporting fact for decreased effect in strength value of higher alumina content composition at high temperatures.

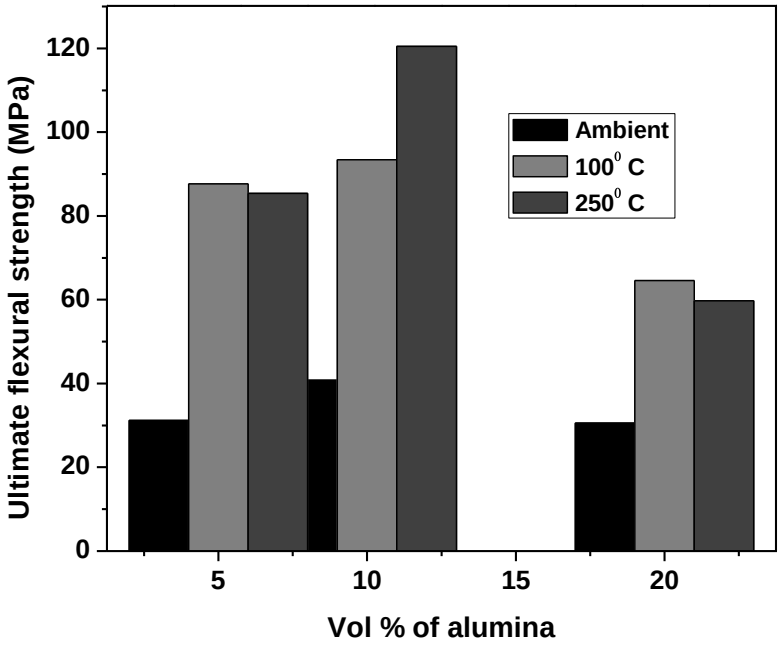

Fig. 3.3.23 High temperature flexural strength of Al-Al_2O_3 microcomposites

Nanocomposite

Fig. 3.3.24 shows flexural strength of Al-Al_2O_3 nanocomposites at 100°C and 250°C temperature. 250°C temperature could be a conducive temperature for nanoparticles to diffuse and subsequently lead to agglomeration. This is why the gripping effect explained above at 100°C could get diminished at 250°C temperature. Due to agglomeration of nanoparticle at high temperature the alumina nanoparticle-matrix interaction will get lowered, the strength getting reduced. At 250°C temperature the agglomeration process will be activated by the enhanced temperature during in-situ test. The degree of agglomeration will be higher at 250°C than 100°C visible in Fig. 3.3.25. The increase in flexural strength at 250°C for Al-1 vol. % Al_2O_3 reveals the thermal conditioning effect at 100°C temperature followed by matrix softening and as this composition contains less number of alumina particles, hence not decreasing the strength to a larger extent.

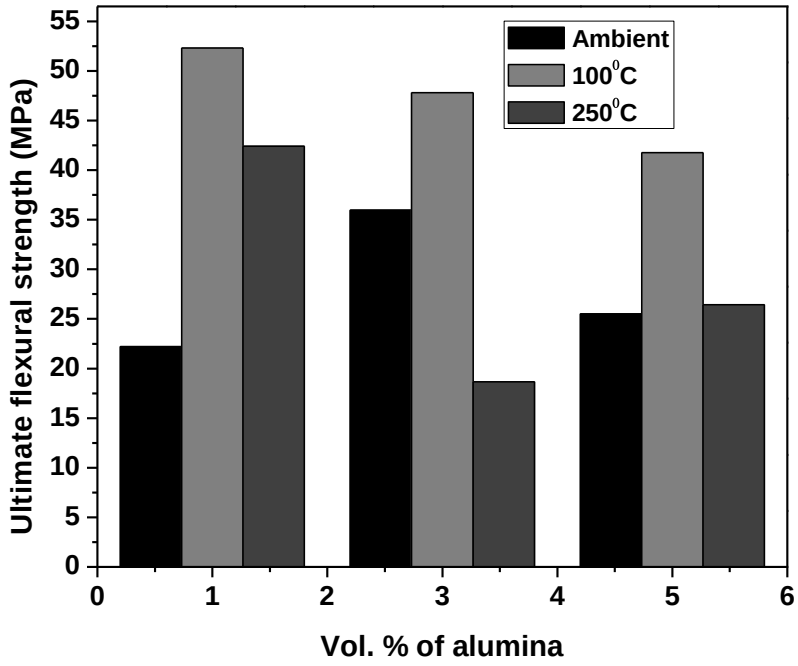

Fig. 3.3.24 High temperature flexural strength of Al-Al_2O_3 nanocomposites

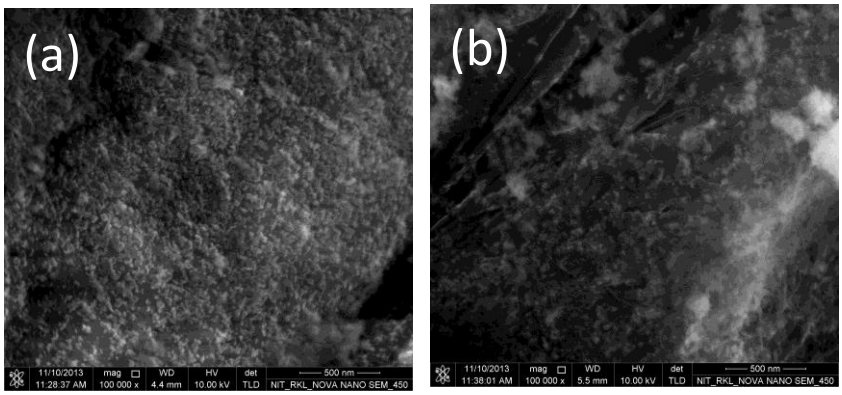

Fig. 3.3.25 SEM micrographs of Al-5 vol. % Al_2O_3 nanocomposite after high temperature flexural test at (a) 100°C and (b) 250°C

3.3.6 Comparison of mechanical behaviour of differently thermal treated composites

The present investigation has largely emphasized the study of damage and/or development of flexural properties under the condition of up-thermal and down-thermal shocks. The experiment has further focused on the variation of flexural behaviour by the imposition of thermal conditioning and high temperature exposure on micro- and nano-particle embedded Cu based composites.

a. Thermal shock

The composites are exposed to temperature gradient of 160°C (from 80°C to -80°C i.e. down-thermal shock, and -80°C to +80°C temperature i.e. up-thermal shock). This thermal shock experiment revealed that the flexural strength of microcomposites increases after down- as well up-thermal shock treatments. Whereas, for nanocomposites there is an incremental improvement in flexural strength after down-thermal shock conditioning and the decrease of its value has been observed after up-thermal shock treatment.

The larger surface/volume ratio in alumina nanoparticles in comparison to microparticles implies more surface area contact with the copper matrix for the former. The implications of thermal treatments for both the up-and down-thermal shocks are likely to affect more particle/matrix interfaces in nanoparticles embedded copper matrix system. Thus it may reasonably be proposed that the differential co-efficient of thermal expansion of copper and alumina may manifest larger amount of interfacial damage in nanosystem, because of an exposure to a temperature gradient in a short span of time. That is why more degradation has been observed in nanocomposites.

The enhancement of property has also been observed in few cases for both the systems. This may be manifested by an improvement in mechanical keying factor. The improvement by keying factor may sometimes get nullified and/or diminished during exposure in an opposite direction of thermal cycling. These contradictory and inconclusive natures of behaviour might be attributed by the generation of opposite and complex residual stresses during exposure to high to low and low to high temperature cycles.

b. Thermal conditioning

The specimens had experienced a temperature of +80°C and -80°C separately which were conditioned at that temperature for an hour. The microcomposites reflect a decrease in flexural strength after +80°C temperature conditioning. Nanocomposites show an increase in flexural value at +80°C temperature, and decrease at -80°C temperature conditioning respectively.

The reduction in mechanical property during cryogenic conditioning may be attributed by the de-cohesion between alumina particle and copper matrix in nanocomposites. This might have been manifested because of large difference in co-efficient of thermal contraction between particle and matrix.

The high temperature exposure of nanocomposites has demonstrated an increase in mechanical property. It may be reasonably assumed that differential expansion may be leading to better particle matrix registry and thereby closer proximity is ensured.

The lower surface area/volume ratio of microparticle in comparison to the nanoparticle embedded copper matrix has shown no significant changes for cryogenic temperature conditioning and a decline in flexural strength at high temperature conditioning. The forced close intimacy of the alumina microparticle and matrix at high temperature leads to development of residual stresses at the particle/matrix interfacial region. This non-uniform distribution of residual stresses may decrease the threshold value of crack nucleation and propagation along the particle/matrix interface region. The differential co-efficient of thermal expansion between alumina particle and copper matrix has lesser impact and implications either in advancement or declination of mechanical property in micro-alumina reinforced copper composites.

c. High temperature in-situ flexural test

The composites were tested at 100°C and 250°C temperatures, and these temperatures were maintained constant throughout the experiment. The increase in flexural strength at 100°C and decrease in flexural strength at 250°C discusses about the poor high temperature sustainability of microcomposites. The nancomposites also reveal low flexural strength at 250°C.

The increase in flexural strength at 100°C is due to the effective gripping of alumina particle and copper matrix due to relatively higher expansion of copper than alumina. The residual stress

development triggers the forced close registry between particle and matrix imposed by high temperature (250°C) conditioning. This may not be conducive for the generated residual stresses to be distributed properly and uniformly. These accumulated non-uniform residual stresses may decrease the threshold value of crack nucleation and propagation along the particle/matrix interface region.

3.3.7 Summary and Conclusions

Cu-Al_2O_3 and Al-Al_2O_3 micro- and nano-composites were fabricated by conventional powder metallurgy route. Both up- and down-thermal shock treatments enhance the ultimate flexural strength of Cu-Al_2O_3 and Al-Al_2O_3 microcomposites. Thermal conditioning at +80°C improves the ultimate flexural strength of Cu-Al_2O_3 nanocomposites and Al-Al_2O_3 micro- and nano-composites. Thermal conditioning at -80°C elevates the ultimate flexural strength of Al-Al_2O_3 nanocomposites. At high operating temperatures (i.e. 250°C) the ultimate flexural strength of both Cu-Al_2O_3 micro- and nano-composites decreases but for Al-Al_2O_3 microcomposites the strength increases. SEM micrographs reveal ductile mode of fracture for both micro- and nano-composites. The nanoparticles in nanocomposites have higher surface area as compared to microparticles in microcomposites. So, the thermal shock induced stress in nanocomposites is more visible in terms of degradation and enhancement of flexural strength. The development and detoriation of physical integrity of composite is predominant in nanocomposites than microcomposites**.** Noticeable differences in the flexural strength and response to thermal exposures of the micro- and nano-composites have been observed, and have been explained in terms of difference in their fracture surface microstructures.

References

[1] B. Inem, G. Pollard, Interface structure and fractography of a magnesium-alloy metal-matrix composite reinforced with SiC particles, *J. Mater. Sci*. 28 (16) (**1993**) 4427-4434.

[2] B.C. Ray, Effects of thermal and cryogenic conditionings on mechanical behaviour of thermally shocked Glass Fiber/Epoxy composites, *J. Reinf. Plast. Compos*. 24 (7) (**2005**) 713-717.

[3] G. Meijer, F. Ellyin, Z. Xia, Aspects of residual thermal stress/strain in particle reinforced metal matrix composites, *Composites: Part B*, 31 (1) (**2000**) 29-37.

[4] A. Kostka, J. Lelatko, M. Gigla, H. Morawiec, A. Janas, TEM study of the interface in ceramic-reinforced aluminium-based composites**,** *Mat. Chem. Phy*. 81 (2) (**2003**) 323-325.

[5] B.C. Ray, Thermal shock on interfacial adhesion of thermally conditioned glass fiber/epoxy composites, *Mater. Lett*. 58 (16) (**2004**) 2175-2177.

[6] S. Ho, E.J. Lavernia, Thermal residual stresses in metal matrix composites: a review *Appl. Compos. Mater*. 2 (1) (**1995**) 1-30.

[7] N. Chawla, C. Andres, L.C. Davis, J.W. Jones, J.E. Allison, The Interactive role of inclusions and SiC reinforcement on the high cycle fatigue resistance of particle reinforced metal matrix composites, *Metall. Mater. Trans. A* 31 (**2000**) 951-957.

[8] M. Zhao, G. Wu, D. Zhu, L. Jiang, Z. Dou, Effects of thermal cycling on mechanical properties of AlN_p/Al composite**,** *Mat Lett*. 58 (12) (**2004**) 1899-1902.

[9] J.J. Bhattacharyya, R. Mitra, Effect of hot rolling temperature and thermal cycling on creep and damage behaviour of powder metallurgy processed Al-SiC particulate composite, *Mat. Sci. Eng. A* 557 (**2012**) 92-105.

[10] B.C. Ray, Temperature effect during humid ageing on interfaces of glass and carbon fibers reinforced epoxy composites**,** *J. Colloid Interf. Sci*. 298 (1) (**2006**) 111-117.

[11] G. Thomas and J. Washburn, Electron microscopy and strength of crystals, Interscience publishers., New York, **1963**, 131-181.

[12] Surajit Kumar Paul, Predicting the flow behavior of metals under different strain rate and temperature through phenomenological modelling, *Comput. Mat. Sc.* 65 **(2012)** 91–99.

[13] G.E. Dieter, Mechanical Metallurgy, McGraw-Hill Book Co., New York, Second Edition **1976**, 145-183.

[14] E. Martin, A. Forn, R. Nogue, Strain hardening behaviour and temperature effect on Al-2124/SiC_p, *J. Mater. Process. Tech*. 143-144 (**2003**) 1-4.

[15] M. Taya, K.E. Lulay, D.J. Lloyd, Strengthening of a particulate metal matrix composite by quenching**,** *Acta. Metal. Mater*. 39 (1) (**1991**) 73-87.

[16] R.W. Hertzberg, Deformation and fracture mechanics of engineering materials, John Wiley and sons., Fourth edition., **1996**.

[17] L. Ceschini, G. Minak, A. Morri, Tensile and fatigue properties of the AA6061/20 vol.% Al_2O_{3p} and AA7005/10 vol.% Al_2O_{3p} composites, *Compos. Sci. Technol.* 66 **(2006)** 333–342.

[18] C.M.L Wu, G.W. Han, Thermal fatigue behaviour of SiC_p/Al composite synthesized by metal infiltration, *Composites: Part A* 37 (**2006**) 1858-1862.

[19] Y. Uematsu , K. Tokaji, M. Kawamura, Fatigue behaviour of SiC-particulate-reinforced aluminium alloy composites with different particle sizes at elevated temperatures**,** *Compos. Sci. Technol*. 68 (13) (**2008**) 2785-2791.

3.4 An exploratory study on the effect of loading rate on flexural strength of Cu-Al_2O_3 and Al-Al_2O_3 micro- and nano-composites

3.4.1 Scope and objectives of the work

Different loading rates are quite probable in several applications of metal matrix composites to evaluate their crashworthiness [1]. High impact loading conditions are withstood at instances such as MMC armours, collision of cars and impact of foreign objects on aerospace structures. Metal matrix composites respond differently to high strain rate loading conditions as compared to monotonic or quasistatic loading [2]. As loading rate is directly proportional to strain rate, we can assume the changes in behaviour of material to possess similarity in both the cases. As strain rate is increased from quasi-static to dynamic, the temperature conditions gradually change from isothermal to fully adiabatic. There is thermo-mechanical coupling in the adiabatic stress-strain curves i.e the effects of strain hardening, strain/rate strengthening and thermal softening caused by the adiabatic temperature increase couple together. The dislocation density is an internal state variable which is a function of plastic deformation [3]. The heterogeneous microstructure of composites necessitates the evaluation of mechanical strength at different loading conditions. Residual stresses also play a vital role in the effect of loading speed on composites. Loading rate sensitivity of metal matrix composites is a function of loading rate sensitivity of the matrix as well as the status and stability between particles and matrix [4].

3.4.2 Fabrication of composites

3.4.2a Copper-alumina composite

Copper powder (Loba Chemie) (average particle size~11μm, purity >99.7%) was used as the matrix material. Alumina powders (Sigma Aldrich) (average particle size~10μm and < 50 nm) were selected as the reinforcement material. The Cu with 5, 10, 20 vol. % Al_2O_3 (10 μm) microcomposites and Cu with 1, 3, 5 vol. % Al_2O_3 (< 50 nm) nanocomposites powders were blended separately. The specimens having dimensions (31.5 x 12.7 x 6.3 mm^3) were prepared by

compacting the powders at a pressure of 500 MPa as per ASTM B 925-08 for 3-point flexural test. The compacted specimens were sintered conventionally at 900°C for 90 minutes in argon atmosphere.

3.4.2b Aluminium-alumina composite

Aluminium powder (Loba Chemie) (average particle size~22μm, purity- >99.7%) was used as the matrix material. Alumina powders (Sigma Aldrich) (average particle size~10μm and < 50 nm) were selected as the reinforcement material. The Al-5, 10, 20 vol. % Al_2O_3 (10 μm) microcomposites and Al-1, 3, 5 vol. % Al_2O_3 (< 50 nm) nanocomposites powders were blended separately. The specimens having dimensions (31.5 x12.7 x 6.3 mm^3) were prepared by compacting the powders at a pressure of 400 MPa as per ASTM B 925-08 for 3-point flexural test. The compacted specimens were sintered conventionally at 600°C for 90 minutes in argon atmosphere.

3.4.3 Effect of loading rate on the flexural strength of composites

3-point flexural test was carried out at loading rates of 0.5, 1, 10, 100, 500, 1000 mm/min for copper-alumina and aluminium-alumina micro- and nano-composites maintaining a span length of 26 mm in universal testing machine (INSTRON-5967).

3.4.3a Copper-alumina composite

The flexural strength of copper-alumina nanocomposites increases with increase in loading rate whereas the microcomposites show an increase-decrease trend (Fig. 3.4.1 & 3.4.2). The effect of loading rate on the flexural strength of Cu-Al_2O_3 microcomposites is not statistically significant. The drop in flexural strength at some instances could be attributed to the presence of non-uniform crack density. A tendency of increase in flexural strength with increasing loading rate has been recorded for Cu-1, 3 vol. % Al_2O_3 nanocomposites. This increase in strength is absent in 5 vol. % alumina reinforced copper nanocomposites, probably because of higher degree of agglomeration of nanoparticles, it indicates analogy with microcomposites behaviour for the loading rate effect. At higher loading rates relaxation time incurred is less hence the composites become stiffer and exhibit strengthening effect.

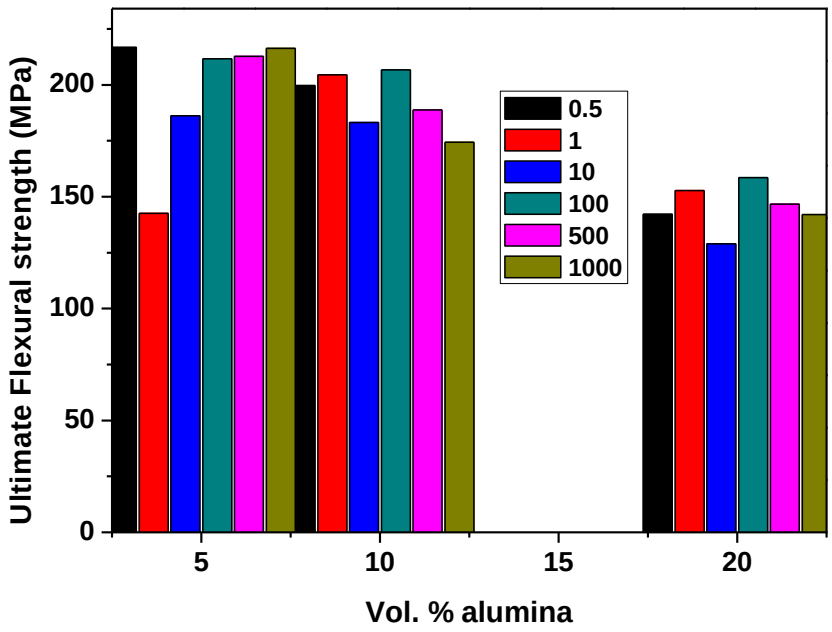

Fig. 3.4.1 Variation in flexural strength of Cu-Al_2O_3 microcomposites at different loading rates

The relationship between loading rate and strain rate is as follows

Strain rate, $\dot{\varepsilon} = \frac{d\varepsilon}{dt}$ (1)

Cross head velocity, $v = \frac{dL}{dt}$ (2)

Engineering / Conventional strain rate, $\dot{e} = \frac{de}{dt}$

$$= \frac{d[\frac{(L-L_0)}{L_0}]}{dt}$$

$$= \frac{1}{L_0}\frac{dL}{dt}$$

$$\dot{e} = \frac{v}{L_0} \quad (3)$$

Hence, $\dot{e} \propto v$

Where L_o is the original length and L is the length after time t [5]

The loading rate sensitivity of composites increases with addition of particles which is visible from Cu-1 vol. % Al_2O_3 to Cu-3 vol% Al_2O_3 nanocomposites. The increase in flexural strength with increasing loading rate could be due to the constrained plastic flow of the matrix, which is sufficiently high in nanoparticle embedded composites. The strain induced in matrix and reinforcement is differential in nature and hence this strain mismatch leads to dislocation generation eventually altering the mobility of dislocations. The degree of misfit strain fluctuates at varied loading speeds and leads to formation of typical dislocation sub-structures [6]. Particle/matrix interfaces are preferential cavity nucleation sites [7]. Cavitation takes place at particle/matrix interface at high loading rates during bending test, which grows and leads to interfacial de-cohesion and ultimately fracture.

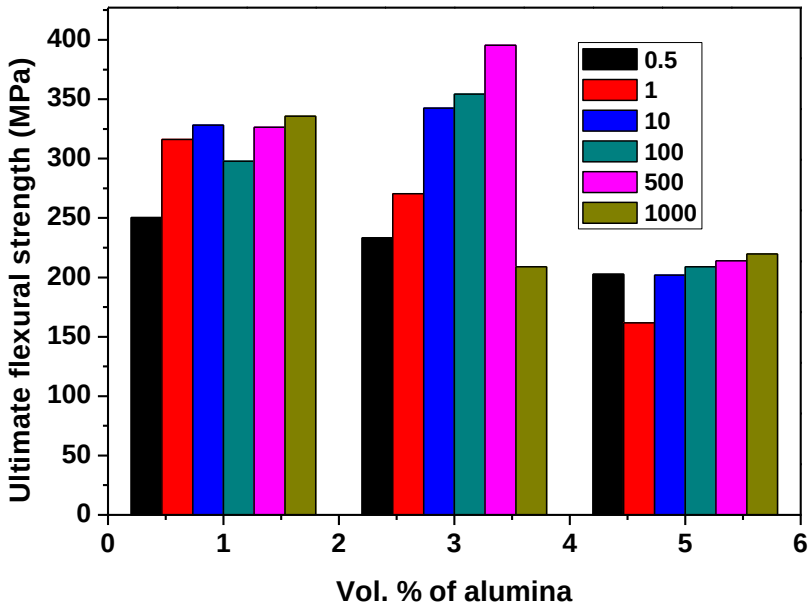

Fig. 3.4.2 Variation in flexural strength of Cu-Al_2O_3 nanocomposites at different loading rates

3.4.3b Aluminium-alumina composite

The flexural strength of Al-Al_2O_3 microcomposites and nanocomposites at different loading rates has been illustrated in Fig. 3.4.3 & 3.4.4. The Al matrix micro- and nano-composites show similar trend of possessing higher strength at medium loading rates. As the loading rates increase the flexural strength initially rises and then drops for both micro- and nano-composites showing

an increase-decrease trend. At high strain rates composites experience higher strain rate sensitivity than the monolithics. Strain rate sensitivity of composites mostly adheres to the strain rate sensitivity behaviour of the corresponding matrices. Increasing particle content increases strain rate sensitivity.

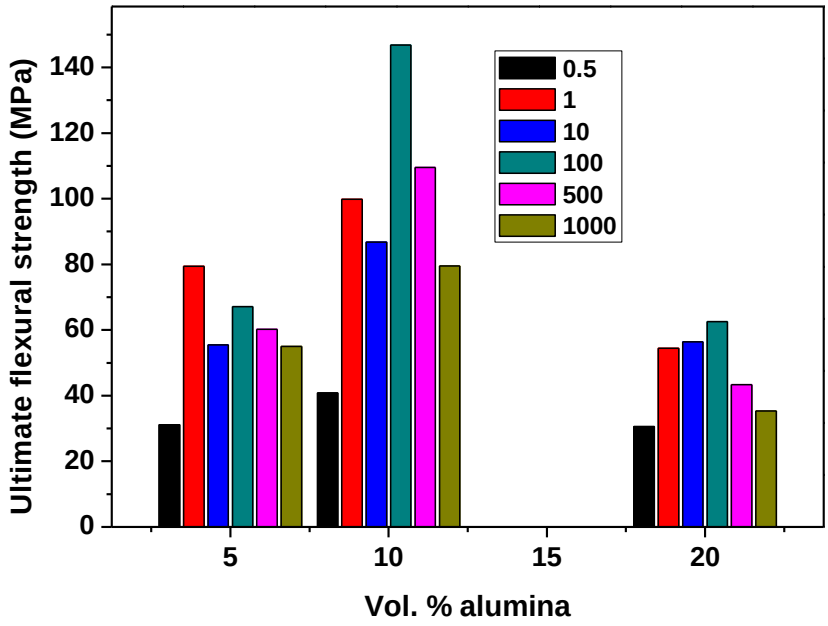

Fig. 3.4.3 Variation in flexural strength of Al-Al_2O_3 microcomposites at different loading rates

At higher loading rates the stress transmissibility from the matrix to reinforcement particle may not take place effectively due to time constraint, so it becomes more of a matrix phenomenon. At medium loading rates near uniform load distribution is anticipated; hence the composites possess higher strength at medium loading rates.

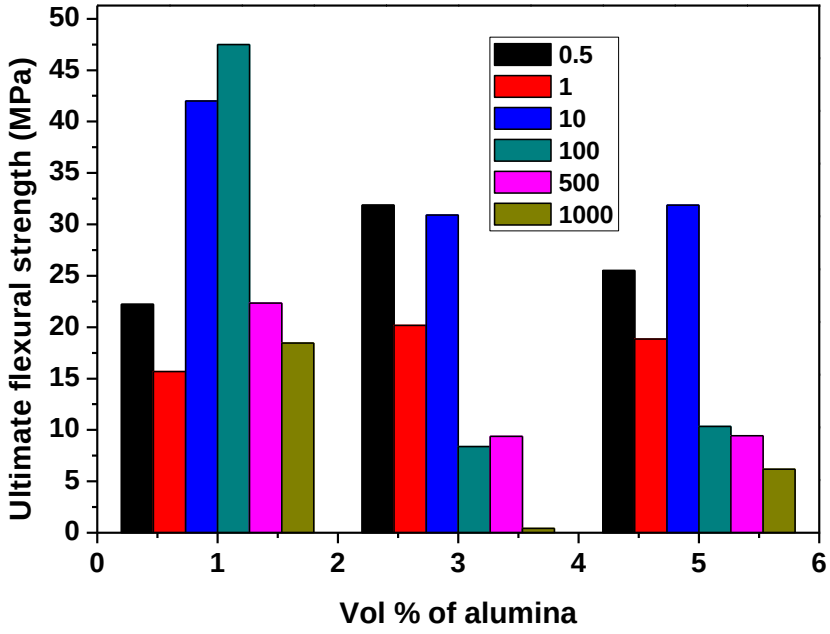

Fig. 3.4.4 Variation in flexural strength of Al-Al_2O_3 nanocomposites at different loading rates

3.4.4 Summary and Conclusions

Loading rate sensitivity is evident at lower range of loading rates, thereafter strength decreases with increase in loading speed. Cu-Al_2O_3 and Al-Al_2O_3 composites are seemingly loading rate sensitive materials. As the dislocation density evolution is different at different loading rates, these materials are loading rate sensitive. The flexural strength with respect to crosshead speed of copper and aluminium based composites varies with size and content of alumina particles.

References

[1] S. K. Paul, Predicting the flow behaviour of metals under different strain rate and temperature through phenomenological modelling, *Comp. Mater. Sci.* 65 (**2012**) 91-99.

[2] Y. Zhou, Y. Xia, Experimental study of the rate sensitivity of SiC_p /Al composites and the establishment of a dynamic constitutive equation, *Compos. Sci. Tech.* 60 (**2000**) 403-410.

[3] J.A. Rodriguez-Martinez, M. Rodriguez-Millan, A. Rusinek, A. Arias, A dislocation-based constitutive description for modelling the behaviour of FCC metals within wide ranges of strain rate and temperature, *Mech. Mater*. 43 (**2011**) 901-912.

[4] G. Bao, Z. Lin, High strain rate deformation in particle reinforced metal matrix composites, *Acta. Mater.* 44 (3) (**1996**) 1011-1019.

[5] G.E. Dieter, Mechanical Metallurgy, McGraw- Hill, London, United Kingdom, Third Edition **1988**.

[6] S. Yadav, D.R. Chichili, K.T. Ramesh, The mechanical response of a 6061-T6 Al/Al_2O_3 MMC at high rates of deformation, *Acta. Metall. Mater*. 43 (12) (**1995**) 4453-4464.

[7] G. Q. Tong, K.C. Chan, High strain rate superplasticity of an Al-4.4Cu-1.5Mg/21SiC_w composite sheet, *Mat. Sci. Eng. A* 286 (**2000**) 218-224.

Chapter 4

Summary and Conclusions

This thesis studies the problem of structural integrity with the variation of fabrication parameters and also by inducing thermal stresses in copper and aluminium matrix composites varying the reinforcement particle size (i.e. micro- and nano-particles) and volume fraction. The comparison in micro-structural integrity both for micro- and nano-composites have been recorded at all points of experimentation (i.e. for variation in fabrication parameters and thermal conditionings) with the help of electron microscopy.

- Cu-5 vol. % Al_2O_3 and Al-5 vol.% Al_2O_3 micro-and nano-composites were fabricated by milling and blending of copper-alumina and aluminium-alumina powders followed by conventional sintering. Milling reduces the particle size of composite powders with increasing milling time. X-ray diffraction, particle size analysis and microstructure reveal particle size reduction and good distribution of alumina particles in copper and aluminium matrix powders. Microhardness values of milled samples are higher than blended samples. Blending of powders followed by sintering impart higher density than

milled and sintered samples. Grain refinement of copper and aluminium is observed with increasing milling time. Milling process demonstrates plastic deformation, micro-welding and particle fragmentation as evident from SEM micrographs.

- The Cu-Al_2O_3 microcomposites fabricated via conventional sintering route in nitrogen, argon and hydrogen atmospheres yielded appreciable properties for hydrogen atmospheres. The densification process is more efficient in the case of hydrogen than in nitrogen or argon atmosphere. The microstructure of the composites sintered in hydrogen atmosphere reveals better matrix-reinforcement bonding. The problem of poor interfacial bonding in nitrogen and argon atmosphere has been addressed up to a certain extent using hydrogen atmosphere. The EDS analysis also proves the same. The formation of Cu_2O during sintering in nitrogen and argon atmosphere reduced the extent of bonding between copper and alumina. The density and hardness values are also in accordance to the above fact.

- The Cu-Al_2O_3 and Al-Al_2O_3 micro- and nano-composites were fabricated by blending-compaction-sintering powder metallurgy route at different sintering temperatures. The microcomposites possess better properties (density and hardness) at higher sintering temperatures. Whereas the nanocomposites show appreciable properties at low temperatures. The incorporation of Al_2O_3 nanoparticles strengthens the matrix to a greater extent resulting in increase of microhardness compared to Al_2O_3 microparticles. The microstructures of micro- as well as nano-composites demonstrate better distribution in the later. Compressive strength is highest for the Cu-15 vol. % Al_2O_3 microcomposites. Flexural strength drops with increase in alumina content. Fractography of the microcomposites and nanocomposites revealed mixed mode of fracture in both the cases. The wear resistance of nanocomposites is higher than the microcomposites under the same experimental conditions. The rise in reinforcement content imparts higher microhardness, low density and high wear resistance values for both the systems.

- Cu-Al_2O_3 and Al-Al_2O_3 micro-(1, 5, 20 vol. %) and nano-(0.5, 1, 3, 5, 7 vol. %) composites were fabricated by spark plasma sintering technique. In Cu-Al_2O_3 system,

XRD analysis shows the presence of Cu, Al_2O_3 and $CuAlO_2$ in both the micro- as well as nano-composites. The SEM micrographs show the presence of annealing twins during fabrication by SPS in both nano- and micro-composites. TEM micrographs suggest the formation of a third phase i.e. $CuAlO_2$ (copper aluminate) around the alumina particles. The hardness measurements show that the nanocomposites are harder than microcomposites. The wear resistance of microcomposites is higher than the nanocomposites. The possible wear mechanisms for both composites are microploughing, delamination as well as microcrack formation. The wear mechanisms operating in the micro- and nano-composites is dominated by the reinforcement particle size effect and their implications. We have obtained 95.82% densification and 93.17 $HV_{0.3}$ hardness for spark plasma sintered Cu-20 vol. % Al_2O_3 microcomposite. The elastic modulus of Cu-1% alumina nanocomposite is obtained as 128 GPa. The wear rate is appreciably low i.e. 0.86×10^{-4} $mm^3N^{-1}m^{-1}$ for 20 vol.% alumina reinforced copper microcomposite.

- In Al-Al_2O_3 system, the distribution of alumina particles in the aluminium matrix is homogeneous and uniform both in nanocomposites and microcomposites (slightly better distribution in nanocomposites than microcomposite). The interface of aluminium and alumina in nanocomposites is seemingly sound than in the case of microcomposite i.e. the compatibility of alumina in aluminum matrix in nanocomposites is better than in the microcomposites. The TEM and SEM micrographs reveal a lack of intimate proximity between matrix and reinforcement entities in microcomposites. Almost full densification in case of 1 vol. % alumina reinforced nano- and microcomposites have been achieved. The density of microcomposites as well as nanocomposites decreases with increasing alumina content. The nanoindentation hardness of nanocomposites is higher than the corresponding microhardness values. The highest nanohardness recorded was 0.85 GPa for 7 vol. % Al-Al_2O_3 nancomposites.

- Up- and down-thermal shock treatments enhance the ultimate flexural strength of Cu-Al_2O_3 and Al-Al_2O_3 microcomposites. The variation of flexural strength is contradictory and far from comprehensive conclusion in Cu-Al_2O_3 nanocomposites. Thermal

conditioning at +80°C temperature improves the ultimate flexural strength of Cu-Al_2O_3 as well as Al-Al_2O_3 nanocomposites. Al-Al_2O_3 nanocomposites get thermally conditioned at -80°C too. At high operating temperatures (i.e. 250°C) the ultimate flexural strength of both Cu-Al_2O_3 micro- and nano-composites decreases. Al-Al_2O_3 nanocomposites show elevation of flexural strength at 100°C, whereas the strength again falls at 250°C, whereas the microcomposites show positive trend for both 100°C and 250°C temperatures. SEM micrographs reveal ductile mode of fracture for both micro- and nano-composites. Ductile fracture characteristics have been observed predominantly for Cu-Al_2O_3 and Al-Al_2O_3 microcomposites. Fracture characters visible in Cu-Al_2O_3 and Al-Al_2O_3 nanocomposites indicate ductile mode of failure. The fracture mechanisms demonstrated were interfacial de-cohesion, particle cracking, interfacial dis-integrity and particle pull-out. The nanoparticles in nanocomposites have higher surface area as compared to microparticles in microcomposites. So, the thermal shock induced stress in nanocomposites is more visible in terms of degradation and enhancement of flexural strength. The development and detoriation of physical integrity of composite is predominant in nanocomposites than microcomposites**.** Noticeable differences in the flexural strength in response to thermal exposures of the micro- and nano-composites have been observed, and have been explained in terms of difference in their fracture surface microstructures.

- Cu-Al_2O_3 and Al-Al_2O_3 composites are loading rate sensitive materials. The flexural strength of copper and aluminium based composites varies with size and content of alumina particles. Loading rate sensitivity is evident at lower range of loading rates, thereafter strength decreases with increase in loading speed. As the dislocation density evolution is different at different loading rates, these materials are loading rate sensitive.

List of papers based on the thesis

International Journal publications

[1] **K. Dash**, S. Panda and B.C. Ray, "*Effect of thermal and cryogenic conditioning on flexural behavior of thermally shocked Cu-Al_2O_3 micro- and nano-composites"*, **Metallurgical and Materials Transactions A** (accepted) DOI: 10.1007/s11661-013-2070-7.

[2] **K. Dash**, D. Chaira, B.C. Ray, "*Synthesis and characterization of aluminium-alumina micro- and nano-composites by spark plasma sintering"*, **Materials Research Bulletin**. 48 (2013) 2535-2542.

[3] **K. Dash**, B.C. Ray and D. Chaira, "*Synthesis and characterization of copper-alumina metal matrix composite by conventional and spark plasma sintering"*, **Journal of Alloys and Compounds**. 516 (2012) 78– 84.

[4] S. Panda, **K. Dash** and B.C. Ray, "*Processing and properties of Cu based micro- and nano-composites"*, **Bulletin of Materials Science** (accepted).

[5] **K. Dash**, S. Panda and B.C. Ray, "*Process and progress of sintering behavior of copper-alumina composite"*, **Emerging Materials Research**. 2 (2013) 32-38.

[6] S. Gupta, **K. Dash** and B.C. Ray, "*Analysis of properties of copper-alumina composites produced by various processing routes: a review"*, **Journal of Materials and Metallurgical Engineering**. 2 (2012) 11-23.

[7] **K. Dash**, D. Chaira and B.C. Ray, "*Microstructural investigation and wear studies on copper-alumina micro- and nano-composites fabricated by spark plasma sintering"*, (under review) **Metallography, Microstructure and Analysis**.

[8] **K. Dash**, S. Sukumaran, B.C. Ray, "*The behaviour of aluminium based composites under thermal stresses"*, (under review) **Science and Engineering of Composite Materials**.

International proceedings

[1] **K. Dash** and B.C. Ray, "*A study on thermal shock response of Al-Al_2O_3 micro-and nanocomposites"*, **19th International conference on composite materials**, 28th July-2nd August, Montreal, Canada.

[2] **K. Dash**, S. Gupta, S. Gupta and B.C. Ray, "*Effect of thermal shock on the microstructure and mechanical properties of Cu-Al_2O_3 composites"*, **International conference on recent advances in composite materials**, Feb 18th-21st 2013, Goa.

Conferences attended and published abstracts

[1] **K. Dash**, D. Chaira and B.C. Ray, "*Microstructural Studies of Al-Al_2O_3 Nanocomposites Prepared by Powder Metallurgy Route"*, **National Metallurgical Day-Annual Technical Meeting** Nov-2011, Hyderabad.

[2] **K. Dash**, D. Chaira and B.C. Ray, "*Characterization of SPS sintered Cu-Al_2O_3 metal matrix nanocomposites"***, ICAMMP**, IIT Kharagpur, Dec 9-11, 2011.

[3] **K. Dash**, D. Chaira and B.C. Ray, "*Comparative study of Al-Al_2O_3 Micro- and Nano-composites Prepared by Powder Metallurgy Route"*, **International Conference on Nanoscience + Technology (ICNT) 2012**, 23-27 July, Paris.

[4] **K. Dash**, S. Panda and B.C. Ray, "*Failure analysis of Cu-Al_2O_3 composites with the variation of reinforcement particle size and content"*, **International conference on strength of materials**, IISc Bangalore, Aug 19-24, 2012.

[5] **K. Dash**, S. Gupta, S. Gupta and B.C. Ray, "*Effect of sintering temperature on Al-Al_2O_3 composites fabricated by powder metallurgy route"*, **National Metallurgical Day-Annual Technical Meeting** Nov-2012, Jamshedpur.

Awards

K. Dash and S. Panda, "*A micromechanics approach to evaluate the interface of metal matrix composites*", **New idea poster competition, CSIR foundation day**, IMMT Bhubaneswar, 26th Sept, 2011.

Biography of the scholar

Khushbu Dash was born in Raipur, Chattisgarh, India on 17th August, 1985. She finished her schooling from Carmel School, Rourkela (ICSE board) and intermediate from Deepika E.M. School, Rourkela (CBSE board). She obtained her bachelors in science (B.Sc) from Osmania University, Hyderabad with biotechnology, biochemistry and chemistry subjects in 2006. She pursued her masters in science (M.Sc chemistry) from National Institute of Technology, Rourkela in 2008. She got selected under the Indian Academy of Science banner to take up her summer project in Indian Institute of Science, Bangalore under Prof D.D. Sarma in solid state structural chemistry unit in the field of zinc oxide nanocrystals. She completed her final year masters project in the field of core-shell nanocomposites under Prof G. Hota in National Institute of Technology, Rourkela. She served a premier institute named FIITJEE ltd in New Delhi for 1 year in 2008-09 where she taught chemistry to intermediate students who were aspirants of IIT-JEE exam which is India's toughest exam to crack to get into undergraduate program in engineering in leading institutes of India i.e. to the IITs. She qualified the CSIR-UGC NET exam in her M.Sc final year which entitled her to obtain fellowship during PhD programme. She enrolled herself for pursuing PhD in the department of Metallurgical and Material Engineering, National Institute of Technology, Rourkela in 2009 financed by MHRD, Govt of India, under Prof Bankim Chandra Ray and Prof. Debasis Chaira working on the thesis titled "Processing and characterization of Cu-Al_2O_3 and Al-Al_2O_3 composites: an evaluation for micro- and nano-particulate reinforcements". She worked with spark plasma sintering in the Indian Institute of Technology, Kanpur, with transmission electron microscopy, in Indian Institute of Technology, Kharagpur and with nanoindentation in the Institute of Materials and Minerals Technology, Bhubaneswar. She has published papers in frontier journals such as Metallurgical and Materials Transactions A, Materials Research Bulletin, Journal of Alloys and Compounds and Bulletin of Material Science. Her research interests comprises of metal matrix composites, powder metallurgy, thermal loadings, loading rate and electron microscopy of interfaces in composites. She is interested to pursue post-doctoral research in an internationally renowned university in the line of core materials engineering to unravel the science of interface behind the composite technology.